ESTIMATION OF TURBULENT HEAT FLUXES VIA THE SYNERGISTIC ASSIMILATION OF LAND SURFACE TEMPERATURE, AIR TEMPERATURE AND SPECIFIC HUMIDITY INTO A VARIATIONAL DATA ASSIMILATION MODEL

A DISSERTATION SUBMITTED TO THE GRADUATE DIVISION OF THE UNIVERSITY OF HAWAIʻI AT MĀNOA IN PARTIAL FULFILLMENT OF THE REQUIREMENTS FOR THE DEGREE OF

DOCTOR OF PHILOSOPHY

IN

CIVIL AND ENVIRONMENTAL ENGINEERING

MAY 2019

By

Elahe Tajfar

Dissertation Committee:

Sayed M. Bateni, Chairperson

Roger W. Babcock Jr

Aly I. El-Kadi

Lin Shen

Tomoaki Miura

DEDICATION

This dissertation is wholeheartedly dedicated to my loving

Mother, *Father*, and only *Brother*

whose love for me knows no bounds.

Your endless kindness enriches my soul and reminds me to be a better person every day.

Acknowledgments

I would like to thank my advisor Dr. Sayed Bateni, for his guidance and support during these past five years. I would also like to thank my committee members, Prof. Roger Babcock, Prof. Aly El-Kadi, Dr. Lin Shen, and Prof. Tomoaki Miura for their insightful comments and encouragement.

I will forever be thankful to my former research advisor, Prof. Jamshid Mousavi. He has been helpful in providing advice many times during my graduate school career. He was and remains my best role model for a scientist, mentor, and educator. I am deeply indebted to him.

My special thanks go to Janis Kusatsu, she is a wonderful and caring person who makes life easier for the people around her.

I extend my gratitude and warmest aloha to all my friends and colleagues in Hawai'i who have provided invaluable love, guidance and friendship. They showed me life was not all about academics.

Finally, I would like to express my deepest love and appreciation to my family. I thank my parents, my brother, and my sister-in-law who have trusted me in every one of my decisions. Thank you for your unconditional love and support every time I needed them. I also extend my special thanks to Sara for her unfailing love and friendship. I thank my grandparents, uncles, and aunts for their constant support and encouragement. I owe you so much for your unquestioning faith in me throughout my entire journey in academia.

ABSTRACT

The balance of energy at the Earth's surface is linked to the overlying atmospheric boundary layer (ABL). The sensible (*H*) and latent (*LE*) heat fluxes are important components of Earth's radiation budget and its climate system, which directly influence the properties of the boundary layer and characterize exchange of heat and moisture between the land surface and its overlying atmosphere. Therefore, their accurate estimation is of crucial importance for a better understanding of land surface-atmosphere exchange processes and obtaining the heat and moisture budgets. Different approaches have been developed to estimate turbulent heat fluxes (i.e., *H* and *LE*). A number of studies used time-series of air temperature and specific humidity observations to estimate turbulent heat fluxes. These works require the specification of surface roughness lengths for heat and momentum and/or ground heat flux, which are often unavailable. This study estimates turbulent heat fluxes and the atmospheric boundary layer (ABL) height, potential temperature, and humidity by assimilating sequences of air temperature and specific humidity into an atmospheric boundary layer model within a new variational data assimilation (VDA) framework. The unknown parameters of the VDA system are neutral bulk heat transfer coefficient (C_{HN}) and evaporative fraction (*EF*). It needs neither the surface roughness parameterization nor ground heat flux measurements. The performance of the developed VDA approach is tested over the First International Satellite Land Surface Climatology Project Field Experiment (FIFE) site for the summer of 1987 and 1988. The results show that the developed VDA framework is capable of estimating the unknown parameters (i.e., *EF* and C_{HN}) reasonably well. The developed VDA model can predict the turbulent heat fluxes fairly accurately at the FIFE site. In addition, the ABL height, specific humidity, and potential temperature estimates from the VDA system are reasonably close to those inferred from the radiosondes both in terms of magnitude and diurnal trend. The introduced VDA framework is advanced by the synergistic assimilation of LST, air temperature and specific humidity into a coupled land surface-ABL model. The augmented VDA system is also validated at the FIFE sites. It outperforms the previous study in which air temperature and specific humidity were assimilated. Finally, both developed VDA approaches are tested at five sites (namely, Desert, Audubon, Bondville, Brookings, and Willow Creek) with contrasting climatic and vegetative conditions. The results show that the first VDA system (that assimilates reference-level air temperature and specific humidity) performs well at wet/densely vegetated sites (e.g., Willow Creek), but its performance degrades at dry/slightly vegetated sites (e.g., Desert). These outcomes show that the sequences of reference-level air temperature and specific humidity have more information on the partitioning of available energy between the sensible and latent heat fluxes in wet and/or densely vegetated sites than the dry and/or slightly vegetated sites. The second VDA approach (that assimilates LST, reference-level air temperature and specific humidity) outperforms the first approach that assimilated only the state variables of atmosphere (i.e., reference-level air temperature and humidity), and can accurately estimate turbulent heat fluxes over a wide variety of environmental conditions.

Table of Content

List of Tables

List of Figures

List of Symbols

A	Entrainment parameter	[-]
B	Stanton number	[-]
B_{EF}^{-1}	inverse background error covariance of EF	[-]
B_R^{-1}	inverse background error covariance of R	[-]
c	Soil volumetric heat capacity	[J m^{-3} K^{-1}]
C_{HN}	neutral bulk heat transfer coefficient	[-]
c_p	specific heat capacity of dry air	[J kg^{-1} K^{-1}]
D_1, D_2	dissipation of mechanical turbulent energy	[m^3 s^{-3}]
d	zero-plane displacement height	[m]
E	evaporative rate from ground	[kg m^{-2} s^{-1}]
EF	evaporative fraction	[-]
f	atmospheric stability correction function	[-]
G	ground heat flux	[W m^{-2}]
G_*	production of mechanical turbulent energy	[m^3 s^{-3}]
g	gravitational acceleration	[m s^{-2}]
H	sensible heat flux	[W m^{-2}]
H_{top}	entrainment sensible heat flux	[W m^{-2}]
H_v	virtual heat flux	[W m^{-2}]
h	mixed-layer height	[m]
J	objective functional	[-]
k	von Karman's constant	[-]
κ	empirical constant	[kg m^{-2}]$^{-1/7}$
L	Monin-Obhukov length	[m]
L_v	latent heat of vaporization	[J kg^{-1}]
LE	latent heat flux	[W m^{-2}]
LE_{top}	entrainment latent heat flux	[W m^{-2}]
LAI	leaf area index	[m^2 m^{-2}]
m	constant	[-]

N	number of days in the assimilation period	[-]
P_h	pressure at height h	[Pa]
P_s	surface pressure	[Pa]
p	soil thermal conductivity	[W m^{-1} K^{-1}]
q	mixed layer specific humidity (equation 5b)	[kg kg^{-1}]
q_a	specific humidity at the reference-level	[kg kg^{-1}]
q_h	specific humidity immediately above mixed layer	[kg kg^{-1}]
q_{SL}	specific humidity at the bottom of mixed layer (equation B2)	[kg kg^{-1}]
R	transformation variable	[-]
R_{Ad}	downwelling longwave radiation from within the mixed layer	[W m^{-2}]
R_{Au}	upwelling longwave radiation from within the mixed layer	[W m^{-2}]
R_{ad}	downwelling longwave radiation from above the mixed layer	[W m^{-2}]
R_d	gas constant for dry air	[J kg K^{-1}]
R_{gu}	upwelling longwave radiation from ground into the mixed layer	[W m^{-2}]
Ri	Richardson number	[-]
$R_l^{\downarrow}$	incoming longwave radiation	[W m^{-2}]
R_n	net radiation at the surface	[W m^{-2}]
$R_s^{\downarrow}$	incoming solar radiation	[W m^{-2}]
R_v	gas constant for water vapor	[J kg K^{-1}]
R_q^{-1}	inverse error covariance of q	[-]
R_T^{-1}	inverse error covariance of T	[K^{-2}]
R_θ^{-1}	inverse error covariance of θ	[K^{-2}]
SL	surface layer	[-]
T	land surface temperature	[K]
T_a	reference-level air temperature	[K]
T_h	air temperature immediately above the mixed layer Tv??	[K]
t	time	[s]
u	wind speed at the reference-level	[m s^{-1}]
u_{SL}	wind speed at the top of the surface layer	[m s^{-1}]
u_*	friction velocity	[m s^{-1}]

z	soil depth	[m]
z_{oh}	roughness length scales for heat	[m]
z_{om}	roughness length scales for momentum	[m]
z_{SL}	surface-layer height	[m]
z_{ref}	reference-level height	[m]
z_{veg}	vegetation height	[m]
α	surface albedo	[-]
δ_q	specific humidity inversion strength	[kg kg^{-1}]
δ_θ	potential temperature inversion strength	[K]
ε_a	atmospheric emissivity	[-]
ε_{ad}	effective emissivity above the mixed-layer	[-]
ε_d	effective mixed-layer downward emissivity	[-]
ε_u	effective mixed-layer upward emissivity	[-]
ε_m	mixed-layer bulk emissivity	[-]
ε_s	surface emissivity	[-]
γ_q	lapse rate of q above the mixed layer	[kg kg^{-1} m^{-1}]
γ_θ	lapse rate of θ above the mixed layer	[K m^{-1}]
$\lambda_1, \lambda_2, \lambda_3$	lagrange multipliers	[-]
Ψ_h	stability function for heat	[-]
Ψ_m	stability function for momentum	[-]
Ψ_q	stability function for water vapor	[-]
ρ	air density	[kg m^{-3}]
σ	Stefan-Boltzmann constant	[W m^{-2} K^{-4}]
θ	Mixed layer potential temperature (equation 5a)	[K]
θ_a	reference-level potential temperature	[K]
θ_{SL}	potential temperature at the bottom of mixed layer (equation B1)	[K]
φ	mechanical turbulence dissipation parameter	[-]
ξ	stability parameter	[-]

Chapter 1: Introduction

1.1. Background

The significance of land-atmosphere interaction in the Earth system has caused many studies to estimate turbulent heat fluxes [i.e., sensible (*H*) and latent (*LE*) heat fluxes] between the land surface and overlying atmosphere. To improve our understanding of the processes controlling land-atmosphere interaction, we need to quantify the turbulent heat fluxes. These fluxes are important components of Earth's energy budget and its climate system, which directly influence the properties of the boundary layer. Using ground-based instruments to measure turbulent heat fluxes is costly and challenging. Consequently, a number of approaches have been developed to estimate these fluxes using a variety of measurements that are indirectly related to fluxes (Kalma et al., 2008; Li et al., 2010; Maes and Steppe, 2012; Bateni et al., 2012b, 2013b; Xu et al., 2014, 2015; Zhuang and Wu, 2015; Lu et al., 2016; Brenner et al., 2017; Abdolghafoorian et al., 2017).

Generally, there are five major groups of studies for estimating turbulent heat fluxes. The first group, known as triangle methods, estimates latent heat flux by using empirical relations between land surface temperature (LST) and an vegetation indices (VI) such as normalized differential vegetation index (NDVI), leaf area index (LAI), etc. (Nishida et al., 2003; Wang et al., 2006; Carlson, 2007; Stisen, 2008; Tang et al., 2010; Sun et al., 2013; Martinez et al., 2017; Majozi et al., 2017). In the second group, diagnostic methods, the surface energy balance (SEB) equation is solved using instantaneous measurements of LST and micrometeorological data (Su, 2002; Liu et al., 2007; Jia et al., 2009; Kustas et al., 2012; Ma et al., 2012, 2015; Song et al.,

2016). The third group, combination methods, estimates turbulent heat fluxes by incorporating the LST observations into the Penman-Monteith equation (Mallick et al., 2013, 2014; Raoufi and Beighley, 2017). The fourth group, land data assimilation system (LDAS), estimates turbulent heat fluxes by the Ensemble Kalman Filter (EnKF) approach (Peters-Lidard et al., 2011; Xia et al., 2014a, 2014b; Bateni and Entekhabi, 2012b; Carrera et al., 2015; Xu et al., 2015, 2018). The fifth group, variational data assimilation (VDA) method, estimates turbulent heat fluxes by assimilating sequences of LST observations into the force-restore and/or heat diffusion equation (Caparrini et al., 2003, 2004a, b; Bateni and Entekhabi, 2012a, 2012b; Bateni et al., 2013a, 2013b, 2014; Xu et al., 2015, 2016, 2018, 2019; Abdolghafoorian et al., 2017; He et al., 2018). In these studies, the implicit information in the sequences of LST observations is used to partition the available energy between the sensible and latent heat fluxes. Performance of these VDA approaches degrades in wet and/or heavily vegetated sites (Crow and Kustas, 2005). This occurs because in these sites evapotranspiration is at stage-I (energy-limited) and is mainly controlled by the state variables of atmosphere (i.e., air temperature and humidity) and not the state variable of the land surface (i.e., LST). More importantly, they need to specify the soil thermal conductivity and heat capacity as well as deep soil temperature, which are often unavailable.

1.2. Motivation

Several studies showed that the reference-level air temperature and humidity measurements in addition to surface parameterization in itself contain useful information about soil moisture (Mahfouf, 1991; Bouttier et al., 1993a, b; Mahfouf et al., 2000, 2009; Douville et al., 2000; Hess, 2001; Drusch and Viterbo, 2007; de Rosnay et al. 2013; Ren and Xue, 2016; de Lannoy et al., 2016), and turbulent heat fluxes (Holtslag and Van Ulden, 1983; Margulis and

Entekhabi, 2001; Alapaty et al., 2001; Balsamo et al., 2007; Shang et al., 2007; Salvucci and Gentine, 2013; Rigden and Salvucci, 2015; Gentine et al., 2016; Lum et al., 2017). These studies typically require specification of surface roughness for heat and momentum as well as ground heat flux, which are mostly unavailable.

To overcome the shortcomings of the abovementioned approaches, this study is aimed at developing a novel VDA framework that estimates *H* and *LE* by assimilating sequences of reference-level air temperature and specific humidity (i.e., state variables of the atmosphere) into an atmospheric boundary layer (ABL) model. The main unknowns of the VDA approach are neutral bulk heat transfer coefficient (C_{HN}) (that scales the sum of the turbulent heat fluxes) and evaporative fraction (*EF*) (that scales their partitioning). The developed VDA approach allows us to address the science question of how much information is contained in the reference-level meteorological data for diagnosing partitioning of available energy at the surface.

Although the proposed VDA does not require the surface roughness for heat and momentum and ground heat flux, it performs poorly in dry/sparsely vegetated sites. This happens because at dry and/or sparsely vegetated sites evapotranspiration is mainly controlled by the land surface state variable (i.e., LST) rather than the atmospheric state variables (i.e., reference-level air temperature and specific humidity). Moreover, it cannot constrain the ground heat fluxes. A remarkable discrepancy is observed between the diurnal cycles of estimated and observed ground heat flux. This is due to the fact that the ground heat flux (*G*) is related to the LST through $G = -p\,dT/dz$ (where p is the soil thermal conductivity, T is the ground temperature, and z is the soil depth), and thus the phase of *G* is strictly dependent upon that of LST, which is not assimilated in the VDA system.

To overcome the aforementioned drawbacks, the developed VDA approach is augmented by the synergistic assimilation of LST (i.e., state variable of the land surface), and air temperature and specific humidity into a coupled land surface-ABL model within a VDA system. Both VDA approaches are initially tested over the First International Satellite Land Surface Climatology Project Field Experiment (FIFE) site in summer of 1987 and 1988. Finally, their performance is evaluated at five sites with contrasting climate and vegetation conditions: Desert, Audubon, Bondville, Brookings, and Willow Creek.

1.3. Thesis Outline

This dissertation includes four chapters:

Chapter 2: Estimation of Turbulent Heat Fluxes via Assimilation of Air Temperature and Specific Humidity into an Atmospheric Boundary Layer Model, submitted to *Journal of Hydrometeorology*.

Chapter 3: Estimation of Surface Heat Fluxes via Variational Assimilation of Land Surface Temperature, Air temperature and Specific Humidity into a Coupled Land Surface-Atmospheric Boundary Layer Model" submitted to *Journal of Hydrology,*

Chapter 4: Evaluating the Information Content of Reference-level Air Temperature and Humidity for Partitioning the Available Energy between the Turbulent Heat Fluxes in Different Vegetative and Climatic Conditions to be submitted to *Remote Sensing*.

Chapter 5: Variational Assimilation of Land Surface Temperature, Air Temperature and Specific Humidity to Estimate Surface Heat Fluxes in Contrasting Hydrologic and Vegetative Conditions to be submitted to *Journal of Geophysical Research-Atmospheres*.

Chapter 2: Estimation of Turbulent Heat Fluxes via Assimilation of Air Temperature and Specific Humidity into an Atmospheric Boundary Layer Model

Estimation of Turbulent Heat Fluxes via Assimilation of Air Temperature and Specific Humidity into an Atmospheric Boundary Layer Model

E. Tajfar[1] and S. M. Bateni[1,*]

[1]Department of Civil and Environmental Engineering

and Water Resources Research Center, University of Hawaii at Manoa, Honolulu, USA.

S. A. Margulis[2], P. Gentine[3], and T. Auligne[4,5]

[2]Department of Civil and Environmental Engineering, University of California, Los Angeles, USA.

[3]Earth and Environmental Engineering and Earth Institute, Colombia University, New York, New York, USA.

[4]Joint Center for Satellite Data Assimilation (JCSDA), Maryland, USA

[5]University Corporation for Atmospheric Research (UCAR), Boulder, USA

[*]*Corresponding author address*: Sayed M. Bateni, Department of Civil and Environmental Engineering and Water Resources Research Center, University of Hawaii at Manoa, Honolulu, USA.

E-mail: smbateni@hawaii.edu

Current affiliation: Assistant Professor, Department of Civil and Environmental Engineering, University of Hawaii at Manoa, Honolulu, USA.

ABSTRACT

A number of studies have used time series of air temperature and specific humidity observations to estimate turbulent heat fluxes. These studies require the specification of surface roughness lengths for heat and momentum (that are directly related to the neutral bulk heat transfer coefficient, C_{HN}) and/or ground heat flux, which are often unavailable. In this study, sequences of air temperature and specific humidity are assimilated into an atmospheric boundary layer model within a new variational data assimilation (VDA) framework to estimate turbulent heat fluxes as well as atmospheric boundary layer (ABL) height, potential temperature, and humidity. The developed VDA approach needs neither the surface roughness parameterization nor ground heat flux measurements. The two main unknowns of the proposed VDA system are C_{HN} and evaporative fraction (*EF*). The VDA approach is tested over the First International Satellite Land Surface Climatology Project Field Experiment (FIFE) site in the summers of 1987 and 1988. The results indicate that the estimated sensible and latent heat fluxes agree well with the corresponding measurements. For FIFE 1987 (1988), the daily sensible and latent heat flux estimates have a root-mean-square-error (RMSE) of 25.72 W m^{-2} (27.77 W m^{-2}) and 53.63 W m^{-2} (48.22 W m^{-2}), respectively. In addition, the ABL height, specific humidity, and potential temperature estimates from the VDA system are in good agreement with those inferred from the radiosondes both in terms of magnitude and diurnal trend.

Keywords: Turbulent heat fluxes; variational data assimilation model; air temperature; specific humidity

2.1. Introduction

The sensible (*H*) and latent (*LE*) heat fluxes are important components of Earth's energy budget and its climate system, which directly influence the properties of the boundary layer. The accurate estimation of turbulent heat fluxes between the land surface and atmospheric boundary layer (ABL) is required in many fields such as drought monitoring, cultivation and irrigation management systems, modeling of global climate regimes, weather forecasting, and water resources management (Liou and Kar, 2014; Santanello et al., 2017).

Using ground-based instruments to measure turbulent heat fluxes is costly and challenging. Consequently, a number of approaches have been developed to estimate turbulent heat fluxes using a variety of measurements that are indirectly related to fluxes (Kalma et al., 2008; Li et al., 2010; Maes and Steppe, 2012; Bateni et al., 2012b, 2013b; Xu et al., 2014, 2015; Zhuang and Wu, 2015; Lu et al., 2016; Brenner et al., 2017; Abdolghafoorian et al., 2017). One of the methods of estimating turbulent heat fluxes is through assimilation of sequences of land surface temperature (LST) observations into the force-restore or heat diffusion equation within a variational data assimilation (VDA) framework (Caparrini et al., 2003; Crow and Kustas, 2005; Bateni and Entekhabi, 2012a, 2012b; Bateni et al., 2013a, 2013b, 2014; Xu et al., 2015, 2016, 2018; Abdolghafoorian et al., 2017). These studies used the implicit information in the sequences of LST observations to partition the available energy into sensible and latent heat fluxes. Performance of these approaches typically degrades in wet and/or heavily vegetated sites where evapotranspiration is often in stage-I (i.e., energy controlled) and controlled mainly by atmospheric factors rather than by land surface processes. More importantly, they need to specify the soil thermal conductivity and heat capacity as well as deep soil temperature, which are often unavailable.

In a departure with using LST measurements, a number of studies showed that the reference-level air temperature and humidity measurements in addition to surface parameterization in itself contain useful information about soil moisture (Mahfouf, 1991; Bouttier et al., 1993a, b; Mahfouf et al., 2000, 2009; Douville et al., 2000; Hess, 2001; Drusch and Viterbo, 2007; de Rosnay et al. 2013; Ren and Xue, 2016; de Lannoy et al., 2016), and turbulent heat fluxes (Holtslag and Van Ulden, 1983; Margulis and Entekhabi, 2001; Alapaty et al., 2001; Balsamo et al., 2007; Shang et al., 2007; Salvucci and Gentine, 2013; Rigden and Salvucci, 2015; Gentine et al., 2016; Lum et al., 2017). These studies typically require specification of surface roughness for heat and momentum (that are directly related to the neutral bulk heat transfer coefficient, C_{HN}) as well as ground heat flux to estimate the sensible and latent heat fluxes, which are mostly unavailable.

Owing to the abovementioned drawbacks of the existing VDA approaches (e.g., poor performance in wet/heavily vegetated sites, and the need for the specification of deep soil temperature and soil thermal properties) and the fact that the sequences of reference-level air temperature and humidity contain information on the turbulent heat fluxes, this study aims at estimating turbulent heat fluxes by assimilating the reference-level air temperature and specific humidity into an ABL model. The proposed VDA approach benefits from the synergistic use of air temperature and specific humidity. These variables are not required as inputs of the land surface model because they are computed internally as diagnostic variables of the ABL model. Instead, reference-level humidity and temperature measurements will be assimilated when they are available. The advantages of the developed VDA approach are 1) it can generate turbulent heat fluxes even when air temperature and humidity observations are not available or there are data gaps, 2) it does not need the surface roughness for heat and momentum (or C_{HN}), and ground

heat flux, 3) it does not require any ancillary input data such as soil type and moisture, 4) it works by routine weather station data (i.e., air temperature and humidity, wind speed, incoming solar radiation), LST, and vegetation height that can be obtained by in-situ measurements and/or remote sensing data (https://www.landfire.gov/vegetation.php), and 5) it maintains physical consistency so that noisy or erroneous observations (such as those polluted by advection and synoptic variability) are given little weight to estimate surface heat fluxes.

A brief description of the surface energy balance (SEB) equation and ABL model is provided in section 2.2. Section 2.3 explains the developed VDA framework. Section 2.4 describes the First International Satellite Land Surface Climatology Project Field Experiment (FIFE) dataset. Section 2.5 presents the results. Finally, conclusions are given in section 2.6.

2.2. Methodology

2.2.1. Surface Energy Balance (SEB)

The surface energy balance (SEB) equation is given by,

$$R_n = H + LE + G \tag{2-1}$$

where R_n is the net surface radiation, H is the sensible, LE is the latent heat flux, and G is the ground heat flux. R_n is defined as,

$$R_n = (1 - \alpha)R_s^{\downarrow} + R_l^{\downarrow} - \varepsilon_s \sigma T^4 \tag{2-2}$$

where α is the surface albedo, $R_s^{\downarrow}$ is the incoming solar radiation, ε_s is the surface emissivity, σ is the Stefan-Boltzman constant, and T is the land surface temperature. $R_l^{\downarrow} = \varepsilon_a \sigma T_a^4$ is the incoming longwave radiation (where T_a is the air temperature at a reference-height (z_{ref}), and ε_a is the atmospheric emissivity, which is obtained from the Idso (1981) formulation).

The sensible heat flux is computed using the Richardson number:

$$H = \rho c_p C_{HN} f(Ri) U (T - T_a) \quad (2\text{-}3)$$

where c_p is the specific heat capacity of air, ρ is the air density, and U is the wind speed at the reference-height. C_{HN} is the neutral bulk heat transfer coefficient, which depends on the characteristics of the landscape (surface roughness and canopy density). The effect of atmospheric stability on sensible heat flux is taken into account by the atmospheric stability correction function (f), which is a function of the Richardson number (Ri). The stability correction function proposed by Caparrini et al. (2003) is used in this study.

The estimation objectives of this study are the sum of turbulent heat fluxes ($H+LE$), and their partitioning (i.e., the evaporative fraction, $EF=LE/(LE+H)$). C_{HN} scales the sum of turbulent heat fluxes (i.e., $H+LE$), and EF scales their partitioning (Bateni et al., 2013; Xu et al., 2014; Lu et al., 2016). C_{HN} represents the effect of land surface characteristics on air turbulent conductivity and is the first unknown of the VDA system. It is dependent mainly on the geometry of the landscape and vegetation, and changes with variations in canopy phenology (Caparrini et al., 2004a, b). In this study, it is assumed that C_{HN} varies on a monthly time-scale.

Gentine et al. (2007, 2011) showed that EF is almost constant for daytime hours on days without precipitation. In this study, EF (the second unknown of the VDA system) is assumed to be constant during the daytime assimilation window [09:00-16:00 LT] for each day so that latent heat flux can then be evaluated as:

$$LE = \frac{EF}{1-EF} H \quad (2\text{-}4)$$

2.2.2. Atmospheric Boundary Layer (ABL) Model

The state of the ABL over a land surface is strongly connected to the magnitude of the surface heat fluxes. Margulis and Entekhabi (2001) used a mixed-layer model to simulate the ABL (Figure 2.1). The entrainment fluxes link the ABL system to the overlying free atmosphere.

These fluxes heat up and dry the mixed-layer, influence the temperature and humidity of the mixed-layer, ultimately affecting the surface energy and moisture budgets. Different components of the ABL model are explained in sections 2.2.3-2.2.6.

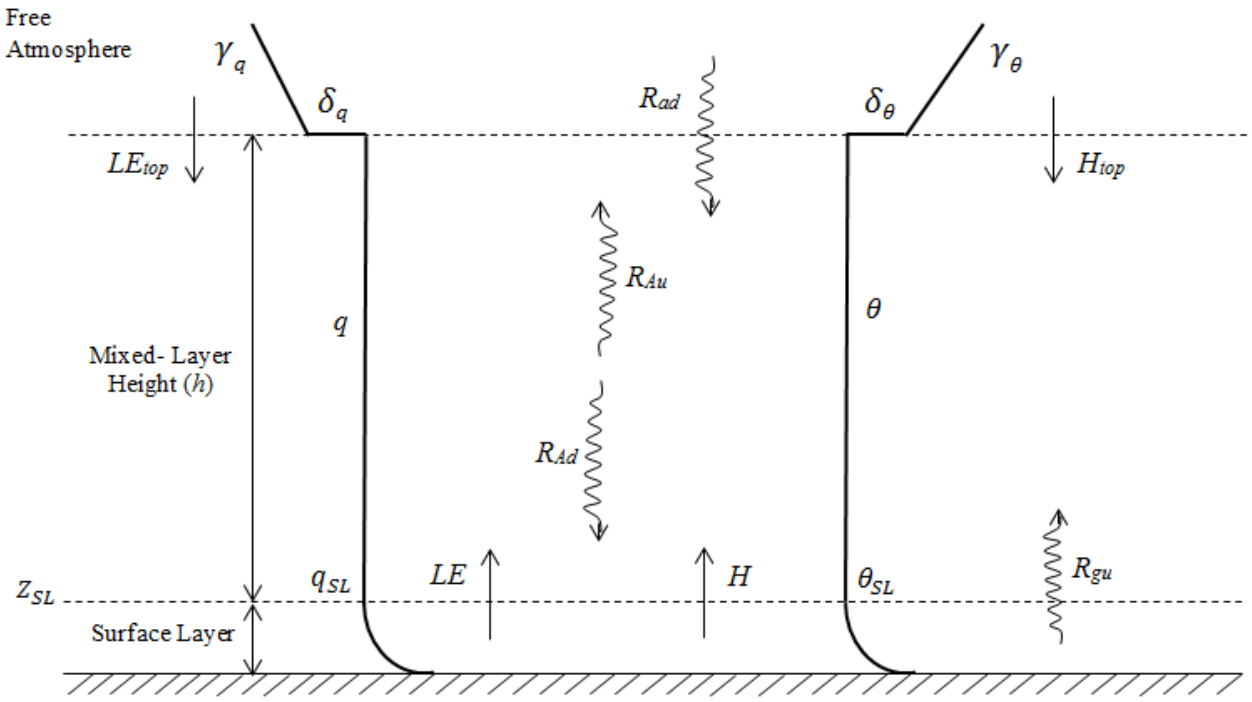

Figure 2. 1. Idealized profiles of ABL states (θ and q) and corresponding fluxes between the surface layer, mixed layer, and overlying atmosphere.

2.2.3. Atmospheric Boundary Layer (ABL) Energy and Moisture Budget

In this study, we used a mixed-layer model, which performs very well against the more complex large eddy simulations (Garcia and Mellado, 2014; Gentine et al., 2015). The profiles of potential temperature (θ) and specific humidity (q) are assumed to be uniform in the mixed-layer. The air layer between the land surface and the mixed-layer is called surface layer, which is convectively unstable during the daytime. The top of the surface layer is specified as 10% of the mixed-layer top (Margulis and Entekhabi, 2001; Gentine et al., 2016). As shown in Figure 2.1,

the entrainment zone connects the mixed layer to the free atmosphere, and is illustrated by instantaneous jumps in the θ and q profiles (Margulis and Entekhabi, 2001; Garcia and Mellado, 2014; Gentine et al., 2015).

The conservation of potential temperature and specific humidity in the mixed layer follow the energy budget:

$$\rho c_p h \frac{d\theta}{dt} = \left(R_{ad} + R_{gu}\right)\varepsilon_m - R_{Ad} - R_{Au} + H + H_{top} \quad (2\text{-}5a)$$

$$\rho h L_v \frac{dq}{dt} = LE + LE_{top} \quad (2\text{-}5b)$$

where h is the mixed-layer height, t is the time, R_{ad} and R_{gu} are the longwave radiation from the free atmosphere overlying the ABL and the land surface beneath, respectively. R_{Ad} and R_{Au} are the downward and upward longwave radiative fluxes originating from within the mixed-layer, respectively. H_{top} and LE_{top} are the entrainment sensible and latent heat flux, respectively, ε_m is the mixed-layer bulk emissivity, and L_v is the latent heat of vaporization. θ and q constitute the state variables of the ABL model, which are obtained by equations (2-5a) and (2-5b), respectively.

Initial conditions for θ and q (i.e., $\theta(t = t_o)$ and $q(t = t_o)$, where t_o = 9 a.m.) are required to solve the ABL state (equations 2-5a and 2-5b). The potential temperature at the level of 1000 mb (i.e., θ_a) is found from the reference-level air temperature (T_a) via $\theta_a = T_a(P_0/P_s)^{R_d/c_p}$ (where R_d is the gas constant of dry air, P_s is the surface pressure, and P_0 is 1000 mb) (Shuttleworth, 2012). Appendix A explains how $\theta(t = t_o)$ and $q(t = t_o)$ are obtained respectively from $\theta_a(t = t_o)$ and $q_a(t = t_o)$ (q_a is the reference-level specific humidity) via the Monin-Obukhov Similarity Theory (MOST) (Rigden and Salvucci, 2015; Gentine et al., 2016).

Advection may undermine the assumption of constant potential temperature and specific humidity in the mixed-layer, resulting in errors in the turbulent heat fluxes estimates. In this study, it is assumed that the advection is insignificant.

2.2.4. Mixed-Layer Height

The height of the mixed-layer (h) evolves dynamically during the day. During the day, the ABL grows mainly because of the virtual heat flux (H_v) at the land surface (Kim and Entekhabi, 1997, 1998a, b). The diurnal range of the ABL height generally changes from ~100–500 m in the early morning to ~1–3 km by late afternoon (Margulis and Entekhabi, 2001). The daytime growth of the ABL height is given by (Smeda, 1979; Kim and Entekhabi, 1997, 1998a, b; Bagley et al., 2011),

$$\frac{dh}{dt} = \frac{2(G_* - D_1 - D_2)\theta}{gh\delta_\theta} + \frac{H_v}{\rho c_p \delta_\theta} \quad (2\text{-}6a)$$

where the different terms are defined by,

$$G_* = u_{SL} u_*^2 \quad (2\text{-}6b)$$

$$D_1 = u_{SL} u_*^2 (1 - e^{-\varphi h}) \quad (2\text{-}6c)$$

$$D_2 = 0.4 \left(\frac{gh}{\theta} \frac{H_v}{\rho c_p} \right) \quad (2\text{-}6d)$$

$$H_v = H + 0.61\theta c_p E \approx H + 0.07LE \quad (2\text{-}6e)$$

The first and second terms on the right hand side of Equation (2-6a) represent the ABL growth due to mechanically generated turbulent energy and the surface virtual heat flux, respectively. G_* is the production of mechanical turbulent energy, g is gravitational acceleration, u_{SL} is the wind speed at the top of the surface layer, which is obtained from the wind speed at the reference-level using the Monin-Obukhov Similarity Theory, MOST (see Appendix A), u_* is the friction velocity, H_v is the virtual heat flux at the surface, E is the evaporative rate from ground,

and φ is the mechanical turbulence dissipation parameter, which is set to 0.01 (Kim and Entekhabi,1998b; Margulis and Entekhabi, 2001; Bagley et al., 2011).

As indicated in Figure 2.1, the ABL model contains discrete jumps in temperature and humidity at the top of the boundary layer. The intensities of these jumps (δ_θ and δ_q) change along with the other components of the ABL system as air from the overlying free-atmosphere entrains into the mixed-layer and surface fluxes change the state of ABL (Bagley et al., 2011). δ_θ increases as the boundary layer grows and decreases when the boundary layer warms. The expression for δ_θ can be written as (Margulis and Entekhabi, 2001),

$$\frac{d\delta_\theta}{dt} = \gamma_\theta \frac{dh}{dt} - \frac{d\theta}{dt} \tag{2-7a}$$

Similarly, δ_q increases as the boundary layer grows and decreases when the boundary layer becomes more moist. The equation for δ_q is (Margulis and Entekhabi, 2001; Bagley et al., 2011),

$$\frac{d\delta_q}{dt} = \gamma_q \frac{dh}{dt} - \frac{dq}{dt} \tag{2-7b}$$

γ_θ and γ_q are the lapse rates in potential temperature and specific humidity above the mixed-layer.

2.2.5. Entrainment Fluxes

The mixed-layer is usually topped by inversions in specific humidity and potential temperature (Figure 2.1). As the boundary layer grows, dry air from above enters into the mixed layer, resulting in the sensible and latent heat fluxes between the free atmosphere and mixed layer. The entrainment heat flux from above the mixed-layer (H_{top}) contributes to the mixed-layer growth (Stull, 1994). The entrainment latent heat flux (LE_{top}) dries up the mixed layer because the free tropospheric air is typically drier than the mixed layer (Stull, 1994). The

equations for H_{top} and LE_{top} can be derived by considering the conservation of heat and moisture across the interface between the free atmosphere and mixed layer,

$$H_{top} = AH \tag{2-8a}$$

$$LE_{top} = \rho L_v \delta_q \frac{dh}{dt} \tag{2-8b}$$

A typical value of 0.2 is used for *A* (Gentine et al., 2015; Garcia and Mellado, 2015).

2.2.6. Radiative Fluxes

Incoming solar radiation ($R_s^{\downarrow}$) measurements at the land surface are used in equation (2-2) to estimate net radiation. The downward longwave radiative flux from the atmosphere above (R_{ad}) enters the atmospheric boundary layer (Figure 2.1). Using the solution proposed by Brutsaert (1975), Brubaker and Entekhabi (1995) derived the expression for R_{ad}, which is given by,

$$R_{ad} = \varepsilon_{ad} \sigma T_h^4 \tag{2-9}$$

where T_h the air temperature exactly above the mixed-layer height *h*, and ε_{ad} is the effective emissivity above the mixed-layer (see Appendix B for the equation for ε_{ad}).

The upward longwave radiative flux from the land surface into the mixed-layer (R_{gu}) is given by,

$$R_{gu} = \varepsilon_s \sigma T^4 \tag{2-10}$$

Only a portion of the entrainment longwave radiative fluxes from the free atmosphere and land surface ($R_{ad} + R_{gu}$) is absorbed by the ABL, which is dependent on the mixed-layer bulk emissivity (ε_m) that itself is a function of the ABL specific humidity. The expression for ε_m can be found in Appendix B.

The ABL cools down by emitting radiative fluxes from within the mixed layer downward and upward (R_{Ad} and R_{Au}). The formulations for the upward and downward longwave radiative fluxes originating from within the mixed-layer follow a gray body emission approximation (Brubaker and Entekhabi, 1995, Margulis and Entekhabi, 2001),

$$R_{Ad} = \varepsilon_d \sigma \theta^4 \tag{2-11a}$$

$$R_{Au} = \varepsilon_u \sigma \theta^4 \tag{2-11b}$$

where ε_d is the effective mixed-layer downward emissivity, and ε_u is the effective mixed-layer upward emissivity. The expressions for ε_d and ε_u are provided in Appendix B.

2.3. Variational Data Assimilation (VDA) Scheme

The VDA system finds optimal values of C_{HN} and EF by minimizing an objective function, which consists of the potential temperature and specific humidity misfit terms, deviations of unknown parameters (C_{HN} and EF) from their prior values, and adjoints. The objective function is formulated as:

$$J(\theta, q, \lambda_1, \lambda_2, R, EF) =$$

$$\sum_{i=1}^{N} \int_{t_o}^{t_1} [\theta_i(t) - \theta_{SL,i}(t)]^T R_\theta^{-1} [\theta_i(t) - \theta_{SL,i}(t)]\, dt + \sum_{i=1}^{N} \int_{t_o}^{t_1} [q_i(t) - q_{SL,i}(t)]^T R_q^{-1} \big[q_i(t) -$$

$$q_{SL,i}(t)\big] dt + (R - R')^T B_R^{-1} (R - R') + \sum_{i=1}^{N} (EF_i - EF_i')^T B_{EF}^{-1} (EF_i - EF_i')$$

$$+ \sum_{i=1}^{N} \int_{t_o}^{t_1} \lambda_{1i}(t) \left[\rho c_p h_i(t) \frac{d\theta_i(t)}{dt} - \big(R_{ad} + R_{gu}\big)\varepsilon_m + R_{Ad} + R_{Au} - H - \right.$$

$$\left. H_{top}\right] dt + \sum_{i=1}^{N} \int_{t_o}^{t_1} \lambda_{2i}(t) \left[\rho h_i(t) L_v \frac{dq_i(t)}{dt} - LE - LE_{top}\right] dt \tag{2-12}$$

where R is related to the neutral bulk heat transfer via $C_{HN} = e^R$. This transformation is done to make C_{HN} strictly positive. N is the number of days in the assimilation period (here taken as $N = 30$). $[t_o, t_1]$ = [09:00, 16:00 LT] constitutes the assimilation window in which EF is assumed

to be constant. The first and second terms in the right-hand side of (2-12) represent the square of misfit between the top of the surface layer potential temperature (θ_{SL}) and specific humidity (q_{SL}), and the corresponding estimates (i.e., θ and q) from (2-5a) and (2-5b) over the whole assimilation period. θ_{SL} and q_{SL} are obtained from θ_a and q_a via the MOST (see Appendix A). R_θ^{-1} and R_q^{-1} are the inverse error covariance matrices of θ and q, respectively. The third and fourth terms respectively express the error of unknown parameters *R* and *EF* with respect to their prior values (R' and EF'). B_R^{-1} and B_{EF}^{-1} are the inverse background error covariance matrices of R and EF, respectively. The physical constraints in the last two terms are adjoined to the objective function via the Lagrange multipliers, λ_1 and λ_2.

The values of R_θ^{-1}, R_q^{-1}, B_R^{-1} and B_{EF}^{-1} can be obtained from the inverse covariance functions of states (i.e., θ and q) and parameters (i.e., *R* and *EF*), if their statistical structures are known (Bennett, 1992). Due to the lack of detailed knowledge about the statistical structure of the states and parameters, R_θ^{-1}, R_q^{-1}, B_R^{-1} and B_{EF}^{-1} are herein regarded as diagonal matrices of numerically constant values whose relative magnitudes control the rate of convergence and the stability of the VDA approach (Bennett, 1992; Castelli et al., 1999).

The magnitudes of the diagonal elements in R_θ^{-1} and R_q^{-1} are respectively set to 10^{-1} K^{-2} and 10^5 to make the order of magnitude of the first and second terms similar. The absolute value of $(\theta(t) - \theta_{SL}(t))$ has an order of magnitude of ~5 K [i.e., $(\theta(t) - \theta_{SL}(t))$ ~ O(5)], and thus $[\theta_i(t) - \theta_{SL,i}(t)]^T[\theta_i(t) - \theta_{SL,i}(t)]$ ~ O(25). The order of magnitude of $(q(t) - q_{SL}(t))$ is ~ 0.005 [i.e., $(q(t) - q_{SL}(t))$ ~ O(0.005)], and therefore $[q(t) - q_{SL}(t)]^T$ $[q(t) - q_{SL}(t)]$ ~ O(25×10^{-6}). With 10^{-1} K^{-2} and 10^5 as the diagonal elements of R_θ^{-1} and R_q^{-1}, both $\sum_{i=1}^{N}\int_{t_o}^{t_1}[\theta_i(t) - \theta_{SL,i}(t)]^T R_\theta^{-1}[\theta_i(t) - \theta_{SL,i}(t)]\,dt$ and $\sum_{i=1}^{N}\int_{t_o}^{t_1}[q_i(t) - q_{SL,i}(t)]^T R_q^{-1}[q_i(t) -$

$q_{SL,i}(t)]dt$ have the order of magnitude of ~2.5. B_R^{-1} and B_{EF}^{-1} are obtained through trial and error by assessing their impact on the magnitude of the objective function (J) (Daley, 1991; Castelli et al., 1999). In the first trial, the diagonal elements of B_R^{-1} and B_{EF}^{-1} are chosen to be equal and varied from 10^3 to 10^{17}. The VDA system is unstable for B_R^{-1} = B_{EF}^{-1} values of 10^3 to 10^5, and the objective function is minimized for B_R^{-1} = B_{EF}^{-1} = 10^8 (Table 2.1, top panel). Thereafter, unequal values for B_R^{-1} and B_{EF}^{-1} are chosen (Table 2.1, bottom panel). After some trials, the minimum value of 0.83×10^6 is obtained for J when the diagonal arrays of B_R^{-1} and B_{EF}^{-1} are set to 10^8 and 10^9, respectively. As the last step of our trial, R_θ^{-1} and R_q^{-1} are increased 10 times, and are set to 1 K^{-2} and 10^6, respectively. It is observed that the same results can be obtained if B_R^{-1} and B_{EF}^{-1} are increased with the same rate (i.e., 10 times). A similar trial-and-error approach was used in Castelli et al. (1999), Caparrini et al. (2003), and Bateni et al. (2013a, 2014) to determine the inverse error covariance matrices of states and variables.

Table 2. 1. The magnitude of cost function (J) for different values of B_R^{-1} and B_{EF}^{-1}. Equal (top panel) and unequal (bottom panel) values for B_R^{-1} and B_{EF}^{-1} are considered.

B_R^{-1}	10^6	10^7	**10^8**	10^9	10^{10}	10^{11}	10^{12}	10^{14}	10^{17}
B_{EF}^{-1}	10^6	10^7	**10^8**	10^9	10^{10}	10^{11}	10^{12}	10^{14}	10^{17}
$J\times10^6$	1.237	1.233	**1.155**	1.901	1.912	1.460	1.539	1.548	1.548
B_R^{-1}	10^6	10^7	10^8	**10^8**	10^9	10^9	10^{10}	10^{12}	10^{17}
B_{EF}^{-1}	10^7	10^8	10^7	**10^9**	10^8	10^{10}	10^9	10^{17}	10^{12}
$J\times10^6$	1.233	1.155	1.233	**0.830**	1.183	1.882	1.954	1.539	1.548

To minimize the objective function (J), its first variation with respect to the independent variables θ, q, λ_1, λ_2, R and EF should be set to zero. Taking the first variation of J (δJ) with

respect to θ, q, λ_1, λ_2, R and EF, grouping them based on $\delta\theta$, δq, $\delta\lambda_1$, $\delta\lambda_2$, δR and δEF, and finally setting them to zero lead to a set of equations (the so-called Euler-Lagrange equations), which should be solved simultaneously. The Euler-Lagrange equations are presented in Appendix C.

Figure 2.2 shows the variation of the first four terms in the objective function versus the iteration number. As shown, by increasing the number of iterations, the misfits between θ and θ_{SL}, and q and q_{SL} reduce and finally reach their asymptotic of 6.005×10^4 (for the first term) and 2.30×10^4 (for the second term) at the iteration of 700. The third and fourth terms are the errors of unknown parameters of the model (*R* and *EF*). At the iteration of 700, there is almost no improvement in the predictions of *R* and *EF*, both terms reach almost zero, and the VDA system converges. At the iteration of 700 (where the VDA converges), the first and second terms have larger values compared to the other terms, indicating that the misfits between θ and θ_{SL}, and q and q_{SL} have the most effect on the magnitude of objective function.

Figure 2.3 indicates the root-mean-square-error (RMSE) of potential temperature and specific humidity estimates from the VDA approach versus the iteration number. As anticipated, the RMSEs of θ and q reduce as the iteration number increases, and reach the asymptotic values of 2.82 K and 1.75×10^{-3} respectively at the iteration of 700. The decrease in the RMSEs of θ and q estimates shows the improvement in the model performance as the iteration number grows. In fact, the developed VDA system finds the optimal *EF* and C_{HN} values by minimizing the misfit between θ and q estimates and observations.

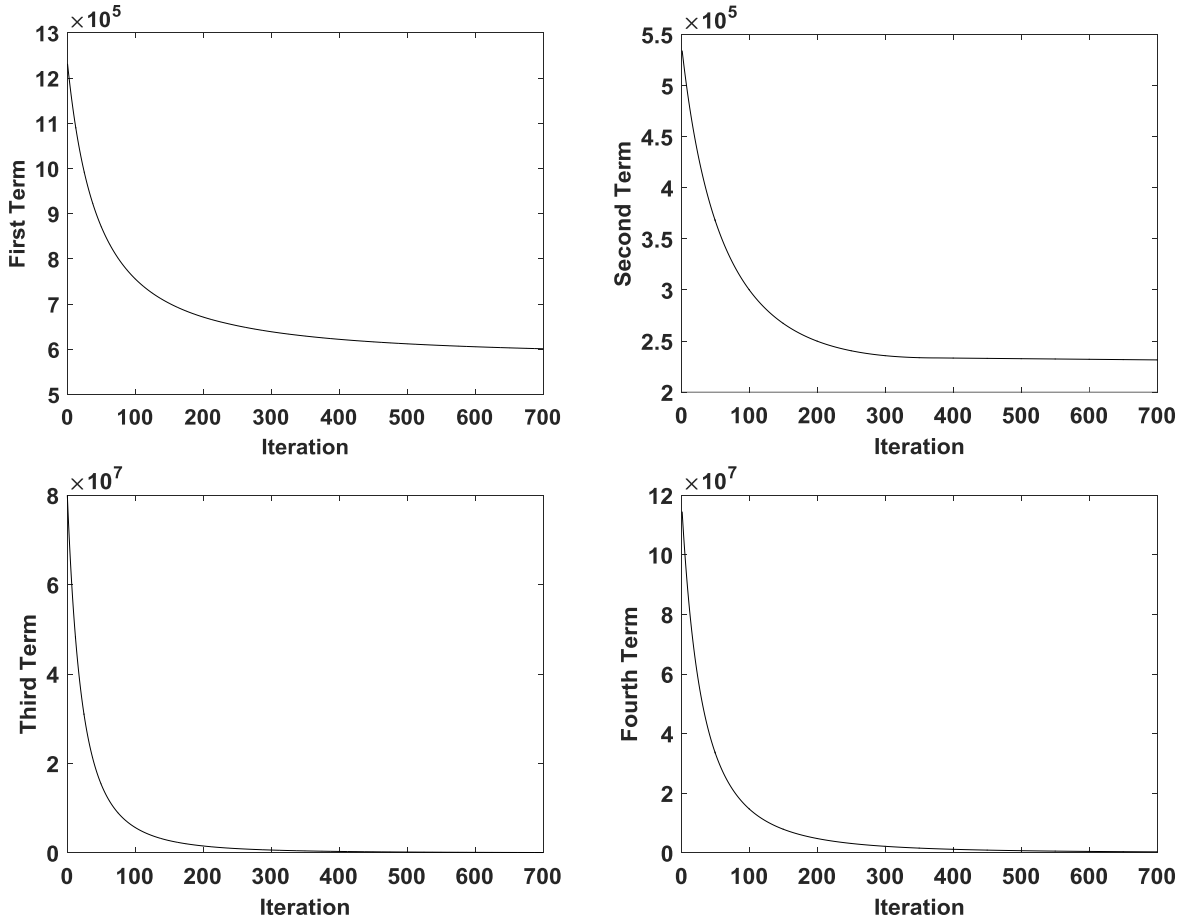

Figure 2. 2. Variations of the first four terms in the objective function as a function of the iteration number.

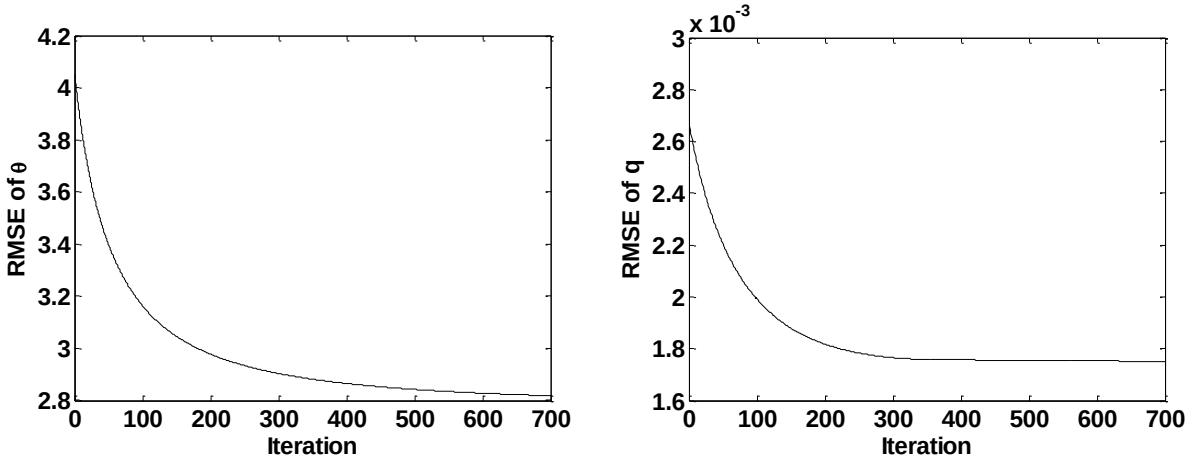

Figure 2. 3. RMSE of θ and q estimates versus the iteration number.

2.4. FIFE Dataset

The VDA approach was tested at the First ISLSCP (International Satellite Land Surface Climatology Project) Field Experiment (FIFE) site. FIFE was carried out on the Konza Prairie in central Kansas from 1987 to 1989. The ground measurements were collected at 32 sites within the Konza Prairie Natural Research Area, a 15 km by 15 km grassland site that is centered at 39.05° N, 96.53° W.

Betts and Ball (1998) produced three different datasets from the raw data in FIFE. Two of them are the land surface temperature (LST), and atmospheric forcing data including air temperature and humidity, wind speed, and incoming solar radiation, which are averaged over the FIFE site. To do so, they cleaned up the surface meteorological data collected from 10 Portable Automatic Meteorological (PAM) stations, and excluded unrealistic data by applying range filters to the time series. The third dataset is a site-averaged surface heat fluxes time series with a 30-minute time step collected from 22 stations in 1987 and 10 in 1988. The FIFE dataset provides us with a nearly continuous (30-minute interval) and fairly precise LST, forcings, and fluxes over the diurnal cycle. The vegetation height measurements at the FIFE site are downloaded from the Oak Ridge National Laboratory-Distributed Active Archive Center (ORNL-DAAC) (https://daac.ornl.gov/FIFE/guides/Vegetation_Biophysical_Data.html).

The radiosonde measurements of potential temperature (θ), specific humidity (q), and mixed-layer height (h) at the FIFE site are also available to verify the model estimates. These radiosonde measurements were conducted during intensive field campaigns (IFCs) 1-3 in the summer of 1987 (Strebel et al., 1994). The radiosonde data include 0–8 launches between sunrise and sunset on specific days during the IFCs at roughly 90-minute intervals and during the growth phase of the boundary layer [09:30-16:00 LT]. From each IFC, some cloud-free days were

chosen to verify the model estimates with the radiosonde data (IFC 1: Jun 4-6, IFC 2: Jun 26, Jul 6, Jul 11, IFC 3: Aug 15-17). However, because of the nature of radiosonde sampling, the observations are not necessarily representative of the spatial average over the site. This makes the comparison between the model estimates and measurements difficult (Margulis, 2002).

Micrometeorological data (i.e., air temperature and humidity, wind speed, and incoming solar radiation), vegetation height, and LST measurements are required to run the VDA model.

The initial ABL height, $h(t_o)$, is needed to integrate equation (2-6a) forward in time, and find the evolution of ABL height. The initial ABL height typically varies from 100 m to 500 m (Margulis and Entekhabi, 2001; Gentine et al., 2016). Similarly, the magnitudes of γ_θ and γ_q as well as the initial conditions for δ_θ and δ_q (i.e., $\delta_\theta(t_o)$ and $\delta_q(t_o)$) are required to find the evolution of δ_θ and δ_q. According to Margulis (2002), Van Heerwaarden et al. (2010), and Gentine et al. (2016), γ_θ, γ_q, δ_θ and δ_q vary over the range of 2 – 8 K km^{-1}, -7×10^{-3} – -0.5×10^{-3} kg kg^{-1} km^{-1}, 2 – 6 K, and -4.8×10^{-3} – -0.5 × 10^{-3} kg kg^{-1}, respectively. In this study, $h(t_o)$, γ_θ, γ_q, $\delta_\theta(t_o)$, and $\delta_q(t_o)$ are changed from 100 to 500 m, 2 to 8 K km^{-1}, -7×10^{-3} to -0.5×10^{-3} kg kg^{-1} km^{-1}, 2 to 6 K, and -4.8×10^{-3} to -0.5×10^{-3} kg kg^{-1} with the increment of 100 m, 0.5 K km^{-1}, 0.5×10^{-3} kg kg^{-1} km^{-1}, 0.4 K, and 0.4×10^{-3} kg kg^{-1}, respectively. The cost function (J) reaches its minimum value with the $h(t_o)$, γ_θ, γ_q, $\delta_\theta(t_o)$, and $\delta_q(t_o)$ of 400 m, 4.5 K km^{-1}, -1×10^{-3} kg kg^{-1} km^{-1}, 3.6 K, and -4.4×10^{-3} kg kg^{-1}, respectively.

Following Betts and Ball (1998), albedo (α) is set to 0.2. A typical value of 0.98 is used for the surface emissivity (ε_s) (Bateni et al., 2013a). All of the fixed-value parameters used in the VDA approach are listed in Table 2.2.

Table 2. 2. Values of time-invariant parameters used in the VDA approach.

Parameter	Value	Unit
Air density (ρ)	1.2	kg m^{-3}
Specific heat capacity (c_p)	1004	J kg^{-1} K^{-1}
Stefan-Boltzmann constant (σ)	5.67×10^{-8}	W K^{-4} m^{-2}
Latent heat of vaporization (L_v)	2.5×10^{6}	J kg^{-1}
Lapse rate of θ above h (γ_θ)	4.5	K km^{-1}
Lapse rate of q above h (γ_q)	-1.0×10^{-3}	kg kg^{-1} km^{-1}
Initial ABL height (h (t_o= 9 a.m.))	400	M
Initial inversion strength of θ ($\delta_\theta(t_o$= 9 a.m.))	3.6	K
Initial inversion strength of q ($\delta_q(t_o$= 9 a.m.))	-4.4×10^{-3}	kg kg^{-1}
Gas constant for dry air (R_d)	287	J kg^{-1} $^oC^{-1}$
Gas constant for water vapor (R_v)	461	J kg^{-1} $^oC^{-1}$
Surface pressure (P_s)	96700	Pa
Mechanical turbulence dissipation	0.01	m^{-1}
Assimilation window [t_o, t_1]	[09:00, 16:00 LT]	hr
Surface emissivity (ε_s)	0.98	-
Albedo (α)	0.2	-
von Karman constant (k)	0.41	-
Entrainment parameter, *A* (equation 8a)	0.2	-
Number of days in the assimilation period (*N*)	30	-

The surface heat fluxes measurements and radiosonde observations are used to validate the surface heat fluxes retrievals as well as ABL height, potential temperature, and specific humidity estimates. In addition, the area-averaged measurements from FIFE dataset give us this opportunity to verify the VDA model over large-scale domains with a computational grid size of a few kilometers (Chen et al., 1996). In this paper, we tested our VDA model in summer 1987 (days 148–243) and 1988 (days 160–243).

2.5. Results

EF is assumed to be constant during the assimilation window [t_0 = 09:00 and t_1 = 16:00 local time], and is obtained on a daily time-scale. *R* is mostly affected by landscape characteristics, changes on a longer time-scale, and is estimated on a monthly basis. The VDA system becomes ill-posed if the two parameters (*EF* and *R*) are allowed to vary on the same time scale. The reason for this problem can be explained by re-writing equation (2-5b) as follows:

$$\rho h L_v \frac{dq}{dt} = LE + LE_{top} = \frac{EF}{1-EF} H + LE_{top} = \frac{EF}{1-EF} \rho c_p e^R f(Ri) U(T - T_a) + LE_{top} \qquad (2\text{-}13)$$

The product of e^R and $EF(1 - EF)^{-1}$ appears in (2-13). The VDA approach is not able to separate the two unknown parameters (*EF* and *R*) and distinguish their difference if they are allowed to change on the same time scale. To make the estimation problem well-posed and realizing that EF and R change on different time sales, daily EF and monthly R are estimated in the VDA approach.

To find a reasonable initial guess for $C_{HN} = e^R$ in each monthly assimilation period, the VDA approach is run for a number of *R* values (*R* is varied from -7.5 to -3.5 with the increment of 0.5). Thereafter, for each utilized *R* value in the VDA approach, the RMSEs of corresponding *EF*, θ, and q estimates are obtained (Figure 2.4). As shown, there is a minimum in the RMSEs of *EF*, θ, and q estimates, which occurs at the *R* value of -4.5, -5.0, and -5.0 for the first (Julian days 178-177), second (Julian days 178-207), and third (Julian days 208-243) assimilation period in FIFE 87, respectively. Similarly, the minimum in the RMSEs of *EF*, θ, and q retrievals happens at the *R* of -6.0, -5.5, -5.5 for the first (Julian days 160-189), second (Julian days 190-219), and third (Julian days 220-243) period in FIFE 88. For each assimilation period, The *R* value that minimizes the RMSEs of *EF*, θ, and q retrievals is used as the initial guess in the

VDA approach. The VDA approach iteratively improves *R*, and finds its optimum value (see Appendix C).

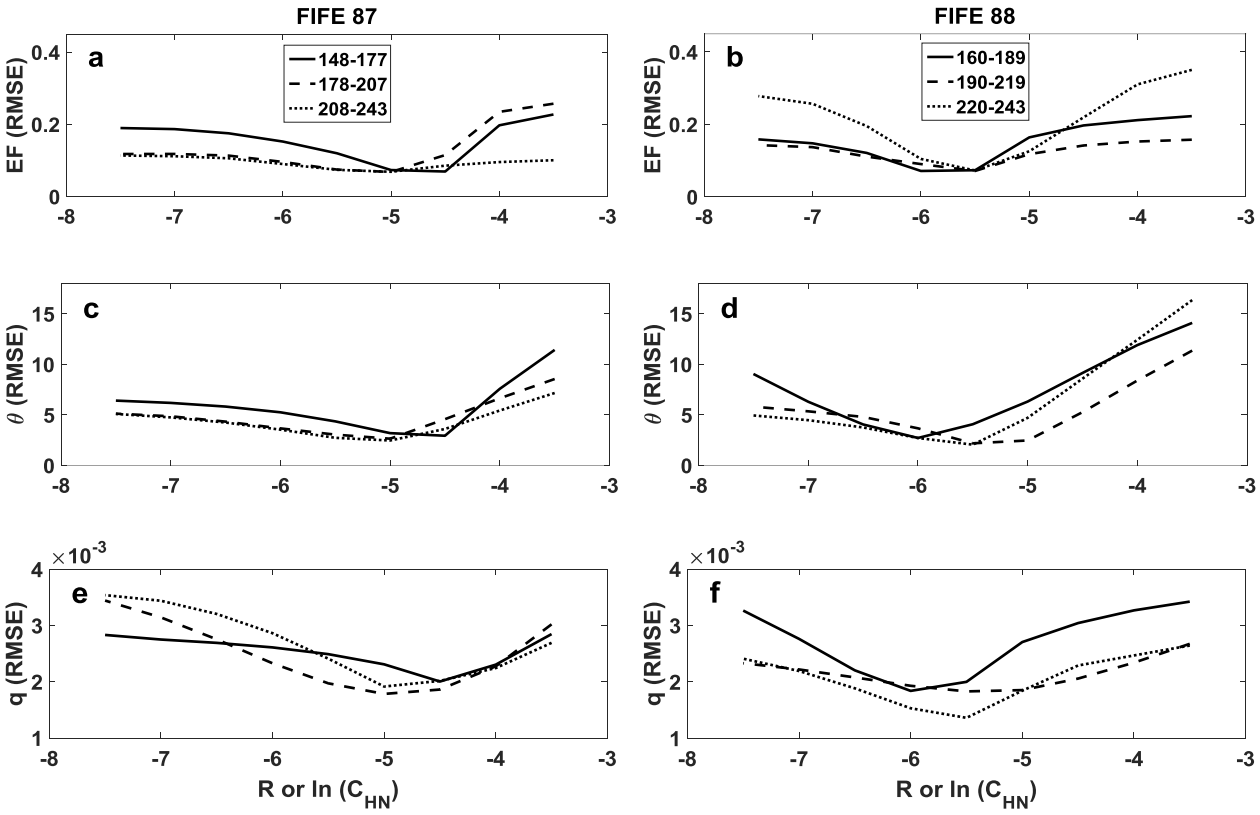

Figure 2. 4. RMSE of estimated *EF* (a and b), and ABL potential temperature (c and d) and specific humidity (e and f) for FIFE 87 (left) and 88 (right).

Table 2.3 shows the estimated C_{HN} values from the VDA model for FIFE 87 and 88. Leaf area index (LAI) values are also indicated in Table 2.3, which are obtained from the LAI-NDVI (Normalized Difference Vegetation Index) exponential relationship proposed by Aparicio et al. (2000) and the site-averaged NDVI data from the Landsat and SPOT satellites presented by Hall et al. (1992). The estimated C_{HN} values fall within a physically accepted range (Stull, 1994; Caparrini et al., 2004a). The changes in the C_{HN} estimates are consistent with the variations in LAI although no information on vegetation dynamics is used in the VDA approach. It should be

noted that the rainfall patterns, and consequently the crop growth and vegetation phonology are different in summer 1987 and 1988. The FIFE site was wet in the beginning of summer 87, followed by a drydown toward the end of summer. As a result, LAI values decreased during the summer 1987. Remarkably, the estimated C_{HN} values decline as the summer progresses. There was a different trend in the canopy phenology in FIFE 88, and LAI grew gradually during the summer 88. An increasing pattern in the C_{HN} values can be seen accordingly.

Table 2. 3. Estimated neutral bulk heat transfer coefficient (C_{HN}) values by the VDA model for FIFE 87 and 88.

FIFE 87			FIFE 88		
Julian days	C_{HN}	LAI	Julian days	C_{HN}	LAI
148 - 177	0.0093	1.7	160 – 189	0.0024	1.2
178 - 207	0.0079	1.2	190 – 219	0.0040	1.3
208 - 243	0.0057	1.1	220 – 243	0.0042	1.4

The estimated daily *EF* values from the VDA approach (solid lines) are compared with the observations (open circles) in Figure 2.5. As shown, there is a good agreement between the measured and estimated *EF* values. The *EF* estimates show a distinct response to drydown and wetting events although no soil moisture or rainfall information is utilized in the assimilation approach. For example, the *EF* estimates can capture the drydown period (days 197-216 in 1987) and the wetting periods (days 195-199 and 226-231 in 1988). The results show that the assimilation system is able to extract the implicit information in the sequences of screen-level air temperature and specific humidity to partition available energy between the turbulent heat fluxes.

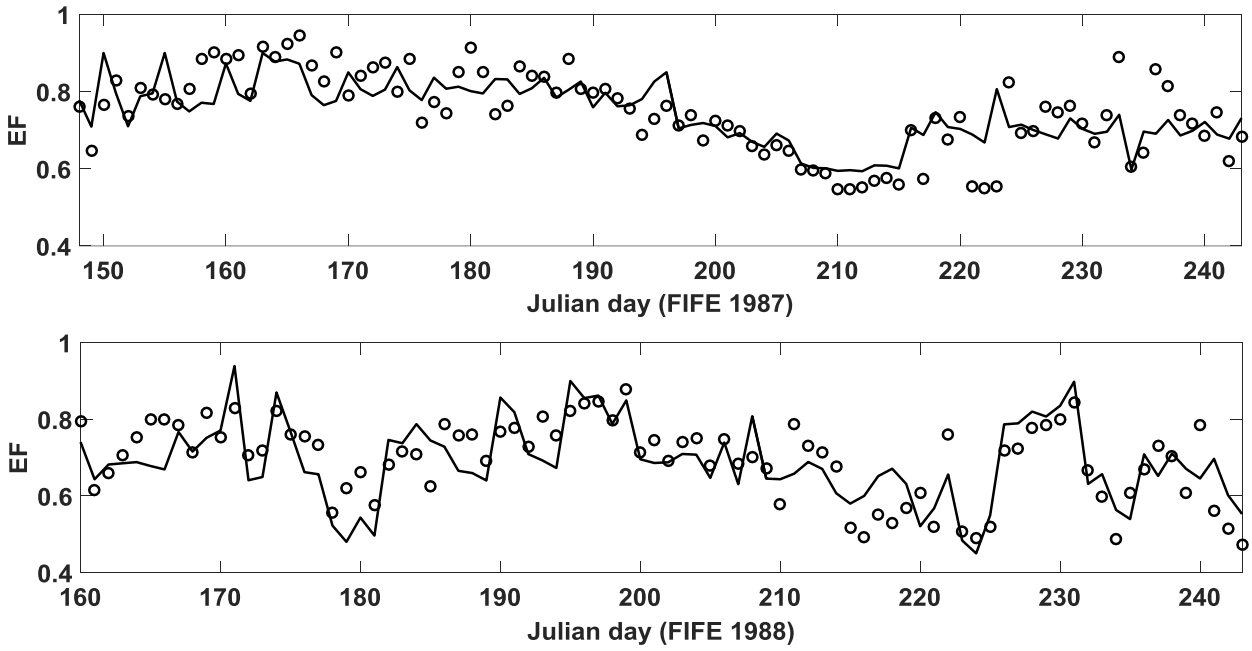

Figure 2. 5. Time series of evaporative fraction for FIFE 87 (top) and 88 (bottom). [Estimated evaporative fraction from measured heat fluxes (circles) and the VDA approach (solid lines)].

The half-hourly estimates of sensible, latent, and ground heat fluxes from the VDA approach are plotted versus observations in Figure 2.6 for FIFE 87 and 88. The ground heat flux (G) is obtained as the residual of the surface energy balance question ($G = Rn - H - LE$). As can be seen, the H and LE estimations are mainly scattered around the 45 degree line, showing a fairly good agreement with the measurements. The G estimations show a large scattering around the 45 degree line, implying that the VDA approach cannot provide accurate G estimates. For FIFE 1987 (1988), the RMSE is 38.61 W m^{-2} (48.42 W m^{-2}) for half-hourly sensible heat flux, 89.05 W m^{-2} (86.63 W m^{-2}) for half-hourly latent heat flux, and 122.14 W m^{-2} (113.29 W m^{-2}) for half-hourly ground heat flux. For FIFE 1987 (1988), the half-hourly H, LE and G estimates have a mean-absolute-error (MAE) of 31.37 W m^{-2} (37.55 W m^{-2}), 70.95 W m^{-2} (66.84 W m^{-2}), and 95.28 W m^{-2} (87.47 W m^{-2}), respectively. The results indicate that the proposed VDA approach can take advantage of the implicit information in the sequences of reference-level air temperature

and specific humidity to estimate sensible and latent heat fluxes. However, assimilating the air temperature and specific humidity observations into the ABL model cannot constrain the G estimates because G is directly related to the gradient of LST via $G = -p(\frac{dT}{dZ})|_{z=0}$ (where p is the soil thermal conductivity, and z is the soil depth).

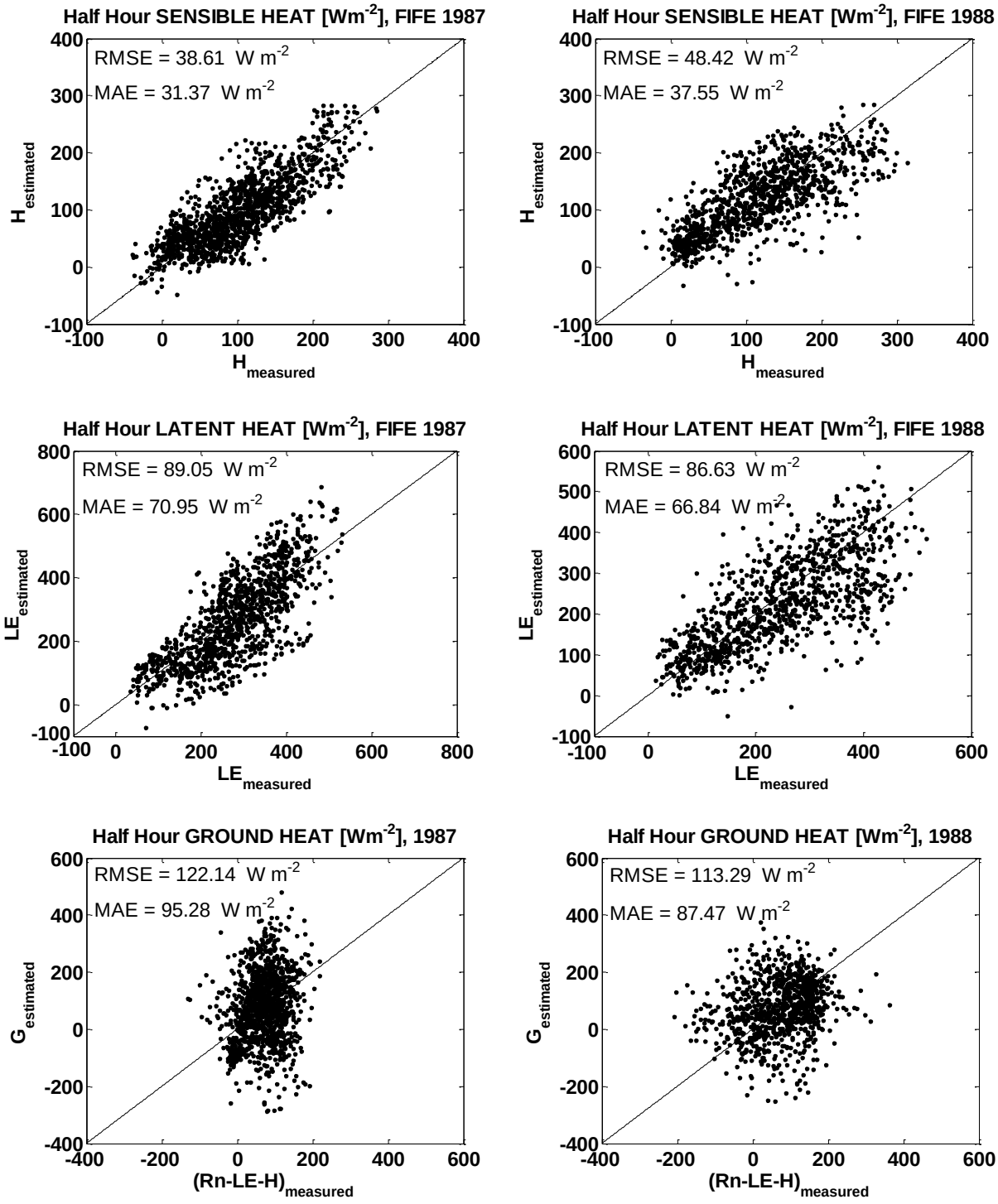

Figure 2. 6. Scatterplot of half-hourly estimated versus measured (top) sensible, (middle) latent, and (bottom) ground heat fluxes for FIFE 87 (left) and FIFE 88 (right).

According to equation (2-3), the error in the estimated *H* values mainly depends on the uncertainty in the estimation of air temperature and C_{HN}. Equation (2-4) indicates that the error in *LE* estimates is dependent on the uncertainty of not only *H* but also *EF* estimates. The RMSE of *LE* estimates is higher than that of *H* because the errors in the air temperature, C_{HN}, and *EF* estimates directly propagate into the *LE* retrievals. The uncertainty of air temperature, C_{HN}, and *EF* estimates is mainly due to the simplistic assumptions of constant daily *EF* and monthly C_{HN}, insignificant advection, and convectively well mixed boundary layer, which results in constant profiles of potential temperature and specific humidity with height (Figure 2.1).

The VDA system finds the optimum values of C_{HN} and *EF* by minimizing the difference between the ABL potential temperature and specific humidity estimates from equations (2-5a) and (2-5b) (i.e., θ and q), and the corresponding values obtained from the reference-level air temperature and specific humidity via the MOST (i.e., θ_{SL} and q_{SL}).

Figure 2.7 shows half-hourly estimated ABL potential temperature and specific humidity from (2-5a) and (2-5b) versus corresponding retrievals from air temperature and specific humidity for FIFE 87 and 88. The close agreement indicates that the data assimilation approach can successfully update the two main unknowns of the problem (C_{HN} and *EF*) and finally obtain their optimal values. For FIFE 1987 (1988), the potential temperature and specific humidity estimates have a RMSE of 2.68 K (2.31 K) and 0.0019 kg kg^{-1} (0.0016 kg kg^{-1}), respectively.

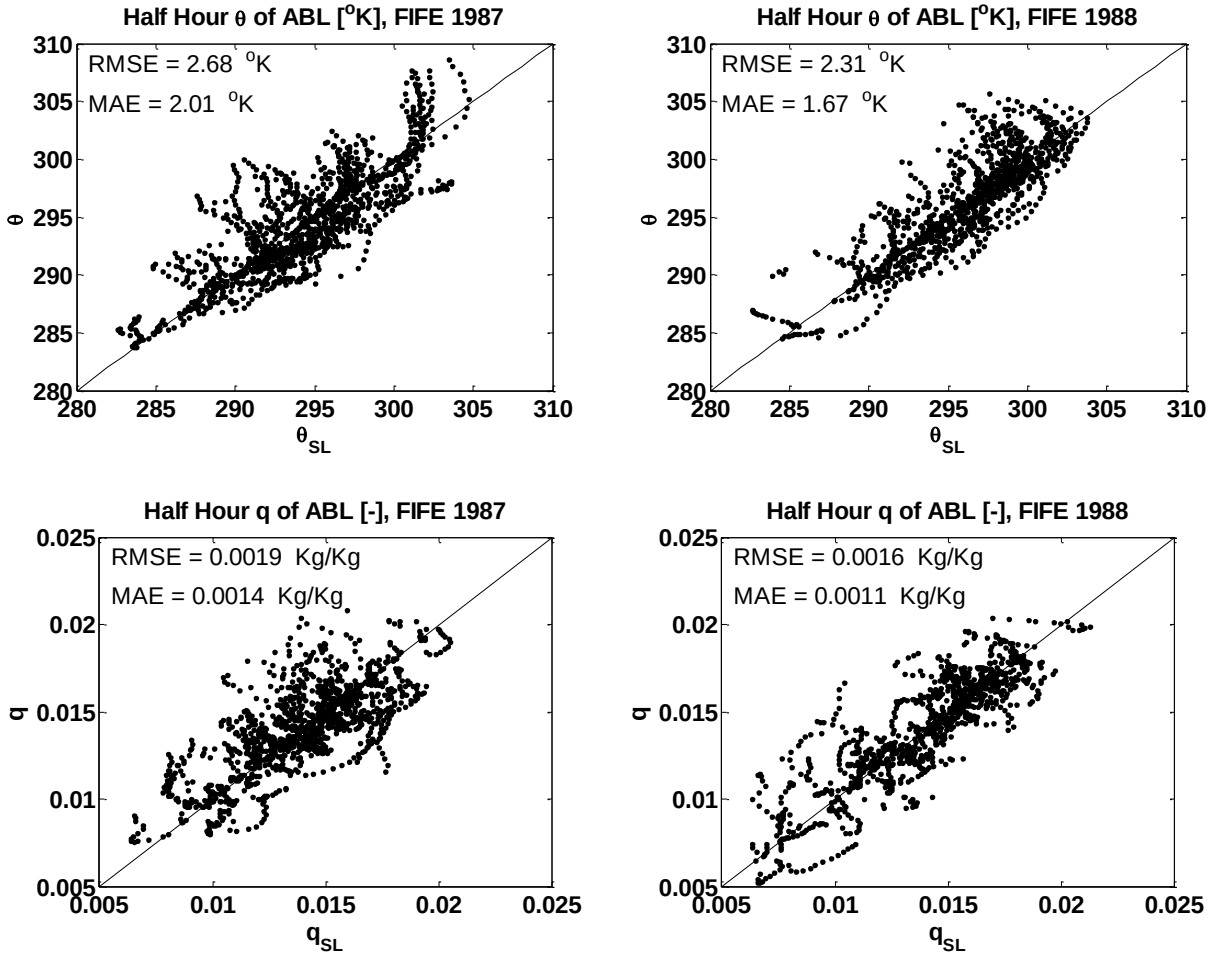

Figure 2. 7. Scatterplot of half-hourly estimated potential temperature (top) and specific humidity (bottom) versus corresponding observations for FIFE 87 (left) and FIFE 88 (right).

Time series of daily-averaged estimated and measured turbulent heat fluxes are shown in Figures 2.8 and 2.9 for FIFE 87 and 88, respectively. As indicated, the magnitude and day-to-day fluctuations of the estimated sensible and latent heat fluxes correspond relatively well with those of the observations. For example, the estimated sensible heat flux can capture the rising pattern in observations during the drydown period (Julian days 197-216) in 1987. The MAE of daily *H* and *LE* estimates are respectively 22.11 W m^{-2} (23.65 W m^{-2}) and 44.39 W m^{-2} (42.93 W m^{-2}) for FIFE 87 (88). The estimated daily *H* and *LE* have RMSE of 25.72 W m^{-2} (27.77 W m^{-2}) and

53.63 W m^{-2} (48.22 W m^{-2}) for FIFE 87 (88). Overall, the results indicate that the VDA approach can effectively use the information contained in the reference-level air temperature and specific humidity and retrieve the turbulent heat fluxes.

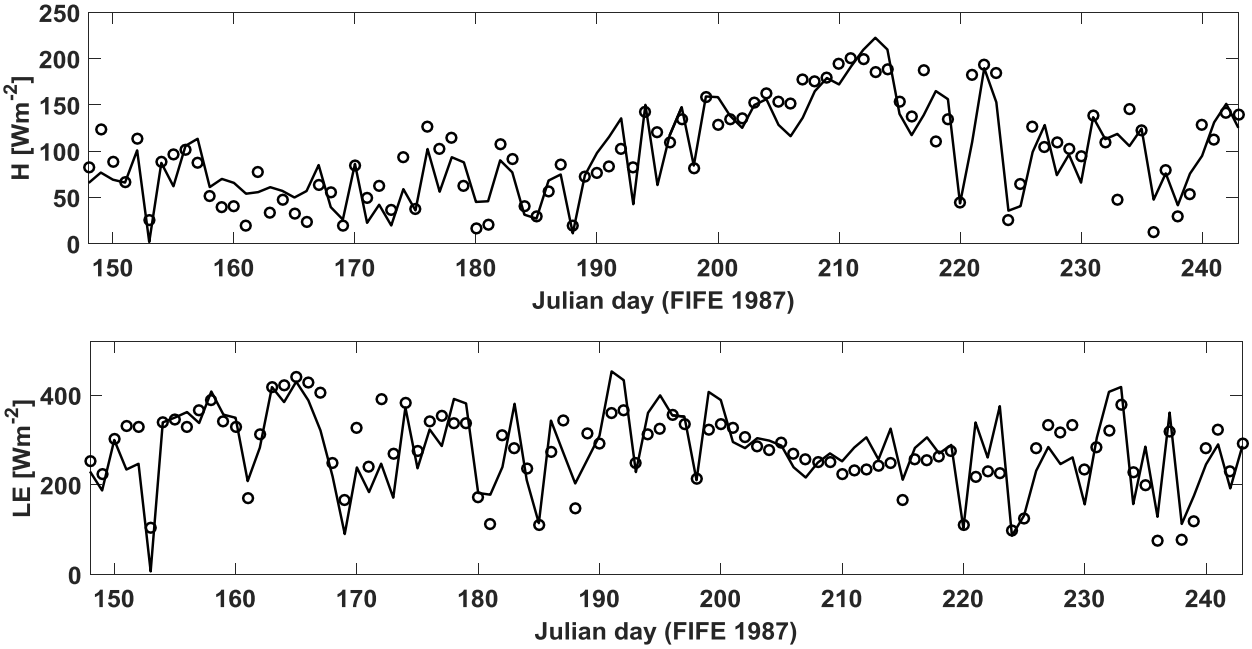

Figure 2. 8. Time series of observed (circles) and predicted (solid lines) daily turbulent heat fluxes from the VDA approach for FIFE 87. (top) sensible, and (bottom) latent heat fluxes.

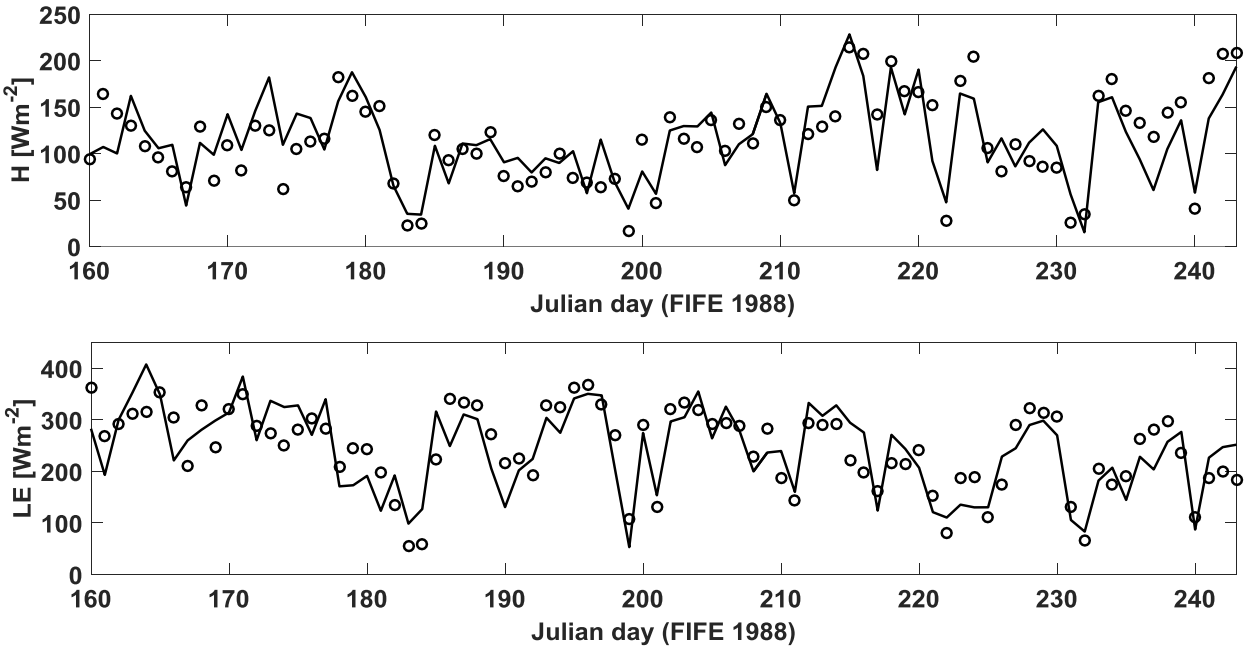

Figure 2. 9. The same as Figure 2. 8 but for FIFE 88.

Figure 2.10 compares time series of estimated half-hourly sensible and latent heat fluxes with the observations for Julian days 178–207 (FIFE 87). As can be seen, the turbulent heat fluxes estimates from the VDA approach are reasonably accurate, and for most of the days the magnitude and phase of *H* and *LE* retrievals agree well with the observations. The discrepancy between the *H* and *LE* estimates and observations is due to the simplifying assumptions including constant monthly C_{HN}, constant daily *EF*, and convectively well mixed boundary layer, which results in constant profiles of potential temperature and specific humidity with height.

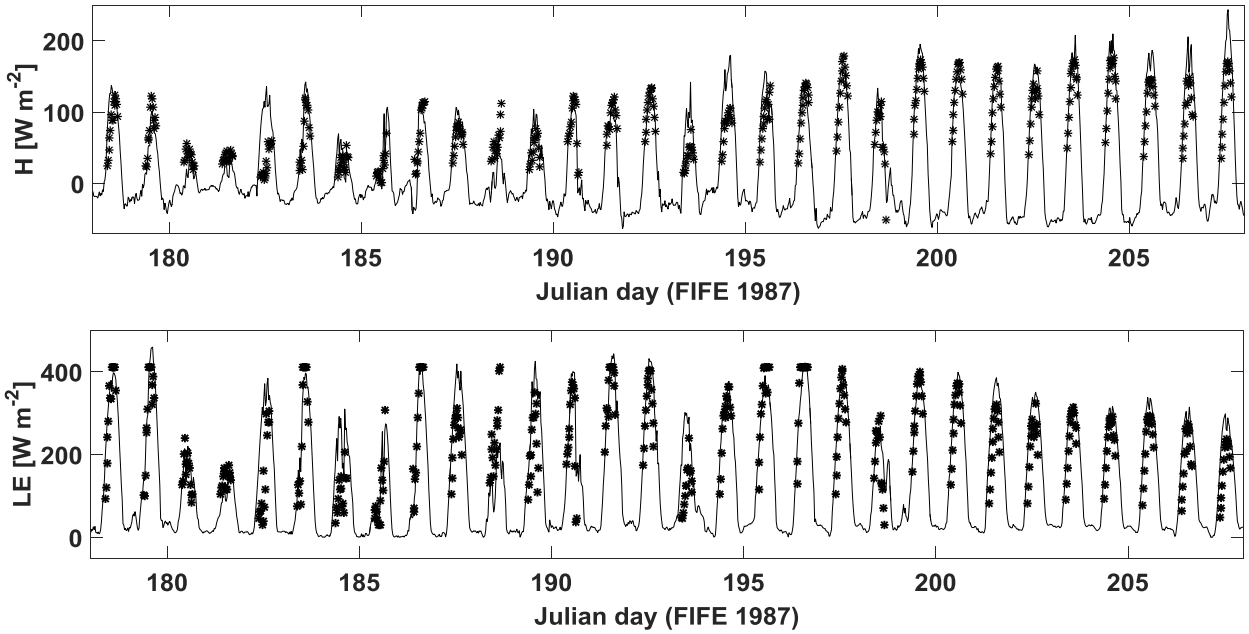

Figure 2. 10. Time series of measured (symbols) and estimated (lines) half-hourly turbulent fluxes for Julian days 178-207. (top) sensible heat flux, and (bottom) latent heat flux.

The RMSEs of half-hourly and daily average turbulent heat fluxes estimates from the proposed VDA approach (that assimilate sequences of reference-level air temperature and specific humidity measurements) are compared to those of Caparrini et al. (2004), Bateni and Entekhabi (2012b), and Bateni et al. (2013a) (that assimilated sequences of LST observations) in Tables 2.4 and 2.5, respectively. Our results are roughly comparable to those of Caparrini et al. (2004), Bateni and Entekhabi (2012b), and Bateni et al. (2013a), implying that the developed VDA can use the implicit information in the time-series of reference-level air temperature and specific humidity to partition the available energy between the sensible and latent heat fluxes.

Table 2. 4. Comparing the RMSEs of half-hourly *H* and *LE* estimates from this study (that assimilates sequences of reference-level air temperature and humidity observations) with those of Caparrini et al. (2004), Bateni and Entekhabi (2012b), and Bateni et al. (2013a) (that assimilated sequences of LST observations) for FIFE 87 and 88.

	FIFE 87		FIFE 88	
	H (W m^{-2})	LE (W m^{-2})	H (W m^{-2})	LE (W m^{-2})
Caparrini et al. (2004)	63.21	102.80	47.95	76.31
Bateni and Entekhabi (2012b)	44.87	112.01	49.53	89.51
Bateni et al. (2013a)	34.12	74.82	44.74	77.94
This study	38.61	89.05	48.42	86.63

Table 2. 5. Comparing the RMSEs of daily average *H* and *LE* estimates from this study (that assimilates sequences of reference-level air temperature and humidity observations) with those of Caparrini et al. (2004), Bateni and Entekhabi (2012b), and Bateni et al. (2013a) (that assimilated sequences of LST observations) for FIFE 87 and 88.

Different studies	FIFE 87		FIFE 88	
	H (W m^{-2})	LE (W m^{-2})	H (W m^{-2})	LE (W m^{-2})
Caparrini et al. (2004)	52.97	53.68	36.90	43.75
Bateni and Entekhabi (2012b)	31.48	61.90	30.11	50.35
Bateni et al. (2013a)	23.24	49.95	22.92	42.70
This study	25.72	53.63	27.77	48.22

Figure 2.11 compares the mean diurnal cycles of measured and estimated SEB components over the whole modelling period (i.e., Julian days 148–243 for FIFE 87 and 160–243 for FIFE 88). As indicated, the phases of mean diurnal cycles of estimated R_n, H, and LE agree reasonably well with those of observations. However, there is a significant difference between the diurnal cycles of estimated and observed ground heat flux. This happens because the phase of G is directly related to that of gradient of LST via $G = -p(\frac{dT}{dZ})|_{z=0}$, while the developed VDA approach does not assimilate the sequences of LST observations. Hence, future studies should be directed towards assimilating sequences of LST observations in addition to the reference-level air temperature and specific humidity measurements. This can be done by incorporating the soil heat diffusion equation (as a constraint) into the proposed VDA system, and assimilating LST observations into it.

The results show that assimilating the state variables of atmosphere (i.e., air temperature and specific humidity) can estimate not only the magnitude of H, LE, and R_n, but also their diurnal cycle (phase). The phase of G is directly related to that of LST via $G = -p\ dT/dz$. The developed VDA approach does not assimilate the sequences of LST, and thus it cannot capture the diurnal cycle of ground heat flux. Hence, there is a significant difference between the diurnal cycles of estimated and observed ground heat flux. In FIFE 87 (88), the VDA approach slightly overestimates (underestimates) net radiation. This may be due to the errors in the estimates ABL potential temperature values that transfer into the air temperature estimates, ultimately causing uncertainties in the net radiation retrievals.

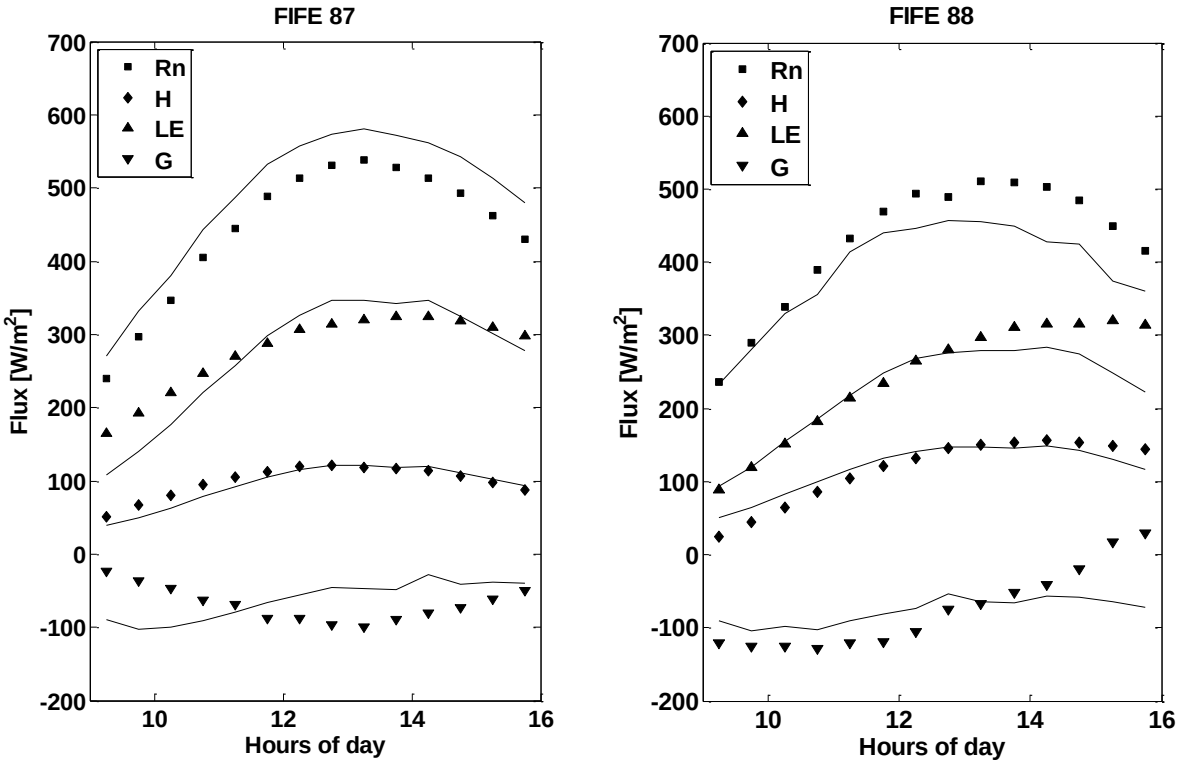

Figure 2. 11. Diurnal cycle of surface energy balance components for FIFE 87 (right) and 88 (left). Measurements (symbols), and estimations (solid lines).

As mentioned before, the $h(t_o)$, γ_θ, γ_q, $\delta_\theta(t_o)$, and $\delta_q(t_o)$ values that lead to a minimum cost function are used in the VDA system. However, the radiosonde data at the FIFE site provide a unique opportunity to run the VDA approach with the measured $h(t_o)$, γ_θ, γ_q, $\delta_\theta(t_o)$, and $\delta_q(t_o)$ values. Figure 2.12 compares the *H* and *LE* estimates using the optimized and measured $h(t_o)$, γ_θ, γ_q, $\delta_\theta(t_o)$, and $\delta_q(t_o)$ values on Julian days 155, 156, 176, 177, 178, 187, 227, 228, and 229. As expected, utilizing the $h(t_o)$, γ_θ, γ_q, $\delta_\theta(t_o)$, and $\delta_q(t_o)$ measurements in the VDA approach (instead of the optimized values) improves the *H* and *LE* estimates, and decreases the MAE and RMSE of daily *H* estimates by 16.12% and 15.21%, respectively (see Table 2.6). Similarly, the MAE (RMSE) of daily *LE* estimates reduces from 48.62 W m^{-2} to 40.44 W m^{-2}

(54.19 W m^{-2} to 46.94 W m^{-2}). However, this improvement is not significant (about 15%), implying that the VDA can provide reasonably accurate *H* and *LE* estimates by using the tuned $h(t_o)$, γ_θ, γ_q, $\delta_\theta(t_o)$, and $\delta_q(t_o)$ values.

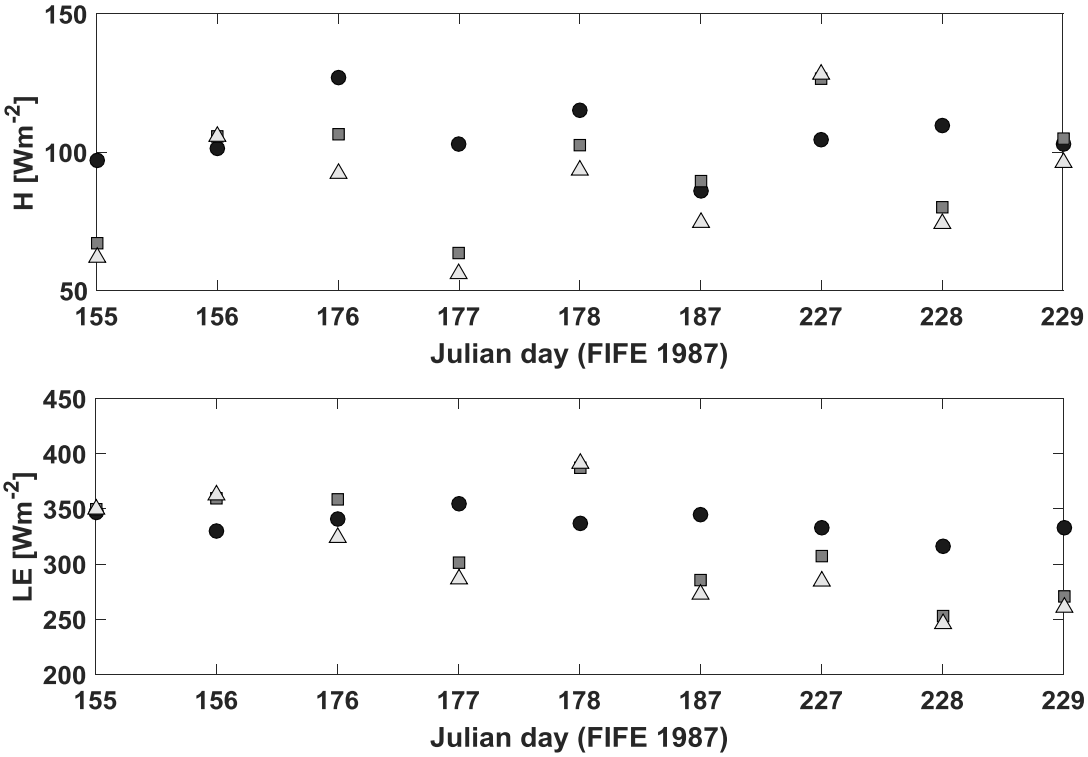

Figure 2. 12. Comparison between observed (circles), predicted with measured variables (squares) and predicted with calibrated variables (triangles) daily turbulent heat fluxes from the VDA approach for FIFE 87. (top) sensible, and (bottom) latent heat fluxes.

Table 2. 6. Comparing the MAE and RMSE of daily *H* and *LE* estimates from the VDA approach, using optimized and measured $h(t_o)$, γ_θ, γ_q, $\delta_\theta(t_o)$, and $\delta_q(t_o)$ values for Julian days 155, 156, 176, 177, 178, 187, 227, 228, and 229 in FIFE 87.

Different scenarios	MAE (W m^{-2})		RMSE (W m^{-2})	
	H	*LE*	*H*	*LE*
Measured $h(t_o)$, γ_θ, γ_q, $\delta_\theta(t_o)$, and $\delta_q(t_o)$	19.13	40.44	22.10	46.94
Optimized $h(t_o)$, γ_θ, γ_q, $\delta_\theta(t_o)$, and $\delta_q(t_o)$	24.32	48.62	28.01	54.19

The ABL observations based on radiosonde profiles of potential temperature, specific humidity, and mixed-layer height at the FIFE site during the summer of 1987 were used to verify the estimations. Figure 2.13a-i compares the mixed-layer height (h), potential temperature (θ), and specific humidity (q) estimates from the VDA approach with those inferred from the radiosondes for Aug 15-17. The error bars represent the standard deviations of the measurements from radiosondes. As indicated, in general, the estimated h, θ and q are reasonably close to the radiosonde observations. On August 15, there is an increasing trend in h, θ and q, which is captured by the corresponding estimates. On August 16, the ABL height and potential temperature grow throughout the day, while the ABL specific humidity diminishes. Remarkably, the VDA estimates capture both the rising (ABL height and potential temperature) and falling (ABL specific humidity) trends in the radiosonde measurements. Finally, on August 17, the ABL h and θ estimates agree relatively well with the observations and follow their rising trend, while there is a discrepancy between the modeled and observed q. The differences between the model estimates and observations from radiosonde data are due to simplistic assumptions (e.g., monthly constant C_{HN}, daily constant *EF*, insignificant advection, etc.), errors in the forcing data, and the

fact that the radiosonde point observations may not be able to accurately represent the spatial average for the FIFE site. Similar results were obtained for other cloud free days (e.g., June 4-6) during summer 87. Herein, for brevity, we presented results for 15-17 August 1987.

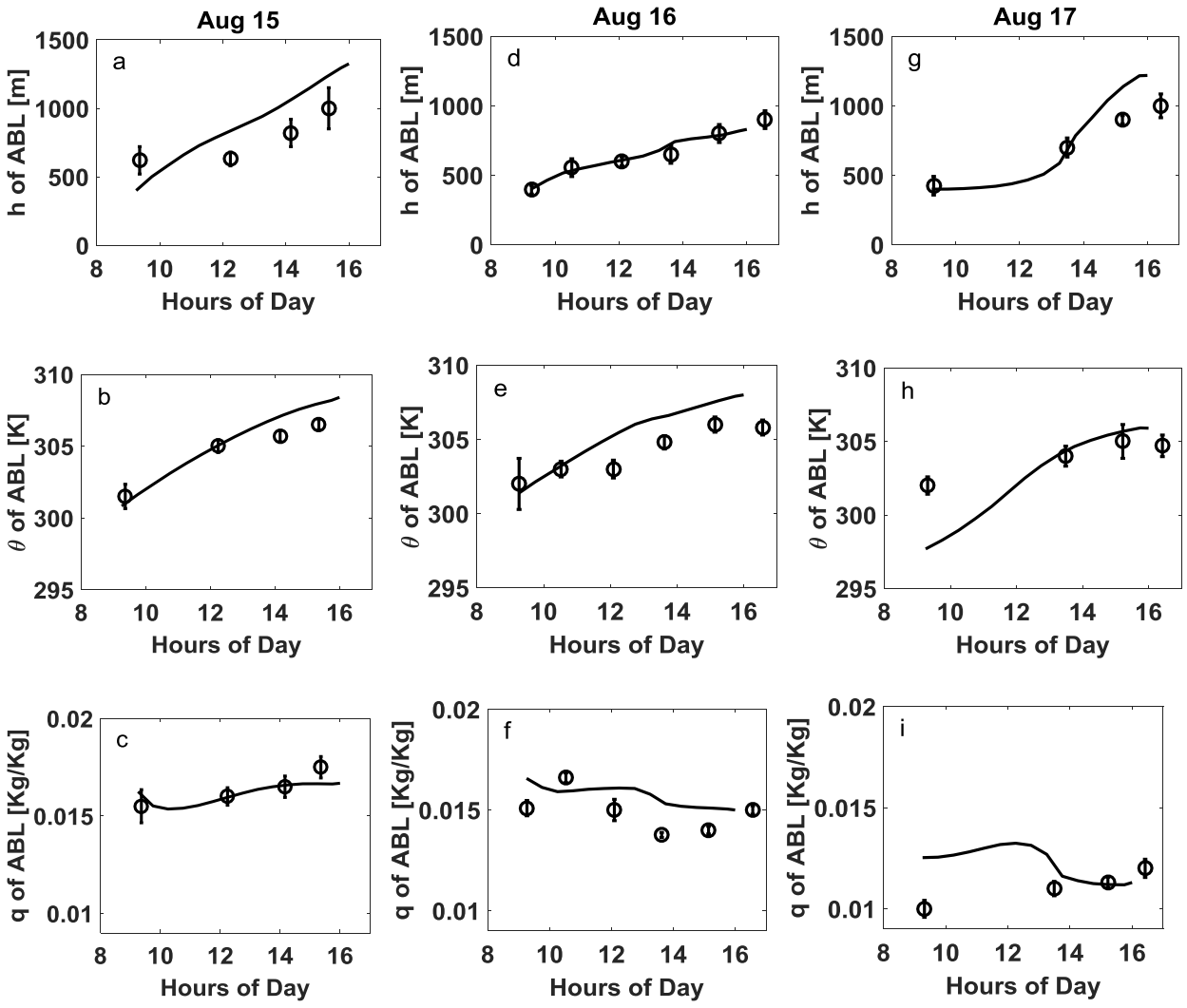

Figure 2. 13. Diurnal evolution of ABL height (top), potential temperature (middle), and humidity (bottom) at the FIFE site for 15-17 August 1987. The solid lines indicate the VDA model results, and the open circles mark the mean ABL radiosonde observations with one standard deviation.

2.6. Conclusion

A variational data assimilation (VDA) approach is developed to estimate sensible (*H*) and latent (*LE*) heat fluxes by assimilating the reference-level air temperature and humidity into an atmospheric boundary layer model. The unknown parameters of the VDA are evaporative fraction (*EF*) and neutral bulk heat transfer coefficient (C_{HN}). *EF* represents partitioning between the turbulent heat fluxes and C_{HN} scales the sum of turbulent heat fluxes.

The developed model is tested at the First ISLSCP (International Satellite Land Surface Climatology Project) Field Experiment (FIFE) site during summer 1987 and 1988. The results indicate that the developed VDA approach is capable of estimating the unknown parameters (i.e., *EF* and C_{HN}) reasonably well. The changes in the estimated C_{HN} are consistent with variations in vegetation phenology, and fall within a physically accepted range. The day-to-day fluctuations in the estimated *EF* are consistent with observations even though no information on precipitation events and soil moisture dynamics is used within the assimilation model.

Comparing the estimated turbulent heat fluxes with measurements over the FIFE site shows that the assimilation of reference-level air temperature and humidity into the developed VDA model can predict the turbulent heat fluxes accurately. For FIFE 1987 (1988), the half-hourly *H* and *LE* estimates have a mean-absolute-error (MAE) of 31.37 W m^{-2} (37.55 W m^{-2}) and 70.95 W m^{-2} (66.84 W m^{-2}), respectively. The root-mean-square-error (RMSE) for half-hourly sensible and latent heat fluxes are 38.61 W m^{-2} (48.42 W m^{-2}) and 89.05 W m^{-2} (86.63 W m^{-2}), respectively for FIFE 87 (88). The estimated daytime-averaged turbulent heat fluxes are in good agreement with the observations. The MAE of daily-averaged *H* and *LE* are 22.11 W m^{-2} (23.65 W m^{-2}) and 44.39 W m^{-2} (42.93 W m^{-2}) for FIFE 87 (88). The estimated daily *H* and *LE* have RMSE of 25.72 W m^{-2} (27.77 W m^{-2}) and 53.63 W m^{-2} (48.22 W m^{-2}) for FIFE 87 (88). This

agreement between the model predictions and observations indicates the feasibility of proposed model. It is worth mentioning that the simplistic assumptions (e.g., constant daily *EF*, constant monthly C_{HN}, insignificant advection, uniform profiles of potential temperature and specific humidity within the mixed-layer, etc.) that are used to build the VDA system generate structural model errors and cause errors in the turbulent heat fluxes estimates.

The mean diurnal cycles of estimated and measured sensible and latent heat fluxes and net radiation are close, implying that the VDA model can robustly capture the phase of *H*, *LE*, and R_n. However, there is a significant difference between the diurnal cycle of estimated and measured ground heat flux, and they are out of phase. This is due to the fact that the ground heat flux (*G*) is related to the LST through $G = - p\, dT/dz$ (where *p* is the soil thermal conductivity, *T* is the ground temperature, and *z* is the soil depth), and thus the phase of *G* is strictly dependent upon that of skin temperature, which is not estimated in our framework. Indeed, the VDA system does not assimilate the sequences of LST and therefore cannot capture the diurnal cycle of ground heat flux.

The mixed layer height, potential temperature, and specific humidity estimates from the VDA approach are reasonably close to those inferred from radiosondes. These estimates can also capture the rising/falling trends of observations during the course of the day. Overall, the results show that the developed VDA approach can extract implicit information from sequences of reference-level air temperature and specific humidity measurements to estimate the turbulent heat fluxes and ABL characteristics.

Future studies should focus on 1) the synergistic assimilation of the LST (as the state variable of land surface) as well as the reference-level air temperature and specific humidity (as the state variables of atmosphere) to improve the turbulent heat fluxes and diurnal cycle (phase)

of *G*, 2) testing the developed VDA over several sites with contrasting hydrological and vegetative conditions, and 3) developing a weak-constraint VDA approach that can capture errors in the turbulent heat fluxes due to advection.

Chapter 3: Estimation of Surface Heat Fluxes via Variational Assimilation of Land Surface Temperature, Air Temperature and Specific Humidity into a Coupled Land Surface-Atmospheric Boundary Layer Model

Estimation of Surface Heat Fluxes via Variational Assimilation of Land Surface Temperature, Air Temperature and Specific Humidity into a Coupled Land Surface-Atmospheric Boundary Layer Model

Elahe Tajfar[1] and Sayed M. Bateni[1]

[1]Department of Civil and Environmental Engineering and Water Resources Research Center, University of Hawaii at Manoa, Honolulu, USA.

Venkataraman Lakshmi[2] and Michael Ek[3]

[2] Department of Engineering Systems and Environment, University of Virginia, Charlottesville, VI, 22904, USA.

[3] University Corporation for Atmospheric Research (UCAR), Boulder, CO 80307, USA.

[*]*Corresponding author address*: Sayed M. Bateni, Department of Civil and Environmental Engineering and Water Resources Research Center, Holmes Hall 342, 2540 Doles Street, Honolulu, Hawaii, 96822, USA.

E-mail: smbateni@hawaii.edu

ABSTRACT

Numerous studies have estimated surface heat fluxes by assimilating land surface temperature (LST) observations (as the state variable of land surface) into the heat diffusion equation. A number of other studies have focused on the estimation of surface energy balance components by assimilating air temperature and specific humidity (as the state variables of atmosphere) into an atmospheric boundary layer model. This study advances the existing variational data assimilation (VDA) approaches by the synergistic assimilation of LST, air temperature, and specific humidity into a coupled land surface-atmospheric boundary layer model. The unknown parameters of the VDA approach are neutral bulk heat transfer coefficient (C_{HN}) and evaporative fraction (EF). C_{HN} scales the sum of turbulent heat fluxes, and EF represents their partitioning. The developed VDA approach is tested at the First International Satellite Land Surface Climatology Project Field Experiment (FIFE) site in the summer of 1987 and 1988. Results indicate that it performs well in both wet and dry down periods. The root-mean-square-errors (RMSEs) of estimated daily sensible and latent heat fluxes are 21.80 W m^{-2} (22.10 W m^{-2}) and 39.32 W m^{-2} (36.89 W m^{-2}) for FIFE 87 (88). The new VDA system outperforms the previous studies that assimilated either LST or air temperature/specific humidity. For FIFE 87, this study decreases the RMSEs of daily sensible and latent heat fluxes estimates by 12.5% and 24.4% compared to assimilating only LST, and by 15.2% and 26.7% compared to assimilating only air temperature and specific humidity. A similar improvement is obtained for FIFE 88 as well. The atmospheric boundary layer height, potential temperature, and specific humidity estimates from the VDA approach are also in good agreement with the corresponding radiosonde observations, and can capture their variations during the course of the day.

Keywords: Surface heat fluxes; variational data assimilation model; air temperature; specific humidity; land surface temperature

3.1. Introduction

Estimation of surface heat fluxes (sensible, latent, and ground heat fluxes) in the earth-atmosphere science has been the subject of many studies (Holtslag and Van Ulden, 1983; Bastiaanssen et al., 1998; Polonio and Soler, 2000; Kalma et al., 2008; Li et al., 2010; Maes and Steppe, 2012; Salvucci and Gentine, 2013; Bateni et al., 2012a, b, 2013a; Yilmaz et al., 2014; Zhuang and Wu, 2015; Gentine et al., 2016; Lu et al., 2016; Brenner et al., 2017). The sensible (*H*) and latent (*LE*) heat fluxes characterize exchange of heat and moisture between the land surface and its overlying atmosphere. Therefore, their accurate estimation is of crucial importance for a better understanding of land-atmosphere exchange processes and obtaining the heat and moisture budgets (Laird and Kristovich, 2002). The ground heat flux (*G*) is one of the key components of the land surface energy budget and explains the energy gained or lost during land surface warming or cooling (Bennett et al., 2008; Purdy et al., 2016).

Surface heat fluxes can be obtained via in situ measurements, which are expensive and labor extensive. Thus, various methods namely, triangle (Margulis et al., 2005; Carlson, 2007; Stisen et al., 2008; Tang et al., 2010; Laxmi et al., 2014; Martinez et al., 2017; Majozi et al., 2017), diagnostic (Jia et al., 2009; Jiang et al., 2009; Ma et al., 2012; Sharma et al., 2015), combination (Mallick et al., 2014, 2015; Raoufi and Beighley, 2017), and variational data assimilation, VDA (Bateni and Entekhabi, 2012a, b; Bateni et al., 2013a, b, 2014; Xu et al., 2015, 2018; 2018; Abdolghafoorian et al., 2017) have been developed to estimate surface heat fluxes.

The existing VDA methods (e.g., Caparrini et al., 2004; Crow and Kustas, 2005; Sini et al., 2008; Bateni and Entekhabi, 2012a, b; Bateni et al., 2013b, 2014; Xu et al., 2014, 2015, 2018, 2019; Abdolghafoorian and Farhadi, 2016; Abdolghafoorian et al., 2017) estimate the surface heat fluxes by assimilating the land surface temperature (LST) measurements into the force-restore or heat diffusion equations (i.e., land surface models without coupling to the overlying atmosphere). Their main shortcoming is that they do not perform well in wet and/or heavily vegetated sites because they assimilate only the state variable of the land surface (i.e., LST) and neglect the implicit information in the state variables of atmosphere (i.e., reference-level air temperature and humidity). Ignoring the implicit information in the reference-level air temperature and humidity may cause errors in the retrieval of turbulent heat fluxes (i.e., *H* and *LE*), especially if they are controlled by atmospheric conditions rather than the land surface properties.

In a departure with assimilating LST observations, several studies showed that the reference-level air temperature and specific humidity contain information about soil moisture (Mahfouf, 1991; Bouttier et al., 1993a, b; Mahfouf et al., 2000, 2009; Douville et al., 2000; Hess, 2001; Drusch and Viterbo, 2007; de Rosnay et al. 2013; Ren and Xue, 2016; de Lannoy et al., 2016), and turbulent heat fluxes (Zaitchik et al., 2013; Salvucci and Gentine, 2013; Rigden and Salvucci, 2015; Gentine et al., 2013b, 2016). Recently, Tajfar et al. (2019a) assimilated the sequences of reference-level air temperature and specific humidity into an atmospheric boundary layer (ABL) within a VDA framework to estimate surface heat fluxes. They showed that sequences of air temperature and specific humidity measurements contain implicit information on the partitioning of the available energy between the turbulent heat fluxes, but they cannot constrain the ground heat flux.

This work is built on Bateni et al. (2013a, b) (that assimilated LST into the soil heat diffusion equation) and Tajfar et al. (2019a) (that assimilated air temperature and specific humidity into an ABL model), but it advances those studies by the synergistic assimilation of LST, air temperature, and specific humidity into a coupled land surface-ABL model within a new VDA system. The main goal of this study is to obtain the sum of the turbulent heat fluxes ($H+LE$) that is scaled by the neutral bulk heat transfer coefficient (C_{HN}), and the partitioning between the turbulent heat fluxes ($LE/(LE+H)$), which is scaled by the evaporative fraction (EF). The advantages of the developed VDA approach are: 1) it can generate turbulent heat fluxes for instances in which LST, air temperature, and humidity are unavailable or there are data gaps, 2) it does not require surface roughness for heat and momentum, 3) it does not need ground heat flux specification, 4) it performs better than the previous studies that assimilated only LST (Bateni et al., 2013a, b) or only air temperature/humidity observations (Tajfar et al., 2019a).

This study is structured as follows: the heat diffusion equation, surface energy balance (SEB) scheme, ABL model, and VDA approach are described in Section 3.2. Section 3.3 explains the First International Satellite Land Surface Climatology Project Field Experiment (FIFE) dataset. The results are provided in Section 3.4. Finally, conclusions are given in Section 3.5.

3.2. Methods and Models

3.2.1. Heat Diffusion Equation

The one-dimensional heat diffusion equation can be described by,

$$c\frac{\partial T(z,t)}{\partial t} = p\frac{\partial^2 T(z,t)}{\partial z^2} \quad (3\text{-}1)$$

where c is the soil volumetric heat capacity (J m^{-3} K^{-1}), p is the soil thermal conductivity (W m^{-1} K^{-1}), and $T(z,t)$ is the ground temperature at depth z and time t. Hereafter, the ground temperature at the surface, $T(z=0,t)$, is denoted by $T(t)$.

To solve the heat diffusion equation, the boundary conditions at the top and bottom of the soil column should be specified. At the top of the soil column, the surface boundary forcing equation is applied,

$$-p\frac{\partial T(0,t)}{\partial z} = G \tag{3-2}$$

where G is the ground heat flux.

The ground temperature at the depth of 0.3-0.5 m is almost constant in daily time-scales (Hu and Islam, 1995). Hence, a Neumann boundary condition is used at the bottom of the soil column,

$$\frac{\partial T(z=0.5,t)}{\partial z} = 0 \tag{3-3}$$

3.2.2. Surface Energy Balance Scheme

The surface energy balance (SEB) equation can be defined as,

$$R_n = H + LE + G \tag{3-4}$$

where R_n is the net radiation.

The sensible heat flux is given by,

$$H = \rho c_p C_{HN} f(Ri) U(T - T_a) \tag{3-5}$$

where ρ is the air density, c_p is the specific heat capacity of air, U is the wind speed, and T_a is the reference-level (z_{ref}) air temperature. f (.) is the atmospheric stability correction function, which depends on the Richardson number (Ri). The expression for f (.) can be found in Caparrini et al. (2003). C_{HN} is the neutral bulk heat transfer coefficient, and varies mainly with changes in

vegetation phenology on a monthly time-scale (Bateni et al., 2013a, b; Xu et al., 2018; He et al., 2018). It constitutes the first unknown of the VDA approach.

Net radiation is calculated via,

$$R_n = (1-\alpha)R_s^{\downarrow} + R_l^{\downarrow} - \varepsilon_s \sigma T^4 \quad (3\text{-}6)$$

where α is the surface albedo, $R_s^{\downarrow}$ is the incoming solar radiation at the land surface, ε_s is the surface emissivity, and σ is the Stefan-Boltzman constant, $R_l^{\downarrow} = \varepsilon_a \sigma T_a^4$ is the incoming longwave radiation (ε_a is the atmospheric emissivity, which is obtained from the Idso (1981) formulation).

EF is defined as the ratio of latent heat flux to the sum of turbulent heat fluxes,

$$EF = \frac{LE}{H+LE} \quad (3\text{-}7a)$$

EF is nearly constant during the assimilation window (09:00-16:00 LT) on days without precipitation (Gentine et al., 2007; Xu et al., 2018; He et al., 2018). It constitutes the second unknown of the VDA approach. By rewriting equation (3-7a), *LE* can be estimated via,

$$LE = \frac{EF}{1-EF} H \quad (3\text{-}7b)$$

3.2.3. Atmospheric Boundary Layer Model

A mixed-layer model, which performs very well compared to the more intricate large-eddy simulations is used in this study to simulate the ABL processes (Margulis and Entekhabi, 2001; Garcia and Mellado, 2014; Gentine et al., 2015; Tajfar et al., 2019a). The idealized profiles of ABL state variables and corresponding fluxes between the surface layer, mixed-layer, and overlying free atmosphere are shown in Figure 3.1. Various elements of the ABL model are described in Sections 3.2.3.1.-3.2.3.5.

3.2.3.1. Atmospheric Boundary Layer (ABL) Energy and Moisture Budget

The surface layer is a thin layer that is most affected by the interaction of land surface and its overlaying air. The top of the surface layer (z_{SL}) is assumed to be equal to 10% of the mixed-layer height, h (i.e., $z_{SL} = 0.1h$) (Margulis and Entekhabi, 2001; Gentine et al., 2016; Tajfar et al., 2019a). Above the surface layer is the mixed-layer in which potential temperature (θ) and specific humidity (q) are well mixed (convectively mixed), and are assumed to be uniform (Margulis and Entekhabi, 2001, Gentine et al., 2016; Tajfar et al., 2019a).

The evolution of potential temperature (θ) and specific humidity (q) in the mixed-layer can be calculated via,

$$\rho c_p h \frac{d\theta}{dt} = \left(R_{ad} + R_{gu}\right)\varepsilon_m - R_{Ad} - R_{Au} + H + H_{top} \quad (3\text{-}8a)$$

$$\rho h L_v \frac{dq}{dt} = LE + LE_{top} \quad (3\text{-}8b)$$

where ε_m is the mixed-layer bulk emissivity. The readers are referred to Kim and Entekhabi (1998) for the equation for ε_m. L_v is the latent heat of vaporization, h is the mixed-layer height, t is the time, H_{top} and LE_{top} are respectively the entrainment heat and moisture fluxes at the top of mixed-layer, R_{ad} and R_{gu} are the longwave radiations that enter the mixed-layer from the free atmosphere above and the land below, respectively, and R_{Ad} and R_{Au} are the longwave radiative fluxes emitted downward and upward from within the mixed-layer, respectively, and θ and q are the state variables of the ABL model, which are estimated by equations (3-8a) and (3-8b).

Initial conditions for θ and q (i.e., $\theta(t_o$ = 9 a.m.) and $q(t_o$ = 9 a.m.)) are needed to solve equations (3-8a) and (3-8b). The potential temperature at the level of 1000 mb (i.e., θ_a) is obtained from the reference-level air temperature (T_a) through $\theta_a = T_a(P_0/P_s)^{\frac{R_d}{cp}}$ (where P_0 is 1000 mb, R_d is the gas constant of dry air, and P_s is the surface pressure) (Shuttleworth, 2012).

$\theta(t_o$ = 9 a.m.) and $q(t_o$ = 9 a.m.) can be obtained from $\theta_a(t_o$ = 9 a.m.) and $q_a(t_o$ = 9 a.m.) (q_a is the reference-level specific humidity) using the Monin-Obukhov Similarity Theory (see Appendix A) (Rigden and Salvucci, 2015; Gentine et al., 2016).

3.2.3.2. Radiative Fluxes

Radiative fluxes from the free atmosphere (R_{ad}) and surface layer (R_{gu}) enter the mixed-layer (Figure 3.1). R_{ad} is given by (Brustsaert, 1975; Brubaker and Entekhabi, 1995),

$$R_{ad} = \varepsilon_{ad}\sigma T_h^4 \tag{3-9}$$

where ε_{ad} is the effective emissivity of free atmosphere, and T_h is the air temperature exactly above the mixed-layer. The expressions for ε_{ad} and T_h can be found in Kim and Entekhabi (1998).

The upward radiative flux from the ground into the mixed-layer (R_{gu}) is estimated via,

$$R_{gu} = \varepsilon_s\sigma T^4 \tag{3-10}$$

The upwelling (R_{Au}) and downwelling (R_{Ad}) longwave radiative fluxes from within the mixed-layer cool down the ABL, and are given by (Brubaker and Entekhabi, 1995; Margulis and Entekhabi, 2001),

$$R_{Ad} = \varepsilon_d\sigma\theta^4 \tag{3-11a}$$

$$R_{Au} = \varepsilon_u\sigma\theta^4 \tag{3-11b}$$

where ε_d and ε_u are the mixed-layer downward and upward emissivities, respectively (Kim and Entekhabi, 1998).

3.2.3.3. Entrainment Fluxes

In addition to R_{gu}, R_{ad}, and H, the entrainment heat flux from the free atmosphere (H_{top}) enters the ABL and warms it up. H_{top} is estimated via,

$$H_{top} = AH \tag{3-12}$$

A typical value of 0.2 is used for A (Gentine et al., 2015; Garcia and Mellado, 2014; Tajfar et al., 2019a).

LE from the surface moisturizes the ABL, but dry air entrainment (LE_{top}) from free atmosphere reduces its humidity (Stull 1994). LE_{top} is given by,

$$LE_{top} = \rho L_v \delta_q \frac{dh}{dt} \tag{3-13}$$

where δ_q is the inversion strength of q, which causes a jump in specific humidity at the top of the mixed-layer (Figure 3.1).

3.2.3.4. Mixed-Layer Height

The daytime growth of the ABL height (h) is given by (Smeda, 1979; Kim and Entekhabi, 1997, 1998a, b; Bagley et al., 2011),

$$\frac{dh}{dt} = \frac{2(G_* - D_1 - D_2)\theta}{gh\delta_\theta} + \frac{H_v}{\rho c_p \delta_\theta} \tag{3-14a}$$

G_*, D_1, D_2, and H_v are defined by,

$$G_* = u_{SL} u_*^2 \tag{3-14b}$$

$$D_1 = u_{SL} u_*^2 (1 - e^{-\varphi h}) \tag{3-14c}$$

$$D_2 = 0.4 \left(\frac{gh}{\theta} \frac{H_v}{\rho c_p} \right) \tag{3-14d}$$

$$H_v \approx H + 0.07LE \tag{3-14e}$$

where δ_θ is the inversion strength of θ which causes a jump in potential temperature at the top of the mixed-layer (Figure 3.1), g is gravitational acceleration, G_* is the production of mechanical turbulent energy (Kim and Entekhabi, 1998; Margulis and Entekhabi, 2001), u_{SL} is the wind speed at the top of the surface layer, which is found from the wind speed at the reference-level using the Monin-Obukhov Similarity Theory (see Appendix A), u_* is the friction velocity that is related to the wind speed measurements at the reference-level (see Appendix A), φ is the mechanical turbulence dissipation parameter, which is set to 0.01 (Kim and Entekhabi,1998b; Margulis and Entekhabi, 2001; Bagley et al., 2011), and H_v is the virtual heat flux at the surface.

3.2.3.5. Potential Temperature and Specific Humidity Inversion Strength

As shown in Figure 3.1, there are jumps in the potential temperature and humidity at the top of the boundary layer. The inversion strengths for potential temperature (δ_θ) and specific humidity (δ_q) are given by,

$$\frac{d\delta_\theta}{dt} = \gamma_\theta \frac{dh}{dt} - \frac{d\theta}{dt} \tag{3-15}$$

$$\frac{d\delta_q}{dt} = \gamma_q \frac{dh}{dt} - \frac{dq}{dt} \tag{3-16}$$

where γ_θ and γ_q are the lapse rates in potential temperature and specific humidity above the mixed-layer (Margulis and Entekhabi, 2003).

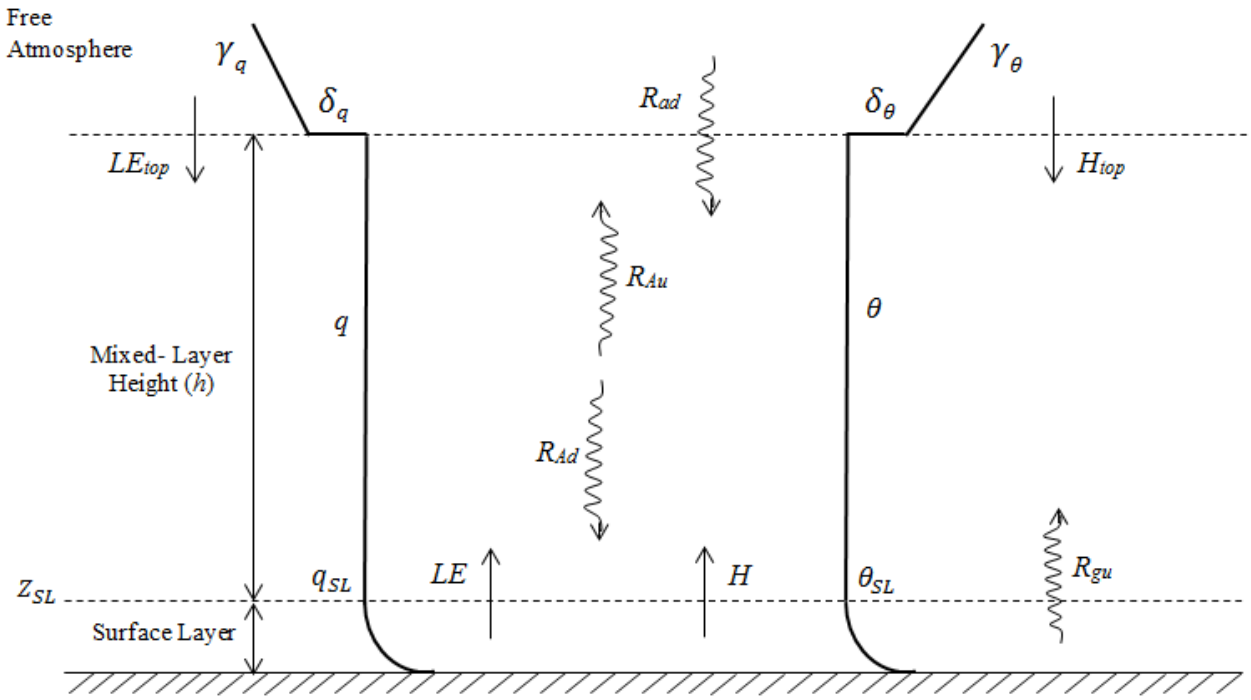

Figure 3. 1. Idealized profiles of ABL states (θ and q) and corresponding fluxes between the surface layer, mixed layer, and overlying atmosphere.

3.2.4. Variational Data Assimilation (VDA) Scheme

Optimal values of C_{HN} and EF are obtained by minimizing the objective function J. Two different integral time scales are used in the objective function. The first one covers the entire assimilation period (N = 30 days) in which C_{HN} is assumed to be constant. The second one spans the assimilation window [t_0 = 09:00 – t_1 = 16:00 LT] in which EF is presumed to be constant. The cost function (J) is given by,

$$J\left(T,\theta,q,\lambda_1,\lambda_2,\lambda_3,R,EF\right) =$$

$$\sum_{i=1}^{N}\int_{t_o}^{t_1}[T_i(t)-T_{obs,i}(t)]^T R_T^{-1}[T_i(t)-T_{obs,i}(t)]\,dt+\sum_{i=1}^{N}\int_{t_o}^{t_1}[\theta_i(t)-\theta_{SL,i}(t)]^T R_\theta^{-1}[\theta_i(t)-$$

$$\theta_{SL,i}(t)]\,dt+\ \sum_{i=1}^{N}\int_{t_o}^{t_1}[q_i(t)-q_{SL,i}(t)]^T\,R_q^{-1}\left[q_i(t)-q_{SL,i}(t)\right]dt+(R-R')^T B_R^{-1}(R-R')+$$

$$\sum_{i=1}^{N}(EF_i-EF_i')^T B_{EF}^{-1}(EF_i-EF_i')+\ \sum_{i=1}^{N}\int_{t_o}^{t_1}\lambda_{1i}(t)\left[\rho c_p h_i(t)\frac{d\theta_i(t)}{dt}-\left(R_{ad}+R_{gu}\right)\varepsilon_m+\right.$$

$$R_{Ad} + R_{Au} - H - H_{top}\Big]\, dt + \sum_{i=1}^{N} \int_{t_o}^{t_1} \lambda_{2i}(t) \left[\rho h_i(t) L_v \frac{dq_i(t)}{dt} - LE - LE_{top}\right] dt +$$

$$\sum_{i=1}^{N} \int_{t_o}^{t_1} \int_{0}^{l} \lambda_{3i} \left(\frac{\partial T_i}{\partial t} - D \frac{\partial^2 T_i}{\partial z^2}\right) dz dt \qquad (3\text{-}17)$$

The first term on the right hand side of the cost function represents the square of misfit between the LST estimates from the heat diffusion equation (T) and its corresponding measurements (T_{obs}). The second and third terms are the square of misfits between the top of the surface layer potential temperature (θ) and specific humidity (q) estimates from equations (3-8a) and (3-8b), and the top of the surface layer potential temperature (θ_{SL}) and specific humidity (q_{SL}) that themselves are obtained from the reference-level air temperature (T_a) and specific humidity (q_a) via the MOST (see Appendix A). To ensure C_{HN} is always positive, it is transformed to R via $C_{HN} = e^R$. The fourth and fifth terms are the squared errors of the unknown parameters (i.e., R and EF) with respect to their prior values (R' and EF'). The last three terms are physical constraints, which are adjoined to the model by the Lagrange multipliers λ_1, λ_2 and λ_3. l is the depth of lower boundary condition in the soil column (herein, taken 0.5 m).

R_T^{-1}, R_θ^{-1} and R_q^{-1} are the inverse error covariance matrices of T, θ and q, respectively. B_R^{-1} and B_{EF}^{-1} are the inverse background error covariance matrices of R and EF, respectively. The values of R_T^{-1}, R_θ^{-1}, R_q^{-1}, B_R^{-1} and B_{EF}^{-1} can be found from the inverse covariance functions of states (i.e., T, θ, and q) and parameters (i.e., R and EF), if their statistical structures are known (Bennett, 1992). Because of the lack of detailed information on the statistical structure of the states and parameters, R_T^{-1}, R_θ^{-1}, R_q^{-1}, B_R^{-1} and B_{EF}^{-1} are here considered as diagonal matrices of numerically constant values whose relative magnitudes control the rate of convergence and the stability of the VDA system (Bennett, 1992; Castelli et al., 1999). $(\theta_i(t) - \theta_{SL,i}(t))$ and $(T_i(t) - T_{obs,i}(t))$ both have the order of magnitude of ~5 K [i.e., $(\theta_i(t) - \theta_{SL,i}(t))$ ~ O(5) and

$(T_i(t) - T_{obs,i}(t)) \sim 5]$, and thus $[\theta_i(t) - \theta_{SL,i}(t)]^T[\theta_i(t) - \theta_{SL,i}(t)] \sim$ O(25) and $[T_i(t) - T_{obs,i}(t)]^T[T_i(t) - T_{obs,i}(t)] \sim$ O(25). $(q_i(t) - q_{SL,i}(t))$ has an order of magnitude of ~ 5×10^{-3} [i.e., $(q_i(t) - q_{SL,i}(t)) \sim O(5\times10^{-3})$]. Consequently, $[q(t) - q_{SL}(t)]^T\ [q(t) - q_{SL}(t)] \sim$ O(25×10^{-6}). Setting the diagonal elements of R_T^{-1}, R_θ^{-1} and R_q^{-1} to 10^{-1} K^{-2}, 10^{-1} K^{-2}, and 10^5 causes the first, second, and third terms in the cost function to have the order of magnitude of ~2.5.

B_R^{-1} and B_{EF}^{-1} are found by trial and error (Daley, 1991). The magnitude of the objective function (*J*) is computed for different values of B_R^{-1} and B_{EF}^{-1}, and the values that lead to a minimum objective function are chosen. In the first test, the diagonal elements of B_R^{-1} and B_{EF}^{-1} are considered to be equal and are changed from 10^1 to 10^{15}. The VDA model is unstable when the diagonal elements of B_R^{-1} and B_{EF}^{-1} are varied from 10^1 to 10^6. For B_R^{-1} and B_{EF}^{-1} of 10^7 to 10^{15}, the cost function is stable and converges (Table 3.1, first row). In the second test, unequal values of B_R^{-1} and B_{EF}^{-1} are used in the objective function (Table 3.1, second row). It is observed that the objective function reaches its minimum value of 1.677×10^6 by setting the diagonal elements of B_R^{-1} and B_{EF}^{-1} to 10^9 and 10^8, respectively. A similar approach was used in Castelli et al., (1999), Caparrini et al. (2004), Bateni et al. (2013a) and Tajfar et al. (2019a).

To obtain the optimal values of *R* and *EF*, the cost function (*J*) should be minimized. For this purpose, the first variation of *J* (δJ) with respect to the independent variables θ, q, T, λ_1, λ_2, λ_3, R and EF need to be set to zero. This results in eight equations (the so-called Euler-Lagrange equations), which should be solved simultaneously to obtain the optimal values of *R* and *EF*. The Euler-Lagrange equations are listed in Appendix D.

Table 3. 1. The magnitude of cost function (J) for different values of B_R^{-1} and B_{EF}^{-1}. Equal (top panel) and unequal (bottom panel) values for B_R^{-1} and B_{EF}^{-1} are considered.

B_R^{-1}	10^7	10^8	10^9	10^{10}	10^{11}	10^{12}	10^{13}	10^{14}	10^{15}
B_{EF}^{-1}	10^7	10^8	10^9	10^{10}	10^{11}	10^{12}	10^{13}	10^{14}	10^{15}
$J\times10^6$	2.187	2.186	1.699	2.799	1.851	1.747	1.736	1.735	1.737
B_R^{-1}	10^8	10^7	10^8	**10^9**	10^9	10^{10}	10^{10}	10^{11}	10^{11}
B_{EF}^{-1}	10^7	10^8	10^9	**10^8**	10^{10}	10^9	10^{11}	10^{10}	10^{12}
$J\times10^6$	2.159	2.175	8.315	**1.677**	8.475	2.052	2.896	1.775	1.859

3.3. FIFE Site

The VDA approach is tested at the First ISLSCP (International Satellite Land Surface Climatology Project) Field Experiment (FIFE) site in central Kansas during Julian days 148–243 in FIFE 87 and 160–243 in FIFE 88 (Sellers et al. 1992). FIFE site is a prairie grassland over a 15 km by 15 km area centered at 39.05° N, 96.53° W. The FIFE dataset provides all the required hydrological variables (i.e., LST, vegetation height, and atmospheric forcing data including incoming solar radiation, air temperature, specific humidity, and wind speed) to run the VDA approach as well as surface heat fluxes and radiosonde measurements of ABL potential temperature (θ), specific humidity (q), and mixed-layer height (h) to verify the model estimates (Betts and Ball 1998).

The meteorological data were collected every 30 minutes from 10 Portable Automatic Meteorological (PAM) stations (1 May 1987 to 10 November 1989), and averaged over the FIFE site. The erroneous data were eliminated from each station by comparing the mean and standard deviation of the time series of all 10 PAM stations. In addition, surface heat fluxes with a 30-

minute time step were collected from 22 and 10 stations respectively in summers of 1987 and 1988, and averaged over the FIFE site. The area-averaged observations over the 15 km by 15 km FIFE site allows to validate the VDA approach over the scale of several kilometers, which is compatible for future use with satellite data over large-scale domains with a computational grid size of a few kilometers (Chen et al., 1996). The vegetation height measurements at the FIFE site are taken from the Oak Ridge National Laboratory-Distributed Active Archive Center (ORNL-DAAC) (https://daac.ornl.gov/FIFE/guides/Vegetation_Biophysical_Data.html).

The radiosonde measurements at the FIFE site allow to verify the ABL potential temperature, humidity, and height estimates from the VDA system. The radiosonde measurements were obtained in the summer of 1987 during intensive field campaigns (IFCs) 1-3 (Strebel et al., 1994). The radiosonde observations were measured using 0–8 launches on particular days during the IFCs with 90-minute intervals and during the growth phase of the boundary layer. The radiosonde measurements of ABL potential temperature, humidity, and height in several cloud-free days during each IFC [June 4-6 in IFC1; Jun 26, July 6, and July 11 in IFC 2; Aug 15-17 in IFC 3] are used to verify the corresponding VDA retrievals.

The initial condition for the ABL height, $h(t_o = 9\ \text{a.m.})$, is required to integrate equation (3-14a) forward in time. The initial conditions for δ_θ (i.e., $\delta_\theta(t_o = 9\ \text{a.m.})$) and γ_θ are needed to solve equation (3-15). Similarly, the initial condition for δ_q (i.e., $\delta_q(t_o = 9\ \text{a.m.})$) and γ_q are required to integrate equation (3-16) forward in time. $h(t_o)$, γ_θ, γ_q, δ_θ and δ_q often change over the range of 100 – 500 m, 2 – 8 K km^{-1}, -7×10^{-3} – - 0.5×10^{-3} kg kg^{-1} km^{-1}, 2 – 6 K, and - 4.8×10^{-3} – - 0.5 × 10^{-3} kg kg^{-1}, respectively (Margulis, 2002; Van Heerwaarden et al., 2010; Gentine et al., 2016). In this study, $h(t_o)$, γ_θ, γ_q, δ_θ and δ_q are varied over the abovementioned ranges with the increment of 100 m, 0.5 K km^{-1}, 0.5×10^{-3} kg kg^{-1} km^{-1}, 0.4 K, and 0.4×10^{-3}

kg kg^{-1}, respectively. It is found that the cost function finds its lowest value with $h(t_o)$ = 400 m, γ_θ = 4.5 K km^{-1}, γ_q = -1.4×10^{-3} kg kg^{-1} km^{-1}, $\delta_\theta(t_o)$ = 3.6 K, and $\delta_q(t_o)$ = - 4.0×10^{-3} kg kg^{-1}.

Following Betts and Ball (1998) and Bateni et al. (2012, 2013a), the soil thermal conductivity (p), soil volumetric heat capacity (c), surface emissivity (ε_s), and albedo (α) are set to 0.65 (W m^{-1} K^{-1}), 2.35×10^6 (J m^{-3} K^{-1}), 0.98, and 0.2, respectively. All of the parameters with fixed-values are listed in Table 3.2.

Table 3. 2. Values of time-invariant parameters used in the VDA approach.

Parameter	Value	Unit
Air density (ρ)	1.2	kg m^{-3}
Specific heat capacity (c_p)	1004	J kg^{-1} K^{-1}
Stefan-Boltzmann constant (σ)	5.67×10^{-8}	W K^{-4} m^{-2}
Latent heat of vaporization (L_v)	2.5×10^{6}	J kg^{-1}
Lapse rate of θ above h (γ_θ)	4.5	K km^{-1}
Lapse rate of q above h (γ_q)	-1.4×10^{-3}	kg kg^{-1} km^{-1}
Initial ABL height (h (t_o= 9 a.m.))	400	M
Initial inversion strength of θ ($\delta_\theta(t_o$= 9 a.m.))	3.6	K
Initial inversion strength of q ($\delta_q(t_o$= 9 a.m.))	$- 4.0 \times 10^{-3}$	kg kg^{-1}
Gas constant for dry air (R_d)	287	J kg^{-1} $^oC^{-1}$
Gas constant for water vapor (R_v)	461	J kg^{-1} $^oC^{-1}$
Surface pressure (P_s)	96700	Pa
Mechanical turbulence dissipation	0.01	m^{-1}
Assimilation window [t_o, t_1]	[09:00, 16:00 LT]	hr
Soil thermal conductivity (p)	0.65	W m^{-1} K^{-1}
Soil volumetric heat capacity (c)	2.35×10^{6}	J m^{-3} K^{-1}
Surface emissivity (ε_s)	0.98	-
Albedo (α)	0.2	-
von Karman constant (k)	0.41	-
Entrainment parameter, *A* (equation 3-12)	0.2	-
Number of days in the assimilation period (*N*)	30	-

3.4. Results

As mentioned earlier, the two main unknowns of the VDA approach are C_{HN} ($C_{HN} = e^R$) and *EF*. In this study, C_{HN} and *EF* are assumed to vary on monthly and daily time-scales, respectively. Substituting equations (3-5) and (3-7b) into (3-8b) leads to,

$$\rho h L_v \frac{dq}{dt} = LE + LE_{top} = \frac{EF}{1-EF} H + LE_{top} = \frac{EF}{1-EF} \rho c_p e^R f(Ri) U(T - T_a) + LE_{top} \quad (3\text{-}18)$$

Also, substituting equations (3-4), (3-5), and (3-7b) into the surface boundary forcing equation yields,

$$-p \frac{dT(0,t)}{dt} = R_n - H - LE = R_n - \frac{H}{(1-EF)} = R_n - \frac{\rho c_p e^R f(Ri) U(T-T_a)}{(1-EF)} \quad (3\text{-}19)$$

The product of e^R and $EF(1-EF)^{-1}$ appears in (3-18). Also, the product of e^R and $(1-EF)^{-1}$ emerges in (3-19). If R and EF are allowed to change on the same time-scale, the VDA scheme cannot distinct them and thus becomes ill-posed. To make the estimation problem well-posed and realizing that EF and R vary on different time scales, daily EF and monthly R are estimated by the VDA approach.

To find a reasonable initial guess for $C_{HN} = e^R$ in each monthly assimilation period, the VDA approach is run for a number of reasonable *R* values. In these tests, *R* is changed from -7.5 to -3.5 with the increment of 0.5. For each utilized *R* value in the VDA approach, the RMSEs of corresponding *EF*, θ, *q*, and LST estimates are calculated (Figure 3.2). As shown, the RMSEs of *EF*, θ, *q*, and LST retrievals reach their minimum at the *R* value of -4.5, -5.0, and -5.5 for the first (Julian days 148-177), second (Julian days 178-207), and third (Julian days 208-243) assimilation periods in FIFE 87, respectively. Similarly, the RMSEs of *EF*, θ, *q*, and LST estimates find their minimum at the *R* of -6.0 for the first (Julian days 160-189), and -5.0 for the second (Julian days 190-219) and third (Julian days 220-243) assimilation periods in FIFE 88. For each assimilation period, the *R* value that minimizes the RMSEs of *EF*, θ, *q*, and LST retrievals is used as the initial guess in the VDA approach. The VDA approach iteratively improves *R*, and finally finds its optimum value (see Appendix D).

Table 3.3 shows C_{HN} estimates from the VDA approach and corresponding LAI values. The LAI- Normalized Difference Vegetation Index (NDVI) relationship suggested by Aparicio

et al. (2000) is used to obtain LAI from NDVI. NDVI data were obtained from Landsat and SPOT satellites by Hall et al. (1992). The estimated C_{HN} values fall within a physically accepted range (Stull, 1994; Caparrini et al., 2004a; Bateni et al., 2013b). For FIFE 87, LAI has its maximum value of 1.7 in the first assimilation period (i.e., Julian days 148-178) and decreases during the course of the summer due to reduction in precipitation. In contrast, LAI increases during the summer of 1988. As indicated, in both years, C_{HN} variations are consistent with those of LAI although no information on vegetation phenology is used in the VDA approach.

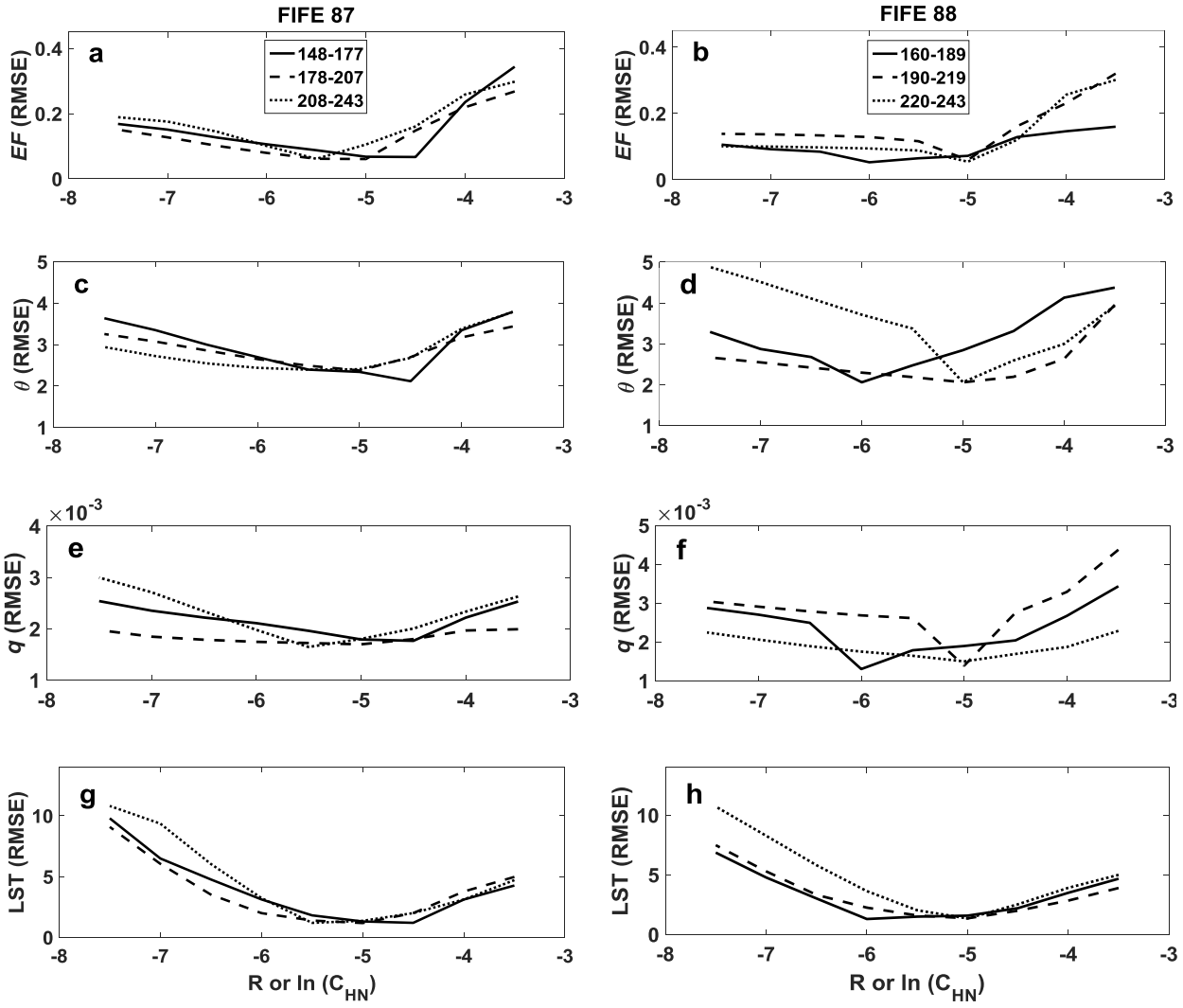

Figure 3. 2. RMSEs of estimated *EF* (a and b), ABL potential temperature (c and d) and specific humidity (e and f), and LST (g and h) for FIFE 87 (left) and 88 (right).

Table 3. 3. C_{HN} estimates by the VDA approach for FIFE 87 and 88, and corresponding LAI values.

FIFE 87			FIFE 88		
Julian days	C_{HN}	LAI	Julian days	C_{HN}	LAI
148 - 177	0.0089	1.7	160 – 189	0.0029	1.2
178 - 207	0.0074	1.2	190 – 219	0.0044	1.3
208 - 243	0.0051	1.0	220 – 243	0.0049	1.5

The second unknown of the VDA approach is *EF*. Figure 3.3 shows time series of *EF* estimates for FIFE 87 and 88. *EF* values from measured *H* and *LE* are also indicated by open circles on the same figure. As shown, *EF* estimates capture both the magnitude and day-to-day variability in the observations although no information on the soil moisture or precipitation was used in the VDA system. For example, the decreasing and increasing trends in the *EF* observations respectively during the dry down (Julian days 190-214 in FIFE 87) and wetting (Julian days 195-199 and 226-231 in FIFE88) periods are captured by the *EF* estimates. This implies that the new VDA scheme can take advantage of the implicit information in the sequences of both land surface and atmosphere state variables (i.e., LST, T_a, and q_a) to retrieve the signature of relative partitioning of available energy between the turbulent heat fluxes.

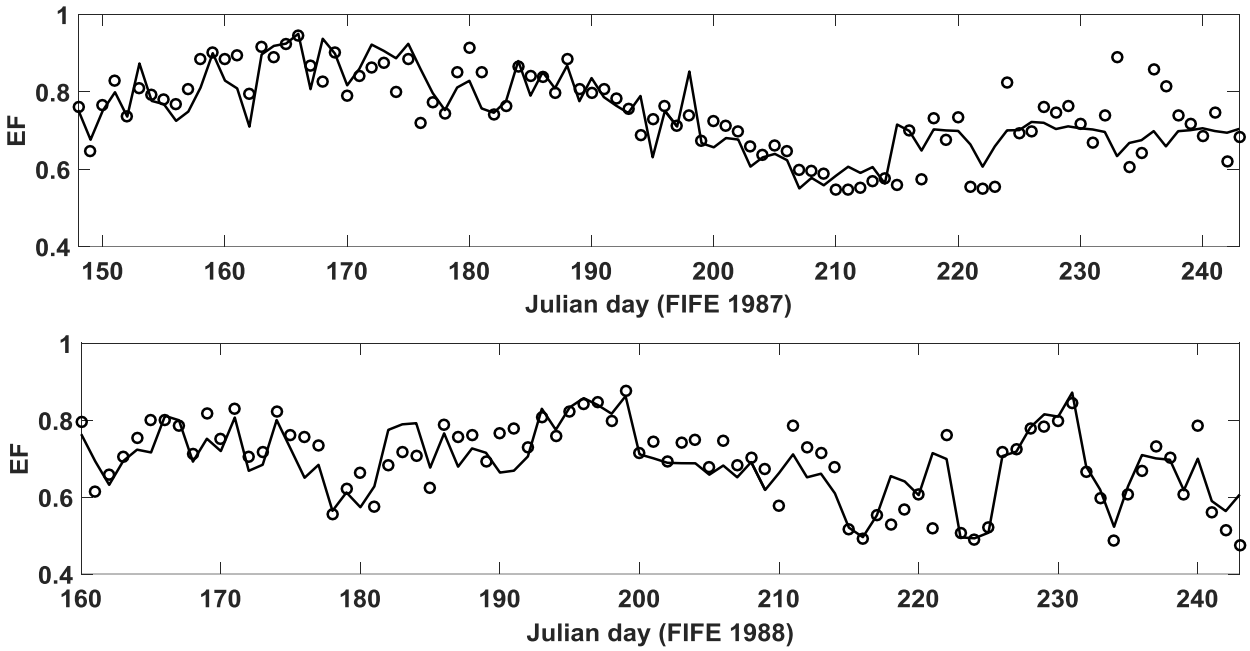

Figure 3. 3. Time series of estimated *EF* values from the VDA approach (solid lines) for FIFE 87 (top) and 88 (bottom). Observed *EF* values are shown by open circles.

Table 3.4 shows the mean-absolute-error (MAE) and root-mean-square-error (RMSE) of *EF* estimates from Bateni et al. (2013a) (that assimilated only LST), Tajfar et al. (2019a) (that assimilated only T_a and q_a), and this study (that assimilated LST, T_a, and q_a). For FIFE 87, Tajfar et al. (2019a) generates slightly more accurate *EF* estimates than Bateni et al. (2013a). In contrast, Bateni et al. (2013a) outperforms Tajfar et al. (2019a) in FIFE 88. This is due to the fact that on average summer 88 was slightly drier than summer 87 (the soil moisture at the depth of 2-5 cm was on average 0.26 for FIFE 87 and 0.18 for FIFE 88). The drier land surface leads to a stronger coupling between *EF* and LST because evaporation is mainly controlled by land surface processes rather than atmospheric variables in water-limited evaporative regimes (Bateni et al., 2013b; Shokri et al., 2008a, b). Hence, retrieval of *EF* from sequences of LST measurements becomes more robust in drier conditions (FIFE 88). In contrast, in wetter conditions (FIFE 87),

the coupling between *EF* and the atmospheric state variables (i.e., air temperature and specific humidity) becomes more robust because evaporation is more influenced by the atmospheric variables in energy-limited evaporative regimes. These findings indicate the both the state variables of the land surface (i.e., LST) and atmosphere (i.e., air temperature and humidity) control *EF*, and thus it is beneficial to take advantage of information in both of them.

For FIFE 87 (88), the RMSE of estimated *EF* values from this study is 0.061 (0.053), which is a reduction of 11.6% (26.4%) compared to the RMSE of 0.069 (0.072) from Tajfar et al. (2019a). Compared to Bateni et al. (2013a), the improvement in the RMSE of *EF* estimates is 18.7% and 10.2% for FIFE 87 and 88, respectively. Similarly, the MAE of *EF* estimates from this study is lower than those of Bateni et al. (2013a) and Tajfar et al. (2019a). Overall, these results indicate that the synergistic assimilation of LST, T_a, and q_a improves *EF* and consequently *LE* estimates (see equation 3-7b).

Table 3. 4. Comparing *EF* estimates from the developed VDA model (that assimilated LST, q_a and T_a) with those of Bateni et al. (2013a) (that assimilated only LST), and Tajfar et al. (2019a) (that assimilated only q_a and T_a) for FIFE 87 (top panel) and 88 (bottom panel).

Different studies	*EF*	
	RMSE	MAE
Bateni et al. (2013a)	0.075	0.061
Tajfar et al. (2019a)	0.069	0.053
This study	**0.061**	**0.044**
Bateni et al. (2013a)	0.059	0.048
Tajfar et al. (2019a)	0.072	0.062
This study	**0.053**	**0.039**

The half-hourly estimated *H*, *LE*, and *G* values are indicated versus measurements in Figure 3.4 for FIFE 87 and 88. As shown, there is a good agreement between the estimations and measurements, and they mostly fall around the 1:1 degree line. For FIFE 1987 (1988), the RMSE of half-hourly *H*, *LE*, and *G* estimates is 33.33 W m^{-2} (43.43 W m^{-2}), 67.19 W m^{-2} (72.02 W m^{-2}), and 60.03 W m^{-2} (80.93 W m^{-2}), respectively. In FIFE 87 (88), the MAE is 27.17 W m^{-2} (33.65 W m^{-2}), 55.57 W m^{-2} (54.22 W m^{-2}), and 46.37 W m^{-2} (60.29 W m^{-2}) for half-hourly sensible, latent, and ground heat fluxes, respectively.

The RMSEs of half-hourly *H* and *LE* estimates from Bateni et al. (2013a), Tajfar et al. (2019a), and this study are compared in Table 3-5 for FIFE 87 and 88. As can be seen, the RMSEs of turbulent heat fluxes estimates from this study are smaller than those of Bateni et al. (2013a) and Tajfar et al. (2019a). The new VDA system decreases the RMSEs of half-hourly *H*

and *LE* estimates for year 1987 (1988) by 10.1% (9.5%) and 17.2% (16.2%) compared to Bateni et al. (2013a), and 13.7% (10.3%) and 24.5% (16.9%) compared to Tajfar et al. (2019a). Overall, these results show that the synergistic assimilation of LST, T_a, and q_a into the VDA approach improves sensible and latent heat fluxes estimates compared to the previous studies in which either LST, or T_a and q_a were assimilated.

The RMSE of half-hourly *G* estimates from this study is 60.03 W m^{-2} and 80.93 W m^{-2} for FIFE 87 and 88, which is 50.9% and 28.6% lower than the RMSE of 122.14 W m^{-2} and 113.29 W m^{-2} from Tajfar et al. (2019a). This happens because *G* is directly related to the gradient of LST via $G = -p(\frac{dT}{dZ})|_{z=0}$. Therefore, assimilating sequences of LST observations into the heat diffusion equation can constrain the ground heat flux, leading to a significant improvement in the *G* estimates. The results show that the VDA approach can take advantage of the implicit information in the sequences of LST measurements to significantly improve the ground heat flux estimates compared to Tajfar et al. (2019a).

As shown in Figure 3.4, the MAE and RMSE of *LE* retrievals are higher than those of *H* estimates. This is due to the fact that the uncertainty of *H* estimates results from errors in the estimated C_{HN} and LST values (equation 3-5), whereas the uncertainty of *LE* retrievals is due to errors in the C_{HN}, LST, and *EF* estimates (equation 3-7b). More sources of errors increase the uncertainty of *LE* estimates. Moreover, *G* retrievals are more scattered around the 45-degree line compared to *H* and *LE* estimates. This happens because *G* is calculated as the residual of the SEB equation (i.e., $G = R_n - H - LE$). Thus, uncertainties in the *H* and *LE* estimates propagate into *G* retrievals, which lead to more errors in *G* estimations.

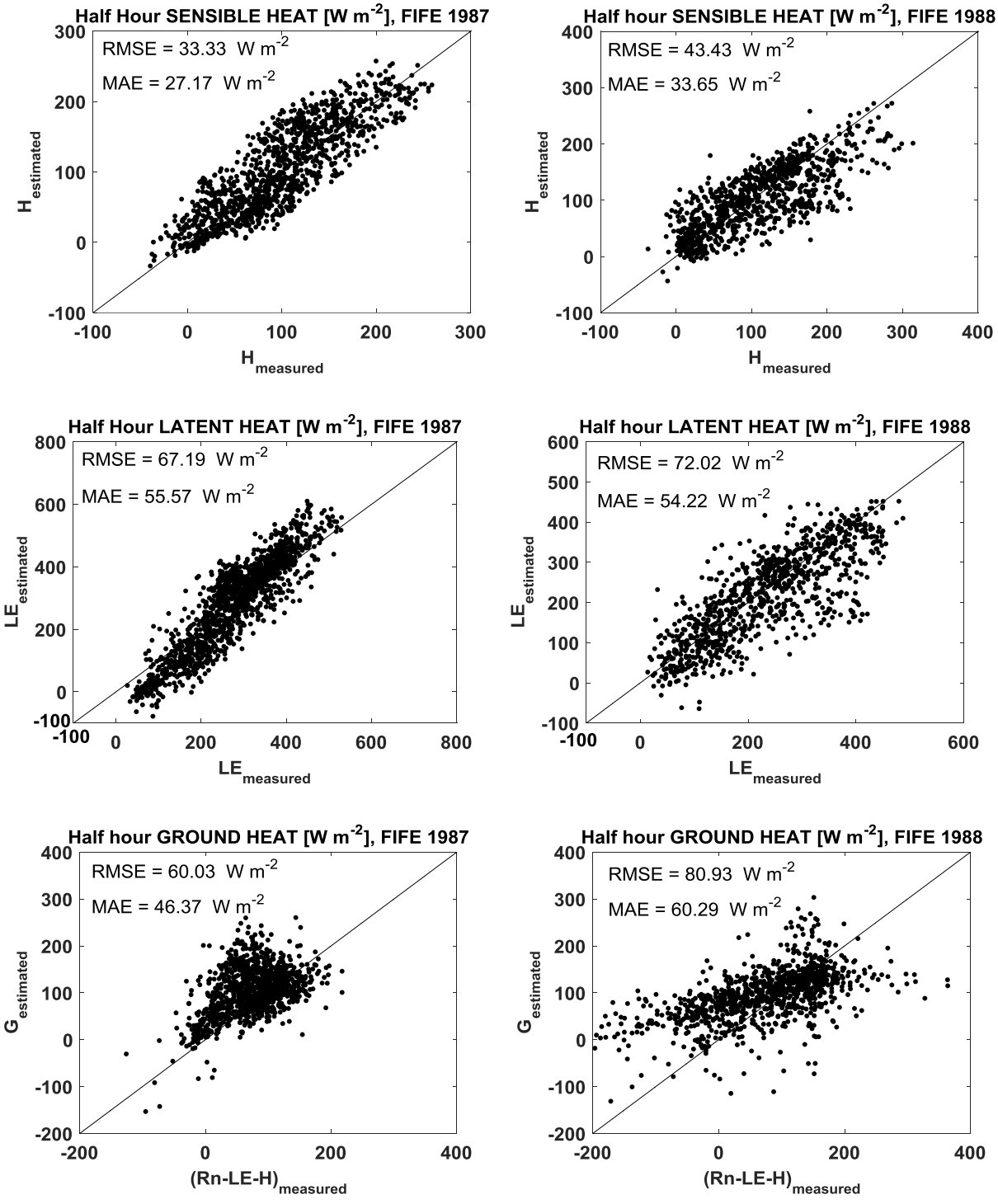

Figure 3. 4. Scatterplot of half-hourly modeled versus measured sensible (top), latent (middle) and ground heat flux (bottom) for FIFE 87 (left) and 88 (right).

Figure 3.5 and 3.6 show time series of daily *H* and *LE* estimates for FIFE 87 and 88, respectively. As indicated, both the magnitude and day-to-day fluctuations of measured sensible and latent heat fluxes are captured well by the estimations from the VDA approach. For example, in FIFE 87, the estimated *H* (*LE*) can capture the rising (falling) pattern of *H* (*LE*) measurements during the dry down period (i.e., Julian days 190-214). Moreover, sharp jumps and drops in observations are reflected well in estimations in both FIFE 87 and 88. For FIFE 87, the RMSE of daytime-average *H* and *LE* estimates from the VDA approach are 21.80 W m^{-2} and 39.32 W m^{-2}, respectively. Corresponding RMSE values for FIFE 88 are 22.10 W m^{-2} and 36.89 W m^{-2}. For FIFE 87 (88), daily *H* and *LE* estimates from this study are improved by 12.5% (17.9%) and 24.4% (22.0%) compared to Bateni et al. (2013a), and 15.2% (20.4%) and 26.7% (23.5%) compared to Tajfar et al. (2019a). The outcomes imply that feeding the land surface and ABL models with observed LST, air temperature, and humidity is an underutilization of these inputs. Remarkably, the VDA approach can extract the implicit information contained in the sequences of LST, air temperature and humidity to estimate surface heat fluxes.

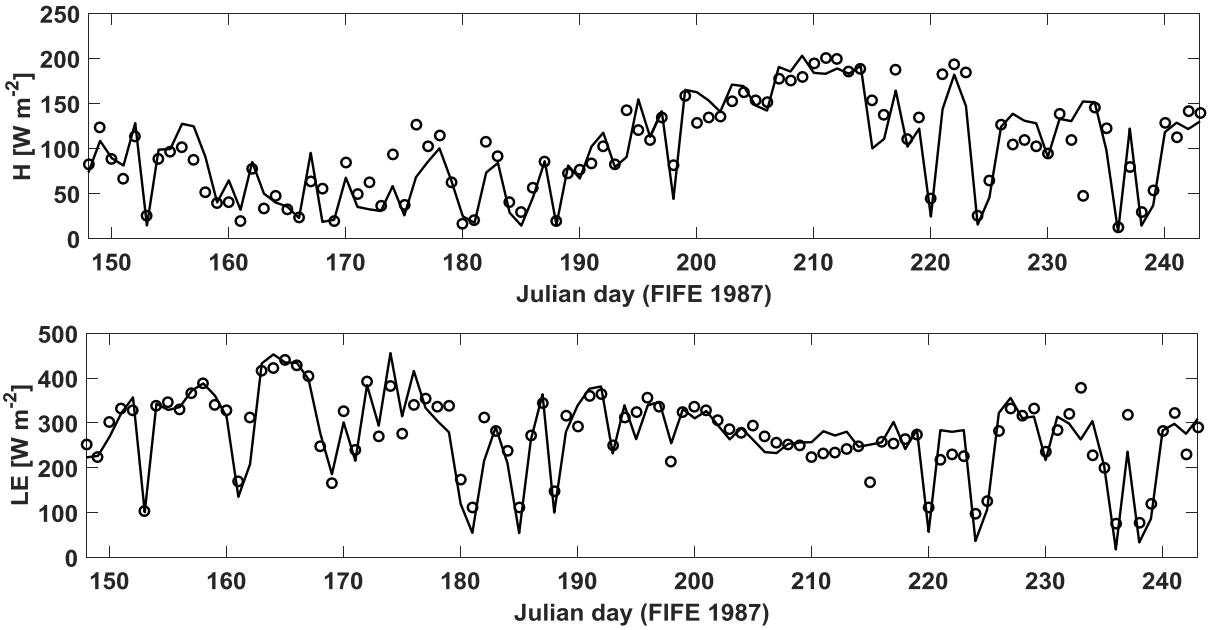

Figure 3. 5. Time series of observed (circles) and predicted (lines) daily turbulent heat fluxes from this study (solid lines). Sensible (top) and latent heat flux (bottom).

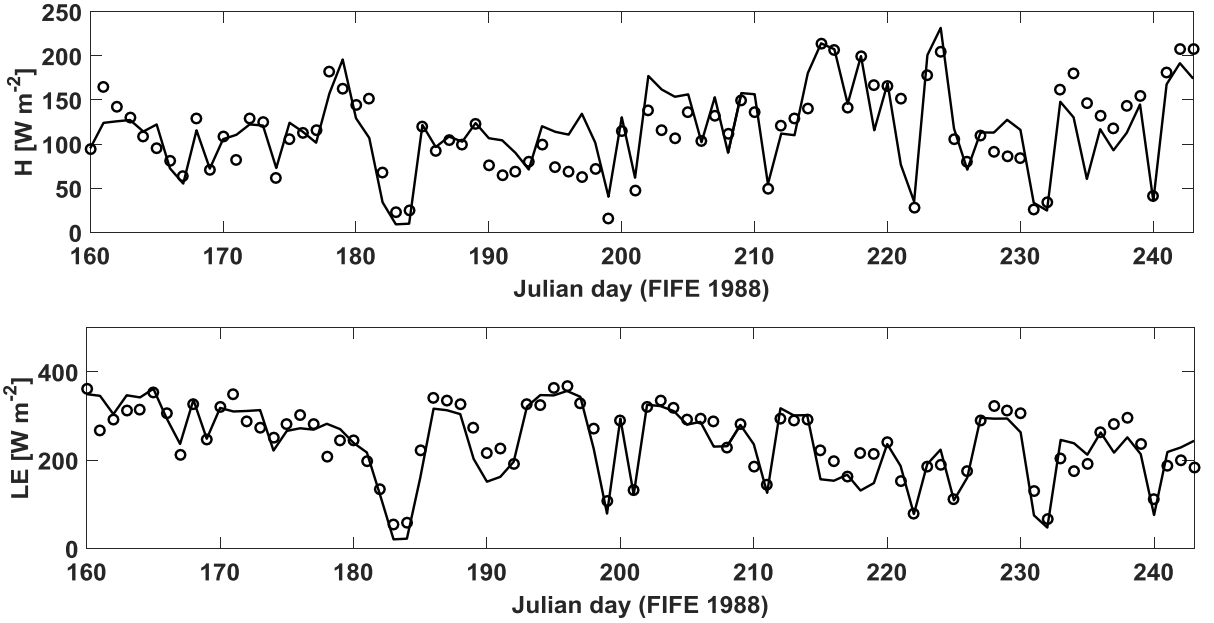

Figure 3. 6. The same as Figure 3.5 but for FIFE 88.

Table 3. 5. Comparing performance of the developed VDA approach (that assimilated LST, T_a, and q_a) with those of Bateni et al. (2013a) (that assimilated only LST), and Tajfar et al. (2019a) (that assimilated only T_a, and q_a) for FIFE 87 (top panel) and 88 (bottom panel).

Different studies	H (W m^{-2})		LE (W m^{-2})	
	Half-hourly	Daily	Half-hourly	Daily
Bateni et al. (2013a)	37.08	24.91	81.18	51.98
Tajfar et al. (2019a)	38.61	25.72	89.05	53.63
This study	**33.33**	**21.80**	**67.19**	**39.32**
Bateni et al. (2013a)	47.99	26.91	85.98	47.31
Tajfar et al. (2019a)	48.42	27.77	86.63	48.22
This study	**43.43**	**22.10**	**72.02**	**36.89**

Time series of half-hourly estimated and observed half-hourly sensible and latent heat fluxes for Julian days 178–207 (FIFE 87) are compared in Figure 3.7. As shown in this figure, the magnitude and phase of retrieved and observed H and LE agree well for all days, implying that the VDA approach can estimate turbulent heat fluxes accurately.

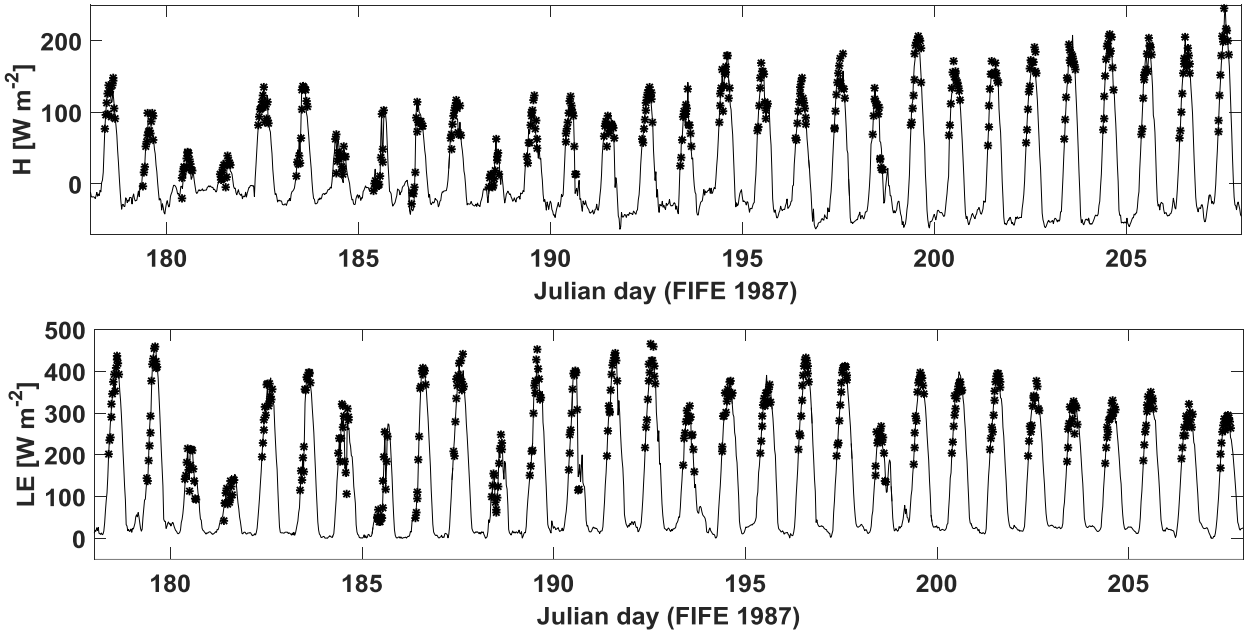

Figure 3. 7. Time series of half-hourly measured (lines) and estimated (symbols) surface heat fluxes for Julian days 178-207 (FIFE 87) (top) sensible, and (bottom) latent heat fluxes.

The VDA approach retrieves C_{HN} and *EF* by minimizing the difference between the LST estimates from equation (3-1) and observations (i.e., T and T_{obs}), as well as the misfit between the estimated potential temperature and specific humidity from equations (3-8a) and (3-8b) (i.e., θ and q) and the corresponding values (i.e., θ_{SL} and q_{SL}) obtained from the measured reference-level air temperature and specific humidity via the MOST (see Appendix A). Figure 3.8 shows that there is a good agreement between the half-hourly T and T_{obs}, θ and θ_{SL}, and q and q_{SL} for FIFE 87 and 88, implying that the VDA framework is able to efficiently optimize the two key unknown parameters of the VDA approach (C_{HN} and *EF*) by minimizing the misfit terms in the objective function. For FIFE 87, the RMSEs of LST, q, and θ estimates are respectively 1.19 K, 2.23 K, and 0.0017 kg kg^{-1}. Corresponding values for FIFE 88 are 1.32 K, 2.06 K, and 0.0014 kg kg^{-1}. The uncertainty of LST, q, and θ estimates is mostly because of the measurement errors,

and simplistic assumptions (e.g., constant daily *EF* and monthly C_{HN}, insignificant advection, and convectively well mixed boundary layer, which results in constant profiles of potential temperature and specific humidity with height).

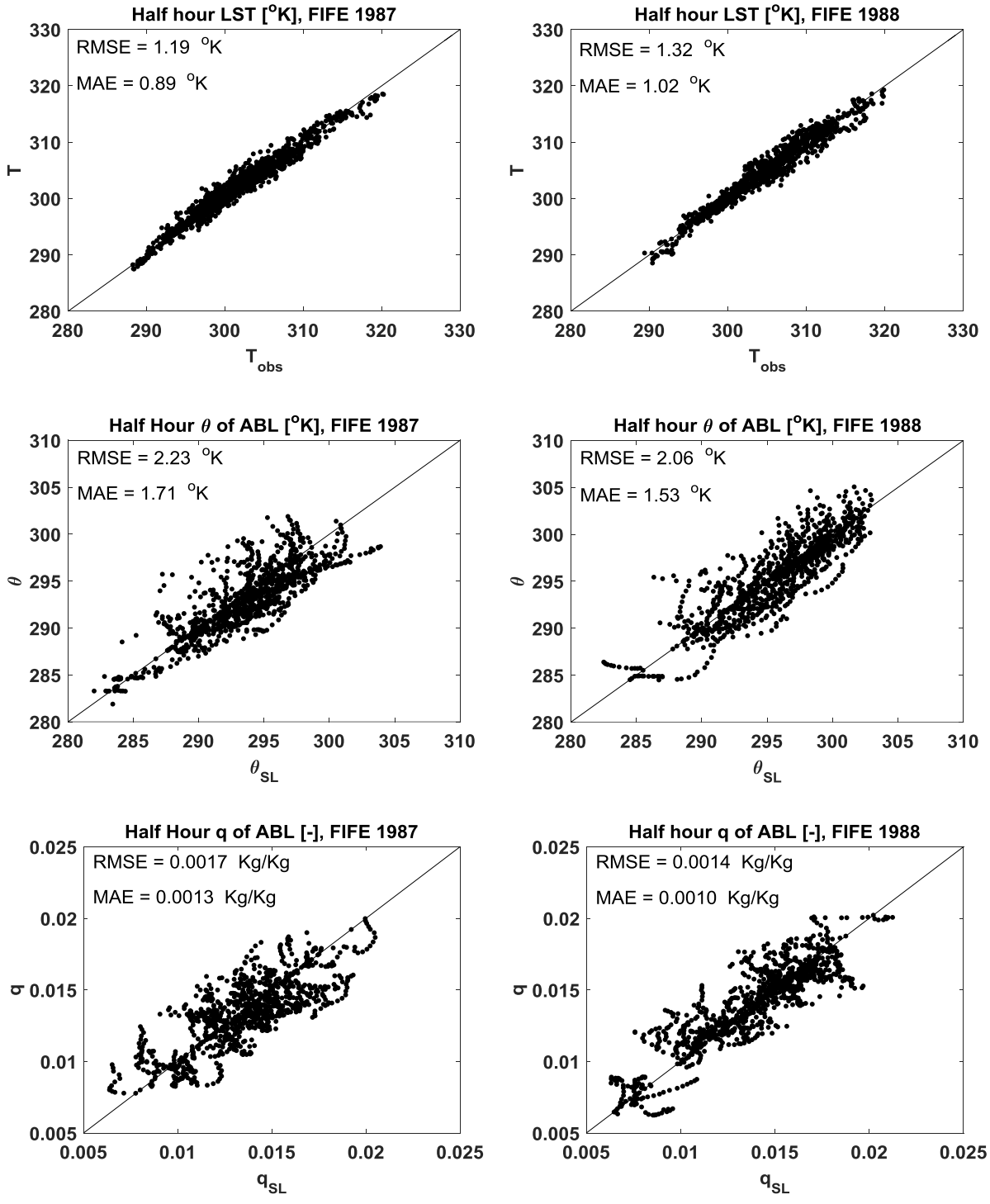

Figure 3. 8. Scatterplot of half-hourly estimated T (top row), θ (middle row), and q (bottom row) versus corresponding observations for FIFE 87 (left) and 88 (right).

The RMSE and MAE of estimated θ and q values from this study are compared with those of Tajfar et al. (2019) for FIFE 87 and 88 (Tables 3.6). Similarly, Table 3.7 compares the RMSE and MAE of T estimates from this study with those of Bateni et al. (2013a). It should be noted that Bateni et al. (2013a) assimilated only LST observations into the heat diffusion equation, and thus it provided the RMSE and MAE of LST estimates. Also, Tajfar et al. (2019a) assimilated only air temperature and specific humidity into an ABL model, and therefore it generated the RMSE and MAE of θ and q estimates. The RMSE and MAE of θ and q estimates from this study are lower than those of Tajfar et al. (2019a). The RMSE of θ and q are reduced respectively by 16.8% (10.8%) and 10.5% (12.5%) for FIFE 87 (88). The RMSE of estimated LST values from this study is also smaller than that of Bateni et al. (2013a), resulting in an improvement of 30.0% (37.4%) for FIFE 87 (88). Similarly, for FIFE 87 (88), the MAE of T estimates is 0.89 K (1.02 K), which is 31.5% (36.7%) lower than the MAE of 1.30 K (1.61 K) from Bateni et al. (2013a). These outcomes indicate that the new VDA approach can provide more accurate C_{HN} and EF estimates as the model finds optimum values of C_{HN} and EF by minimizing the misfits between T and T_{obs}, θ and θ_{SL}, and q and q_{SL}.

Table 3. 6. Comparing RMSE and MAE of θ and q estimates from this study with those of Tajfar et al. (2019a) for FIFE 87 (top panel) and 88 (bottom panel).

Different studies	θ (K)		q (kg kg^{-1})	
	RMSE	MAE	RMSE	MAE
Tajfar et al. (2019a)	2.68	2.01	0.0019	0.0014
This study	**2.23**	**1.71**	**0.0017**	**0.0013**
Tajfar et al. (2019a)	2.31	1.67	0.0016	0.0011
This study	**2.06**	**1.53**	**0.0014**	**0.0010**

Table 3. 7. Comparing RMSE and MAE of T estimates from this study with those of Bateni et. al. (2013a) for FIFE 87 (top panel) and 88 (bottom panel).

Different studies	LST (K)	
	RMSE	MAE
Bateni et al. (2013a)	1.70	1.30
This study	**1.19**	**0.89**
Bateni et al. (2013a)	2.11	1.61
This study	**1.32**	**1.02**

The mean diurnal cycles of observed and estimated sensible, latent, and ground heat fluxes as well as net radiation from this study and Tajfar et al. (2019a) are shown in Figure 3.9 for FIFE 87 and 88. As can be seen, there is a remarkable difference between the diurnal cycles of observed and estimated ground heat flux from Tajfar et al. (2019a). G is directly related to the LST via $G = -p\, dT/dz$. Tajfar et al. (2019a) did not assimilate the sequences of LST observations

and consequently could not capture the diurnal cycle of ground heat flux. By assimilating LST measurements into the heat diffusion equation in this study, the diurnal cycle of predicted ground heat flux is improved significantly. Assimilating sequences of LST observations into the heat diffusion equation also improves the diurnal cycles of latent heat flux for FIFE 87 and net radiation for FIFE 88.

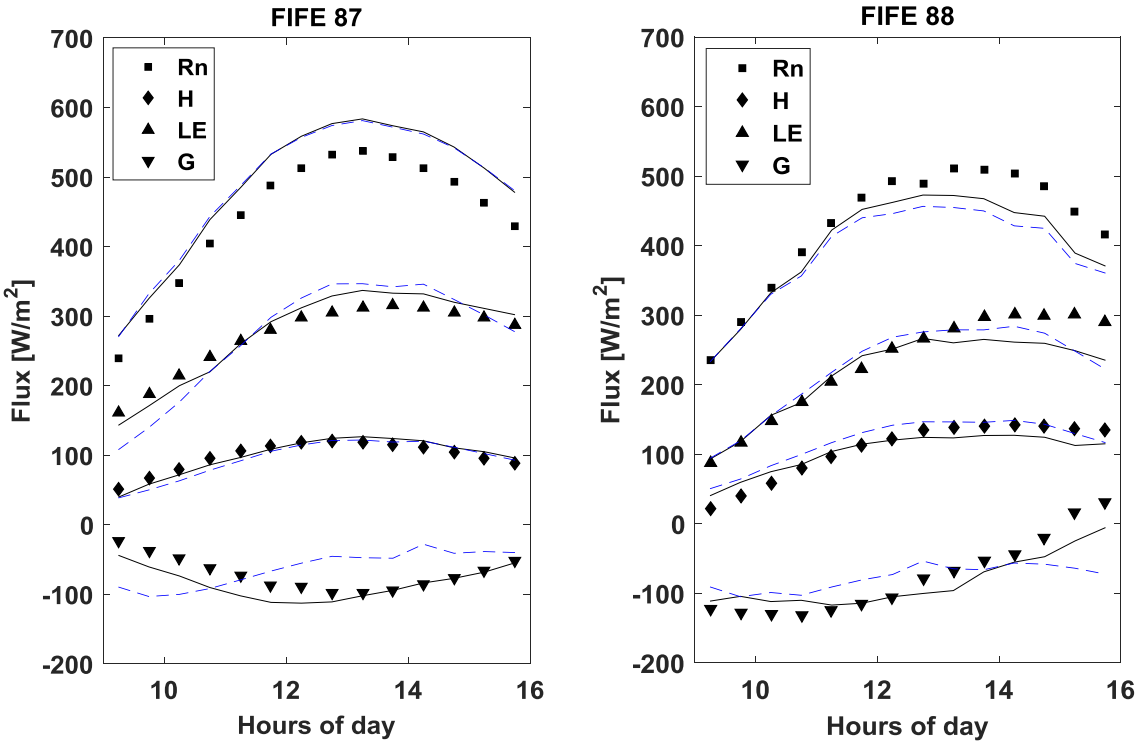

Figure 3. 9. Diurnal cycle of surface energy balance components for FIFE 87 and 88. Measured fluxes (symbols), this study (solid lines) and Tajfar et al. (2019a) (dashed lines).

As explained in section 3.3, the $h(t_o)$, γ_θ, γ_q, $\delta_\theta(t_o)$, and $\delta_q(t_o)$ values that lead to a minimum objective function are used in this study. On the other hand, the radiosonde measurements of the abovementioned variables are available at the FIFE site (1987) for Julian days 155, 156, 176, 177, 178, 187, 227, 228, and 229. The turbulent heat fluxes estimates by using the optimized and measured $h(t_o)$, γ_θ, γ_q, $\delta_\theta(t_o)$, and $\delta_q(t_o)$ values in the VDA approach are compared in Figure 3.10. As shown, the *H* and *LE* estimates from the aforementioned measured variables are slightly closer to the observations. According to Table 3.8, by utilizing the measured $h(t_o)$, γ_θ, γ_q, $\delta_\theta(t_o)$, and $\delta_q(t_o)$ values in the VDA approach, the RMSE of daily *H* (*LE*) estimates decreases from 27.66 W m^{-2} to 25.03 W m^{-2} (31.15 W m^{-2} and 28.48 W m^{-2}), leading to an improvement of 9.5% (8.6%). These results denote that by using the measured $h(t_o)$, γ_θ, γ_q, $\delta_\theta(t_o)$, and $\delta_q(t_o)$ values (in lieu of the calibrated values) in the VDA approach, the turbulent heat fluxes estimates only slightly improve, indicating that the VDA approach can provide accurate estimates of *H* and *LE* via utilizing the optimized $h(t_o)$, γ_θ, γ_q, $\delta_\theta(t_o)$, and $\delta_q(t_o)$ values.

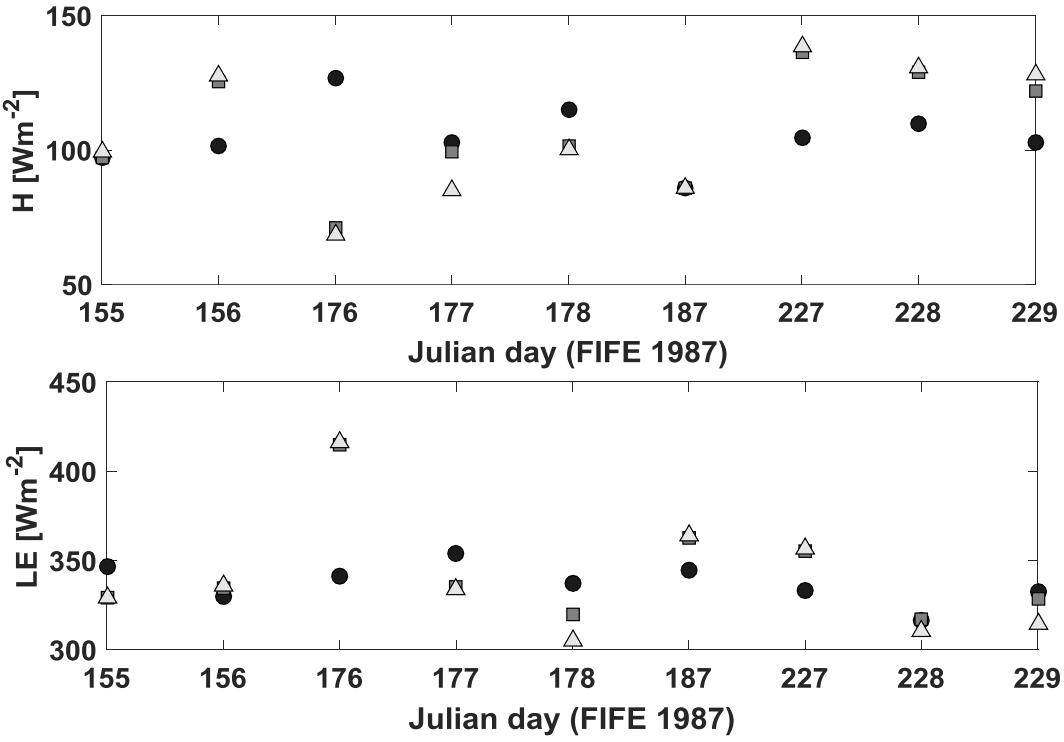

Figure 3. 10. Comparison of the observed and predicted sensible (top) and latent (bottom) heat fluxes for Julian days 155, 156, 176, 177, 178, 187, 227, 228, and 229. Observed H and LE are shown by circles. Estimated H and LE using the optimized and measured $h(t_o)$, γ_θ, γ_q, $\delta_\theta(t_o)$, and $\delta_q(t_o)$ values are indicated by triangles and squares, respectively.

Table 3. 8. Comparing the RMSE and MAE of daily *H* and *LE* estimates from the VDA approach, using the optimized and measured $h(t_o)$, γ_θ, γ_q, $\delta_\theta(t_o)$, and $\delta_q(t_o)$ values for Julian days 155, 156, 176, 177, 178, 187, 227, 228, and 229 in FIFE 87.

Different scenarios	RMSE (W m^{-2})		MAE (W m^{-2})	
	H	*LE*	*H*	*LE*
Measured $h(t_o)$, γ_θ, γ_q, $\delta_\theta(t_o)$, and $\delta_q(t_o)$	25.03	28.48	18.54	19.69
Optimized $h(t_o)$, γ_θ, γ_q, $\delta_\theta(t_o)$, and $\delta_q(t_o)$	27.66	31.15	22.20	24.19

Radiosonde measurements of mixed-layer potential temperature (θ), specific humidity (q), and height (h) over the FIFE site during summer 87 are used to validate the corresponding estimations from the VDA approach. Figures 3.11a-i compare the estimated mixed-layer height, specific humidity, and potential temperature from the VDA approach with those obtained from the radiosonde for 15-17 August 1987. The error bars show the standard deviations of the measurements from radiosonde. On August 15 (Figures 3.11a-c), the ABL height, potential temperature and specific humidity grow throughout the day. The model estimates capture the increasing trend of the radiosonde data and agree well with them. On August 16 (Figures 3.11d-f), the measured ABL height and potential temperature increase, but ABL specific humidity does not show a clear trend during the course of the day. The ABL height and potential temperature estimates rise during the day and are consistent with the radiosonde data in terms of magnitude and daily variation. The model estimations can also capture the daily variations in the ABL specific humidity measurements. On August 17 (Figures 3.11g-i), the estimations capture the rising patterns in θ, q, and h. The small discrepancies between model estimates and radiosonde data can be because of the fact that the radiosonde point observations might not be representative of a spatial average over for the FIFE site (Margulis, 2002), the simplistic assumptions of daily constant EF and monthly constant C_{HN}, and noise in the input data. These sources of errors make the comparison between the model estimates and measurements difficult (Margulis and Entekhabi, 2001). Similar results are obtained for other cloud-free days in June 1987 where the radiosonde measurements are available (not shown herein).

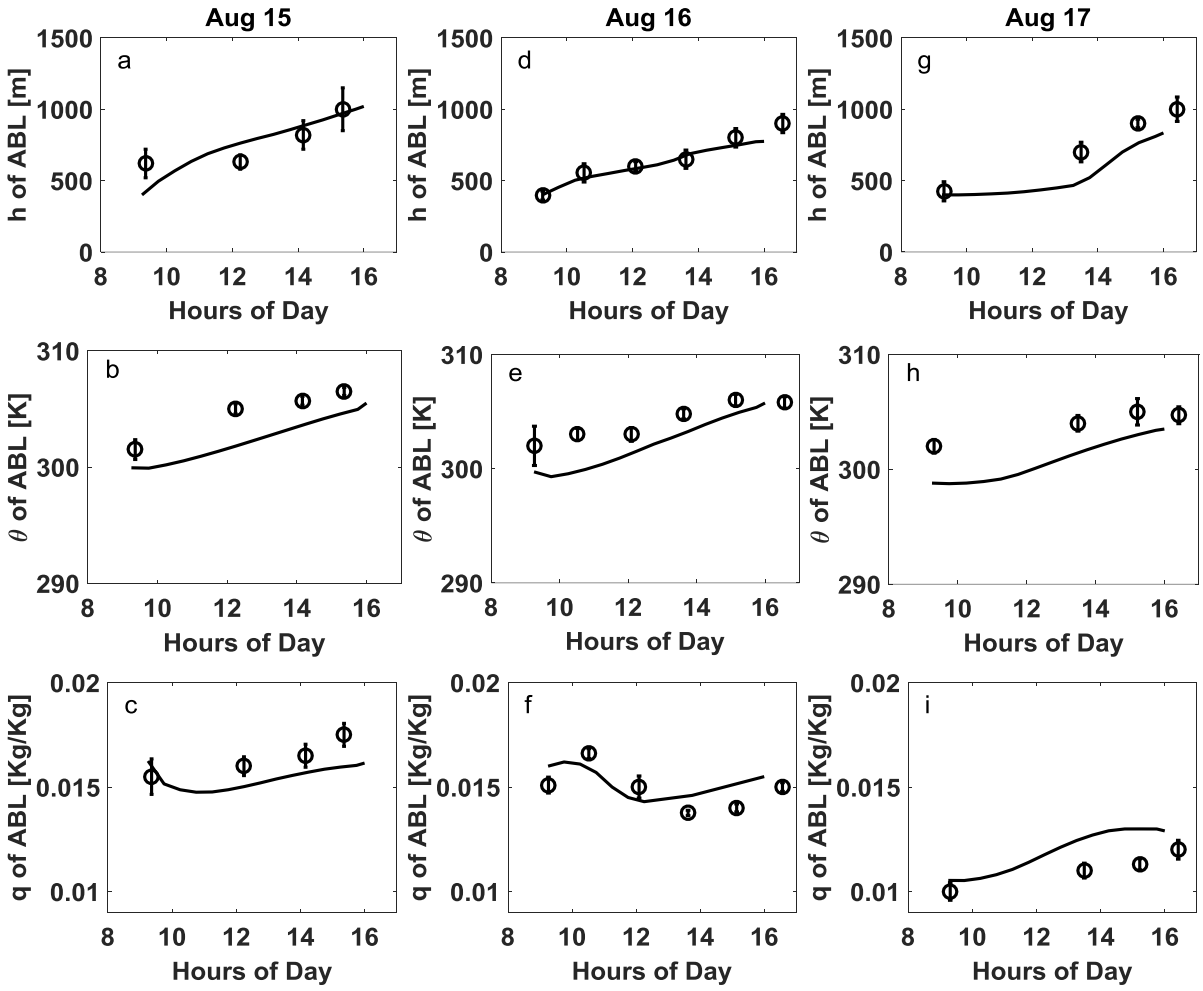

Figure 3. 11. Diurnal evolution of ABL height (top), potential temperature (middle), and humidity (bottom) at the FIFE site for 15-17 August 1987 from the VDA approach (solid lines) and radiosonde observations with one standard deviation (open circles).

3.5. Conclusion

The sequences of land surface temperature (as the state variable of land surface) and reference-level air temperature and specific humidity (as the state variables of atmosphere) measurements are assimilated into a coupled land surface-atmospheric boundary layer (ABL) model within a variational data assimilation (VDA) approach to estimate surface heat fluxes. The main unknown parameters of the VDA system are neutral bulk heat transfer coefficient

(C_{HN}) and evaporative fraction (*EF*). The VDA approach is tested at the First ISLSCP (International Satellite Land Surface Climatology Project) Field Experiment (FIFE) site in summer 1987 and 1988. The results show that the developed VDA scheme can accurately estimate the sensible (*H*) and latent (*LE*) heat fluxes. The root-mean-square-errors (RMSEs) of half-hourly *H* and *LE* estimates are 33.33 W m^{-2} (43.43 W m^{-2}) and 67.19 W m^{-2} (72.02 W m^{-2}) for FIFE 87 (88). These RMSEs are compared to those of Bateni et al. (2013a) (that assimilated only LST) and Tajfar et al. (2019a) (that assimilated only reference-level air temperature and specific humidity). The results indicate that there is an improvement in the turbulent heat fluxes estimates. For FIFE 87 (88), the RMSEs of half-hourly *H* and *LE* estimates are decreased respectively by 13.7% (10.3%) and 24.5% (16.9%) compared to Tajfar et al. (2019a), and 10.1% (9.5%) and 17.2% (16.2%) compared to Bateni et al. (2013a). Time series of half-hourly and daily *H* and *LE* estimates from the VDA approach agree well with the observations both in terms of magnitude and day-to-day fluctuations.

For FIFE 87 (88), the RMSEs of daily *H* and *LE* estimates from this study are 21.80 W m^{-2} (22.10 W m^{-2}) and 39.32 W m^{-2} (36.89 W m^{-2}), which are improved by 15.2% (20.4%) and 26.7% (23.5%) compared to Tajfar et al. (2019a), and 12.5% (17.9%) and 24.4% (22.0%) compared to Bateni et al. (2013a). For FIFE 87 (88), the RMSEs of estimated land surface temperature, and ABL specific humidity (q) and potential temperature (θ) are respectively 1.19 K (1.32 K), 0.0017 kg kg^{-1} (0.0014 kg kg^{-1}), and 2.23 K (2.06 K). Compared to Tajfar et al. (2019a), this study reduces the RMSEs of θ and q estimates by 16.8% (10.8%) and 10.5% (12.5%) for FIFE 87 (88). Also, compared to Bateni et al. (2013a), the RMSE of LST estimates is reduced by 30.0% (37.4%) for FIFE 87 (88). These findings indicate that the new VDA scheme can take advantage of the implicit information in the sequences of both land surface and

atmosphere state variables (i.e., land surface temperature, and reference-level air temperature and specific humidity) to retrieve the signature of relative partitioning of available energy between the turbulent heat fluxes. The ABL height, potential temperature, and specific humidity estimates from the VDA approach are reasonably close to the radiosonde observations and can capture their diurnal variations.

Future studies should be directed towards 1) testing the developed VDA over large-scale domains using remote sensing data, and 2) developing a weak-constraint VDA approach that can capture uncertainties in the turbulent heat fluxes due to measurements and structural model errors.

Chapter 4: Evaluating the Information Content of Reference-level Air Temperature and Humidity for Partitioning the Available Energy between the Turbulent Heat Fluxes in Different Vegetative and Climatic Conditions

Evaluating the Information Content of Reference-level Air Temperature and Humidity for Partitioning the Available Energy between the Turbulent Heat Fluxes in Different Vegetative and Climatic Conditions

E. Tajfar[1], S. M. Bateni[1]

[1]Department of Civil and Environmental Engineering and Water Resources Research Center, University of Hawaii at Manoa, Honolulu, USA.

T. Xu[2]

[2]State Key Laboratory of Remote Sensing Science, Research Center for Remote Sensing and GIS, and School of Geography, Beijing Normal University, Beijing, China

[*]*Corresponding author address*: Elahe Tajfar, Department of Civil and Environmental Engineering and Water Resources Research Center, University of Hawaii at Manoa, Honolulu, USA.

E-mail: etajfar@hawaii.edu

Current affiliation: Ph.D. candidate, Department of Civil and Environmental Engineering, University of Hawaii at Manoa, Honolulu, USA.

ABSTRACT

Sequences of reference-level air temperature and specific humidity are assimilated into an atmospheric boundary layer model within a variational data assimilation (VDA) framework to estimate sensible (*H*) and latent (*LE*) heat fluxes. The VDA approach is tested at five sites (namely, Desert, Audubon, Bondville, Brookings, and Willow Creek) with contrasting climatic and vegetative conditions. The unknowns of the VDA system are neutral bulk heat transfer coefficient (C_{HN}) (that scales the sum of *H* and *LE*) and evaporative fraction (*EF*) (that scales the partitioning between *H* and *LE*). The *EF* estimates agree well with the observations in terms of magnitude and day-to-day fluctuations in wet and/or densely vegetated sites, while in dry and/or sparsely vegetated sites, the agreement between the *EF* estimates and observations weakens. Similarly, in wet and/or densely vegetated sites, the variations in the C_{HN} estimates and leaf area index (LAI) are consistent, while this consistency is deteriorated in dry and/or sparely vegetated sites. The RMSEs of daily *H* and *LE* estimates at the Willow Creek site (wet) are 37.03 W m^{-2} and 74.46 W m^{-2} , which are 38.28% and 27.15% smaller than the corresponding RMSEs of 60.00 W m^{-2} and 102.21 W m^{-2} at the Desert site (dry). Overall, the results show that the VDA system performs well at wet/densely vegetated sites (e.g., Willow Creek), but its performance degrades at dry/slightly vegetated sites (e.g., Desert and Audubon). These outcomes show that the sequences of reference-level air temperature and specific humidity have more information on the partitioning of available energy between the sensible and latent heat fluxes in wet and/or densely vegetated sites than the dry and/or slightly vegetated sites.

Keywords: Surface heat fluxes; variational data assimilation; air temperature; specific humidity; information content

4.1. Introduction

Accurate estimation of sensible (*H*) and latent (*LE*) heat fluxes is of vital importance in different disciplines such as meteorology, ecology, agronomy, and hydrology (McCabe and Wood, 2006; Lu et al., 2016). Turbulent heat fluxes (*H* and *LE*) can be measured directly by different approaches such as eddy covariance stations, lysimeters, bowen ratio methods, and large aperture scintillometer (Alfieri et al., 2012; Liu et al., 2013; Gebler et al., 2015; Hirschi et al., 2017; Moorhead et al., 2017). However, the direct measurements of turbulent heat fluxes are difficult and costly, and thus are only available from a handful of sparse flux tower networks (e.g., Fluxnet, AsiaFlux, EuroFlux, AmeriFlux), and field experiments (e.g., Bushland Evapotranspiration and Agricultural Remote Sensing Experiment 2008 (BEAREX08), Heihe Watershed Allied Telemetry Experimental Research (HiWATER), and First International Satellite Land Surface Climatology Project (ISLSCP) Field Experiment (FIFE)) (Baldocchi et al., 2001; Li et al., 2013; Xu et al., 2015; Liu et al., 2018).

Consequently, different approaches have been developed to estimate turbulent heat fluxes (Bastiaanssen et al., 1998; Kalma et al., 2008; Allen at al., 2011; Yilmaz et al., 2014). Generally, there are five major groups of studies for estimating turbulent heat fluxes. The first group, known as triangle methods, estimates latent heat flux by using empirical relations between land surface temperature (LST) and vegetation index (VI) (Nishida et al., 2003; Wang et al., 2006; Carlson, 2007; Stisen, 2008; Tang et al., 2010; Sun et al., 2013; Martinez et al., 2017; Majozi et al., 2017). In the second group, diagnostic methods, the surface energy balance (SEB) equation is solved using instantaneous measurements of LST and micrometeorological data (Su, 2002; Liu et al., 2007; Jia et al., 2009; Kustas et al., 2012; Ma et al., 2012, 2015; Song et al., 2016). The third group, combination methods, estimates turbulent heat fluxes by incorporating the LST

observations into the Penman-Monteith equation (Mallick et al., 2013, 2014; Raoufi and Beighley, 2017). The fourth group, land data assimilation system (LDAS), estimates turbulent heat fluxes by the Ensemble Kalman Filter (EnKF) approach (Peters-Lidard et al., 2011; Xia et al., 2014a, 2014b; Bateni and Entekhabi, 2012b; Carrera et al., 2015; Xu et al., 2015, 2018). The fifth group, variational data assimilation (VDA) method, estimates turbulent heat fluxes by assimilating sequences of LST observations into the force-restore and/or heat diffusion equation (Caparrini et al., 2003, 2004a, b; Bateni and Entekhabi, 2012a, 2012b; Bateni et al., 2013a, 2013b, 2014; Xu et al., 2015, 2016, 2018, 2019; Abdolghafoorian et al., 2017; He et al., 2018). In these studies, the implicit information in the sequences of LST observations is used to partition the available energy between the sensible and latent heat fluxes. Performance of these VDA approaches degrades in wet and/or heavily vegetated sites (Crow and Kustas, 2005). This occurs because in these sites evapotranspiration is at stage-I (energy-limited) and is mainly controlled by the state variables of atmosphere (i.e., air temperature and humidity) and not the state variable of the land surface (i.e., LST). These VDA approaches also require the specification of soil thermal conductivity and heat capacity as well as the deep soil temperature, which are typically unavailable.

In addition to using LST measurements, several studies showed that the reference-level air temperature and humidity measurements along with surface parameterization in itself contain useful information about soil moisture (Mahfouf, 1991; Bouttier et al., 1993a, b; Mahfouf et al., 2000, 2009; Douville et al., 2000; Hess, 2001; Drusch and Viterbo, 2007; de Rosnay et al. 2013; Ren and Xue, 2016; de Lannoy et al., 2016), and turbulent heat fluxes (Holtslag and Van Ulden, 1983; Margulis and Entekhabi, 2001; Alapaty et al., 2001; Balsamo et al., 2007; Shang et al., 2007; Salvucci and Gentine, 2013; Rigden and Salvucci, 2015; Gentine et al., 2016; Lum et al.,

2017). However, these studies generally require specification of surface roughness for heat and momentum along with ground heat flux, that are mainly unavailable.

To overcome the abovementioned shortcomings of the existing VDA approaches, Tajfar et al. (2019a) developed a VDA approach that estimates *H* and *LE* by assimilating sequences of reference-level air temperature and specific humidity (i.e., state variables of the atmosphere) into an atmospheric boundary layer model. The main unknowns of the Tajfar et al. (2019a) VDA approach are neutral bulk heat transfer coefficient (C_{HN}) (that scales the sum of the turbulent heat fluxes) and evaporative fraction (*EF*) (that scales their partitioning). Tajfar et al. (2019a) tested their approach only at the First International Field Experiment (FIFE) site.

This study is aimed at evaluating performance of Tajfar et al. (2019a) VDA approach in contrasting vegetative and climatic conditions to address the science question of how much information is contained in the reference-level meteorological data for diagnosing partitioning of available energy at the surface.

This paper is structured as follows. Section 4.2 explains the methodology including the surface energy balance (SEB) equation, the atmospheric boundary layer (ABL) model, and the variational data assimilation (VDA) scheme. Section 4.3 describes the study sites. The results are given in Section 4.4. Finally, conclusions are reported in Section 4.5.

4.2. Methodology

4.2.1. Surface Energy Balance (SEB)

The SEB equation can be written as,

$$R_n = H + LE + G \tag{4-1}$$

where R_n is the net radiation, and *G* is the ground heat flux. The net radiation is calculated via,

$$R_n = (1 - \alpha)R_s^{\downarrow} + \varepsilon_s \sigma T^4 - \varepsilon_a \sigma T_a^4 \tag{4-2}$$

where $R_s^{\downarrow}$ is the incoming solar radiation, α is the surface albedo. ε_s is the surface emissivity, σ is the Stefan-Boltzman constant, T is the land surface temperature, T_a is the air temperature at the reference height (z_{ref}), and ε_a is the atmospheric emissivity, which can be found in Idso (1981).

The sensible heat flux is given by,

$$H = \rho c_p C_{HN} f(Ri) U (T - T_a) \tag{4-3}$$

where ρ is the air density, c_p is the specific heat capacity of air, U is the wind speed at z_{ref}, C_{HN} is the neutral bulk heat transfer coefficient, which depends on the characteristics of the landscape, and f is the atmospheric stability correction function, which is a function of the Richardson number (Ri).

EF characterizes partitioning between the turbulent heat fluxes, and is defined as the ratio of latent heat flux to the sum of turbulent heat fluxes,

$$EF = \frac{LE}{LE+H} \tag{4-4a}$$

Caparrini et al., (2003) and Gentine et al., (2007, 2011) showed that EF is almost constant for near-peak radiation hours [09:00-16:00 LT] on days without precipitation. Therefore, equation (4-4a) can be re-written as,

$$LE = \frac{EF}{1-EF} H \tag{4-4b}$$

4.2.2. Atmospheric Boundary Layer (ABL) Model

A mixed-layer model, which performs very well compared to the complicated large eddy simulations is used to simulate ABL processes (Garcia and Mellado, 2014; Gentine et al., 2015). The profiles of potential temperature (θ) and specific humidity (q) are uniform with height through the mixed-layer, and take on constant values in the mixed-layer. As shown in Figure 4.1, the thin layer between the ground and the mixed layer is called the surface layer (SL). Surface

layer is assumed to be 10% of the mixed-layer top, h (i.e., $z_{SL} = 0.1h$) and is convectively unstable during the growth phase of the boundary layer (Margulis and Entekhabi, 2001; Gentine et al., 2016). *SL* is characterized by air temperature (T_a) and specific humidity (q_a). The following sections explain the detailed representations of physical processes associated with the ABL model.

4.2.3. Energy and Moisture Budget Equations and Radiative Fluxes

The potential temperature and specific humidity in the mixed-layer are given by,

$$\rho c_p h \frac{d\theta}{dt} = \left(R_{ad} + R_{gu}\right)\varepsilon_m - R_{Ad} - R_{Au} + H + H_{top} \quad (4\text{-}5a)$$

$$\rho h L_v \frac{dq}{dt} = LE + LE_{top} \quad (4\text{-}5b)$$

where H_{top} is the entrainment flux at the top of the mixed-layer, and LE_{top} is the entrainment flux from above the mixed-layer. ε_m is the mixed-layer bulk emissivity (Kim and Entekhabi, 1998). R_{ad} and R_{gu} are downward longwave radiation from above the mixed-layer and upward longwave radiation from the ground into the mixed layer, respectively,

$$R_{ad} = \sigma \varepsilon_{ad} T_{h+}^4 \quad (4\text{-}6a)$$

$$R_{gu} = \sigma \varepsilon_s T^4 \quad (4\text{-}6b)$$

where ε_{ad} is the effective emissivity above the mixed layer (Kim and Entekhabi, 1998), and T_{h+} is the air temperature exactly above the mixed-layer height. R_{Ad} and R_{Au} are upward and downward longwave radiative fluxes within the ABL, respectively,

$$R_{Ad} = \sigma \varepsilon_d \theta^4 \quad (4\text{-}7a)$$

$$R_{Au} = \sigma \varepsilon_u \theta^4 \quad (4\text{-}7b)$$

where ε_d is the effective mixed-layer downward emissivity, and ε_u is the effective upward emissivity (Kim and Entekhabi, 1998).

4.2.4. Mixed Layer Height

The daytime ABL height growth is calculated by (Smeda, 1979; Kim and Entekhabi, 1997, 1998a, b; Bagley et al., 2011),

$$\frac{dh}{dt} = \frac{2(G_* - D_1 - D_2)\theta}{gh\delta_\theta} + \frac{H_v}{\rho c_p \delta_\theta} \tag{4-8a}$$

where G_* is the production of mechanical turbulent energy (Kim and Entekhabi, 1998),

$$G_* = u_{SL} u_*^2 \tag{4-8b}$$

u_{SL} is the wind speed at the top of the surface layer (see Appendix A) and u_* is friction velocity. D_1 and D_2 are given by,

$$D_1 = u_{SL} u_*^2 (1 - e^{-\varphi h}) \tag{4-8c}$$

$$D_2 = 0.4 \left(\frac{gh}{\theta} \frac{H_v}{\rho c_p} \right) \tag{4-8d}$$

where φ is the mechanical turbulence dissipation parameter, which is set to 0.01 (Kim and Entekhabi,1998b; Margulis and Entekhabi, 2001; Bagley et al., 2011). H_v is the virtual heat flux at the surface, which causes free-convection mixing and ABL growth during the day (Kim and Entekhabi, 1998),

$$H_v = H + 0.61\theta c_p E \approx H + 0.07LE \tag{4-8e}$$

4.2.5. Laps Rates and Inversion Strengths of θ and q

At the top of the mixed layer, there are instantaneous jumps (inversion strengths) in temperature and humidity (δ_θ and δ_q) that can be calculated by the following prognostic equations,

$$\frac{d\delta_\theta}{dt} = \gamma_\theta \frac{dh}{dt} - \frac{d\theta}{dt} \tag{4-9a}$$

$$\frac{d\delta_q}{dt} = \gamma_q \frac{dh}{dt} - \frac{dq}{dt} \tag{4-9b}$$

where t is the time, γ_θ and γ_q are the lapse rates in potential temperature and specific humidity above the mixed-layer (Margulis and Entekhabi, 2003).

4.2.6. Entrainment Fluxes

Sensible and latent heat fluxes entrainment (H_{top} and LE_{top}) from free atmosphere enter the ABL. H_{top} heats up the ABL and LE_{top} reduces its humidity (Stull 1994),

$$H_{top} = AH \tag{4-10a}$$

$$LE_{top} = \rho L_v \delta_q \frac{dh}{dt} \tag{4-10b}$$

where L_v is the latent heat of vaporization, A is entrainment parameter and is set to 0.2 (Gentine et al., 2015; Garcia and Mellado, 2014; Tajfar et al., 2019a, b).

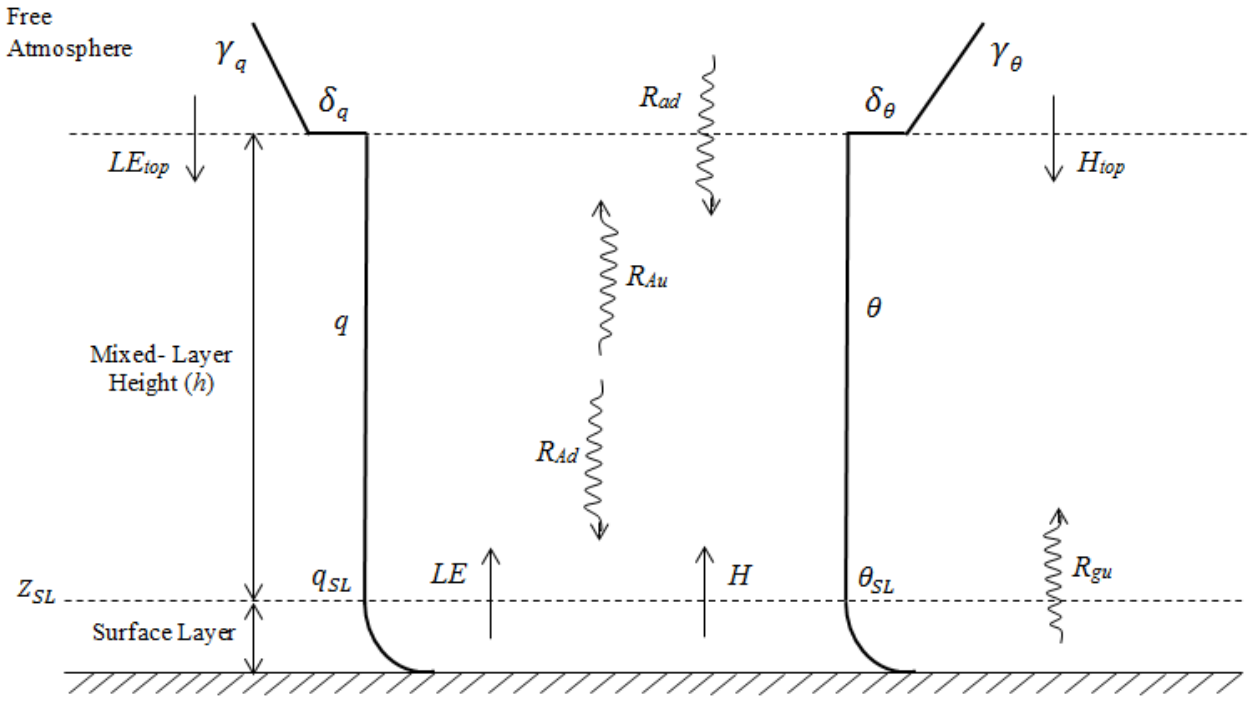

Figure 4. 1. Idealized profiles of potential temperature and specific humidity (θ and q) in the ABL, and corresponding turbulent, radiative and entrainment fluxes.

4.2.7. Variational Data Assimilation (VDA) Scheme

To write the objective function (J), two different integral time scales are used. The first one covers the entire assimilation period in which C_{HN} is assumed to be constant (N = 30 days). The second time scale constitutes the assimilation window in which EF is presumed to be constant $[t_0,t_1]$ = [09:00-16:00 LT]. Optimal values of C_{HN} and EF are obtained by minimizing the following objective function,

$$J(\theta, q, \lambda_1, \lambda_2, R, EF) =$$

$$\sum_{i=1}^{N} \int_{t_o}^{t_1} [\theta_i(t) - \theta_{SL,i}(t)]^T R_\theta^{-1} [\theta_i(t) - \theta_{SL,i}(t)]\, dt + \sum_{i=1}^{N} \int_{t_o}^{t_1} [q_i(t) - q_{SL,i}(t)]^T R_q^{-1} \big[q_i(t) -$$

$$q_{SL,i}(t)\big] dt + (R - R')^T B_R^{-1} (R - R') + \sum_{i=1}^{N} (EF_i - EF_i')^T B_{EF}^{-1} (EF_i - EF_i')$$

$$+ \sum_{i=1}^{N} \int_{t_o}^{t_1} \lambda_{1i}(t) \left[\rho c_p h_i(t) \frac{d\theta_i(t)}{dt} - \big(R_{ad} + R_{gu}\big)\varepsilon_m + R_{Ad} + R_{Au} - H - \right.$$

$$\left. H_{top}\right] dt + \sum_{i=1}^{N} \int_{t_o}^{t_1} \lambda_{2i}(t) \left[\rho h_i(t) L_v \frac{dq_i(t)}{dt} - LE - LE_{top}\right] dt \qquad (4\text{-}11)$$

The first and second terms in the right hand side of equation (4-11) are the square of misfit between the top of the surface layer potential temperature (θ_{SL}) and specific humidity (q_{SL}) and their equivalent estimates (θ and q) from equations (4-5a) and (4-5b). The variation of potential temperature and specific humidity profiles within the surface layer can be explained by the Monin-Obukhov Similarity Theory (MOST) (Gentine et al., 2016). Hence, the potential temperature and specific humidity at the top of the surface layer (θ_{SL} and q_{SL}) can be obtained from θ_a and q_a using MOST. For more information, the readers are referred to Appendix A.

To make C_{HN} strictly positive, it is transformed to R via $C_{HN} = e^R$. The third and fourth terms are the square errors of the unknown parameters (i.e., R and EF) with respect to their prior values (R' and EF'). The last two terms are the physical constraints adjoined to the model through the Lagrange multipliers λ_1 and λ_2. R_θ^{-1} and R_q^{-1} are the inverse error covariance

matrices of θ and q, respectively. B_R^{-1} and B_{EF}^{-1} are the inverse background error covariance matrices of R and EF, respectively. Following Tajfat et al. (2019a), the diagonal terms of R_θ^{-1}, R_q^{-1}, B_R^{-1} and B_{EF}^{-1} are set to 10^{-1} K^{-2}, 10^5, 10^8, and 10^9, respectively.

To minimize the objective function, its first variation (δJ) with respect to the independent variables θ, q, λ_1, λ_2, R, and EF is set to zero, which leads to a set of the so-called Euler-Lagrange equations that should be solved simultaneously. The Euler-Lagrange equations are presented in Appendix C.

4.3. Study Sites

The ability of the VDA approach to partition the available energy between the turbulent heat fluxes is tested at five sites (namely, Desert, Audubon, Bondville, Brookings, and Willow Creek) with contrasting climatic and vegetative conditions. Audubon, Bondville, Brookings, and Willow Creek are in the US (see Figure 4.2) and are part of the AmeriFlux data network (http://ameriflux.ornl.gov/). Desert (in northwestern China) is located in the middle reach of Heihe River basin (HRB) (http://card.westgis.ac.cn/) (see Figure 4.3). The study sites have four different land cover types including barren land, grassland, cropland, and forest (Table 4.1). The leaf area index (LAI) ranges from 0.00 in Desert (barren land) to 5.67 in Willow Creek (dense forest). Soil moisture (SM) also varies from 0.03 in Desert (dry) to 0.29 in Brookings (wet). LAI and SM are the key factors affecting the ratio between the sensible and latent heat fluxes (Gentine et al., 2007; Bateni et al., 2013b; Xu et al., 2014). Hence, testing the VDA approach over five sites with a broad range of LAI and SM enables us to provide insight into how the sequences of reference-level air temperature and specific humidity contain the implicit information of partitioning the available energy between *H* and *LE*.

Audubon (in Arizona) is a grassland water-limited monsoonal site with a temperate arid climate. Bondville (in Illinois) is a cropland that has a humid continental climate with hot summers. Brookings (in South Dakota) is a grassland with temperate continental climate and no dry season. Willow Creek (in Wisconsin) is a deciduous broad-leaf forest with dense vegetation cover and significant precipitation. Desert is barren dry soil.

The AmeriFlux data network (data available at http://www.ameriflux.lbl.gov) provides half-hourly meteorological data including air temperature and specific humidity, wind speed, atmospheric pressure, and incoming shortwave radiation. The sensible and latent heat fluxes are measured by an eddy covariance (EC) instrument. LAI data are obtained from the Global Land Surface Satellites LAI product (GLASS) (Liang et al., 2013; Xiao et al., 2014). This product is available on the Beijing Normal University data center for global change data processing and analysis (http://glass-product.bnu.edu.cn/) and the University of Maryland global land cover facility archive (http://glcf.umd.edu/data/lai/). Soil moisture at each site is also available at the AmeriFlux data network. The Multiscale Observation Experiment on Evapotranspiration over the Heihe Watershed Allied Telemetry Experimental Research (HiWATER-MUSOEXE) project provides half-hourly measurements of micrometeorological data including wind speed, air temperature, relative humidity, and pressure as well as incoming shortwave radiation (Li et al. 2013; Xu et al. 2013; Liu et al. 2016). The sensible and latent heat fluxes are obtained by an eddy covariance (EC) instrument. LAI data at the Desert site are also obtained from the GLASS LAI product. SM is retrieved from the automatic weather stations (http://www.heihedata.org/hiwater/hmon2015/page/2) (Liu et al., 2011, 2018). All the micrometeorological and flux data were collected every 30 minutes time step.

Table 4. 1. Characteristics of the study sites.

Site	Year	DOY	Latitude	Longitude	Vegetation type	SM	LAI	Elevation (m)
Willow Creek	2005	170-259	45.8059 ^{o}N	90.0799 ^{o}W	Forest	0.22	5.67	520
Brookings	2009	176-265	44.3453 ^{o}N	96.8362 ^{o}W	Grassland	0.29	1.72	510
Bondville	2005	182-271	40.0062 ^{o}N	88.2904 ^{o}W	Cropland	0.16	2.24	219
Audubon	2006	170-259	31.5907 ^{o}N	110.5092 ^{o}W	Grassland	0.11	0.54	1469
Desert	2015	170-259	42.1100 ^{o}N	100. 9900 ^{o}E	Barren land	0.03	0	1000

To solve equations (4-5a), (4-5b), (4-8a), (4-9a), and (4-9b), initial conditions for θ, q, h, δ_θ, and δ_q, and the magnitudes of γ_θ and γ_q are required. As q and θ are uniform through the mixed-layer, the initial conditions for equations (4-5a) and (4-5b) (i.e., $\theta(t = t_o)$ and $q(t = t_o)$) are set to be equal to $\theta_{SL}(t = t_o)$ and $q_{SL}(t = t_o)$, respectively. Following Tajfar et al. (2019a), the initial condition for δ_θ and δ_q (i.e., $\delta_\theta(t_o)$ and $\delta_q(t_o)$), ABL height (i.e., $h(t_o)$), and the magnitudes of γ_θ and γ_q are varied from 2 to 6 K, -4.8×10^{-3} to -0.5×10^{-3} kg kg^{-1}, 100 to 500 m, 2 – 8 K km^{-1}, and -7×10^{-3} – -0.5×10^{-3} kg kg^{-1} km^{-1} with the increment of 0.4 K, 0.4×10^{-3} kg kg^{-1}, 100 m, 0.5 K km^{-1}, and 0.5×10^{-3} kg kg^{-1} km^{-1}, respectively. The initial conditions for h, δ_θ, and δ_q, and the magnitudes of γ_θ and γ_q at which the cost function (J) reaches its minimum value for the five study sites are listed in Table 4.2.

The VDA is applied to the Desert (DOYs 170-259, 2015), Audubon (DOYs 170-259, 2006), Bonville (DOYs 182-271, 2005), Brookings (DOYs 176-265, 2009), and Willow Creek (DOYs 170-259, 2005). These years and DOYs are chosen because they have a minimum data gap.

Table 4. 2. Initial conditions for h, δ_θ, and δ_q, and the magnitudes of γ_θ and γ_q for the study sites.

Site	$h(t_o)$ (m)	$\delta_\theta(t_o)$ (K)	$\delta_q(t_o)$ (kg kg^{-1})	γ_θ (K km^{-1})	γ_q (kg kg^{-1} km^{-1})
Willow Creek	400	4.4	-3.2×10^{-3}	5.5	-1.5×10^{-3}
Brookings	400	4.0	-2.0×10^{-3}	4.5	-0.5×10^{-3}
Bondville	400	4.0	-4.0×10^{-3}	4.5	-3.0×10^{-3}
Audubon	400	2.8	-4.4×10^{-3}	3.0	-4.0×10^{-3}
Desert	400	2.4	-4.4×10^{-3}	3.0	-4.5×10^{-3}

Figure 4. 2. Locations of the four Ameriflux study sites (i.e., Audubon, Brookings, Bondville and Willow Creek) in the United States.

Figure 4. 3. Location of the Desert site in China.

4.4. Results

As mentioned previously, C_{HN} and *EF* are the two key unknowns of the VDA system. Table 4.3 shows the estimated C_{HN} values from the VDA approach and corresponding LAI values at the five study sites. C_{HN} is mainly affected by vegetation phenology (Caparrini et al., 2004a, b; Bateni et al., 2013b; Xu et al., 2016, 2018; Abdolghafoorian et al., 2017). As shown in Table 4.3, the variations in C_{HN} estimates are consistent with those of LAI in wet and/or densely vegetated sites. For example, at the Willow Creek site, C_{HN} and LAI decrease slightly during the modeling periods. At the Brookings site, C_{HN} reaches its highest value in the second monthly period, and reduces in the third month. A similar trend is observed in LAI. At the Bondville site, LAI and C_{HN} estimates remain almost constant in DOY 182-271.

The consistency between the C_{HN} retrievals and LAI weakens in dry/sparsely vegetated sites. At Audubon, C_{HN} estimates decrease slightly in the second monthly period and increase in

the third modeling period, which is less consistent with the changes in the LAI values that increase continuously during the modeling periods. Although LAI is invariant at the Desert site, C_{HN} shows minor changes in different assimilation periods. The slight variations in C_{HN} estimates is attributed to the changes in friction velocity, solar elevation and wind speed (Bateni et al., 2013b; He et al., 2018). Desert has the lowest C_{HN} estimates compared to the other sites because it has no vegetation (LAI = 0). Willow Creek has the highest C_{HN} estimates due to its dense vegetation cover (LAI = 5.67). In general, the sites with higher LAI values (e.g., Willow Creek) have higher C_{HN} estimates compared to the sites with lower LAI (e.g., Desert and Audubon).

Overall, the results show that the C_{HN} estimates are positively correlated with the vegetation phenology at wet and/or densely vegetated sites although no information on vegetation density is used in the VDA approach. These findings indicate that the VDA can extract the implicit information contained in the air temperature and specific humidity to estimate C_{HN} while applying on wet and/or densely vegetated sites.

Table 4. 3. Estimated neutral bulk heat transfer coefficient (C_{HN}) values by the VDA model at the five study sites.

Site	DOY	C_{HN}	LAI
Willow Creek	170-199	0.0245	5.87
	200-229	0.0242	5.84
	230-259	0.0222	5.29
Brookings	176 – 206	0.0054	1.93
	207 – 237	0.0102	2.15
	238 – 265	0.0048	1.07
Bondville	182-211	0.0130	2.23
	212-241	0.0150	2.24
	242-271	0.0140	2.24
Audubon	170-199	0.0031	0.27
	200-229	0.0029	0.57
	230-259	0.0033	0.77
Desert	170-199	0.0022	0
	200-229	0.0020	0
	230-259	0.0010	0

Figure 4.4 shows time series of *EF* estimates at the five study sites. *EF* values from measured *H* and *LE* are also shown by open circles in Figure 4.4. The *EF* retrievals agree well with the observations in terms of both magnitude and day-to-day variations in wet and/or densely vegetated sites (e.g., Willow Creek), but their accuracy decreases in dry and/or sparsely

vegetated sites (e.g., Desert and Audubon). In addition, *EF* values are consistent with the wetting and dry down events although precipitation measurements are not used in the VDA approach. The drying rate of land surface is controlled by both land surface properties as well as atmospheric conditions (Shokri et al., 2008a, b). At dry/sparsely vegetated sites (e.g., Desert and Audubon), evapotranspiration is at its second stage (water-limited), and is mainly controlled by the land state variable (i.e., LST) rather than the atmospheric state variables (i.e., air temperature and specific humidity). Consequently, the coupling between *EF* and the atmospheric state variables is weak, and retrieval of *EF* from air temperature and specific humidity becomes more uncertain. As an example, at Desert site, the site was mostly dry (DOYs 170-245). In this period, the VDA model performs poorly and spikes are observed, indicated that sequences of air temperature and humidity do not have enough information to constrain *EF*. Toward the end of the modeling period (DOYs 246-259), the site becomes wet and the *EF* estimates capture the variations in the observations.

The high soil moisture can result in negative sensible heat flux, which makes *EF* observations larger than one (Xu et al., 2015; 2018). This occurs in the Willow Creek, Brookings, and Bondwille sites. As shown in Figure 4.4, the VDA approach can capture high *EF* observations when the soil is very wet. This shows that the sequences of air temperature and humidity has a significant amount of information on relative partitioning of turbulent heat fluxes in wet and/or densely vegetated sites. Table 4.4 shows the MAE and RMSE of *EF* estimates at the five study sites. As anticipated, the MAE and RMSE of *EF* estimates are lower in wet and/or densely vegetated sites than dry and/or slightly vegetated sites. *EF* estimates have the highest and lowest RMSE of 0.198 and 0.085 at Desert (dry and barren land) and Willow Creek (wet and dense vegetation cover), respectively. This shows that the sequences of reference-level air

temperature and specific humidity contain the implicit information on the partitioning of available energy between the turbulent heat fluxes at wet/densely vegetated sites. The results for Brookings and Bondville sites are close and comparable as are their characteristics.

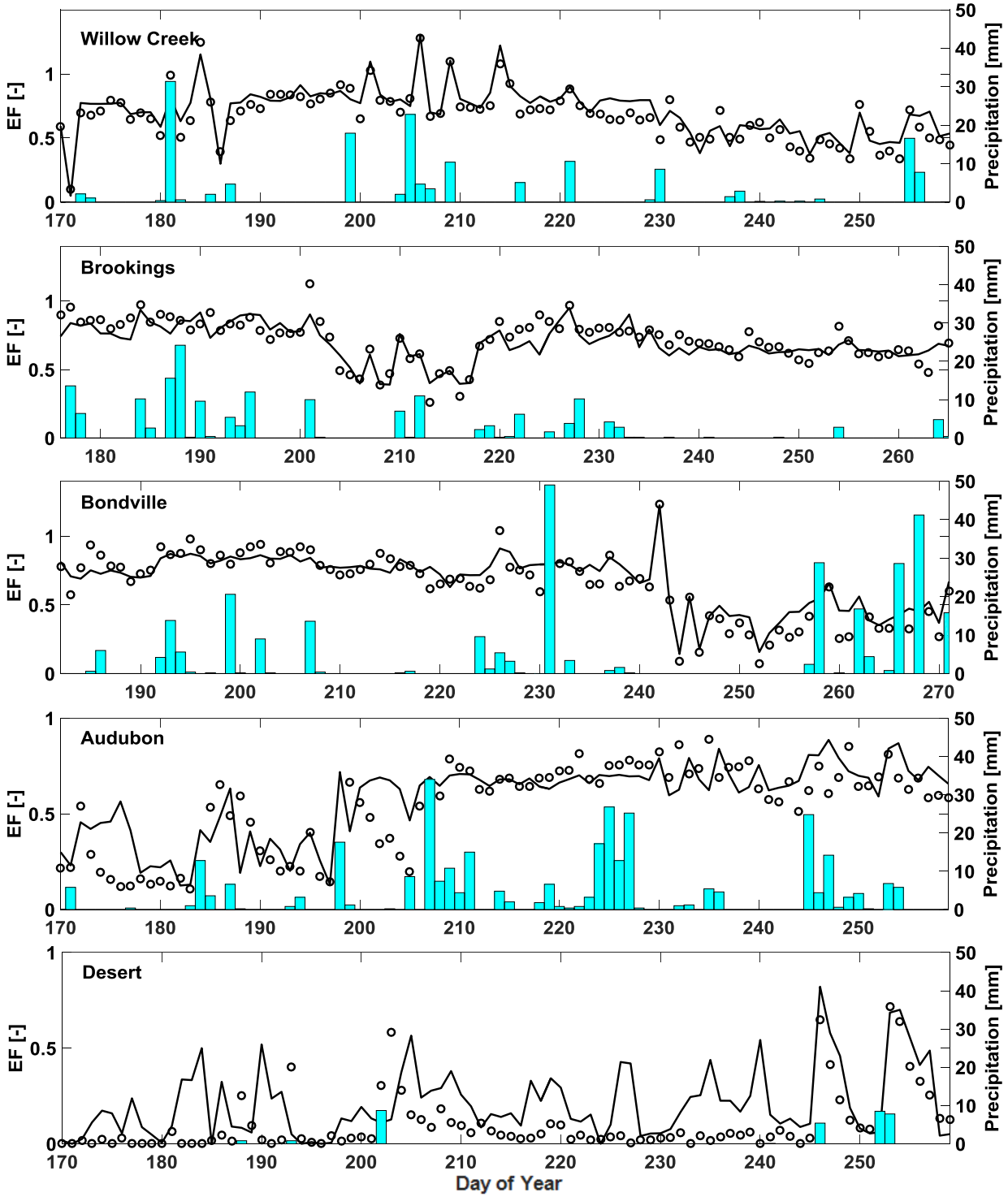

Figure 4. 4. Time series of evaporative fraction (*EF*) observations (open circles), estimates from VDA model (solid lines), and precipitation (blue bars) at the five study sites.

Table 4. 4. MAE and RMSE of *EF* estimates from the VDA model at the five study sites.

Site	*EF*	
	MAE	RMSE
Willow Creek	0.072	0.085
Brookings	0.065	0.083
Bondville	0.071	0.088
Audubon	0.146	0.178
Desert	0.152	0.198

To evaluate performance of the VDA approach in various vegetative and hydrological conditions, the scatterplot of half-hourly *H* and *LE* estimates are compared with observations in Figures 4.5 and 4.6. As shown, the VDA model performs better at the wet and/densely vegetated site. The best and worst turbulent heat fluxes estimates are observed at Willow Creek and Desert, respectively. For Willow Creek, *H* and *LE* estimates mostly fall around the 45-degree line, while for Desert, *LE* estimates are far from the 45-degree line. This shows that the information content of the atmospheric state variables (e.g., air temperature and specific humidity) on the turbulent heat fluxes significantly reduces in dry/sparsely vegetated sites. The results for Bondville site are comparable to those generated for Brookings and are well scattered around the 1:1 line.

Overall, the results indicate that the model can partition the available energy between *H* and *LE* relatively well at sites with high and medium SM and/or LAI values, but it performs poorly in sites with low SM and/or LAI. At all the study sites, *LE* estimates are more sparsely scattered around the 1:1 line compared to *H* estimates. This is due to the fact that the errors in *H* estimates comes from the errors in C_{HN} estimates, but the errors in *LE* stems from the errors in *H*

and *EF* estimates. More sources of errors expand scattering of *LE* estimates (Xu et al., 2018; Tajfar et al., 2019a).

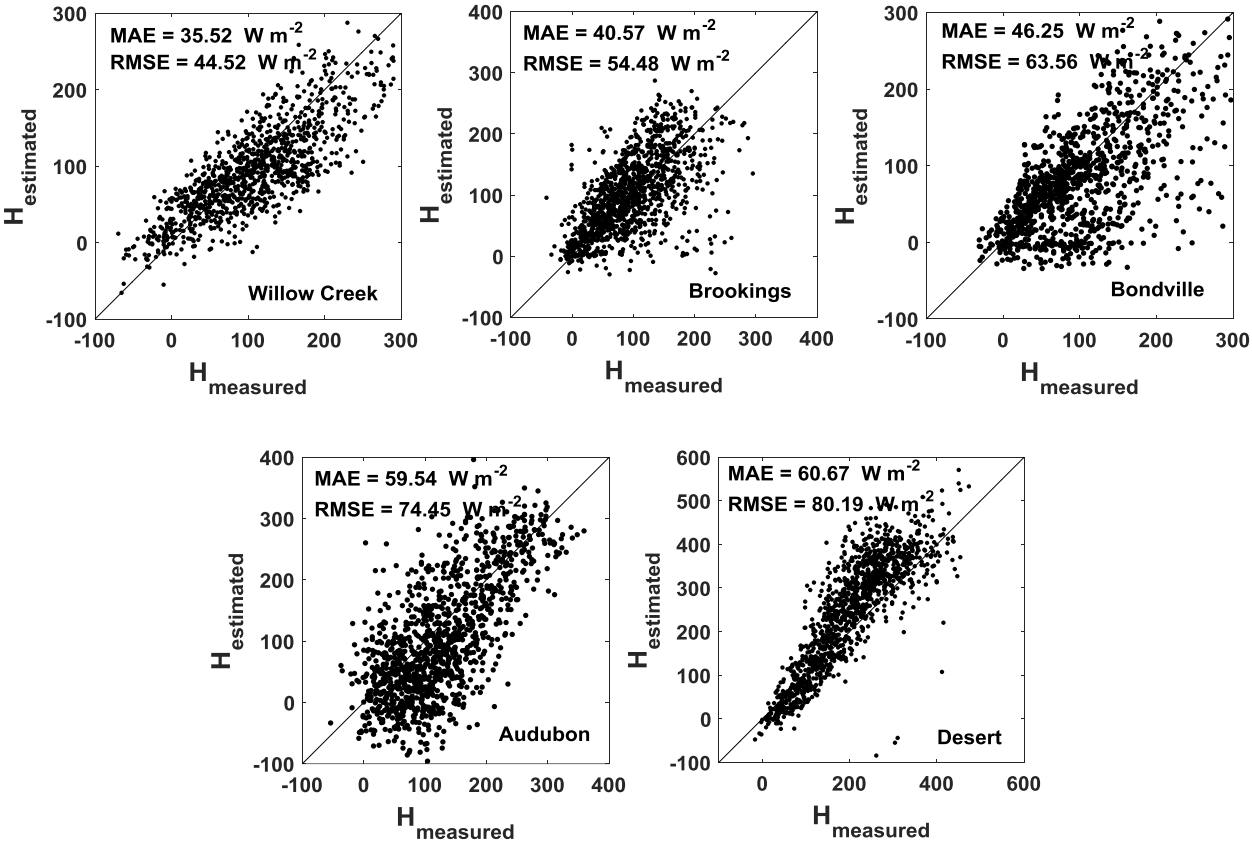

Figure 4. 5. Scatterplot of half-hourly modeled sensible heat flux (*H*) versus corresponding observations at the five experimental sites.

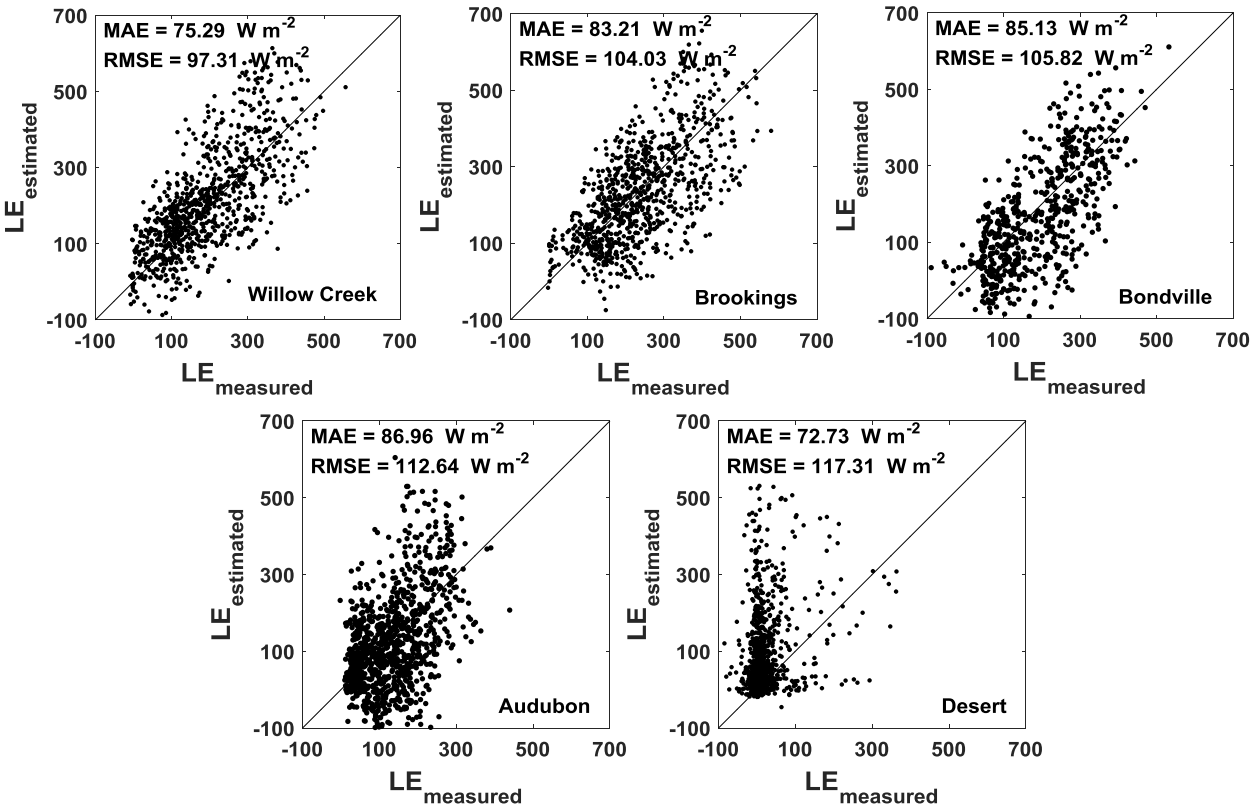

Figure 4. 6. Scatterplot of half-hourly modeled latent heat flux (*LE*) versus corresponding observations at the five experimental sites.

Figures 4.7 and 4.8 compare the time series of daily *H* and *LE* estimates from open-loop and VDA model with the corresponding measurements at the Desert, Audubon, Bondville, Brookings, and Willow Creek sites. The open-loop model does not assimilate q and θ data. As expected, the VDA approach generates more accurate *H* and *LE* values at the energy-limited sites (e.g., Willow Creek). At Desert and Audubon sites, the VDA model cannot capture the trend of latent heat flux well. The VDA approach overestimates and underestimates *H* at Desert and Audubon sites, respectively. However, the VDA model yields much better estimates of *H* and *LE* at Bondville and Brookings and can capture the daily fluctuations in the observations. For Willow Creek, the magnitude and variations of the *H* and *LE* observations are captured by the model estimates and the model track the dry down and wetting events well.

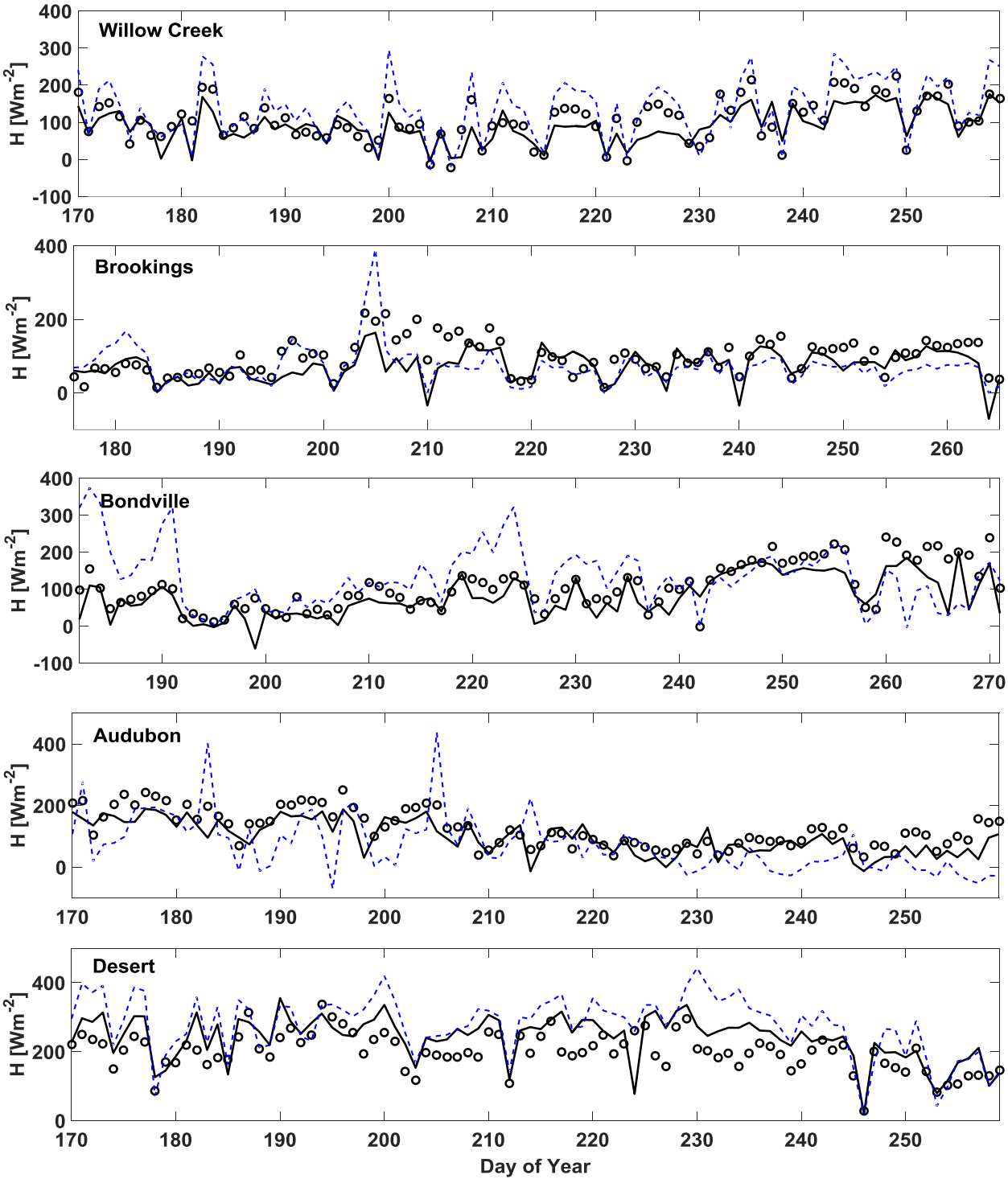

Figure 4. 7. Time series of sensible heat flux (*H*) observations (open circles), estimates from VDA model (solid lines), and open-loop (blue dashed lines) at the five experimental sites.

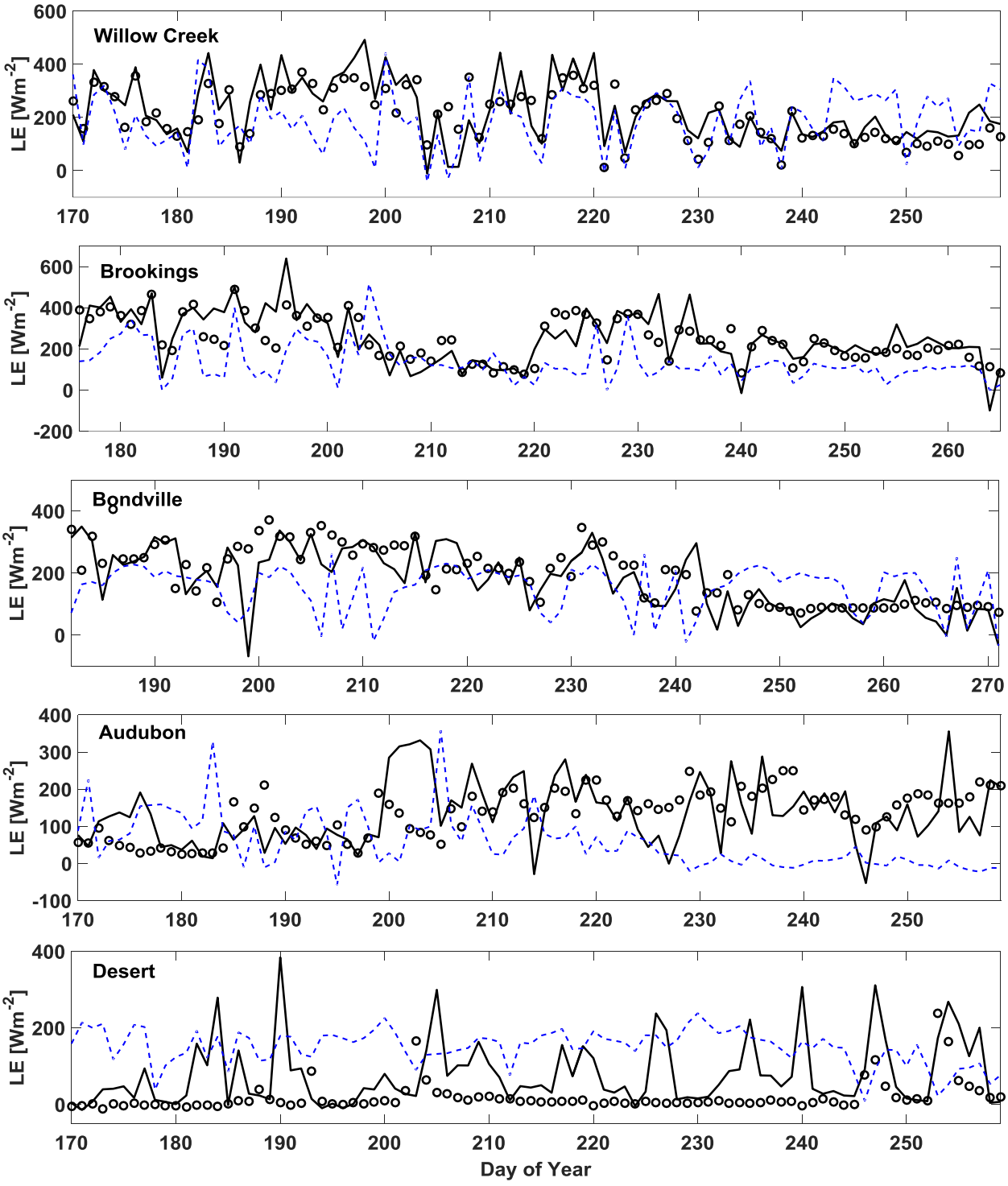

Figure 4. 8. Time series of latent heat flux (*LE*) observations (open circles), estimates from VDA model (solid lines), and open-loop (blue dashed lines) at the five experimental sites.

The lower MAEs and RMSEs from VDA model show that the assimilation of θ and q results in better H and LE estimates. For daily H estimates, the five-site averages of RMSE (MAE) from VDA and open-loop models are 49.08 W m^{-2} (38.06 W m^{-2}) and 73.80 W m^{-2} (58.80 W m^{-2}), respectively. Corresponding RMSE (MAE) values for daily LE estimates are 85.28 W m^{-2} (62.11 W m^{-2}) and 134.84 W m^{-2} (115.87 W m^{-2}), respectively. The five-site average of RMSEs (MAEs) of daily H estimates from VDA model are reduced by 33.5% (35.3%) by assimilating θ and q. Likewise, the five-site average of RMSEs (MAEs) of daily LE estimates from VDA model are decreased by 36.8% (46.4%). The RMSEs of daily H estimates for Desert, Audubon, Bondville, Brookings, and Willow Creek sites are 60.00 W m^{-2}, 58.13 W m^{-2}, 45.21 W m^{-2}, 45.01 W m^{-2}, and 37.03 W m^{-2}, respectively. Corresponding RMSE values for daily LE estimates are 102.21 W m^{-2}, 89.57 W m^{-2}, 77.88 W m^{-2}, 82.28 W m^{-2}, and 74.46 W m^{-2}, respectively. As expected, The higher RMSEs of H and LE estimates at the Desert and Audubon sites compared to those of the other sites is mostly due to their particular hydrological and vegetative conditions. Compared to the other sites, Desert and Audubon have a drier land and sparser vegetation cover that worsens the performance of the VDA model at these sites. On the contrary, Willow Creek site has lower RMSE and MAE of H and LE estimates compared to those of the other sites, because it has a wetter land and denser vegetation cover that improves the model performance at this site. The errors for Bondville and Brookings sites are relatively close and reasonable, showing that the VDA model works well at these two sites.

Table 4. 5. MAE and RMSE of half-hourly *H* (top panel) and *LE* (bottom panel) estimates at the five experimental sites.

Site	VDA (W m^{-2})		Open-loop (W m^{-2})	
	MAE	RMSE	MAE	RMSE
Willow Creek	35.52	44.52	50.92	67.36
Brookings	40.57	54.48	43.89	58.19
Bondville	46.25	63.56	67.73	96.99
Audubon	59.54	74.45	118.69	164.79
Desert	60.67	80.19	91.12	121.14
Five-site-average	**48.51**	**63.44**	**74.47**	**101.69**
Willow Creek	75.29	97.31	102.29	136.66
Brookings	83.21	104.03	140.09	168.28
Bondville	85.13	105.82	125.96	157.44
Audubon	86.96	112.64	143.75	180.47
Desert	72.73	117.31	145.85	170.04
Five-site-average	**80.66**	**107.42**	**131.59**	**162.58**

Table 4. 6. MAE and RMSE of daily *H* (top panel) and *LE* (bottom panel) estimates at the five experimental sites.

Site	VDA (W m^{-2})		Open-loop (W m^{-2})	
	MAE	RMSE	MAE	RMSE
Willow Creek	30.05	37.03	37.87	46.33
Brookings	32.05	45.01	39.59	49.66
Bondville	31.97	45.21	60.47	84.75
Audubon	46.16	58.13	74.73	91.77
Desert	50.08	60.00	81.34	96.50
Five-site-average	**38.06**	**49.08**	**58.80**	**73.80**
Willow Creek	56.93	74.46	91.55	112.25
Brookings	57.79	82.28	123.10	144.97
Bondville	55.34	77.88	98.75	123.77
Audubon	71.77	89.57	124.04	142.82
Desert	68.74	102.21	141.93	150.40
Five-site-average	**62.11**	**85.28**	**115.87**	**134.84**

The VDA model finds the optimum values of C_{HN} and *EF* by minimizing the difference between the ABL potential temperature and specific humidity estimates from equations (4-5a) and (4-5b) (i.e., θ and q), and the corresponding values obtained from the reference-level air temperature and specific humidity via the MOST (i.e., θ_{SL} and q_{SL}). Figure 4.9 and 4.10 show the half-hourly estimated ABL potential temperature and specific humidity versus their corresponding retrievals from air temperature and specific humidity. As shown, for Willow

Creek, the θ and q estimates agree well with their corresponding retrievals from air temperature and specific humidity, and the scatterplots mostly fall around the 45-degree line. This shows that in wet and/or densely vegetated sites, the VDA approach can extract the significant amount of information in the sequences of air temperature and humidity to move the initial guesses of C_{HN} and EF to their true values and consequently minimize the difference between the θ and q estimates. At the Brookings and Bondville sites, θ and q estimates are in fairly good agreement with the observations, implying that the time series of atmospheric state variable have some information on the C_{HN} and EF. At the Desert and Audubon sites, θ and q estimates are sparsely scattered around the 1:1 line, showing the lack of sufficient information in the sequence of air temperature and humidity to tune C_{HN} and EF.

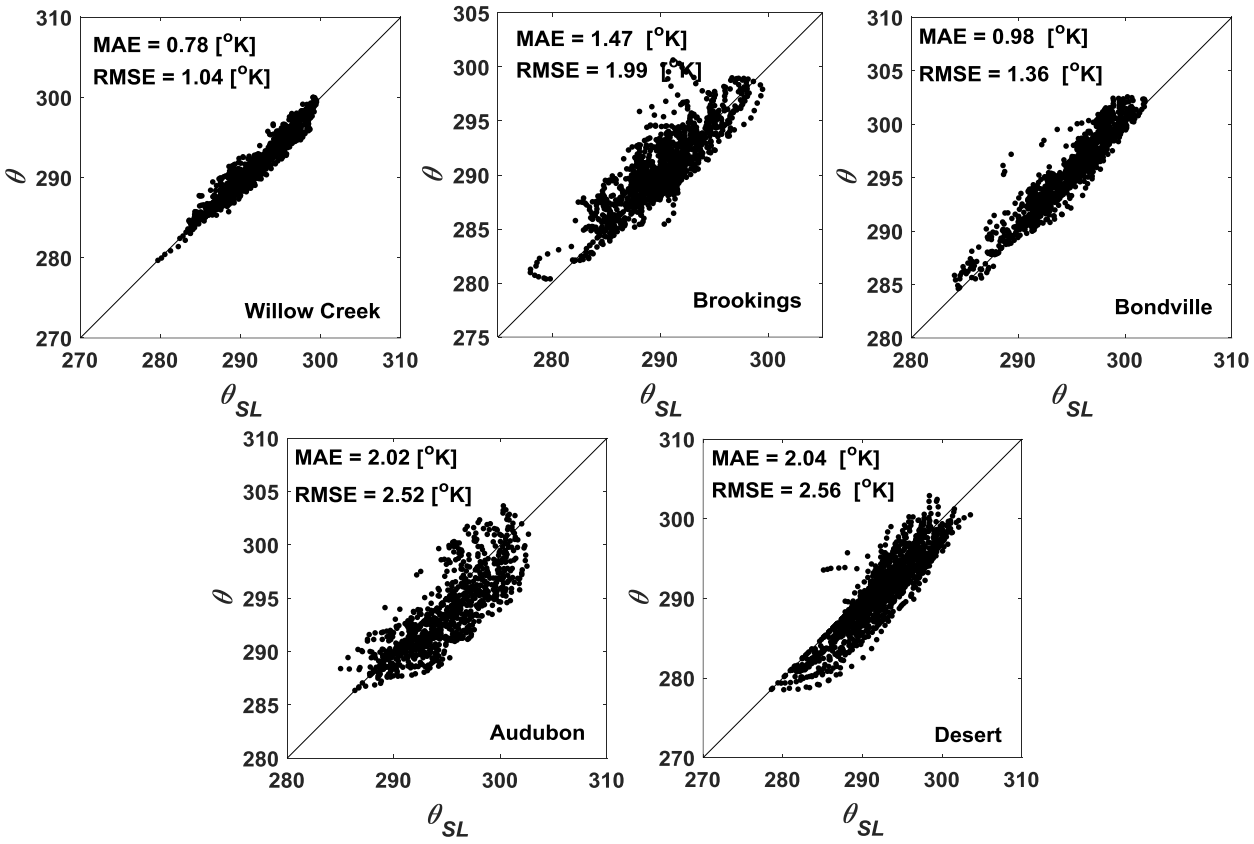

Figure 4. 9. Scatterplot of half-hourly modeled potential temperature (θ) versus corresponding observations at the five experimental sites.

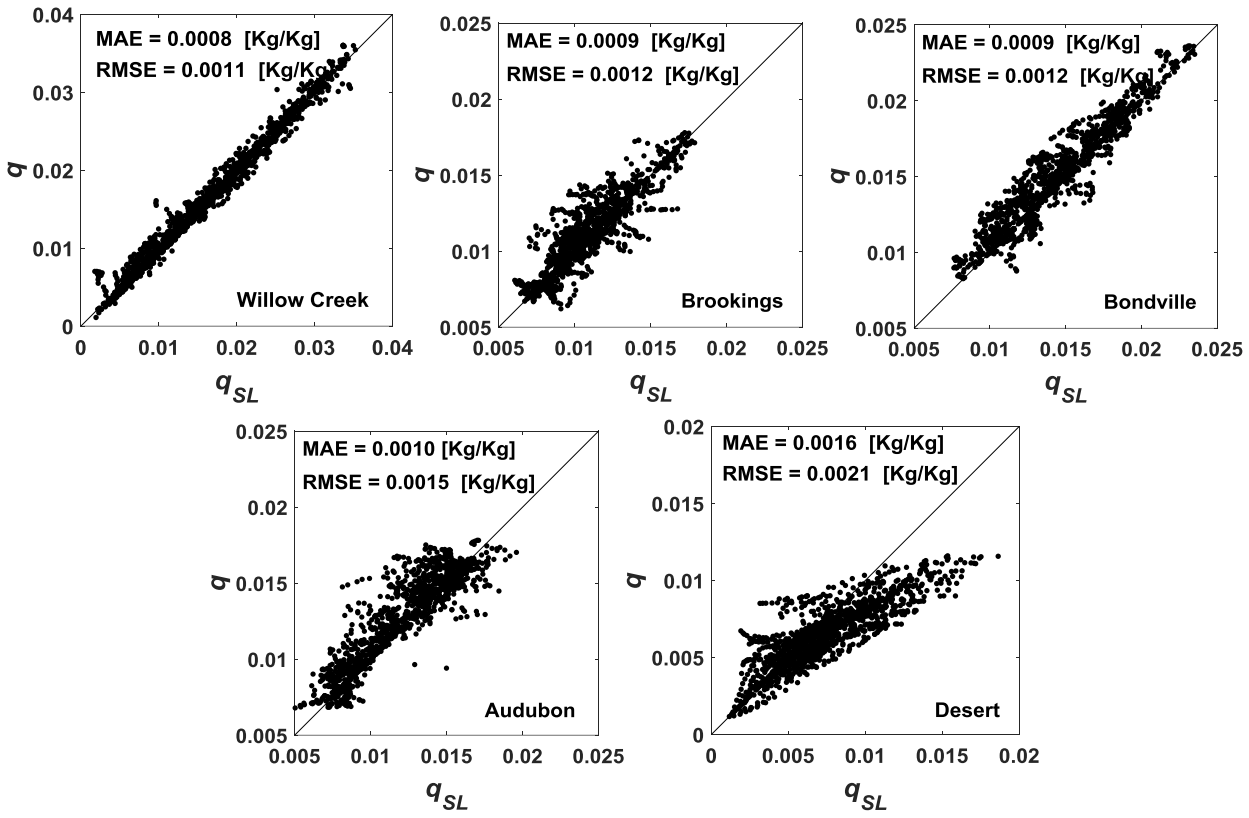

Figure 4. 10. Scatterplot of half-hourly modeled specific humidity (q) versus corresponding observations at the five experimental sites.

The RMSEs of q estimates at the Desert, Audubon, Bondville, Brookings, and Willow Creek sites are 0.0021 kg kg^{-1}, 0.0015 kg kg^{-1}, 0.0012 kg kg^{-1}, 0.0012 kg kg^{-1}, and 0.0011 kg kg^{-1}, respectively. As discussed earlier, the VDA model generates better q estimates as LAI and SM of the study sites increase. The LAI and SM of Bondville and Brookings sites are relatively close, thus their RMSEs and MAEs of half-hourly q for these two sites are the same. As expected, Willow Creek site with highest LAI and relatively high SM (second place after Brookings) has the lowest RMSE and MAE and Desert site with the lowest LAI and SM has the highest RMSE and MAE. The RMSE of θ estimates for Desert, Audubon, Bondville, Brookings, Daman, and Willow Creek sites are 2.56 K, 2.52 K, 1.36 K, 1.99 K, and 1.04 K, respectively. As

anticipated, the RMSE of θ estimates increases significantly as LAI and SM of the studied sites decrease. As previously stated, in dry sites (e.g., Desert and Audubon), the role of LST observations in estimating *EF* and consequently θ is essential.

Figure 4.11 presents the mean diurnal cycles of measured and estimated *H* and *LE* over the whole modelling period for the five sites. As expected, the magnitude and phase of the diurnal cycles of retrieved sensible and latent heat fluxes agree well with the observations at the Willow Creek site. For the dry/sparsely vegetated sites (especially Desert), there is a large discrepancy between the diurnal cycles of estimated and observed *H* and *LE*, showing poor performance of the VDA approach in dry and/or sparsely vegetated sites. The results for Bondville and Brookings sites show that assimilating the state variables of atmosphere (i.e., q and θ) can relatively capture the phase and magnitude of the diurnal cycle of *H* and *LE* with small discrepancies.

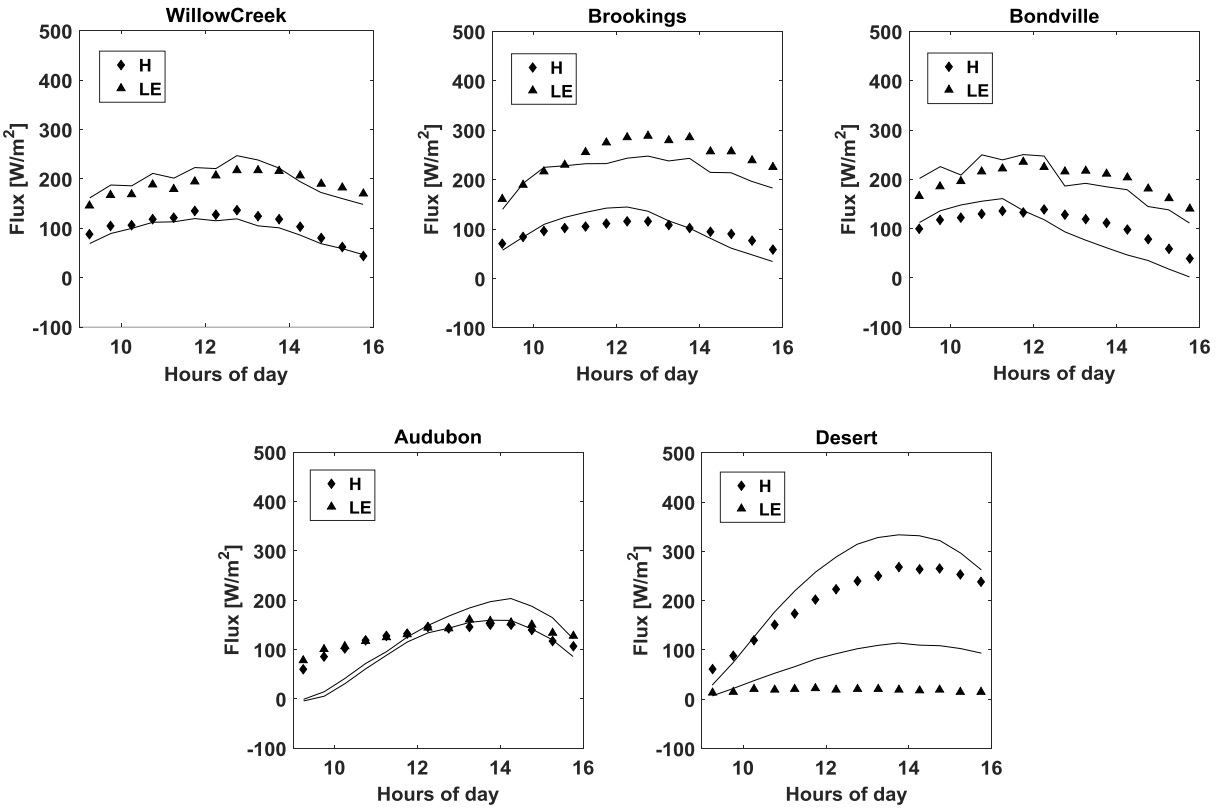

Figure 4. 11. Estimated (solid lines) and measured (symbols) mean diurnal cycle of turbulent heat fluxes from the VDA model for the five study sites (*H* and *LE* mean sensible and latent heat fluxes).

4.5. Conclusion

In this study, the information content of reference-level air temperature and humidity for partitioning the available energy between the turbulent heat fluxes is evaluated at five sites with different vegetative and climatic conditions: Desert, Audubon, Bondville, Brookings, and Willow Creek. The VDA approach takes advantage of the information in the sequences of reference-level air temperature and specific humidity (as the state variables of the atmosphere) to partition the available energy between the sensible and latent heat fluxes. The two key unknown parameters of the VDA are evaporative fraction (*EF*) and neutral bulk heat transfer coefficient

(C_{HN}). *EF* characterizes partitioning between the turbulent heat fluxes and C_{HN} scales the sum of turbulent heat fluxes.

The sites with higher LAI values (denser canopies) have higher C_{HN} estimates (e.g., Willow Creek) and sites with lower LAI values (sparsely vegetated sites) have lower C_{HN} estimates (e.g., Desert and Audubon). Overall, the C_{HN} estimates are positively correlated with the vegetation phenology and follow the LAI trends for wet and/or densely vegetated sites. The consistency between the C_{HN} retrievals and LAI weakens in dry and /or sparsely vegetated sites. The *EF* estimates agree well with the observations in terms of magnitude and day-to-day variations in wet and/or densely vegetated sites (e.g., Willow Creek), but their accuracy declines in dry and/or sparsely vegetated sites (e.g., Desert and Audubon). The results show that the sequences of air temperature and specific humidity have a significant amount of information on the partitioning of available energy between *H* and *LE*. This information content decreases by the reduction in SM and/or LAI. RMSE of *EF* estimates at Desert (dry site) is 57.1% higher than the RMSE of 0.085 at Willow Creek (wet site).

The RMSE of daily sensible (latent) heat flux estimates at Desert, Audubon, Bondville, Brookings, and Willow Creek sites are 60.00 W m^{-2} (102.21 W m^{-2}), 58.13 W m^{-2} (89.57 W m^{-2}), 45.21 W m^{-2} (77.88 W m^{-2}), 45.01 W m^{-2} (82.28 W m^{-2}), and 37.03 W m^{-2} (74.46 W m^{-2}), respectively. The RMSEs of daily *H* and *LE* increases continuously as the site becomes drier and/or sparser in vegetation density. This is due to the fact that at dry and/or sparsely vegetated sites evapotranspiration is mainly controlled by the land surface state variable (i.e., LST) rather than the atmospheric state variables (i.e., reference-level air temperature and specific humidity). Accordingly, the coupling between *EF* and the atmospheric state variables weakens and the estimation of *EF* from sequences of air temperature and specific humidity becomes uncertain. In

contrast, at wet and/or densely vegetated sites (e.g., Willow Creek), the evaporative demand is generally controlled by atmospheric state variables and the VDA system can extract those information to estimate *H* and *LE*.

The RMSEs of estimated ABL q (θ) at the Desert, Audubon, Bondville, Brookings, and Willow Creek sites are 0.0021 kg kg^{-1} (2.56 K), 0.0015 kg kg^{-1} (2.52 K), 0.0012 kg kg^{-1} (1.36 K), 0.0012 kg kg^{-1} (1.99 K), and 0.0011 kg kg^{-1} (1.04 K), respectively. The close agreement between θ and θ_{SL}, and q and q_{SL} at wet and/or densely vegetated sites (e.g., Willow Creek) indicates that (by increasing the number of iterations) the VDA approach can effectively update the two key unknowns of the model (C_{HN} and *EF*) and obtain their optimal values. The largest and smallest RMSEs of q (θ) estimates occur at Desert and Willow Creek. The RMSEs of 0.0012 kg kg^{-1} (1.36 K) and 0.0012 kg kg^{-1} (1.99 K) at the Bondville and Brookings sites fall between those of dry/sparsely vegetated and wet/densely vegetated sites.

The magnitude and phase of the diurnal cycles of retrieved sensible and latent heat fluxes agree well with the observations at wet/densely vegetated sites (e.g., Willow Creek). In contrast, for the dry/lightly vegetated sites (especially Desert), there is a significant difference between the diurnal cycles of retrieved *H* and *LE* and observations.

Future studies should focus on the synergistic assimilation of the LST (as the state variable of land surface) and the reference-level air temperature and specific humidity (as the state variables of atmosphere) to improve the turbulent heat flux estimates at the dry and/or sparsely vegetated sites.

Chapter 5: Variational Assimilation of Land Surface Temperature, Air Temperature and Specific Humidity to Estimate Surface Heat Fluxes in Contrasting Hydrologic and Vegetative Conditions

Variational Assimilation of Land Surface Temperature, Air Temperature and Specific Humidity to Estimate Surface Heat Fluxes in Contrasting Hydrologic and Vegetative Conditions

E. Tajfar[1] and S. M. Bateni[1]

[1]Department of Civil and Environmental Engineering and Water Resources Research Center, University of Hawaii at Manoa, Honolulu, USA.

[*]*Corresponding author address*: Elahe Tajfar, Department of Civil and Environmental Engineering and Water Resources Research Center, University of Hawaii at Manoa, Honolulu, USA.

E-mail: etajfar@hawaii.edu

Current affiliation: Ph.D. candidate, Department of Civil and Environmental Engineering, University of Hawaii at Manoa, Honolulu, USA.

ABSTRACT

Performance of a recently developed variational data assimilation (VDA) approach that estimates surface heat fluxes by assimilating the sequences of land surface temperature (LST), and air temperature and specific humidity measurements into a coupled land surface-atmospheric boundary layer model is tested at five sites (Desert, Audubon, Bondville, Brookings, and Willow Creek) with contrasting climate and vegetation conditions. The unknown parameters of the VDA approach are neutral bulk heat transfer coefficient (C_{HN}) and evaporative fraction (EF). In all the study sites, the EF estimates agree well with the observations in terms of magnitude and day-to-day fluctuations. Also, the variations in the C_{HN} estimates are consistent with those of leaf area index (LAI) in all the experimental sites. The results show that the VDA system can accurately estimate surface heat fluxes over a wide variety of environmental conditions. Compared to the previous study that assimilated only the state variables of atmosphere (i.e., air temperature and humidity) into an atmospheric boundary layer model, this study decreases the five-site mean root-mean-square-error (RMSE) of daily sensible and latent heat flux estimates by 26.5% and 32.7%, respectively.

Keywords: Turbulent heat fluxes; variational data assimilation model; air temperature; specific humidity; land surface temperature

5.1. Introduction

Turbulent heat fluxes describe the mass and energy exchanges between the surface and its overlying atmosphere. The accurate estimation of turbulent heat fluxes has been the subject of various disciplines such as irrigation scheduling, weather forecasts, global climate change, and water resources planning and management (Kalma et al. 2008; Lu et al., 2016; Xu et al., 2018). Sensible (*H*) and latent (*LE*) heat fluxes can be measured by different methods (e.g., Bowen ratio methods, eddy covariance (EC) technique, lysimeters, and large aperture scintillometer). Nevertheless, these techniques are expensive and inapplicable to large-scale domains (Xu et al., 2014; Liu et al., 2016). As a result, different models have been developed to estimate sensible and latent heat fluxes (Holtslag and Van Ulden, 1983; Bastiaanssen et al., 1998; Polonio and Soler, 2000; Kalma et al., 2008; Li et al., 2010; Maes and Steppe, 2012; Salvucci and Gentine, 2013; Bateni et al., 2012b, 2013a; Yilmaz et al., 2014; Zhuang and Wu, 2015; Gentine et al., 2016; Lu et al., 2016; Brenner et al., 2017).

In General, the existing models for estimating sensible and latent heat fluxes can be divided into five major groups. The first group (triangle methods) takes advantage of the empirical relationship between land surface temperature (LST) and vegetation indices (i.e., leaf area index (LAI), normalized differential vegetation index (NDVI), etc.) to estimate *H* and *LE* (Margulis et al., 2005; Carlson, 2007; Stisen et al., 2008; Tang et al., 2010; Sun et al., 2013; Laxmi et al., 2014; Martinez et al., 2017; Majozi et al., 2017, Zhu et al., 2017). The second group (diagnostic methods) estimates turbulent heat fluxes by solving the surface energy balance (SEB) equation (Su, 2002; Liu et al., 2007; Kalma et al., 2008; Jia et al., 2009; Jiang et al., 2009; Kustas et al., 2012; Ma et al., 2012, 2015, 2018; Sharma et al., 2015; Sharma et al., 2015; Song et al., 2016). The third group (combination methods) predicts *H* and *LE* by incorporating LST

observations into the Penman-Monteith equation (Mallick et al., 2014, 2015; Raoufi and Beighley, 2017). The forth group (land data assimilation systems (LDAS)) estimates turbulent heat fluxes by the Ensemble Kalman Filter (EnKF) approach (Peters-Lidard et al., 2011; Xia et al., 2014a, 2014b; Bateni and Entekhabi, 2012b; Carrera et al., 2015; Xu et al., 2015, 2018).

The fifth group (variational data assimilation (VDA) method) predicts turbulent heat fluxes by assimilating sequences of land surface temperature observations into the force-restore and/or heat diffusion equation (Caparrini et al., 2003, 2004a, b; Crow and Kustas, 2005; Sini et al., 2008; Bateni and Entekhabi, 2012a; Bateni et al., 2014, 2015; Xu et al., 2014, 2016, 2018; Abdolghafoorian et al., 2017; He et al., 2018). The VDA approaches take advantage of the implicit information in the sequences of LST measurements to partition the available energy between the sensible and latent heat fluxes. The main disadvantage of the VDA approaches is that their performance degrades in wet/densely vegetated sites in which evapotranspiration is mostly controlled by the atmospheric factors (i.e., air temperature and specific humidity) rather than land surface processes (i.e., LST).

Several studies showed that the reference-level air temperature and humidity measurements contain useful information about soil moisture (Mahfouf, 1991; Bouttier et al., 1993a, b; Mahfouf et al., 2000, 2009; Douville et al., 2000; Hess, 2001; Drusch and Viterbo, 2007; de Rosnay et al. 2013; Ren and Xue, 2016; de Lannoy et al., 2016), and turbulent heat fluxes (Holtslag and Van Ulden, 1983; Margulis and Entekhabi, 2001; Alapaty et al., 2001; Balsamo et al., 2007; Shang et al., 2007; Salvucci and Gentine, 2013; Rigden and Salvucci, 2015; Gentine et al., 2016; Lum et al., 2017; Tajfar et al., 2019a). These studies typically require specification of surface roughness for heat and momentum as well as ground heat flux, which are mostly unavailable.

Given the abovementioned drawback of VDA approaches and the fact that the sequences of air temperature and humidity contain information on the turbulent heat fluxes, Tajfar et al. (2019b) developed a VDA method that estimates turbulent heat fluxes by the synergistic assimilation of LST, and reference-level air temperature and specific humidity into a coupled land surface-atmospheric boundary layer model. Their VDA approach can obtain the two main parameters of the land surface that control the partitioning of the available energy between turbulent heat fluxes [i.e., neutral bulk heat transfer coefficient (C_{HN}) and evaporative fraction (EF)]. C_{HN} scales the sum of the turbulent heat fluxes ($H+LE$), and EF scales their partitioning ($LE/(LE+H)$). Their VDA model was tested only at the First International Field Experiment (FIFE) site.

The objective of this study is to assess the performance of Tajfar et al. (2019b) VDA approach at five sites (namely, Desert, Audubon, Bondville, Brookings, and Willow Creek) with different hydrological and vegetative conditions. Results of this study are also compared to those of the previous study (Tajfar et al., 2019c) that assimilated the reference-level air temperature and humidity into an atmospheric boundary layer (ABL) model. This paper is organized as follows. Section 5.2 describes the methodology (the heat diffusion equation, the surface energy balance (SEB) equation, the ABL model, and the VDA approach). Section 5.3 presents the study sites and data. Results and discussions are given in Section 5.4. Finally, conclusions are described in Section 5.5.

5.2. Methodology

5.2.1. Heat Diffusion Equation

The one-dimensional heat diffusion equation explains the variation of soil temperature throughout the soil column,

$$c\frac{\partial T(z,t)}{\partial t} = p\frac{\partial^2 T(z,t)}{\partial z^2} \quad (5\text{-}1)$$

where c is the soil volumetric heat capacity (J m^{-3} K^{-1}), p is the soil thermal conductivity (W m^{-1} K^{-1}), and $T(z,t)$ is the soil temperature at depth z and time t. Herein, the ground temperature at the surface, $T(z=0,t)$, is denoted by $T(t)$.

To solve the heat diffusion equation, the boundary conditions at the top and bottom of the soil column should be specified. At the top of the soil column, the boundary condition is found by the land surface forcing,

$$-p\frac{\partial T(0,t)}{\partial z} = G \quad (5\text{-}2)$$

where G is the ground heat flux at the land surface. At the bottom of the soil column, a Neumann boundary condition is used,

$$\frac{\partial T(l,t)}{\partial z} = 0 \quad (5\text{-}3)$$

where l is the depth of the bottom boundary. The soil temperature at the depth of 0.3-0.5 m is almost constant on a daily time-scale (Hu and Islam, 1995). Therefore, l = 0.5 m is used as the depth of the lower boundary condition at which soil temperature changes slightly.

5.2.2. Surface Energy Balance Scheme

The surface energy balance (SEB) equation is described as,

$$R_n = H + LE + G \quad (5\text{-}4)$$

where R_n is the net radiation, and H and LE are the sensible and latent heat fluxes. The sensible heat flux is defined as,

$$H = \rho c_p C_{HN} f(Ri) U(T - T_a) \quad (5\text{-}5)$$

where ρ is the air density, c_p is the specific heat capacity of air, C_{HN} is the neutral bulk heat transfer coefficient, and *f* is the atmospheric stability correction function, which depends on the Richardson number (*Ri*). *U* is the wind speed, and T_a is the reference-level (z_{ref}) air temperature.

The net radiation can be defined as,

$$R_n = (1-\alpha)R_s^{\downarrow} + R_l^{\downarrow} - R_l^{\uparrow} \quad (5\text{-}6)$$

where α is the surface albedo, $R_s^{\downarrow}$ is the incoming solar radiation, $R_l^{\downarrow} = \varepsilon_a \sigma T_a^4$ is the incoming longwave radiation (ε_a is the atmospheric emissivity and can be found in Idso (1981)), $R_l^{\uparrow} = \varepsilon_s \sigma T^4$ is the outgoing longwave radiation (ε_s is the surface emissivity, and σ is the Stefan-Boltzman constant).

As mentioned earlier, *EF* scales the partitioning between the sensible and latent heat fluxes and is given by the ratio of latent heat flux to the sum of turbulent heat fluxes,

$$EF = \frac{LE}{LE+H} \quad (5\text{-}7)$$

EF is nearly constant during the daytime assimilation window [09:00–16:00 LT] in each day (Crago, 1996; Gentine et al., 2007). Equation (5-7) can be re-written as follows,

$$LE = \frac{EF}{1-EF} H \quad (5\text{-}8)$$

5.2.3. Atmospheric Boundary Layer Model

To describe the atmospheric boundary layer components, a mixed-layer model is used (Margulis and Entekhabi, 2001; Garcia and Mellado, 2014; Gentine et al., 2015). As shown in Figure 5.1, the boundary layer is assumed to be convectively mixed, i.e., the profiles of potential temperature (θ) and specific humidity (q) are constant with height. Surface layer (*SL*) is the thin layer of air between the mixed layer and the ground, which is characterized by temperature T_a

and specific humidity q_a (Margulis and Entekhabi, 2001). The components of the idealized ABL model are explained in the following sections.

5.2.4. Mixed Layer Height

The mixed-layer height (h) evolves throughout the day and can be obtained by (Smeda, 1979; Kim and Entekhabi, 1997, 1998a, b; Bagley et al., 2011),

$$\frac{dh}{dt} = \frac{2(G_* - D_1 - D_2)\theta}{gh\delta_\theta} + \frac{H_v}{\rho c_p \delta_\theta} \quad (5\text{-}9a)$$

D_1 and D_2 are calculated by,

$$D_1 = u_{SL} u_*^2 (1 - e^{-\varphi h}) \quad (5\text{-}9b)$$

$$D_2 = 0.4 \left(\frac{gh}{\theta} \frac{H_v}{\rho c_p} \right) \quad (5\text{-}9c)$$

Where δ_θ is potential temperature inversion strength, u_{SL} is the wind speed at the top of the surface layer (see Appendix A), u_* is friction velocity, and φ is the mechanical turbulence dissipation parameter, which is set to 0.01 (Kim and Entekhabi,1998; Margulis and Entekhabi, 2001; Bagley et al., 2011). G_* is the production of mechanical turbulent energy (Kim and Entekhabi, 1998) and is given by,

$$G_* = u_{SL} u_*^2 \quad (5\text{-}9d)$$

The virtual heat flux at the surface (H_v) causes the ABL height growth during the day (Margulis and Entekhabi, 2001), and is calculated via,

$$H_v = H + 0.61\theta c_p E \approx H + 0.07LE \quad (5\text{-}9e)$$

To solve equation (5-9a), initial condition for h is set to 400 m (Tajfar et al., 2019c).

5.2.5. Energy and Moisture Budget Equations

The energy and moisture budget equations for the mixed layer are given by,

$$\rho c_p h \frac{d\theta}{dt} = \left(R_{ad} + R_{gu}\right)\varepsilon_m - R_{Ad} - R_{Au} + H + H_{top} \quad (5\text{-}10a)$$

$$\rho h L_v \frac{dq}{dt} = LE + LE_{top} \quad (5\text{-}10b)$$

where L_v is the latent heat of vaporization, ε_m is the mixed-layer bulk emissivity (Kim and Entekhabi,1998). R_{ad} is the downward longwave radiation from above the mixed layer, and R_{gu} is the upward longwave radiation from the ground into the mixed layer,

$$R_{ad} = \sigma \varepsilon_{ad} T_{h+}^4 \quad (5\text{-}11a)$$

$$R_{gu} = \sigma \varepsilon_s T^4 \quad (5\text{-}11b)$$

where T_{h+} is the air temperature exactly above the mixed-layer height, and ε_{ad} is the effective emissivity above the mixed layer (Kim and Entekhabi, 1998).

R_{Ad} and R_{Au} are upward and downward longwave radiative fluxes within the ABL, respectively,

$$R_{Ad} = \sigma \varepsilon_d \theta^4 \quad (5\text{-}12a)$$

$$R_{Au} = \sigma \varepsilon_u \theta^4 \quad (5\text{-}12b)$$

where ε_d is the effective mixed-layer downward emissivity, and ε_u is the effective upward emissivity (Kim and Entekhabi, 1998).

The entrainment fluxes of heat and moisture (H_{top} and LE_{top}) from free atmosphere enter the ABL and are given by,

$$H_{top} = AH \quad (5\text{-}13a)$$

$$LE_{top} = \rho L_v \delta_q \frac{dh}{dt} \quad (5\text{-}13b)$$

The value of *A* is set to 0.2 (Gentine et al., 2015; Garcia and Mellado, 2015).

5.2.6. Inversion Strengths of θ and q

As can be seen in Figure 5.1, instantaneous jumps in potential temperature (δ_θ) and specific humidity (δ_q) are seen at the top of the mixed layer, which can be obtained by,

$$\frac{d\delta_\theta}{dt} = \gamma_\theta \frac{dh}{dt} - \frac{d\theta}{dt} \quad (5\text{-}14a)$$

$$\frac{d\delta_q}{dt} = \gamma_q \frac{dh}{dt} - \frac{dq}{dt} \quad (5\text{-}14b)$$

where γ_θ and γ_q are the lapse rates in potential temperature and specific humidity above the mixed layer.

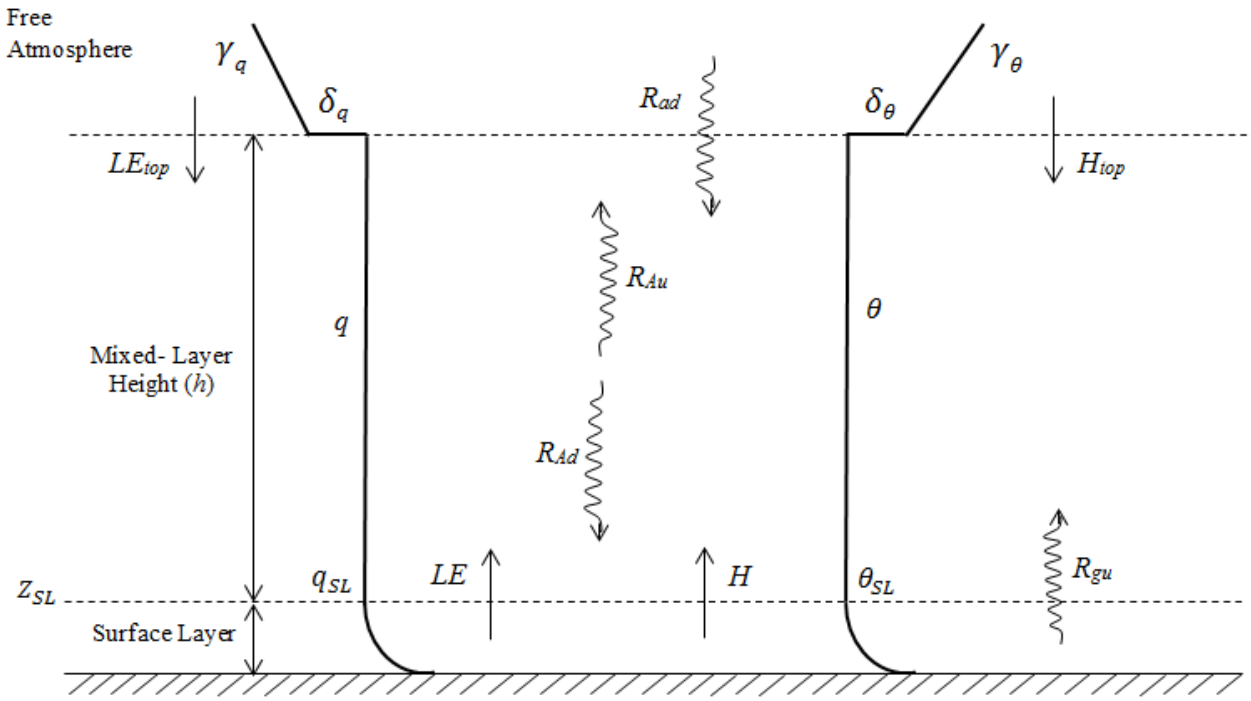

Figure 5. 1. Idealized profiles of ABL states (θ and q) and corresponding fluxes between the surface layer, mixed layer, and overlying atmosphere.

5.2.7. Variational Data Assimilation (VDA) Scheme

The objective function (J) is defined as,

$$J(T, \theta, q, \lambda_1, \lambda_2, \lambda_3, R, EF\ ) =$$

$$\sum_{i=1}^{N}\int_{t_o}^{t_1}[T_i(t)-T_{obs,i}(t)]^T R_T^{-1}[T_i(t)-T_{obs,i}(t)]\,dt+\sum_{i=1}^{N}\int_{t_o}^{t_1}[\theta_i(t)-\theta_{SL,i}(t)]^T R_\theta^{-1}[\theta_i(t)-\theta_{SL,i}(t)]\,dt+\sum_{i=1}^{N}\int_{t_o}^{t_1}[q_i(t)-q_{SL,i}(t)]^T R_q^{-1}\big[q_i(t)-q_{SL,i}(t)\big]dt+(R-R')^T B_R^{-1}(R-R')+\sum_{i=1}^{N}(EF_i-EF_i')^T B_{EF}^{-1}(EF_i-EF_i')+\sum_{i=1}^{N}\int_{t_o}^{t_1}\lambda_{1i}(t)\left[\rho c_p h_i(t)\frac{d\theta_i(t)}{dt}-\big(R_{ad}+R_{gu}\big)\varepsilon_m+R_{Ad}+R_{Au}-H-H_{top}\right]dt+\sum_{i=1}^{N}\int_{t_o}^{t_1}\lambda_{2i}(t)\left[\rho h_i(t)L_v\frac{dq_i(t)}{dt}-LE-LE_{top}\right]dt+\sum_{i=1}^{N}\int_{t_o}^{t_1}\int_0^l\lambda_{3i}\left(\frac{\partial T_i}{\partial t}-D\frac{\partial^2 T_i}{\partial z^2}\right)dzdt \quad (5\text{-}15)$$

The first term on the right hand side of the objective function is the square of misfit between the LST estimates from the heat diffusion equation (T) and its corresponding measurements (T_{obs}) over the assimilation period. The second and third terms are the square of misfit between the top of the surface layer potential temperature (θ_{SL}) and specific humidity (q_{SL}), and the corresponding estimates (i.e., θ and q) from equations (5-10a) and (5-10b). R_T^{-1}, R_θ^{-1} and R_q^{-1} are the inverse error covariance matrices of T, θ and q, respectively. The fourth and fifth terms represent the square errors of the unknown parameters (i.e., *R* and *EF*) with respect to their prior values (R' and EF'). B_R^{-1} and B_{EF}^{-1} are the inverse background error covariance matrices of R and EF, respectively. The last three terms are physical constraints, which are adjoined to the model by the Lagrange multipliers λ_1, λ_2 and λ_3. Following Tajfar et al. (2019b), R_T^{-1}, R_θ^{-1}, R_q^{-1}, B_R^{-1} and B_{EF}^{-1} are set to 10^{-1} K^{-2}, 10^{-1} K^{-2}, 10^5, 10^9, and 10^8, respectively.

To obtain the optimal values of *R* and *EF*, the objective function (*J*) is minimized. To do so, the first variation of *J* (δJ) with respect to the independent variables θ, q, T, λ_1, λ_2, λ_3, R and EF are set to zero. This leads to eight equations (the so-called Euler-Lagrange equations, see the Appendix D), which are solved simultaneously to obtain the optimal values of *R* and *EF*.

5.3. Study Sites

The VDA approach is evaluated at five sites (namely, Desert, Audubon, Bondville, Brookings, and Willow Creek) with a wide range of vegetative and soil moisture conditions. The characteristics of these sites are listed in Table 5.1. Audubon, Bondville, Brookings, and Willow Creek are located in the US (http://ameriflux.ornl.gov/) (see Figure 5.2). Desert (in northwestern China) is located in the middle reach of Heihe River basin (HRB) (http://card.westgis.ac.cn/) (see Figure 5.3). The study sites have four land cover types: cropland, grassland, barren land, and forest. The vegetation cover ranges from dense forest in Willow Creek (LAI = 5.67) to barren land in Desert (LAI = 0.00). The soil moisture (SM) varies from 0.03 in Desert to 0.29 in Brookings. The wide range of SM and LAI values enable us to evaluate the performance of VDA approach under different hydrological and vegetative conditions. Willow Creek (in Wisconsin) is a deciduous broad-leaf forest with dense vegetation cover and heavy precipitation events. Brookings (in South Dakota) is a grassland with temperate continental climate and no dry season. Bondville (in Illinois) is a cropland that has a humid continental climate. Audubon (in Arizona) is a grassland water-limited monsoonal site with a temperate arid climate. Desert is barren dry soil.

The soil volumetric heat capacity (C) and thermal conductivity (P) depend on soil moisture and soil texture (Chen, 2008; Xu et al., 2018). The C and P values for each site are shown in Table 5.1. For the Audubon, Bondville, Brookings, and Willow Creek sites in USA, the half-hourly micrometeorological data (e.g., air temperature and specific humidity, wind speed, atmospheric pressure, and incoming shortwave radiation) are available on the AmeriFlux archive (http://www.ameriflux.lbl.gov). For Desert site in China, the Multiscale Observation Experiment on Evapotranspiration over the Heihe Watershed Allied Telemetry Experimental Research (HiWATER-MUSOEXE) project provides half-hourly measurements of micrometeorological

data (wind speed, air temperature, relative humidity, and pressure as well as incoming shortwave radiation) (Li et al. 2013; Xu et al. 2013; Liu et al. 2016). In all the study sites, the sensible and latent heat fluxes are measured by the eddy covariance (EC) flux tower stations. The LAI data are obtained from the Global Land Surface Satellites LAI product, GLASS (http://glass-product.bnu.edu.cn/) (Liang et al., 2013; Xiao et al., 2014).

The initial conditions for θ, q, δ_θ, and δ_q, and the magnitudes of γ_θ and γ_q are required to solve equations (5-10a), (5-10b), (5-14a), and (5-14b). For more details, the readers are referred to Tajfar et al. (2019c).

The VDA is tested at the Desert (DOYs 170-259, 2015), Audubon (DOYs 170-259, 2006), Bonville (DOYs 182-271, 2005), Brookings (DOYs 176-265, 2009), and Willow Creek (DOYs 170-259, 2005). These years and DOYs are selected because they have a minimum data gap.

Table 5. 1. Characteristics of the study.

Site	Latitude	Longitude	Vegetation type	SM ($m^3\ m^{-3}$)	LAI ($m^2\ m^{-2}$)	Elevation (m)	C ($J\ m^{-3}\ K^{-1}$)	P ($J\ m^{-1}\ K^{-1}\ s^{-1}$)
Willow Creek	45.8059 ^{o}N	90.0799 ^{o}W	Forest	0.22	5.67	520	2.56×10^{6}	1.70
Brookings	44.3453 ^{o}N	96.8362 ^{o}W	Grassland	0.29	1.72	510	3.20×10^{6}	0.99
Bondville	40.0062 ^{o}N	88.2904 ^{o}W	Cropland	0.16	2.24	219	2.76×10^{6}	0.61
Audubon	31.5907 ^{o}N	110.5092 ^{o}W	Grassland	0.11	0.54	1469	1.83×10^{6}	1.45
Desert	42.1100 ^{o}N	100. 9900 ^{o}E	Barren land	0.03	0	1000	1.52×10^{6}	1.27

Figure 5. 2. Locations of the four Ameriflux study sites (i.e., Audubon, Brookings, Bondville and Willow Creek) in the United States.

Figure 5. 3. Location of the Desert site in China.

5.4. Results

As mentioned earlier, C_{HN} is one of the two key unknowns of the VDA system that scales the sum of turbulent heat fluxes. C_{HN} changes with vegetation phenology on a monthly basis (Caparrini et al., 2004a, b; Bateni et al., 2013b; Xu et al., 2018; Abdolghafoorian et al., 2017). The estimated C_{HN} values from the VDA approach and corresponding LAI values at the five experimental sites are presented in Table 5.2. As shown, the changes in C_{HN} estimates are consistent with those of LAI in all the study sites (both wet/densely vegetated and dry/sparsely vegetated sites). For example, at the Willow Creek site, C_{HN} decreases marginally during the modeling period, which follows the variation in LAI values. At the Brookings site, C_{HN} and LAI have their peak values in the second monthly modeling period, and decrease in the third period. At the Bondville site, LAI and C_{HN} estimates remain almost constant in the three modeling periods. At the Audubon site, C_{HN} estimates increase continuously over the monthly periods. The same pattern can be seen in the LAI values. LAI is constant at Desert (LAI = 0), but minor variations in the C_{HN} estimates can be seen. These slight changes in C_{HN} estimates are due to the changes in friction velocity, solar elevation and wind speed (Bateni et al., 2013b; He et al., 2018). Overall, the C_{HN} estimates increase with the growth of LAI. For example, Willow Creek has the largest C_{HN} estimates because of its dense vegetation cover (LAI = 5.67) and Desert has the smallest C_{HN} estimates because it has no vegetation (LAI = 0). In general, the results show that the VDA can extract the implicit information contained in the air temperature and specific humidity, and land surface temperature to estimate C_{HN} although no information on vegetation density is used in the VDA approach.

Table 5. 2. Estimated neutral bulk heat transfer coefficient (CHN) values by the VDA model at the five study sites.

Site	DOY	C_{HN}	LAI
Willow Creek	170-199	0.0295	5.87
	200-229	0.0291	5.84
	230-259	0.0277	5.29
Brookings	176 – 206	0.0057	1.93
	207 – 237	0.0109	2.15
	238 – 265	0.0052	1.07
Bondville	182-211	0.0149	2.23
	212-241	0.0153	2.24
	242-271	0.0151	2.24
Audubon	170-199	0.0035	0.27
	200-229	0.0038	0.57
	230-259	0.0044	0.77
Desert	170-199	0.0025	0
	200-229	0.0022	0
	230-259	0.0027	0

EF is the second unknown parameter of the VDA system that scales the partitioning between the turbulent heat fluxes. Time series of *EF* estimates from VDA approach as well as *EF* values from measured *H* and *LE* (open circles) at the five study sites are shown in Figure 5.4. As illustrated, the magnitude and day-to-day variations of *EF* estimates from the VDA approach

agree well with the observations at both wet and/or densely vegetated sites (e.g., Willow Creek) and dry and/or sparsely vegetated sites (e.g., Desert and Audubon). This indicates that the VDA system can take advantage of the implicit information in the sequences of land surface temperature (LST), reference-level air temperature (T_a), and specific humidity (q_a) to estimate the signature of relative partitioning of available energy between the sensible and latent heat fluxes. At wet/densely vegetated sites (e.g., Desert and Audubon), evapotranspiration is mostly controlled by the atmospheric state variables (i.e., air temperature and specific humidity). Hence, there is a stronger coupling between *EF* and the atmospheric state variables (rather than LST), and more accurate *EF* estimates are obtained by assimilating sequences of air temperature and specific humidity observations (Bateni and Entekhabi, 2012b; Bateni et al., 2013b; Tajfar et al., 2019b). Also, at wet/densely vegetated sites, assimilation of LST in addition to q_a and T_a results in a slight improvement in the *EF* estimates.

In contrast, at dry/slightly vegetated sites, assimilation of reference-level air temperature and humidity generates relatively poor *EF* estimates (Tajfar et al., 2019c). However, at these sites, assimilation of LST in addition to q_a and T_a significantly improves the *EF* estimates. These results illustrate that both the state variables of the land surface (i.e., LST) and atmosphere (i.e., air temperature and humidity) control *EF*, and consequently the synergic assimilation of reference-level air temperature, specific humidity, and LST yields accurate *EF* estimates over a wide variety of environmental conditions.

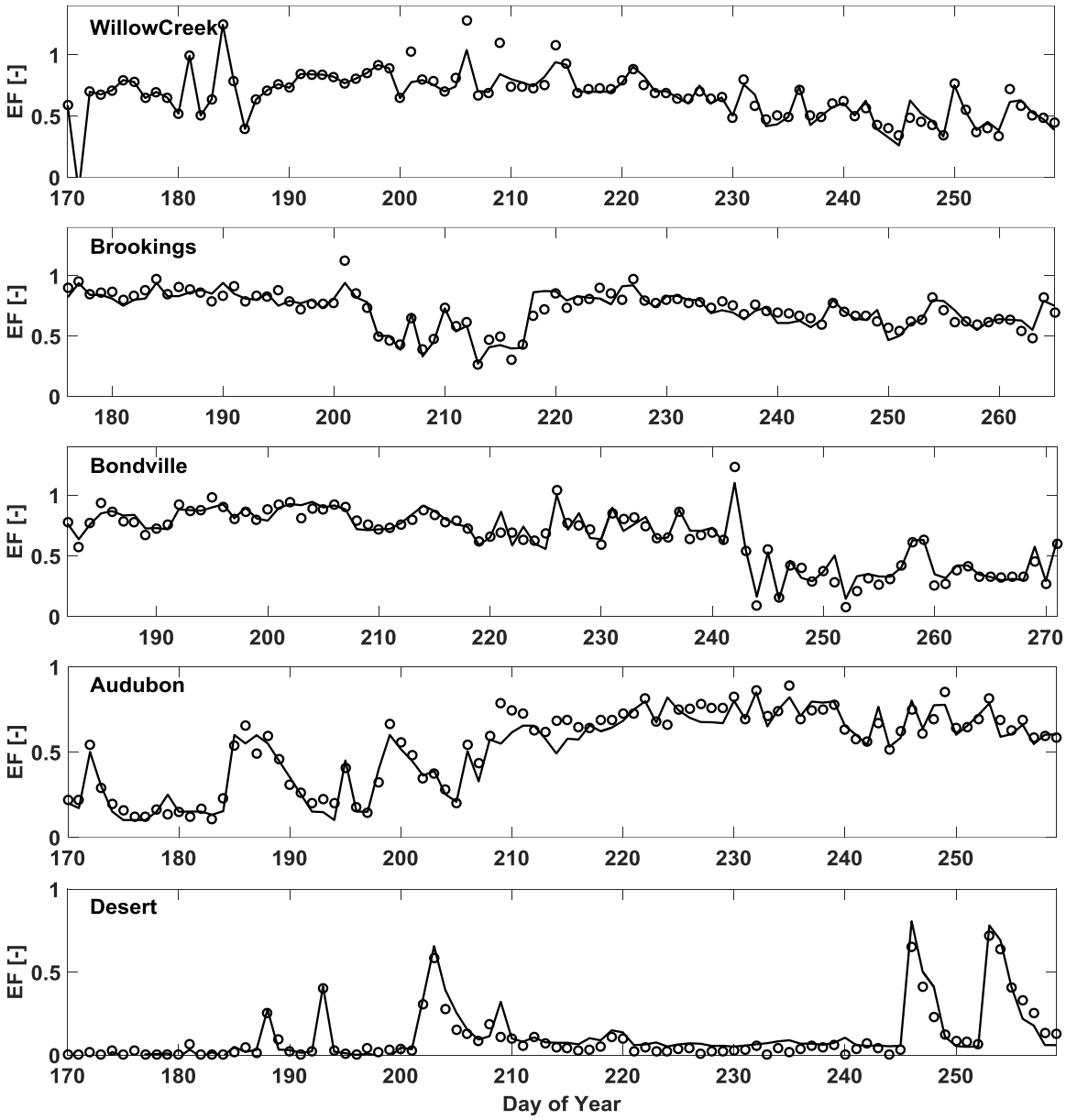

Figure 5. 4. Time series of evaporative fraction (*EF*) observations (open circles) and estimates from VDA model (solid lines) at the five study sites.

Figures 5.5 and 5.6 show the scatterplot of half-hourly *H* and *LE* estimates from the VDA approach versus observations at the five study sites. The *H* and *LE* estimates are in good consistency with the observations and mainly fall around the 45-degree line at the five study

sites. This shows that the combined information content of the atmospheric state variables (i.e., air temperature and specific humidity) and land surface state variable (i.e., LST) allows the VDA approach to partition the available energy between *H* and *LE* well at all the study sites with contrasting vegetative and hydrological conditions.

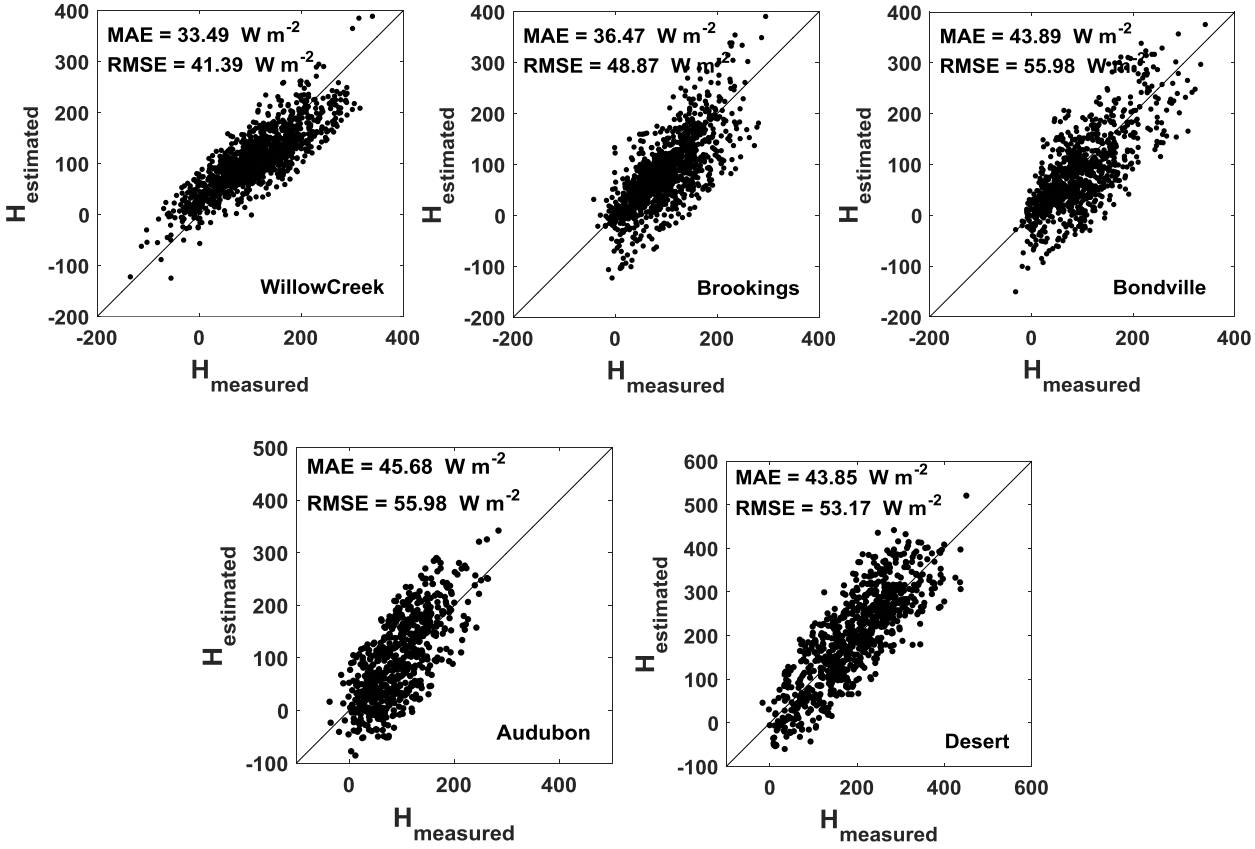

Figure 5. 5. Scatterplot of half-hourly modeled sensible heat flux (*H*) versus corresponding observations at the five experimental sites.

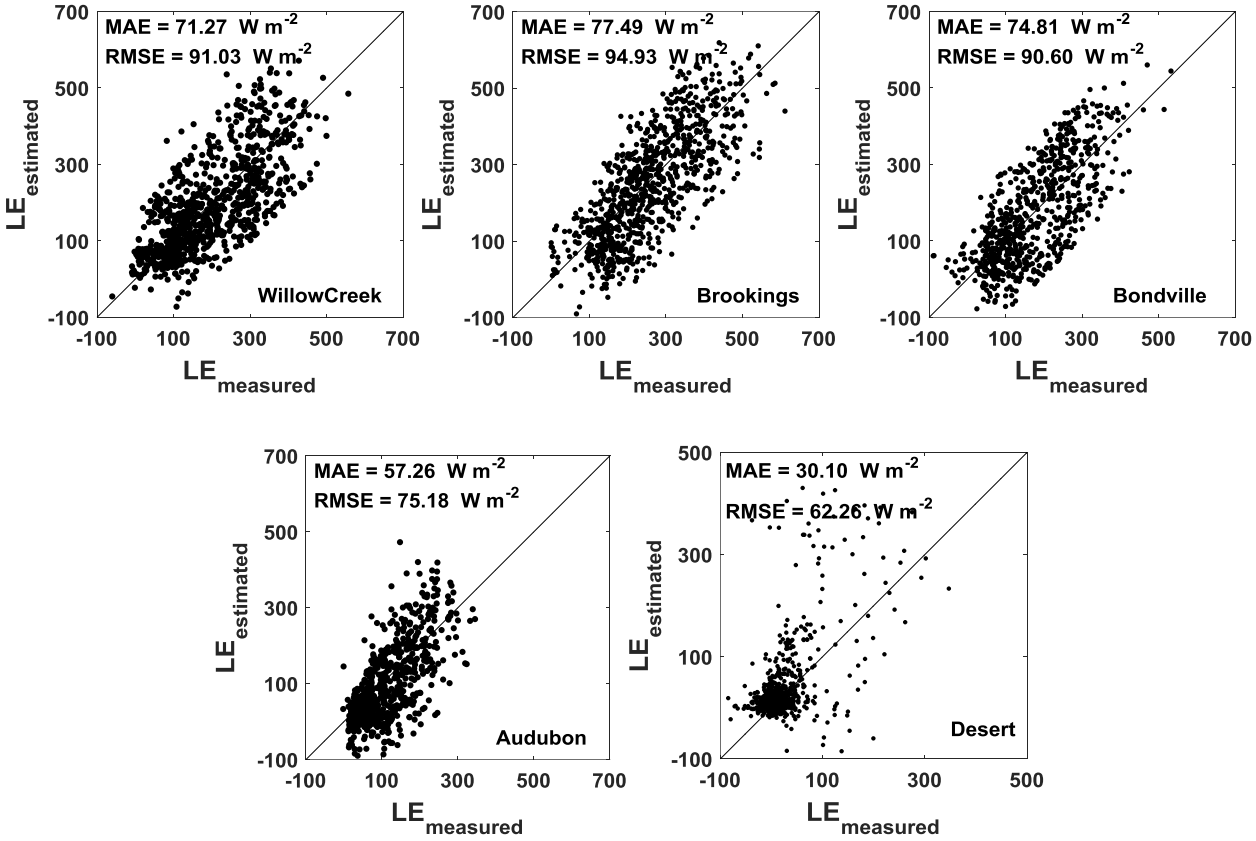

Figure 5. 6. Scatterplot of half-hourly modeled latent heat flux (*LE*) versus corresponding observations at the five experimental sites.

Figures 5.7 and 5.8 show the time series of daily *H* and *LE* estimates and the corresponding measurements at the Desert, Audubon, Bondville, Brookings, and Willow Creek sites. At all the sites, the VDA *H* and *LE* estimates can capture the magnitude and day-to-day oscillations of the *H* and *LE* observations. Unlike the Tajfar et al. (2019c), VDA approach that generates more accurate turbulent heat fluxes at wet/densely vegetated sites and its performance weakens in dry/sparsely vegetated sites, the estimated *H* and *LE* from this VDA approach agree with the observations in both wet/densely vegetated sites (e.g., Willow Creek) and dry/sparsely vegetated sites (e.g., Desert). This indicates that the synergistic assimilating of LST, and air

temperature and specific humidity provide information for partitioning of the available energy between the turbulent heat fluxes at different vegetative and climatic conditions.

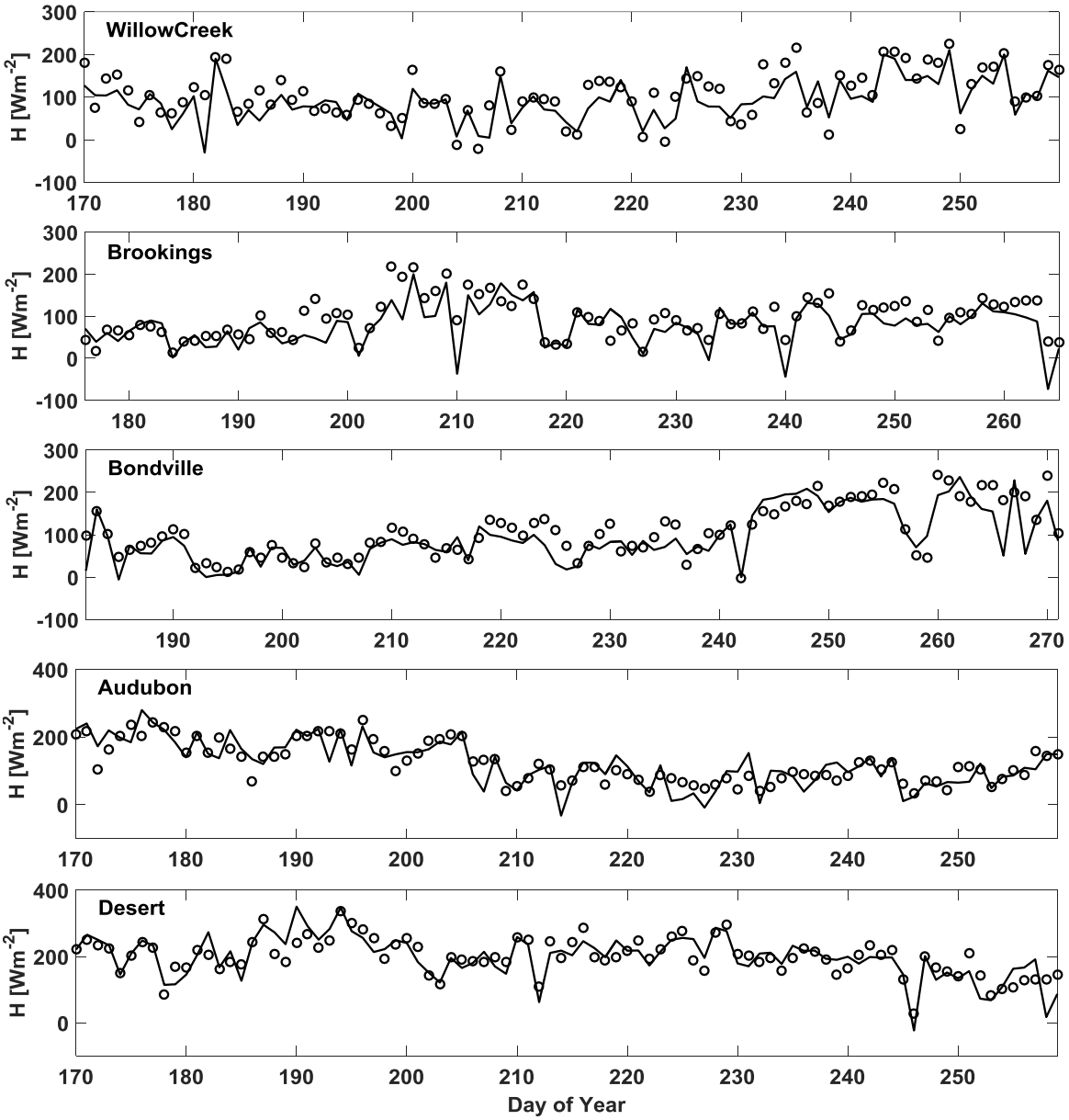

Figure 5. 7. Time series of sensible heat flux (*H*) observations (open circles) and estimates from VDA model (solid lines) at the five experimental sites.

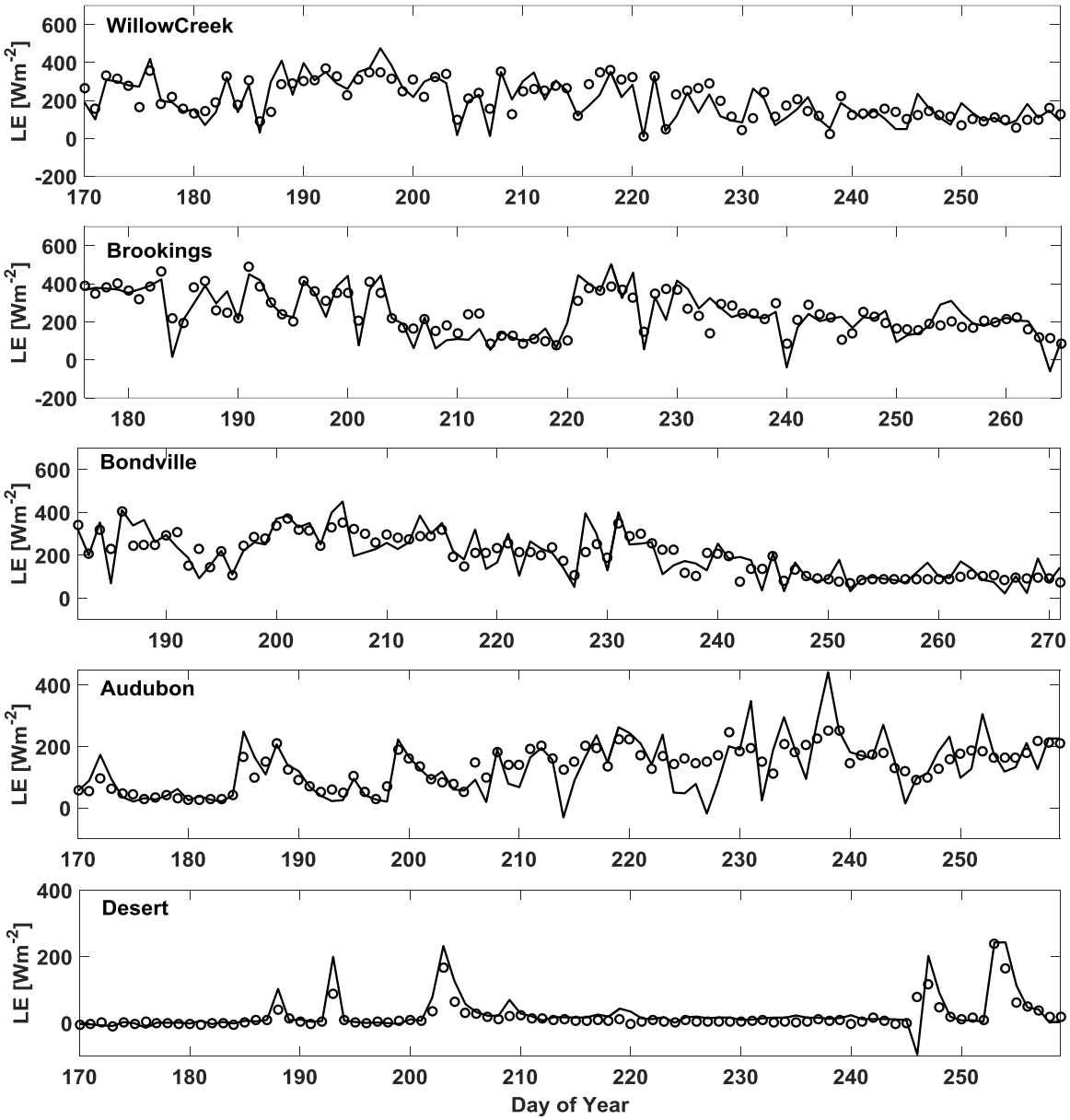

Figure 5. 8. Time series of latent heat flux (*LE*) observations (open circles) and estimates from VDA model (solid lines) at the five experimental sites.

The MAE and RMSE of half-hourly and daily sensible and latent heat fluxes estimates from this study are compared with those of Tajfar et al. (2019c) in Table 5.3 and 5.4. The highest reduction in MAE and RSME values is attributed to dry/slightly vegetated sites (e.g., Desert and Audubon). The wet/densely vegetated sites (e.g., Willow Creek) have the lowest decrease in

MAE and RMSE values. At sites with wetter land and denser vegetation cover, the drying rate is mainly controlled by atmospheric properties (e.g., T_a, and q_a) rather than land surface conditions (e.g., LST) (Shokri et al., 2008a, b; Abdolghafoorian et al., 2017). Thus, *EF* has a stronger coupling with atmospheric state variables. Therefore, estimating turbulent heat fluxes from T_a and q_a yields accurate results, and assimilating LST slightly improves the *H* and *LE* estimations (e.g., Willow Creek and Brookings). On the other hand, at sites with drier land and sparser vegetation cover, the coupling between *EF* and LST is strong. Hence, the VDA approach that assimilates T_a and q_a generates less accurate *H* and *LE* estimates. However, by assimilating LST measurements in the VDA approach, the turbulent heat fluxes improve significantly (e.g., Desert and Audubon). For half-hourly *H* estimates, the five-site average RMSE (MAE) from this study and Tajfar et al. (2019c) are 51.08 W m^{-2} (40.68 W m^{-2}) and 63.44 W m^{-2} (48.51 W m^{-2}), respectively. Corresponding RMSE (MAE) values for half-hourly *LE* estimates are 82.80 W m^{-2} (62.19 W m^{-2}) and 107.42 W m^{-2} (80.66 W m^{-2}). As a result, this study reduces the RMSE (MAE) of half-hourly *H* and *LE* estimates over the five sites on average by 19.5% (16.1%) and 22.9% (22.9%), respectively. Similarly, this study also decreases the RMSE (MAE) of daytime-average *H* and *LE* estimates over the five sites on average by 28.2% (26.5%) and 32.7% (34.0%), respectively. The improved half-hourly and daily *H* and *LE* estimates show the benefit of the synergistic assimilation of LST, T_a, and q_a.

Table 5. 3. Comparing the half-hourly H and LE estimates from this study (that assimilates LST, qa and Ta) (top panel) with those of Tajfar et al. (2019c) (that assimilates qa and Ta) (bottom panel) for the five study sites.

Site	*H* (W m^{-2})		*LE* (W m^{-2})	
	MAE	RMSE	MAE	RMSE
Willow Creek	33.49 (5.7%)	41.39 (7.0%)	71.27 (5.3%)	91.03 (6.5%)
Brookings	36.47 (10.1%)	48.87 (10.3%)	77.49 (6.9%)	94.93 (8.7%)
Bondville	43.89 (5.1%)	55.98 (11.9%)	74.81 (12.1%)	90.60 (14.4%)
Audubon	45.68 (23.3%)	55.98 (24.8%)	57.26 (34.2%)	75.18 (33.3%)
Desert	43.85 (27.7%)	53.17 (33.7%)	30.10 (58.6%)	62.26 (46.9%)
Five-site-average	**40.68 (16.1%)**	**51.08 (19.5%)**	**62.19 (22.9%)**	**82.80 (22.9%)**
Willow Creek	35.52	44.52	75.29	97.31
Brookings	40.57	54.48	83.21	104.03
Bondville	46.25	63.56	85.13	105.82
Audubon	59.54	74.45	86.96	112.64
Desert	60.67	80.19	72.73	117.31
Five-site-average	**48.51**	**63.44**	**80.66**	**107.42**

Table 5. 4. Comparing the daily H and LE estimates from this study (that assimilates LST, qa and Ta) (top panel) with those of Tajfar et al. (2019c) (that assimilates qa and Ta) (bottom panel) for the five study sites.

Site	*H* (W m^{-2})		*LE* (W m^{-2})	
	MAE	RMSE	MAE	RMSE
Willow Creek	28.51 (5.1%)	35.82 (3.3%)	49.33 (13.4%)	63.52 (14.7%)
Brookings	27.05 (15.6%)	37.43 (16.8%)	50.25 (13.0%)	71.59 (13.0%)
Bondville	26.06 (18.5%)	35.87 (20.7%)	46.77 (15.5%)	60.88 (21.8%)
Audubon	27.90 (39.6%)	35.98 (38.1%)	42.83 (40.3%)	60.33 (32.6%)
Desert	27.17 (45.7%)	35.13 (41.5%)	15.89 (76.9%)	30.76 (69.9%)
Five-site-average	**27.34 (28.2%)**	**36.05 (26.5%)**	**41.01 (34.0%)**	**57.42 (32.7%)**
Willow Creek	30.05	37.03	56.93	74.46
Brookings	32.05	45.01	57.79	82.28
Bondville	31.97	45.21	55.34	77.88
Audubon	46.16	58.13	71.77	89.57
Desert	50.08	60.00	68.74	102.21
Five-site-average	**38.06**	**49.08**	**62.11**	**85.28**

The VDA approach retrieves the optimum values of C_{HN} and EF by minimizing the difference between the LST estimates from equation (5.1) (T) and observations (T_{obs}), as well as the misfit between the estimated potential temperature and specific humidity from equations (5.10a) and (5.10b) (i.e., θ and q) and the corresponding values (i.e., θ_{SL} and q_{SL}) obtained from the measured reference-level air temperature and specific humidity via the MOST (see Appendix A). Figure 5.9, 5.10 and 5.11 show the half-hourly estimated θ, q and T versus θ_{SL}, q_{SL}, and T_{obs} at the five sites. As indicated, the half-hourly θ, q and T estimates are in good agreement with θ_{SL}, q_{SL}, and T_{obs}, and scatterplots mainly fall around the 1:1 line. This indicates that the VDA approach is able to efficiently update the two key unknown parameters of the VDA approach (C_{HN} and EF).

The MAE and RMSE of half-hourly θ, q, and T estimates at the five experimental sites are shown in Table 5.5. For comparison, the MAE and RMSE of half-hourly θ and q estimates from Tajfar et al. (2019c) are also presented in Table 5.6. The five-site mean RMSE (MAE) of half-hourly θ, q and T estimates from this study are 1.36 K (1.08 K) , 0.0011 kg kg^{-1} (0.0009 kg kg^{-1}), and 1.36 K (0.99), respectively. The five-site average RMSE (MAE) of half-hourly θ and q estimates from Tajfar et al. (2019c) are reduced by 28.0% (26.0%) and 19.7% (15.4%), respectively. These results show that the VDA approach can provide more accurate C_{HN} and EF estimates by minimizing the misfits between T and T_{obs}, θ and θ_{SL}, and q and q_{SL}.

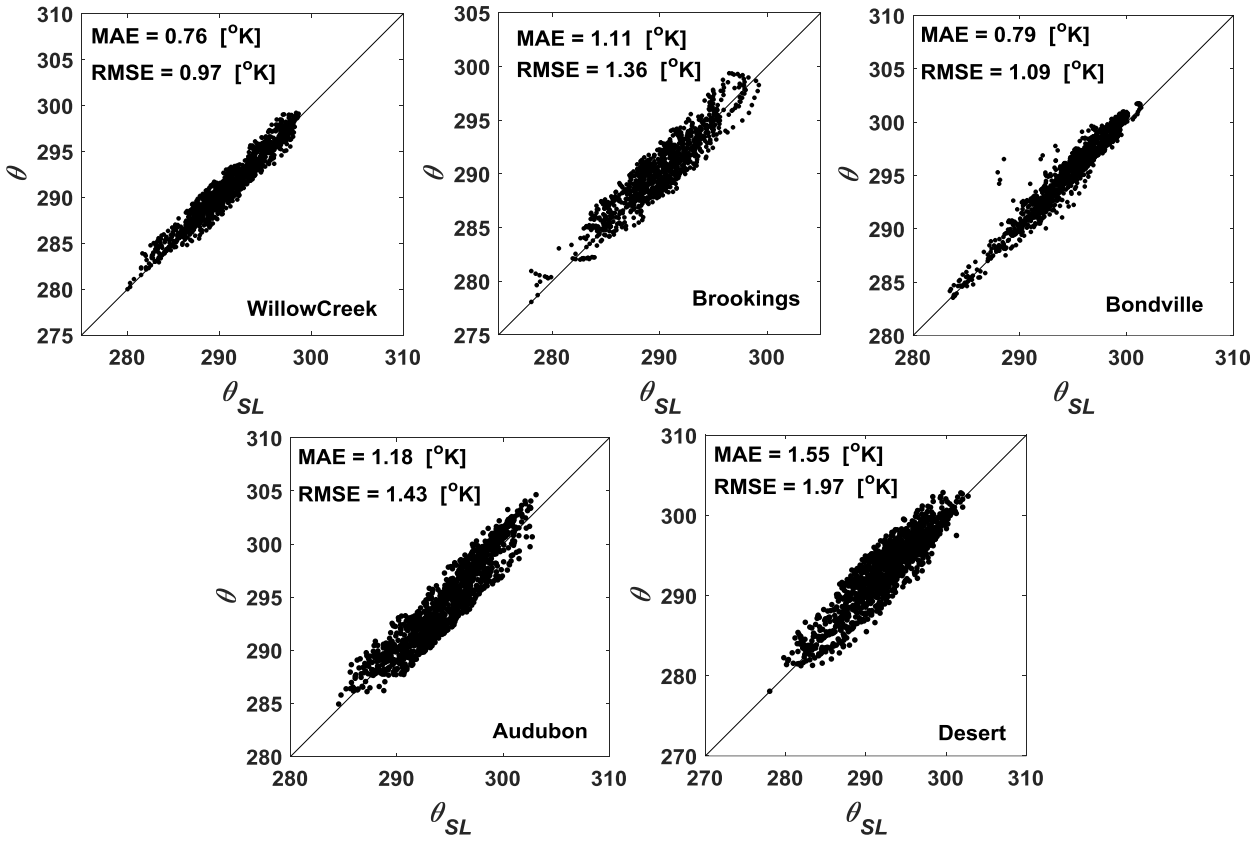

Figure 5. 9. Scatterplot of half-hourly modeled potential temperature (θ) versus corresponding observations at the five experimental sites.

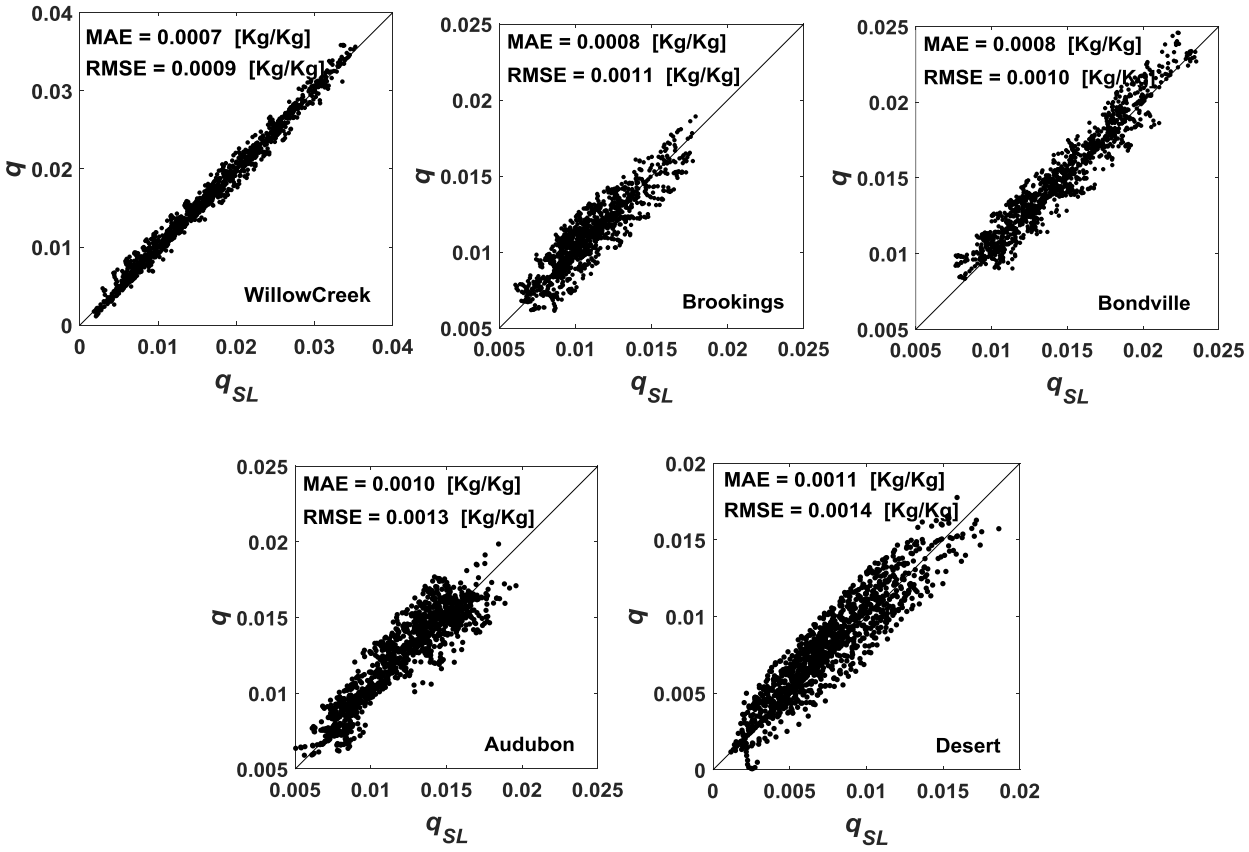

Figure 5. 10. Scatterplot of half-hourly modeled specific humidity (q) versus corresponding observations at the five experimental sites.

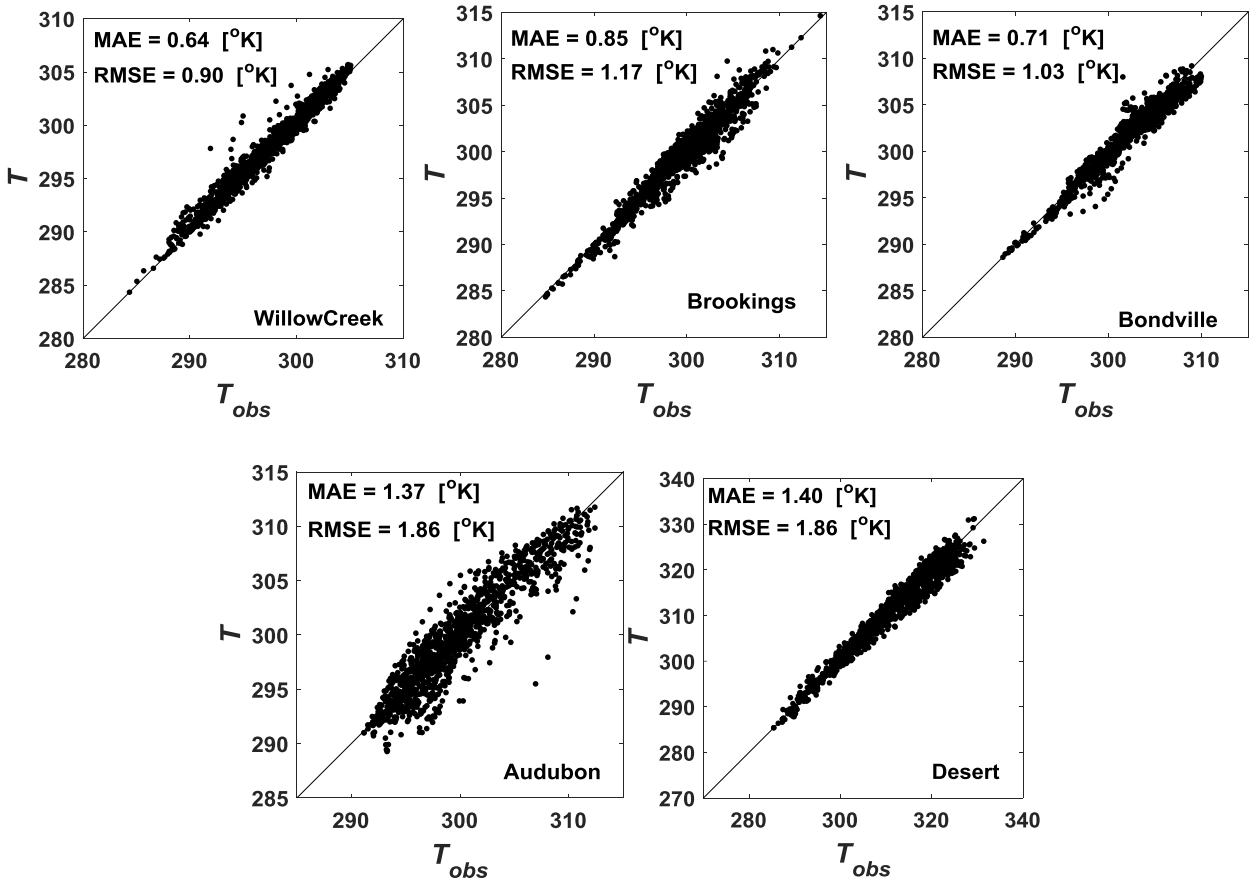

Figure 5. 11. Scatterplot of half-hourly modeled land surface temperature (*T*) versus corresponding observations at the five experimental sites.

Table 5. 5. MAE and RMSE of half-hourly θ, q and T estimates at the five experimental sites.

Site	θ (K)		q (kg kg^{-1})		T (K)	
	MAE	RMSE	MAE	RMSE	MAE	RMSE
Willow Creek	0.76	0.97	0.0007	0.0009	0.64	0.90
Brookings	1.11	1.36	0.0008	0.0011	0.85	1.17
Bondville	0.79	1.09	0.0008	0.0010	0.71	1.03
Audubon	1.18	1.43	0.0010	0.0013	1.37	1.86
Desert	1.55	1.97	0.0011	0.0014	1.40	1.86
Five-site-average	**1.08 (26%)**	**1.36 (28%)**	**0.0009 (15.4%)**	**0.0011 (19.7%)**	**0.99**	**1.36**

Table 5. 6. MAE and RMSE of half-hourly θ and q estimates from Tajfar et al. (2019c) at the five experimental sites.

Site	θ (K)		q (kg kg^{-1})	
	MAE	RMSE	MAE	RMSE
Willow Creek	0.78	1.04	0.0008	0.0011
Brookings	1.47	1.99	0.0009	0.0012
Bondville	0.98	1.36	0.0009	0.0012
Audubon	2.02	2.52	0.0010	0.0015
Desert	2.04	2.56	0.0016	0.0021
Five-site-average	**1.46**	**1.89**	**0.0010**	**0.0014**

The mean diurnal cycles of measured and estimated *H* and *LE* over the modelling period from this study and Tajfar et al. (2019c) for the five study sites are shown in Figure 5.12. As anticipated, the magnitude and phase of the diurnal cycles of retrieved sensible and latent heat fluxes from this study agree well with the observations at all the experimental sites. At Desert and Audubon sites, Tajfar et al. (2019c) shows a large discrepancy between the diurnal cycles of estimated and observed *H* and *LE*. Assimilating LST measurements into the heat diffusion equation in this study improves the diurnal cycle of estimated turbulent heat fluxes, especially at dry and/or sparsely vegetated sites (e.g., Desert and Audubon). As indicated, there is a slight improvement in the diurnal cycles of *H* and *LE* estimates at wet and/or densely vegetated sites (e.g., Willow Creek), implying that the air temperature and humidity have a significant amount of information for partitioning the available energy between the turbulent heat fluxes at wet/densely vegetated sites (e.g., Willow Creek), and adding the information of LST measurements into the model results in an insignificant improvement.

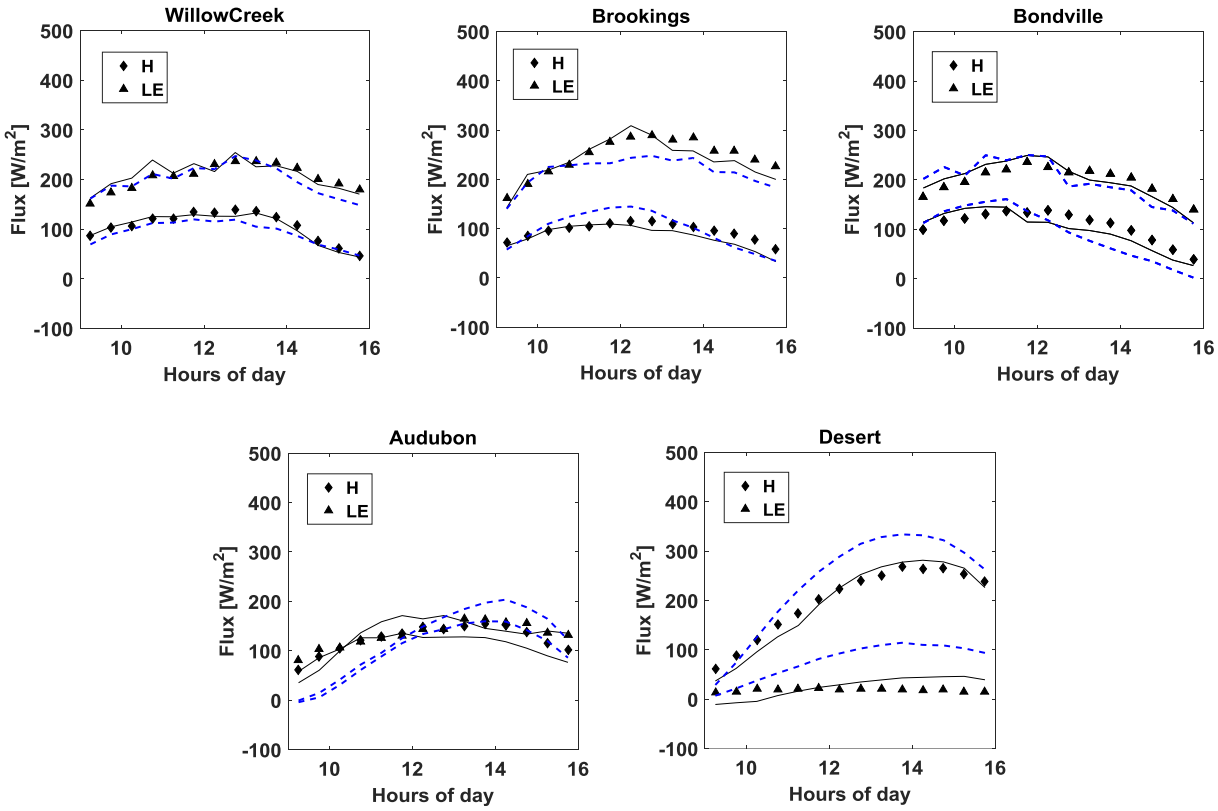

Figure 5. 12. Mean diurnal cycle of turbulent heat fluxes for the five study sites. Measured fluxes (symbols), this study (solid lines) and Tajfar et al. (2019c) (blue lines).

5.5. Conclusion

The information content of LST, and air temperature and humidity for partitioning the available energy between the sensible and latent heat fluxes is evaluated at five sites, namely Desert, Audubon, Bondville, Brookings, and Willow Creek. The VDA approach exploits the information in the sequences of land surface temperature (as the state variable of land surface), and reference-level air temperature and specific humidity (as the state variables of the atmosphere) to estimate turbulent heat fluxes. The main unknown parameters of the VDA are evaporative fraction (*EF*) and neutral bulk heat transfer coefficient (C_{HN}). The variations in C_{HN} estimates are consistent with those of leaf area index (LAI) in all the five study sites. In general,

densely vegetated sites (with larger LAI values) have higher C_{HN} estimates (e.g., Willow Creek), and sparsely vegetated sites (smaller LAI values) have lower C_{HN} estimates (e.g., Desert and Audubon). The *EF* estimates can capture the daily fluctuations in the observations in each site. The results indicate that the assimilation of LST along with reference-level air temperature and specific humidity improves the performance of the VDA scheme, especially at dry and/or sparsely vegetated sites (e.g., Desert and Audubon). The five-site average RMSEs of half-hourly sensible and latent heat flux estimates are 51.08 W m^{-2} and 82.05 W m^{-2}, respectively, which are 19.5% and 23.6% lower than those of Tajfar et al. (2019c). Time series of daytime-average *H* and *LE* estimates from this study agree well with the observations both in terms of magnitude and day-to-day fluctuations. The RMSE of daily sensible (latent) heat flux estimates at the Desert, Audubon, Bondville, Brookings, and Willow Creek sites are 35.13 W m^{-2} (30.76 W m^{-2}), 35.98 W m^{-2} (60.33 W m^{-2}), 35.87 W m^{-2} (60.88 W m^{-2}), 37.43 Wm^{-2} (71.59 W m^{-2}), and 35.82 W m^{-2} (63.52 W m^{-2}), respectively. Compared to Tajfar et al. (2019c) (that assimilated only reference-level air temperature and specific humidity), the RMSE of daily sensible (latent) heat flux estimates at Desert, Audubon, Bondville, Brookings, and Willow Creek sites are decreased by 41.5% (69.9%), 38.1% (32.6%), 20.7% (21.8%), 16.8% (13.0%), and 3.3% (14.7%), respectively. The improvement in *H* and *LE* estimates increases by the reduction in soil moisture (SM) and/or LAI (e.g., Desert and Audubon). This is due to the fact that at dry and/or sparsely vegetated sites evapotranspiration is mainly controlled by the land surface state variable (i.e., LST) rather than the atmospheric state variables (i.e., reference-level air temperature and specific humidity). Therefore, the coupling between *EF* and LST is strong and assimilating LST into the VDA model adds more information for partitioning the available energy between turbulent heat fluxes. As the reference-level air temperature and specific humidity contain significant amount

of information for partitioning the available energy between *H* and *LE* at wet/densely vegetated sites (e.g., Willow Creek), adding the information content of LST measurements slightly improves the *H* and *LE* estimates. The RMSEs of estimated ABL q (θ) at the Desert, Audubon, Bondville, Brookings, and Willow Creek sites are 0.0014 Kg Kg^{-1} (1.97 K), 0.0013 Kg Kg^{-1} (1.43 K), 0.0010 Kg Kg^{-1} (1.09 K), 0.0011 Kg Kg^{-1} (1.36 K), and 0.0009 Kg Kg^{-1} (0.97 K), respectively. The five-site average RMSE of half-hourly q (θ) estimates from this study and Tajfar et al. (2019c) are 0.0011 Kg Kg^{-1} (1.36 K) and 0.0014 Kg Kg^{-1} (1.89 K). Compared to Tajfar et al. (2019c), this study reduces the RMSE of half-hourly q (θ) estimates by 19.7% (28.0%). Finally, by assimilating sequences of LST observations, this study substantially improves the diurnal cycle of retrieved sensible and latent heat fluxes at dry/lightly vegetated sites (e.g., Desert and Audubon). Future studies should focus on developing a weak-constraint VDA approach that can capture errors in the turbulent heat fluxes due to advection.

Chapter 6: Conclusions

6.1. Summary of Original Contributions

Turbulent heat fluxes [i.e., sensible (*H*) and latent (*LE*) heat fluxes] describe the heat and moisture exchanges between the land surface and its overlying atmosphere. The accurate estimation of turbulent heat fluxes in the earth-atmosphere science has been the subject of many studies.

In Chapter 2 (Tajfar et al., 2019a), the turbulent heat fluxes are estimated by assimilating the reference-level air temperature and specific humidity into an atmospheric boundary layer (ABL) model. The two key unknown parameters of the VDA are evaporative fraction (*EF*) and neutral bulk heat transfer coefficient (C_{HN}). *EF* represents partitioning between the turbulent heat fluxes and C_{HN} scales the sum of turbulent heat fluxes. The performance of the developed VDA approach (Tajfar et al., 2019a) is tested at the First ISLSCP (International Satellite Land Surface Climatology Project) Field Experiment (FIFE) site during summer 1987 and 1988. The results show that the developed VDA framework is capable of estimating the unknown parameters (i.e., *EF* and C_{HN}) reasonably well. The variations in the estimated C_{HN} are consistent with changes in vegetation phenology, and fall within a physically accepted range. The day-to-day fluctuations in the estimated *EF* are consistent with observations even though no information on precipitation events and soil moisture dynamics is used within the assimilation model. Comparing the estimated turbulent heat fluxes with corresponding measurements over the sub-humid FIFE site shows that the assimilation of reference-level air temperature and humidity into the developed VDA model can predict the turbulent heat fluxes fairly accurately at the FIFE site. In addition,

the mean diurnal cycles of estimated and measured sensible and latent heat fluxes and net radiation are close, implying that the VDA model can robustly capture the phase of *H*, *LE*, and R_n. In contrast, there is a significant discrepancy between the diurnal cycles of estimated and measured ground heat flux, and they are out of phase. This is due to the fact that the ground heat flux (*G*) is related to the LST through $G = - p\, dT/dz$ (where *p* is the soil thermal conductivity, *T* is the ground temperature, and *z* is the soil depth), and thus the phase of *G* is strictly dependent upon that of LST, which is not assimilated in the VDA system. The mixed layer height, potential temperature, and specific humidity estimates from the VDA approach are reasonably close to those inferred from radiosondes. These estimates can also capture the rising/falling trends of observations during the course of the day.

In Chapter 3 (Tajfar et al. 2019b), the Tajfar et al. (2019a) VDA approach is advanced by the synergistic assimilation of LST, and air temperature and specific humidity into a coupled land surface-atmospheric boundary layer model. The main goal of this model is to obtain the sum of the turbulent heat fluxes ($H+LE$) that is scaled by the neutral bulk heat transfer coefficient (C_{HN}), and the partitioning between the turbulent heat fluxes ($LE/(LE+H)$), which is scaled by the evaporative fraction (*EF*). The performance of the new VDA approach (Tajfar et al., 2019b) is also tested over the FIFE site. Results indicate that the developed VDA approach performs well in both water- and energy-limited evaporation regimes because it assimilates both the land surface and atmospheric state variables. The new VDA system outperforms the previous studies in which either LST (Bateni et al., 2013b) or air temperature/humidity (Tajfar et al., 2019a) was assimilated. For FIFE 87 (88), the RMSEs of half-hourly sensible and latent heat flux estimates are decreased respectively by 13.7% (10.3%) and 24.5% (16.9%) compared to Tajfar et al., (2019a), and 10.1% (9.5%) and 17.2% (16.2%) compared to Bateni et al. (2013b). For FIFE 87

(88), the RMSEs of daily-average *H* and *LE* estimates from this study are 21.80 W m^{-2} (22.10 W m^{-2}) and 39.32 W m^{-2} (36.89 W m^{-2}), which are improved by 15.2% (20.4%) and 26.7% (23.5%) compared to Tajfar et al., (2019a), and 12.5% (17.9%) and 24.4% (22.0%) compared to Bateni et al. (2013b). Compared to Tajfar et al., (2019a), the new model reduces the RMSEs of q and θ estimates by 10.5% (12.5%) and 16.8% (10.8%) for FIFE 87 (88). Also, compared to Bateni et al. (2013b), the RMSE of LST estimates is reduced by 30.0% (37.4%) for FIFE 87 (88). The estimated ABL height, potential temperature, and specific humidity from the VDA approach agree reasonably well with those of the radiosonde observations. By assimilating sequences of LST observations, the VDA system significantly improves the diurnal cycle of ground heat flux.

In Chapter 4 (Tajfar et al. 2019c), the Tajfar et al. (2019a) VDA approached is evaluated at five sites, namely Desert, Audubon, Bondville, Brookings, and Willow Creek with contrasting climatic and vegetative conditions. The results show that the *EF* estimates agree well with the observations in terms of magnitude and day-to-day fluctuations in wet and/or densely vegetated sites, while, in dry and/or sparsely vegetated sites, the agreement between the *EF* estimates and observations weakens. Similarly, in wet and/or densely sites, the variations in the C_{HN} estimates and leaf area index (LAI) are consistent, while this consistency is deteriorated in dry and/or sparely vegetated sites. The RMSEs of daily *H* and *LE* estimates at the Willow Creek site (wet) are 37.03 W m^{-2} and 74.46 W m^{-2}, which are 38.3% and 27.2% smaller than the corresponding RMSEs of 60.00 W m^{-2} and 102.21 W m^{-2} at the Desert site (dry). The RMSE of daily *H* and *LE* increases continuously as the site becomes drier and/or sparser in vegetation density. This is due to the fact that at dry and/or sparsely vegetated sites evapotranspiration is mainly controlled by the land surface state variable (i.e., LST) rather than the atmospheric state variables (i.e., reference-level air temperature and specific humidity). The magnitude and phase of the diurnal

cycles of retrieved sensible and latent heat fluxes agree well with the observations at wet/densely vegetated sites (e.g., Willow Creek). In contrast, for the dry/lightly vegetated sites (e.g., Desert), there is a significant difference between the diurnal cycles of retrieved *H* and *LE* and observations. Overall, the results show that the VDA system performs well at wet/densely vegetated sites (e.g., Willow Creek), but its performance degrades at dry/slightly vegetated sites (e.g., Desert). These outcomes show that the sequences of reference-level air temperature and specific humidity have more information on the partitioning of available energy between the sensible and latent heat fluxes in wet and/or densely vegetated sites than the dry and/or slightly vegetated sites.

In Chapter 5 (Tajfar et al. 2019d), the Tajfar et al. (2019b) VDA approach is evaluated at the five study sites, namely Desert, Audubon, Bondville, Brookings, and Willow Creek. The variations in C_{HN} estimates are consistent with those of LAI in all the five study sites. In general, densely vegetated sites (with larger LAI values) have higher C_{HN} estimates (e.g., Willow Creek), and sparsely vegetated sites (smaller LAI values) have lower C_{HN} estimates (e.g., Desert and Audubon). The *EF* estimates can capture the daily fluctuations in the observations in each site. The results indicate that inclusion of heat diffusion equation into the VDA approach in conjunction with reference-level air temperature and specific humidity improves the performance of the VDA scheme, especially at dry and/or sparsely vegetated sites (e.g., Desert and Audubon). The five-site-average RMSEs of half-hourly sensible and latent heat flux estimates are 51.08 W m^{-2} and 82.80 W m^{-2}, respectively, which are 19.5% and 22.9% lower than those of Tajfar et al. (2019c). The RMSE of daily sensible (latent) heat flux estimates at Desert, Audubon, Bondville, Brookings, and Willow Creek sites are 35.13 W m^{-2} (30.76 W m^{-2}), 35.98 W m^{-2} (60.33 W m^{-2}), 35.58 W m^{-2} (60.88 W m^{-2}), 37.43 W m^{-2} (71.59 W m^{-2}), and 35.82 W m^{-2} (63.52 W m^{-2}),

respectively. Compared to Tajfar et al. (2019c) (that assimilated only reference-level air temperature and specific humidity), the RMSE of daily sensible (latent) heat flux estimates at the Desert, Audubon, Bondville, Brookings, and Willow Creek sites are decreased by 41.5% (69.9%), 38.1% (32.6%), 20.7% (21.8%), 16.8% (13.0%), and 3.3% (14.7%), respectively. The improvement in *H* and *LE* estimates increases by the reduction in soil moisture (SM) and/or LAI (e.g., Desert and Audubon). This is due to the fact that at dry and/or sparsely vegetated sites evapotranspiration is mostly controlled by the land surface state variable (i.e., LST) rather than the atmospheric state variables (i.e., reference-level air temperature and specific humidity). Therefore, the coupling between *EF* and LST is strong and assimilating LST into the VDA model adds more information for partitioning the available energy between turbulent heat fluxes.

As the reference-level air temperature and specific humidity contain enough information for partitioning the available energy between *H* and *LE* at wet/densely vegetated sites (e.g., Willow Creek), adding the information content of LST measurements slightly improves the *H* and *LE* estimates. The RMSEs of estimated ABL q (θ) at the Desert, Audubon, Bondville, Brookings, and Willow Creek sites are 0.0014 Kg Kg^{-1} (1.97 K), 0.0013 Kg Kg^{-1} (1.43 K), 0.0010 Kg Kg^{-1} (1.09 K), 0.0011 Kg Kg^{-1} (1.36 K), and 0.0009 Kg Kg^{-1} (0.97 K), respectively. The five-site-average of RMSE of half-hourly q (θ) estimates from Tajfar et al., (2019d) and Tajfar et al., (2019c) VDA models are 0.0011 Kg Kg^{-1} (1.36 K) and 0.0014 Kg Kg^{-1} (1.89 K). Compared to Tajfar et al. (2019c), this study reduces the RMSE of half-hourly q (θ) estimates by 19.7% (28.0%). Finally, by assimilating sequences of LST observations, this study significantly improves the diurnal cycle of retrieved sensible and latent heat fluxes at dry/lightly vegetated sites (e.g., Desert and Audubon).

6.2. Future Work

Future studies should focus on developing a weak-constraint VDA approach (WC-VDA) that can capture errors in LST and micrometeorological measurements, as well as structural model errors in the turbulent heat flux estimates by adding a model error term. The developed VDA models consider soil and vegetation as a combined source (CS), future studies may focus on developing a dual-source (DS) VDA model that considers the contribution of soil and canopy to the LST and turbulent heat fluxes, separately.

APPENDIX A: Monin-Obukhov Similarity Theory (MOST)

The Monin-Obukhov length (L) is defined as,

$$L = \frac{-\rho c_p \theta_a \left(1 + \frac{R_d}{R_v} q_a\right) u_*^3}{kgH} \tag{A1}$$

where R_d is the gas constant for dry air, R_v is the gas constant for water vapor, g is the gravitational acceleration, k is the von Karman's constant, ρ is the air density, and c_p is the specific heat capacity of air (see Table 2.1). u_* is the friction velocity, *H* is the sensible heat flux, and q_a and θ_a are the specific humidity and potential temperature at the reference-level, respectively. The neutral bulk heat transfer coefficient for heat (C_{HN}) can be related to the roughness length scale for heat (z_{oh}) via (Bateni et al., 2013b),

$$C_{HN} = \frac{k^2}{ln^2\left(\frac{z_{ref}}{z_{oh}}\right) - kB^{-1} ln\left(\frac{z_{ref}}{z_{oh}}\right)} \tag{A2}$$

The roughness length scales for heat (z_{oh}) and momentum (z_{om}) are related through (Garratt, 1994; Brutsaert, 2005; Bateni et al., 2013b),

$$B^{-1} = ln\left(\frac{z_{om}}{z_{oh}}\right) \tag{A3}$$

were *B* is the Stanton number.

Duynkerke (1992) related kB^{-1} to the leaf area index (LAI) and friction velocity via (u_*) via,

$$kB^{-1} = \left(\frac{-13u_*^{0.4}}{\text{LAI}} + 0.85\right)^{-1} \tag{A4}$$

The friction velocity can be related to the wind speed measurements at the reference-level via (Rigden and Salvucci, 2015),

$$u_* = \frac{k u_a}{ln\left(\frac{z_{ref} - d}{z_{om}}\right) - \Psi_{\mathrm{m}}\left(\frac{z_{ref} - d}{L}\right) + \Psi_{\mathrm{m}}\left(\frac{z_{om}}{L}\right)} \tag{A5}$$

where u_a is the wind speed at the reference-level, and d is the zero-plane displacement height (d is 2/3 of the vegetation height, z_{veg}). The stability function for momentum (Ψ_{m}) is given in terms of dimensionless height ξ as (Garratt, 1994; Brutsaert, 2005; Rigden and Salvucci, 2015),

$$\Psi_{\mathrm{m}}(\xi) = \begin{cases} 2ln\left(\frac{1+(1-16\xi)^{1/4}}{2}\right) + ln\left(\frac{1+\sqrt{1-16\xi}}{2}\right) - 2tan^{-1}(1-16\xi)^{1/4} + \frac{\pi}{2} & \xi < 0 \\ -5\xi & 0 \ll \xi \ll 1 \\ -5 - 5ln(\xi) & \xi > 1 \end{cases} \tag{A6}$$

The following algorithm explains how θ_{SL} and q_{SL} are obtained from θ_a and q_a:

1) Guess a reasonable value for u_*.

2) Substitute u_* from step 1 in A1 to estimate L, and A4 to estimate kB^{-1}.

3) Substitute the C_{HN} estimate from the VDA approach and obtained kB^{-1} from step 2 in A2 to find z_{oh}.

4) Substitute z_{oh} from step 3 in A3 to find z_{om}.

5) Substitute z_{om} from step 4 and L from step 2 in A5 to find u_*.

6) Repeat steps 2-5 until the algorithm converges (i.e., the difference between u_* estimates from the last two iterations becomes smaller than 0.01 m/s) to the optimal values of u_*, z_{oh}, z_{om}, and L for a given C_{HN} value.

Using the u_* and L estimates from step 6, the potential temperature, specific humidity, and wind speed at the top of the surface layer (i.e., θ_{SL}, q_{SL}, and u_{SL}) are obtained by expanding θ_a,

q_a, and u_a from the reference height z_{ref} to the bottom of the mixed-layer z_{SL} (z_{SL}~$0.1h$) by the Monin-Obukhov Similarity Theory (MOST) (Rigden and Salvucci, 2015):

$$\theta_{SL} = \theta_a - \frac{H}{ku_*\rho c_p}\left[ln\left(\frac{z_{SL}-d}{z_{ref}-d}\right) - \Psi_{\mathrm{h}}\left(\frac{z_{SL}-d}{L}\right) + \Psi_{\mathrm{h}}\left(\frac{z_{ref}-d}{L}\right)\right] \tag{A7}$$

$$q_{SL} = q_a - \frac{LE}{ku_*\rho L_v}\left[ln\left(\frac{z_{SL}-d}{z_{ref}-d}\right) - \Psi_{\mathrm{q}}\left(\frac{z_{ref}-d}{L}\right) + \Psi_{\mathrm{q}}\left(\frac{z_{ref}-d}{L}\right)\right] \tag{A8}$$

$$u_{SL} = u_a + \frac{u_*}{k}\left[ln\left(\frac{z_{SL}-d}{z_{ref}-d}\right) - \Psi_{\mathrm{m}}\left(\frac{z_{SL}-d}{L}\right) + \Psi_{\mathrm{m}}\left(\frac{z_{ref}-d}{L}\right)\right] \tag{A9}$$

The stability functions for heat (Ψ_{h}) and water vapor (Ψ_{q}) are given in terms of dimensionless height ξ as (Garratt, 1994; Brutsaert, 2005; Rigden and Salvucci, 2015),

$$\Psi_{\mathrm{h}}(\xi) = \Psi_{\mathrm{q}}(\xi) = \begin{cases} 2ln\left[\left(1+\sqrt{1-16\xi}\right)/2\right] & \xi < 0 \\ -5\xi & 0 \ll \xi \ll 1 \\ -5-5ln(\xi) & \xi > 1 \end{cases} \tag{A10}$$

The estimated θ_{SL} and q_{SL} are used to integrate equations (C1) and (C3) and also (D1) and (D3) backward in time. The estimated u_{SL} is utilized to integrate equation (2-6a) [and also (3-14a); (4-8a); and (5-9a)] forward in time. As the potential temperature and specific humidity are invariant through the mixed-layer, the initial conditions for equations (2-5a) and (2-5b) [and also (3-8a) and (3-8b); (4-5a) and (4-5b); and (5-10a) and (5-10b)] (i.e., $\theta(t=t_o)$ and $q(t=t_o)$) are set to be equal to $\theta_{SL}(t=t_o)$ and $q_{SL}(t=t_o)$, respectively. The obtained initial conditions (i.e., $\theta(t=t_o)$ and $q(t=t_o)$) are used in Appendix C and D to solve equations (2-5a) and (2-5b) [and also (3-8a) and (3-8b); (4-5a) and (4-5b); and (5-10a) and (5-10b)] forward in time.

APPENDIX B: Radiation

The effective emissivity of the atmosphere above the ABL is given by (Brubaker and Entekhabi, 1995; Margulis and Entekhabi, 2001),

$$\varepsilon_{ad} = 1.24(\frac{R_v P_h q_h}{100 R_d T_h})^m \quad \text{(B1)}$$

where $m = 1/7$, $q_h = q + \delta_q$, $T_h = (\theta + \delta_\theta)\,(\frac{P_h}{P_s})^{\frac{R_d}{cp}}$, and P_h is pressure at height h.

The incoming and outgoing longwave radiations are attenuated by absorption in the mixed-layer. The expression for the mixed-layer bulk emissivity is given by,

$$\varepsilon_m = \kappa \left\{ \frac{2}{3} \frac{q P_s}{g} \left[1 - \left(\frac{P_h}{P_s} \right)^{3/2} \right] \right\}^m \quad \text{(B2)}$$

where κ is an empirical constant with a value of 0.54 (kg m^{-2})$^{-1/7}$

The equations for the effective mixed-layer downward and upward emissivities (ε_d and ε_u) are,

$$\varepsilon_d = \kappa \left(\frac{2}{3} \frac{q P_s}{g} \right)^m m \int_{y_h}^{1} y^{\frac{8R_d}{3c_p}} (1 - y)^{m-1} dy \quad \text{(B3)}$$

$$\varepsilon_u = \kappa \left(\frac{2}{3} \frac{q P_s}{g} \right)^m m \int_{y_h}^{1} y^{\frac{8R_d}{3c_p}} (y - y_h)^{m-1} dy \quad \text{(B4)}$$

where $y = (P/P_s)^{3/2}$

APPENDIX C: Euler-Lagrange Equations for Model 1

The data assimilation approach iteratively improves estimates of *EF* and *R*, starting from the initial guesses $EF'$and R'. This procedure is done iteratively through the following steps: (1) integrate the ABL potential temperature and specific humidity [i.e., equations (2-5a) and (2-5b); and (4-5a) and (4-5b)] forward in time every 30-minutes using the initial conditions $\theta(t = t_o)$ and $q(t = t_o)$ (Appendix A describes how $\theta(t = t_o)$ and $q(t = t_o)$ are obtained in each iteration), (2) integrate the adjoint models (i.e., equations C1 and C3) backward in time every 30-minutes using the final conditions C2 and C4, (3) updating the parameters *EF* and *R* using equations C5 and C6 (in the first iteration, R' and EF' are obtained by an initial guess. In the next iterations, R' and EF' are the corresponding estimates in the previous iteration), and (4) repeating steps (1)-(3) until convergence is reached.

$$\frac{d\lambda_1}{dt} = \frac{1}{h}\left\{\frac{2R_\theta^{-1}(\theta-\theta_{SL})}{\rho c_p} + \lambda_1 \times \left[-\frac{4\theta G_* e^{-\varphi h}}{gh\delta_\theta} - \frac{0.2f(Ri)u(T-T_a)e^R}{\delta_\theta}\left(1 + \frac{0.07EF}{1-EF}\right) + \frac{0.2\theta e^R f(Ri)u}{\delta_\theta}\left(1 + \frac{0.07EF}{1-EF}\right)\left(\frac{P_s}{P_h}\right)^{\frac{R_d}{c_p}} - \frac{\varepsilon_m\varepsilon_{ad}\sigma\left(4\theta^3+12\theta^2\delta\theta+4\delta\theta^3+12\theta\delta\theta^2\right)}{\rho c_p}\left(\frac{P_h}{P_s}\right)^{\frac{4R_d}{c_p}} + \frac{4\varepsilon_u\sigma\theta^3}{\rho c_p} - \frac{4\varepsilon_d\sigma\theta^3}{\rho c_p} + 1.2e^R f(Ri)u\left(\frac{P_s}{P_h}\right)^{\frac{R_d}{c_p}}\right] + \lambda_2\left[-\frac{2q}{c_p}\frac{G_* e^{-\varphi h}}{gh\delta_\theta} + \frac{0.2qe^R f(Ri)u}{c_p\delta_\theta}\left(\frac{P_s}{P_h}\right)^{\frac{R_d}{c_p}}\left(1 + \frac{0.07EF}{1-EF}\right) + \frac{EFe^R f(Ri)u}{(1-EF)L_v}\left(\frac{P_s}{P_h}\right)^{\frac{R_d}{c_p}} - \frac{\delta_q}{c_p}\frac{2G_* e^{-\varphi h}}{gh\delta_\theta} + \frac{0.2\delta_q}{c_p\delta_\theta}e^R f(Ri)u\left(\frac{P_s}{P_h}\right)^{\frac{R_d}{c_p}}\left(1 + \frac{0.07EF}{1-EF}\right)\right]\right\} \quad \text{(C1)}$$

$$\lambda_1(t_1) = 0 \quad \text{(C2)}$$

$$\frac{d\lambda_2}{dt} = \frac{1}{h}\left[\frac{2R_q^{-1}(q-q_{SL})}{\rho} - \frac{2\lambda_2\theta G_* e^{-\varphi h}}{gh\delta_\theta} - \frac{0.2\lambda_2 e^R f(Ri)u(T-T_a)}{\delta_\theta}\left(1 + \frac{0.07EF}{1-EF}\right)\right] \quad \text{(C3)}$$

$$\lambda_2(t_1) = 0 \tag{C4}$$

$$EF_i = \frac{1}{2B_{EF}^{-1}} \int_{t_0}^{t_1} \left[\frac{0.07\lambda_1 \theta \rho c_p e^R f(Ri) u(T-T_a)}{(1-EF)^2} \times \frac{0.2}{\delta_\theta} + \frac{0.07\lambda_2 \rho q e^R f(Ri) u(T-T_a)}{(1-EF)^2} \times \frac{0.2}{\delta_\theta} + \frac{\lambda_2 \rho c_p e^R f(Ri) u(T-T_a)}{L_v (1-EF)^2} + \frac{0.07\lambda_2 \rho \delta_q e^R f(Ri) u(T-T_a)}{(1-EF)^2} \times \frac{0.2}{\delta_\theta} \right] dt + EF_i' \tag{C5}$$

$$R = \frac{1}{2B_R^{-1}} \sum \int_{t_0}^{t_1} \left[\left(1 + \frac{0.07EF}{1-EF}\right) \times \frac{0.2\lambda_1 \theta \rho c_p e^R f f(Ri) u(T-T_a)}{\delta_\theta} + 1.32\lambda_1 \rho c_p e^R f(Ri) u(T-T_a) + \left(1 + \frac{0.07EF}{1-EF}\right) \times \frac{0.2\lambda_2 \rho q e^R f(Ri) u(T-T_a)}{\delta_\theta} + \frac{EF\lambda_2 \rho c_p e^R f(Ri) u(T-T_a)}{(1-EF) L_v} + \left(1 + \frac{0.07EF}{1-EF}\right) \times \frac{0.2\lambda_2 \rho \delta_q e^R f(Ri) u(T-T_a)}{\delta_\theta} \right] dt + R' \tag{C6}$$

APPENDIX D: Euler-Lagrange Equations for Model 2

The VDA approach iteratively improves *EF* and *R* estimates, starting from the initial guesses $EF'$and R'. The iterative procedure comprises 1) integrating the heat diffusion equation [equations (3-1), and (5-1)], and the ABL potential temperature and specific humidity [equations (3-8a) and (3-8b); and (5-10a) and (5-10b)] forward in time every 30-minutes using the initial conditions $\theta(t = t_o)$ and $q(t = t_o)$ (Appendix A describes how $\theta(t = t_o)$ and $q(t = t_o)$ are obtained in each iteration), 2) integrating the adjoint equations D1, D3, and D5 backward in time using the final conditions D2, D4, and D6, 3) updating *EF* and *R* via equations D9 and D10, respectively (in the first iteration, R' and EF' are obtained by an initial guess. In the next iterations, R' and EF' are the corresponding estimates in the previous iteration), and (4) repeating steps (1)-(3) until convergence is reached.

$$\frac{d\lambda_1}{dt} = \frac{1}{h}\left\{\frac{2R_\theta^{-1}(\theta-\theta_{SL})}{\rho c_p} + \lambda_1 \times \left[-\frac{4\theta G_* e^{-\varphi h}}{gh\delta_\theta} - \frac{0.2f(Ri)U(T-T_a)e^R}{\delta_\theta}\left(1 + \frac{0.07EF}{1-EF}\right) + \frac{0.2\theta e^R f(Ri)U}{\delta_\theta}\left(1 + \frac{0.07EF}{1-EF}\right)\left(\frac{P_s}{P_h}\right)^{\frac{R_d}{c_p}} - \frac{\varepsilon_m\varepsilon_{ad}\sigma\left(4\theta^3+12\theta^2\delta\theta+4\delta\theta^3+12\theta\delta\theta^2\right)}{\rho c_p}\left(\frac{P_h}{P_s}\right)^{\frac{4R_d}{c_p}} + \frac{4\varepsilon_u\sigma\theta^3}{\rho c_p} - \frac{4\varepsilon_d\sigma\theta^3}{\rho c_p} + 1.32e^R f(Ri)U\left(\frac{P_s}{P_h}\right)^{\frac{R_d}{c_p}}\right] + \lambda_2\left[-\frac{2q}{c_p}\frac{G_* e^{-\varphi h}}{gh\delta_\theta} + \frac{0.2qe^R f(Ri)U}{c_p\delta_\theta}\left(\frac{P_s}{P_h}\right)^{\frac{R_d}{c_p}}\left(1 + \frac{0.07EF}{1-EF}\right) + \frac{EFe^R f(Ri)U}{(1-EF)L_v}\left(\frac{P_s}{P_h}\right)^{\frac{R_d}{c_p}} - \frac{\delta_q}{c_p}\frac{2G_* e^{-\varphi h}}{gh\delta_\theta} + \frac{0.2\delta_q}{c_p\delta_\theta}e^R f(Ri)U\left(\frac{P_s}{P_h}\right)^{\frac{R_d}{c_p}}\left(1 + \frac{0.07EF}{1-EF}\right)\right] - \left[\frac{D\lambda_3(t,0)}{p(1-EF)}e^R f(Ri)U\left(\frac{P_s}{P_h}\right)^{\frac{R_d}{c_p}} + \frac{D\lambda_3(t,0)}{p\rho c_p}4T_a(t)^3\varepsilon_m\sigma\left(\frac{P_s}{P_h}\right)^{\frac{R_d}{c_p}}\right]\right\} \quad \text{(D1)}$$

$$\lambda_1(t_1) = 0 \tag{D2}$$

$$\frac{d\lambda_2}{dt} = \frac{1}{h}\left[\frac{2R_q^{-1}(q-q_{SL})}{\rho} - \frac{2\lambda_2\theta G_* e^{-\varphi h}}{gh\delta_\theta} - \frac{0.2\lambda_2 e^R f(Ri)u(T-T_a)}{\delta_\theta}\left(1 + \frac{0.07EF}{1-EF}\right)\right] \tag{D3}$$

$$\lambda_2(t_1) = 0 \tag{D4}$$

$$\frac{\partial\lambda_3}{\partial t} + D\frac{\partial^2\lambda_3}{\partial z^2} = 0 \tag{D5}$$

$$\lambda_3(t_1, z) = 0 \tag{D6}$$

$$\left(\frac{\partial\lambda_3(t,z)}{\partial z}\middle| z = l\right) = 0 \tag{D7}$$

$$\left(\frac{d\lambda_3(t,z)}{dz}\middle| z = 0\right) = \frac{2R_T^{-1}(T-T_{obs})}{D} + \frac{\lambda_3(t,0)}{p}\left[4\varepsilon_s\sigma T^3 + \frac{\rho c_p e^R f(Ri)u}{1-EF}\right] - \frac{1}{D}\left[\frac{0.2\lambda_1\theta\rho c_p e^R f(Ri)u}{\delta_\theta}\left(1 + \frac{0.07EF}{1-EF}\right) + 4\lambda_1\varepsilon_a\varepsilon_s\sigma T^3 + 1.32\lambda_1\rho c_p e^R f(Ri)u + \frac{0.2\lambda_2\rho q e^R f(Ri)u}{\delta_\theta}\left(1 + \frac{0.07EF}{1-EF}\right) + \lambda_2\rho c_p e^R f(Ri)u\frac{EF}{(1-EF)L_v} + \frac{0.2\lambda_2\rho\delta_q e^R f(Ri)u}{\delta_\theta}\left(1 + \frac{0.07EF}{1-EF}\right)\right] \tag{D8}$$

$$EF_i = \frac{1}{2B_{EF}^{-1}}\int_{t_0}^{t_1}\left[\frac{0.07\lambda_1\theta\rho c_p e^R f(Ri)u(T-T_a)}{(1-EF)^2}\times\frac{0.2}{\delta_\theta} + \frac{0.07\lambda_2\rho q e^R f(Ri)u(T-T_a)}{(1-EF)^2}\times\frac{0.2}{\delta_\theta} + \frac{\lambda_2\rho c_p e^R f(Ri)u(T-T_a)}{L_v(1-EF)^2} + \frac{0.07\lambda_2\rho\delta_q e^R f(Ri)u(T-T_a)}{(1-EF)^2}\times\frac{0.2}{\delta_\theta} - \frac{D\lambda_3(t,0)}{p(1-EF)^2}\rho c_p e^R f(Ri)u(T-T_a)\right]dt + EF_i' \tag{D9}$$

$$R = \frac{1}{2B_R^{-1}} \sum \int_{t_0}^{t_1} \left[\left(1 + \frac{0.07EF}{1-EF}\right) \times \frac{0.2\lambda_1 \theta \rho c_p e^R f(Ri) u(T-T_a)}{\delta_\theta} + 1.32\lambda_1 \rho c_p e^R f(Ri) u(T-T_a) + \right.$$

$$\left(1 + \frac{0.07EF}{1-EF}\right) \times \frac{0.2\lambda_2 \rho q e^R f(Ri) u(T-T_a)}{\delta_\theta} + \frac{EF\lambda_2 \rho c_p e^R f(Ri) u(T-T_a)}{(1-EF)L_v} + \left(1 + \frac{0.07EF}{1-EF}\right) \times$$

$$\left. \frac{0.2\lambda_2 \rho \delta_q e^R f(Ri) u(T-T_a)}{\delta_\theta} - \frac{D\lambda_3(t,0)}{p(1-EF)} \rho c_p e^R f(Ri) u(T-T_a) \right] dt + R' \qquad \text{(D10)}$$

References

Abdolghafoorian, A., Farhadi, L., Bateni, S. M., Margulis, S., and T., Xu, 2017: Characterizing the effect of vegetation dynamics on the bulk heat transfer coefficient to improve variational estimation of surface turbulent fluxes. *J. Hydrometeorol.*, 18 (2), 321-333, doi:10.1175/JHM-D-16-0097.1.

Abdolghafoorian, A., and L., Farhadi, 2016: Uncertainty quantification in land surface hydrologic modeling: Toward an integrated variational data assimilation framework. *IEEE J Sel Top Appl Earth Obs Remote Sens*, 9, 2628–2637, doi:10.1109/JSTARS.2016.2553444.

Alapaty, K., Seaman, N. L., Niyogi, D. S., and A. F., Hanna, 2001: Assimilating surface data to improve the accuracy of atmospheric boundary layer simulations, *J. Appl. Meteor.*, 40, 2068-2082.

Alfieri, J., Kustas, W. P., Prueger, J. H., Chavez, J. L., Evett, S. R., et al., 2012: A comparison of the eddy covariance and lysimetry-based measurements of the surface energy fluxes during BEAREXo8. *Int. Assoc. Hydrol. Sci*., 352, 215-218.

Allen, R., A. Irmak, R. Trezza, J. M. H. Hendrickx, W. Bastiaanssen, and J., Kjaersgaard, 2011: Satellite-based ET estimation in agriculture using SEBAL and METRIC. *Hydrol. Processes*, 25, 4011–4027, doi:10.1002/hyp.8408.

Anderson, M. C., Norman, J. M., Diak, G. R., Kustas, W. P., and J. R., Mecikalski, 1997: A two-source time-integrated model for estimating surface fluxes using thermal infrared remote sensing. *Remote Sens. Environ*., 60(2), 195–216.

Aparicio, N., Villegas, D., Casadesús, J., Araus, J. L., and C., Royo, 2000: Spectral vegetation indices as nondestructive tools for determining durum wheat yield. *Agron. J.*, 92, 83–91.

Bagley, J. E., Desai, A. R., West, P. C., and J. A., Foley, 2011: A simple, minimal parameter model for predicting the influence of changing land cover on the land-atmosphere system, *Earth Interactions*, 15, 1-32.

Baldocchi, D., Falge, E., Gu, L. H., and Olson, R. (2001). FLUXNET: A new tool to study the temporal and spatial variability of ecosystem-scale carbon dioxide, water vapor, and energy flux densities. *Bull. Amer. Meteorol. Soc.*, 82(11), 2415–2434.

Balsamo, G., Mahfouf, J. F., Belair, S., and G., Deblonde, 2007: A land data assimilation system for soil moisture and temperature: An information content study, *J. Hydrometeorol*., 8, 1225-1242.

Bastiaanssen, W. G. M., Menenti, M., Feddes, R. A., and A. A. M., Holtslang, 1998a: A remote sensing surface energy balance algorithm for land (SEBAL) 1. Formulation. *J. Hydrol.*, v. 212–213, p.198–212.

Bastiaanssen, W. G. M., Pelgrum, H., Wang, J., MA, Y., Moreno, J. F., Roenrink, G. J., and T., Van Der Wal, 1998b: A remote sensing surface energy balance algorithm for land (SEBAL) 2. Validation. *J. Hydrol.*, v. 212–213, p.213-229.

Bateni, S. M., and D., Entekhabi, 2012a: Relative efficiency of land surface energy balance components. *Water Resour. Res.*, 48(4).

Bateni, S. M., and D., Entekhabi, 2012b: Surface heat flux estimation with the ensemble Kalman smoother: Joint estimation of state and parameters. *Water Resour. Res.*, 48(8).

Bateni, S. M., and Entekhabi, D., and D.-S., Jeng, 2013a: Variational assimilation of land surface temperature and the estimation of surface energy balance components. *J. Hydrol.*, 481, 143-156.

Bateni, S. M., and Entekhabi, D., and F., Castelli, 2013b: Mapping evaporation and estimation of surface control of evaporation using remotely sensed land surface temperature from a constellation of satellites. *Water Resour. Res.*, 49(2), 950-968.

Bateni, S. M., Entekhabi, D., Margulis, S., Castelli, F., and L., Kergoat, 2014: Coupled estimation of surface heat fluxes and vegetation dynamics from remotely sensed land surface temperature and fraction of photosynthetically active radiation. *Water Resour. Res.*, 50(11), 8420-8440, doi:10.1002/2013WR014573.

Balsamo, G., Mahfouf, J. F., Belair, S., and G. Deblonde, 2007: A land data assimilation system for soil moisture and temperature: An information content study, *J. Hydrometeorolo*., 8, 1225-1242.

Bennett, A. F., 1992: Inverse methods in physical oceanography. *Cambridge University Press*, 346 pp.

Bennett, W.B., Wang, J., Bras, R.L., 2008. Estimation of global ground heat flux. *J. Hydromet*., 9, 744-759.

Betts, A. K., and J. H., Ball, 1998: FIFE surface climate and site-average dataset 1987–89. *J. Atmos. Sci.*, 55(7), 1091–1108.

Boni, G., Entekhabi, D., and F., Castelli, 2001: Land data assimilation with satellite measurements for the estimation of surface energy balance components and surface control on evaporation. *Water Resour. Res*., 37(6), 1713–1722.

Bouttier, F., J. F. Mahfouf, and J., Noilhan, 1993a: Sequential assimilation of soil moisture from atmospheric low-level parameters. Part I: Sensitivity and calibration studies. *J. Appl. Meteorol.*, 32(8), 1335-1351.

Bouttier, F., J. F. Mahfouf, and J., Noilhan, 1993b: Sequential assimilation of soil moisture from atmospheric low-level parameters. II: Implementation in a mesoscale model. *J. Appl. Meteorol.*, 32(8), 1352-1364.

Brenner, C., Thiem, C. E., Wizemann, H., Bernhardi, M., and K., Schulz, 2017: Estimating spatially distributed turbulent heat fluxes from high-resolution thermal imagery acquired with a UAV system. *Int. J. Remote Sens.*, 38(8-10), 3003-3026, doi:10.1080/01431161.2017.1280202.

Brubaker, K. L., and D., Entekhabi, 1995: An analytic approach to modeling the land-atmosphere interaction: 1. Construct and equilibrium behavior. *Water Resour. Res.*, 31, 619-632.

Brutsaert, W., 1975: On a derivable formula for long-wave radiation from clear skies. *Water Resour. Res.*, 11**,** 742–744, doi:10.1029/WR011i005p00742.

Brutsaert, W., 2005: Hydrology: An Introduction, *Cambridge Univ. Press*, N. Y.

Businger, J. A., J. C. Wyngaard, Y. Izumi, and E. F., Bradley, 1971: Flux profile relationships in the atmospheric surface layer, *J. Atmos. Sci.*, 28, 181-189, 1971.

Caparrini, F., Castelli, F., and D., Entekhabi, 2003: Mapping of land-atmosphere heat fluxes and surface parameters with remote sensing data. *Bound.-Layer Meteor.*, 107(3), 605-633.

Caparrini, F., Castelli, F., and D., Entekhabi, 2004a: Estimation of surface turbulent fluxes through assimilation of radiometric surface temperature sequences. *J. Hydrometeorol.*, 5(1), 145-159.

Caparrini, F., Castelli, F., and D., Entekhabi, 2004b: Variational estimation of soil and vegetation turbulent transfer and heat flux parameters from sequences of multisensor imagery. *Water Resour. Res.*, 40, W12515, 1713-1722, doi:10.1029/2004WR003358.

Carlson, T., 2007: An overview of the “triangle method” for estimating surface evapotranspiration and soil moisture from satellite imagery. *Sensors*, 7(12), 1612–1629.

Carrera, M., Belair, S., and B., Bilodeau, 2015: The Canadian Land Data Assimilation System (CaLDAS): Description and synthetic evaluation study. *J. Hydrometeor*., 16, 1293–1314.

Castelli, F., D. Entekhabi, and E., Caporali, 1999: Estimation of surface heat flux and an index of soil moisture using adjoint-state surface energy balance. *Water Resour. Res.*, 35(10), 3115-3125.

Chen, F., Mitchell, K., Schaake, J., Xue, Y., Pan, H.-L., Koren, V., Duan, Q. Y., Ek, M., and A., Betts, 1996: Modeling of land surface evaporation by four schemes and comparison with FIFE observations. *J. Geophys. Res.*, 101 (D3), 7251–7268.

Crago, R.D., 1996: Conservation and variability of the evaporative fraction during the daytime. *J. Hydrol*. 180 (1‑4), 173‑194. https://doi.org/10.1016/0022-1694(95) 02903-6.

Crow, W. T., and W. P., Kustas, 2005: Utility of assimilating surface radiometric temperature observations for evaporative fraction and heat transfer coefficient retrieval. *Bound. -Layer Meteor.*, 115(1), 105–130, doi:10.1007/s10546-004-2121-0.

Daley, R., 1991: Atmospheric Data Analysis, *Cambridge Univ. Press*, New York.

de Lannoy, G.J.M., de Rosnay, P., and R. H., Reichle, 2016: Soil Moisture Data Assimilation. In: Duan Q., Pappenberger F., Thielen J., Wood A., Cloke H., and J., Schaake (eds) *Handbook of Hydrometeorological Ensemble Forecasting*. Springer, Berlin, Heidelberg.

de Rosnay, P., M., Drusch, D., Vasiljevic, G., Balsamo, C., Albergel, and L., Isaksen, 2013: A simplified Extended Kalman Filter for the global operational soil moisture analysis at ECMWF. *Q. J. Roy. Meteor. Soc.*, 139(674), 1199-1213.

de Vries, D. A., 1963: Thermal properties of soils. In W. R. van Wijk (Ed.), *Phys. Plant Environ.*, 210–235. New York: North-Holland.

Douville, H., P. Viterbo, J. F. Mahfouf, and A. C., Beljaars, 2000: Evaluation of the optimum interpolation and nudging techniques for soil moisture analysis using FIFE data. *Mon. Wea. Rev.*, 128(6), 1733-1756.

Drusch, M., and P., Viterbo, 2007: Assimilation of screen-level variables in ECMWF's integrated forecast system: a study on the impact on the forecast quality and analyzed soil moisture, *Mon. Wea. Rev.*, 135, 300-314.

Dunne, S., and D., Entekhabi, 2005: An ensemble-based reanalysis approach to land data assimilation. *Water Resour. Res.*, 41, W02013.

Dunne, S., and D., Entekhabi, 2006: Land surface state and flux estimation using the ensemble Kalman smoother during the Southern Great Plains 1997 field experiment. *Water Resour. Res*., 42, W01407.

Duynkerke, P. G., 1992: The roughness length for heat and other vegetation parameters for a surface of short grass, *J. Appl. Meteor.*, 31, 579-586. doi: 10.1175/1520-0450(1992)031<0579:TRLFHA>2.0.CO;2.

Evett, S. R., Kustas, W. P., Gowda, P. H., Anderson, M. C., Prueger, J. H., and T. A., Howell, 2011: Overview of the Bushland Evapotranspiration and Agricultural Remote sensing EXperiment 2008 (BEAREX08): A field experiment evaluating methods for quantifying ET at multiple scales. *Adv. Water Resour*., 50, 4–19.

Farouki, O. T., 1981: The thermal properties of soils in cold regions. *Cold Reg. Sci. Technol.*, 5(1), 67–75.

Fertig, E. J., Baek, S.-J., Hunt, B. R., Ott, E., Szunyogh, I., Aravequia, J. A., et al. 2009: Observation bias correction with an ensemble Kalman filter. *Tellus Series A*, 61(2), 210–226.

Fisher, J. B., Melton, F., Middleton, E., Hain, C., Anderson, M., Allen, R., et al. 2017: The future of evapotranspiration: Global requirements for ecosystem functioning, carbon and climate feedbacks, agricultural management, and water resources. *Water Resour. Res*., 53, 2618–2626.

Garcia, J. R., and J. P., Mellado, 2014: The two-layer structure of the entrainment zone in the convective boundary layer, *J. Atmos. Sci.*, 71(6), 1935-1955.

Garratt, J. R., 1994: The Atmospheric Boundary Layer, *Cambridge Univ. Press*, N. Y.

Gebler, S., Hendricks Franssen, H.-J., Putz, T., Post, H., Schmidt, M., and H., Vereecken, 2015: Actual evapotranspiration and precipitation measured by lysimeters: a comparison with eddy covariance and tipping bucket. *Hydrol. Earth Sys. Sci*., 19, 2145-2161, doi:10.5194/hess-19-2145-2015.

Gentine, P., Entekhabi, D., Chehbouni, A., Boulet, G., and B. Duchemin, 2007: Analysis of evaporative fraction diurnal behavior. *Agric. Forest Meteor.*, 143, 13-29.

Gentine, P., Entekhabi, D., and J. Polcher, 2011: The diurnal behavior of evaporative fraction in the soil-vegetation-atmospheric boundary layer, *J. Hydrometeorol.*, 12, 1530-1546, doi:10.1175/2011JHM1261.1.

Gentine, P., Ferguson, C. R., and A. A. M., Holtslag, 2013b: Diagnosing evaporative fraction over land from boundary-layer clouds, *J. Geophys. Res.: Atmos.*, 118(15), 8185–8196, doi:10.1002/jgrd.50416.

Gentine, P., Bellon, G., and C. C., van Heerwaarden, 2015: A closer look at boundary layer inversion in large-eddy simulations and bulk models: buoyance-driven case. *J. Atmos. Sci.*, 72, 728-749.

Gentine, P., Chhang, A., Rigden, A., and G., Salvucci, 2016: Evaporation estimates using weather station data and boundary layer theory. *Geophys. Res. Lett.*, 43, 11,661–11,670, doi:10.1002/2016GL070819.

Gentine, P., Guillod, B. P., Geerwaardem, C. V., Roundy, J., and V., Wulfmeyer, 2018: Land-Atmosphere Interactions: The LoCo Perspective, *Bull. Amer. Meteor. Soc.*, 99 (June), 1253-1272. doi: 10.1175/BAMS-D-17-0001.1.

Hall, F.G., Huemmrich, K. F., Goetz, S. J., Sellers, P. J., and J. E., Nickerson, 1992: Satellite remote sensing of surface energy balance: success, failures, and unresolved issues in FIFE. *J. Geophys. Res.*, 97 (D17), 19061–19089.

He ,X., Xu, T., Bateni, S. M., Neale, C. M. U., Auligne, T., Liu, S., Wang, K., Mao, K., and Y., Yao, 2018: Evaluation of the Weak Constraint Data Assimilation Approach for stimating Turbulent Heat Fluxes at Six Sites, *Remote Sens.*, 10(12), 1994; https://doi.org/10.3390/rs10121994.

Hess, R., 2001: Assimilation of screen-level observations by variational soil moisture analysis. *Meteorol. Atmos. Phys.*, 77, 145-154.

Hirschi, M., Michel, D., Lehner, I., and S. I., Seneviratne, 2017: A site-level comparison of lysimeter and eddy covariance flux measurements of evapotranspiration. *Hydrol. Earth Sys. Sci*., 21, 1809-1825, doi:10.5194/hess-21-1809-2017.

Holtslag A. A. M., and A. P., Van Ulden, 1983: A single scheme for daytime estimates of the surface fluxes from routine weather data. *J. Climate Appl. Meteor.*, 22(4), 517-529.

Hu, Z., and S., Islam, 1995: Prediction of ground temperature and soil moisture content by the force-restore method. *Water Resour. Res.*, 31, 2531–2539.

Idso, S. B., 1981: A set of equations for full spectrum and 8- to 14-mum and 10.5- to 12.5-mum thermal radiation from cloudless skies. *Water Resour. Res.*, 17(2), 295-304.

Jia, L., Xi, G. Liu, S. Huang, C. Yan, Y. and G., Liu, 2009: Regional estimation of daily to annual regional evapotranspiration with MODIS data in the Yellow River Delta wetland. *Hydrol. Earth Syst. Sci.*, 13(10), 1775–1787.

Jiang, L., and Islam, S., 2003: An intercomparison of regional latent heat flux estimation using remote sensing data. *Int. J. Remote Sens*., 24(11), 2221–2236.

Jiang, L., Islam, S., Guo, W., Singh Jutla, A., Senarath, S. U. S., Ramsay, B. H., and E., Eltahir, 2009: A satellite-based daily actual evapotranspiration estimation algorithm over south Florida. *Glob. Planet. Change*, 67(1), 62–77, doi:10.1016/j.gloplacha.2008.12.008.

Kalma, J. D., McVicar, T. R., and M. F., McCabe, 2008: Estimating land surface evaporation: A review of methods using remotely sensed surface temperature data. *Surv. Geophys*., 29(4-5), 421-469, doi:10.1007/s10712-008-9037-z.

Kim, C. P., and D., Entekhabi, 1997: Examination of two methods for estimating regional evaporation using a coupled mixed layer and land surface mode, *Water Resour. Res*., 33(9), 2109-2116.

Kim, C. P., and D., Entekhabi, 1998a: Impact of soil heterogeneity in a mixed-layer model of the planetary boundary layer, *Hydrol. Sci.*, 43(4), 633-658.

Kim, C. P., and D., Entekhabi, 1998b: Feedbacks in the Land-Surface and Mixed-Layer Energy Budgets. *Bound. -Layer Meteor.*, 88, 1-21.

Kustas, W. P., Alfieri, J. G., Anderson, M. C., Colaizzi, P. D., Prueger, J. H., Evett, S. R., et al. 2012: Evaluating the two-source energy balance model using local thermal and surface flux observations in a strongly advective irrigated agricultural area. *Adv. Water Resour*., 50, 120–133.

Laird, N. F., and D. A. R., Kristovich, 2002: Variations of sensible and latent heat fluxes from a great lakes buoy and associated synoptic weather patterns. *J. Hydrometeo.*, DOI: 10.1175/1525-7541(2002)003.

Laxmi, K., and L., Nandagiri, 2014: Latent heat flux estimation using trapezoidal relationship between MODIS land surface temperature and fraction of vegetation–application and validation in a humid tropical region. *Remote Sens. Lett.*, 5, 981–990.

Lei, F. N., Huang, C. L., Shen, H. F., and X., Li, 2014: Improving the estimation of hydrological states in the SWAT model via the ensemble Kalman smoother: Synthetic experiments for the Heihe River Basin in northwest China. *Adv. Water Resour*., 67, 32–45.

Li, Y., Gao, Z., Lenschow, D. H., and F., Chen, 2010: An improved approach for parameterizing surface-layer turbulent transfer coefficients in numerical models. *Bound. -Layer Meteor.*, 137, 153-165, doi:10.1007/s10546-010-9532-y.

Li, X., Cheng, G. D., Liu, S. M., Xiao, Q., Ma, M. G., Jin, R., et al., 2013: Heihe watershed allied telemetry experimental research (HiWATER): Scientific objectives and experimental design. *Bull. Amer. Meteor. Soc.*, 94(8), 1145–1160. https://doi.org/10.1175/BAMS-D-12-00154.1.

Liang, S., Zhao, X., Yuan, W., Liu, S., Cheng, X., Xiao, Z., et al., 2013: A long-term Global Land Surface Satellite (GLASS) dataset for environmental studies. *Int. J. Digit. Earth*, 6(1), 5–33.

Liou, Y.-A, and S. K., Kar, 2014: Evapotranspiration estimation with remote sensing and various surface energy balance algorithms- a review. *Energies*, 7, 2821-2849, doi:10.3390/en7052821.

Liu, S. M., Hu, G., Lu, L., and D. F., Mao, 2007: Estimation of regional evapotranspiration by TM/ETM+ data over heterogeneous surfaces. *Photogramm. Eng. Remote Sens*., 73(10), 1169–1178.

Liu, S. M., Xu, Z. W., Wang, W. Z., Bai, J., Jia, Z., Zhu, M., J. M., Wang, 2011: A comparison of eddy-covariance and large aperture scintillometer measurements with respect to the energy balance closure problem. *Hydrol. Earth Sys. Sci*., 15(4): 1291-1306. doi:10.5194/hess-15-1291-2011.

Liu, S. M., Z. W. Xu, Z. L. Zhu, Z. Z. Jia, and M. J., Zhu, 2013: Measurements of evapotranspiration from eddy-covariance systems and large aperture scintillometers in the Hai River Basin, China, *J. Hydrol.*, 487, 24–38.

Liu, S. M., Xu, Z. W., Song, L. S., Zhao, Q. Y., Xu, T. R., Ge, Y., Ma, Y. F., Zhu, Z. L., Jia, Z. Z., and F., Zhang, 2016: Upscaling evapotranspiration measurements from multi-site to the satellite pixel scale over heterogeneous land surfaces. *Agric. For. Meteorol*. 230‑231, 97‑113. https://doi.org/10.1016/j.agrformet.2016.04.008.

Liu, S., Li, X., Xu, Z., Che, T., Xiao, Q., Ma, M., Liu, Q., Jin, R., et al., 2018: The Heihe integrated observatory network: A basin-scale land surface processes observatory in China,*Vadose Zone J.*, doi:10.2136/vzj2018.04.0072.

Lu, Y., Dong, J., Steele-Dunne, S. C., and N., van de Giesen, 2016: Estimating surface turbulent heat fluxes from land surface temperature and soil moisture observations using the particle batch smoother. *Water Resour. Rese.*, 52, 9086-9108, doi:10.1002/2016WR018943.

Lum, M., Bateni, S. M., Shiri, J., and A., Keshavarzi, 2017: Estimation of reference evapotranspiration from climatic data. *Int. J. Hydrolo.*, 1(1): 00005. doi:10.15406/ijh.2017.01.00005.

Ma, W., Hafeez, M., Rabbani, U., Ishikawa, H., and Y., Ma, 2012: Retrieved actual ET using SEBS model from Landsat-5 TM data for irrigation area of Australia. *Atmos. Environ.*, 59, 408–414.

Ma, Y. F., Liu, S. M., Zhang, F., Zhou, J., Jia, Z. Z., and L. S., Song, 2015: Estimations of regional surface energy fluxes over heterogeneous oasisdesert surfaces in the middle reaches of the Heihe River during HiWATER-MUSOEXE. IEEE Geosci. *Remote Sens. Lett*., 12, 671–675.

Ma, Y., Liu, S., Song, L., Xu, Z., Liu, Y., Xu, T., Zhu, T., 2018: Estimation of daily evapotranspiration and irrigation water efficiency at a Landsat-like scale for an arid irrigation area using multi-source remote sensing data. *Remote Sens. Environ*., 216, 715–734.

MacCabe, M. F., and E. F., Wood, 2006: Scale influences on the remote estimation of evapotranspiration using multiple satellite sensors, Remote Sens. Environ., 105(4), 271-285.

Maes W. H., and K., Steppe, 2012: Estimating evapotranspiration and drought stress with ground-based thermal remote sensing in agriculture: a review. *J. Exp. Bot.*, 63(13), 4671–4712.

Mahfouf, J.-F., 1991: Analysis of soil moisture from near-surface parameters: A feasibility study, *J. App. Meteor.*, 30(11), 1534-1547.

Mahfouf, J.-F., Viterbo, P., Douville, H., Beljaars, A., and S., Saarinen, 2000: A Revised land-surface analysis scheme in the Integrated Forecasting System. *ECMWF Newsletter*, 88.

Mahfouf, J.-F., Bergaoui, K., Draper, C., Bouyssel, F., Taillefer, F., and L., Taseva, 2009: A comparison of two off-line soil analysis schemes for assimilation of screen level observations, *J. Geophys. Res.*, 114, D08105, doi:10.1029/2008JD011077.

Majozi, N. P., Mannaerts, C. M., Ramoelo, A., Mathieu, R., Mudau, A. E., and W., Verhoef, 2017: An intercomparison of satellite-based daily evapotranspiration estimates under different eco-climatic regions in south Africa. *Remote Sens.*, 9 (4), 307.

Mallick, K., Jarvis, A. J., Fisher, J. B., Tu, K. P., Boegh, E., and D., Niyogi, 2013: Latent heat flux and canopy conductance based on Penman-Monteith, Priestly-Taylor equation, and Bouchets complementary hypothesis. *J. Hydrometeorol*. 2013, 14, 419–442.

Mallick, K., Jarvis, A. J., Boegh, E., Fisher, J. B., Drewry, D. T., Tu, K. P., Hook, S. J., Hulley, G., Ardö, J., Beringer, J., et al., 2014: A surface temperature initiated closure (STIC) for surface energy balance fluxes. *Remote Sens. Environ*. 2014, 141, 243–261.

Mallick, K., Boegh, E., Trebs, I., Alfieri, J. G., Kustas, W. P., Prueger, J. H., Niyogi, D., Das, N., Drewry, D. T., Hoffmann, L. and A. J., Jarvis, 2015: Reintroducing radiometric surface temperature into the Penman-Monteith formulation. *Water Resour. Res.*, 51(8), 6214-6243, DOI: 10.1002/2014WR016106.

Margulis, S. A., and D., Entekhabi, 2001: A coupled land surface-boundary layer model and its adjoint. *J. Hydrometeorol.*, 2(3), 274-296.

Margulis, S. A., 2002: Variational sensitivity analysis and data assimilation studies of the coupled land surface-atmospheric boundary layer system. Doctor of Philosophy at the Massachusetts Institute of Technology.

Margulis, S. A., and D., Entekhabi, 2003: Variational assimilation of radiometric surface temperature and reference-level micrometeorology into a model of the atmospheric boundary layer and land surface. *Mon. Wea. Rev.*, 131(7), 1272-1288.

Margulis, S., Kim, J. and T., Hogue, 2005: A comparison of the Triangle retrieval and variational data assimilation methods for surface turbulent flux estimation. *J. Hydrometeorol*., 6, 1063–1072.

Martínez Pérez, J. Á., García-Galiano, S. G., Martin-Gorriz, B., and A., Baille, 2017: Satellite-Based Method for Estimating the Spatial Distribution of Crop Evapotranspiration: Sensitivity to the Priestley-Taylor Coefficient. *Remote Sens*., 9(6), 611.

Moorhead, J. E., Marek, G. W., Colaizzi, P. D., Gowda, P. H., Evett, S. R., et al. 2017: Evaluation of sensible heat flux and evapotranspiration estimates using a surface layer scintillometer and a large weighing lysimeter. *Sensors,* 17 (10), 2350.

Moran, M. S., Kustas, W. P., Vidal, A., Stannard, D. I., Blanford, J. H., and W. D., Nichols, 1994: Use of ground-based remotely sensed data for surface energy balance evaluation of a semiarid rangeland. *Water Resour. Res*., 30(5), 1339–1349.

Nishida, K., Nemani, R. R., Running, S. W., and J. M., Glassy, 2003: An operational remote sensing algorithm of land surface evaporation. *J. Geophys. Res*.: *Atm*., 108.

Norman, J. M., Kustas, W. P., and K., Humes, 1995: A two-source approach for estimation of soil and vegetation energy fluxes from observations of directional radiometric surface temperature. *Agricul. For. Meteor*., 77(3-4), 263–293.

Pardy, A.J., Fisher, J.B., Goulden, M.L., Famiglietti, J. S., 2016. Ground heat flux: An analytical review of 6 models evaluated at 88 sites and globally. J. Geophys. Res. Biogeosci., 121(12), https://doi.org/10.1002/2016JG003591.

Peters-Lidard, C. D., Kumar, S. V., Mocko, D. M., and Y., Tian, 2011: Estimating evapotranspiration with land data assimilation systems, hydrological processes. *Hydrol. Processes*, 2011, 25, 3979–3992.

Polonio, D., and M. R., Soler, 2000: Surface fluxes estimation over agricultural areas. Comparison of methods and the effects of land surface inhomogeneity. *Theor. Appl. Meteor.*, 67: 65-79.

Qin, J., Liang, S., Liu, R., Zhang, H., and B., Hu, 2007: A weak-constraint based data assimilation scheme for estimating surface turbulent fluxes. *IEEE Geosci. Remote Sens. Lett.*, 4(4), 649–653.

Raoufi, R., and E., Beighley, 2017: Estimating Daily Global Evapotranspiration Using Penman–Monteith Equation and Remotely Sensed Land Surface Temperature. *Remote Sens*., 9, 1138.

Reichle, R. H., Crow, W. T., and C. L., Keppenne, 2008: An adaptive ensemble Kalman filter for soil moisture data assimilation. *Water Resour. Res*., 44, W03423

Ren, D., and M., Xue, 2016: Retrieval of land surface model state variables through assimilating screen level humidity and temperature measurements, *Adv. Meteor.*, http://dx.doi.org/10.1155/2016/1905076.

Rigden, A. J., and G. D., Salvucci, 2015: Evapotranspiration based on equilibrated relative humidity (ETRHEQ): Evaluation over the continental U. S., *Water Resour. Rese.*, 51(4), 2951-2973. doi:10.1002/2014WR016072.

Sandholt, I., Rasmussen, K., and J., Andersen, 2002: A simple interpretation of the surface temperature/vegetation index space for assessment of surface moisture status. *Remote Sens. Environ.*, 79, 213−224.

Salvucci, G. D., and P. Gentine, 2013: Emergent relation between surface vapor conductance and relative humidity profiles yields evaporation rates from weather data. *Article in Proceedings of the National Academy of Sciences*, 110(16), 6287-6291.

Santanello, J. A., Dirmeyer, P. A., Ferguson, C. R., Findell, K. L., Tawfik, A. B., Berg, A., Ek, M., Gentine, P., Guillod, B. P., Geerwaardem, C. V., Roundy, J., and V. Wulfmeyer, 2018: Land-Atmosphere Interactions: The LoCo Perspective, *Bull. Amer. Meteor. Soc.*, 99 (June), 1253-1272. doi: 10.1175/BAMS-D-17-0001.1.

Sellers, P. J., Hall, F. G., Asrar, G., Strebel, D. E., and R. E., Murphy, 1992: An overview of the first international satellite land surface climatology project (ISLSCP) field experiment (fife). *J. Geophys. Res.*, 97 (18), 345–371.

Shang, K. Z., Wang, S. G., Ma, Y. X., Zhou, Z. J., Wang, J. Y., Liu, H. L., and Y. Q. Wang, 2007: A scheme for calculating soil moisture content by using routine weather data, *Atmos. Chem. Phys*., 7, 5197-5206.

Sharma, V., Irmak, S., Kilic, A., and D., Mutiibwa, 2015: Application of remote sensing for quantification and mapping surface energy fluxes in south central Nebraska: Analyses with respect to field measurements. *Trans. ASABE*, 58(5), 1265–1285, doi:10.13031/trans.58.11091.

Shokri, N., Lehmann, P., Vontobel, P., and D., Or, 2008a: Drying front and water content dynamics during evaporation from sand delineated by neutron radiography. *Water Resour. Res.*, 44, W06418.

Shokri, N., Lehmann, P., and D., Or, 2008b: Characteristics of evaporation from partially wettable porous media. *Water Resour. Res.*, 45, W02415.

Shuttleworth, W. J., 2012: Terrestrial Hydrometeorology, John Wiley, West Sussex, U. K., doi:10.1002/9781119951933.

Sini, F., Boni, G., Caparrini, F., and D., and D., Entekhabi, 2008: Estimation of large-scale evaporation fields based on assimilation of remotely sensed land temperature. *Water Resour. Res.*, 44, W06410, doi:10.1029/2006WR005574.

Smeda, M. S., 1979: A bulk model for the atmospheric planetary boundary layer. *Bound.-Layer Meteor.*, 17, 411-428.

Song, L. S., Kustas, W. P., Liu, S. M., Colaizzi, P. D., Nieto, H., Xu, Z. W., et al., 2016: Applications of a thermal-based two-source energy balance model using Priestley-Taylor approach for surface temperature partitioning under advective conditions. *J. Hydrol*., 540, 574–587.

Stisen, S., Sandholt, I., Nørgaard, A., Fensholt, R., and K. H., Jensen, 2008: Combining the triangle method with thermal inertia to estimate regional evapotranspiration—Applied to MSG-SEVIRI data in the Senegal River basin. *Remote Sens. Environ.*, 112, 1242–1255.

Strebel, D. E., Landis, D. R., Huemmrich, K.F., and B. W., Meeson, 1994: Collected data of the First ISLSCP Field Experiment, Vol. 1: Surface observations and non-image data sets. CD-ROM. National Aeronautics and Space Aministration, Goddard Space Flight Center, Greenbelt, Maryland, USA. (available from http://www.daac.ornl.gov).

Stull, R. B., 1994: An Introduction to Boundary Layer Meteorology. Kluwer Academic.

Su, Z., 2002: The surface energy balance system (SEBS) for estimation of turbulent heat fluxes. *Hydrol. Earth Syst. Sci*., 6(1), 85–100.

Sun, L., Liang, S., Yuan, W., and Z., Chen, 2013: Improving a Penman-Monteith evapotranspiration model by incorporating soil moisture control on soil evaporation in semiarid areas. *Int. J. Digit. Earth*, 6(sup1), 134–156.

Tajfar, E., Bateni, S. M., Margulis, S. A., Gentine, P., and T., Auligne, 2019a: Estimation of turbulent heat fluxes via assimilation of air temperature and specific humidity into an atmospheric boundary layer model. Submitted to *J. Hydrometeorol*.

Tajfar, E., Bateni, S. M., Lakshmi, V., and M., Ek, 2019b: Estimation of surface heat fluxes via variational assimilation of land surface temperature, air temperature and specific humidity into a coupled land surface-atmospheric boundary layer model. Submitted to *J. Hydrol*.

Tajfar, E., Bateni, S. M., and T., Xu, 2019c: Evaluating the information content of reference-level air temperature and humidity for partitioning the available energy between the turbulent heat fluxes in different vegetative and climatic conditions. Submitted to *Remote Sens.*

Tang, R., Z.-L. Li, and B., Tang, 2010: An application of the Ts-VI triangle method with enhanced edges determination for evapotranspiration estimation from MODIS data in arid and semi-arid regions: Implementation and validation, *Remote Sens. Environ.*, 114, 540–551.

Van Heerwaarden, C. C., Vilà-Guerau de Arellano, J., Gounou, A., Guichard F., and F., Couvreux, 2010: Understanding the daily cycle of evapotranspiration: a method to quantify the influence of forcings and feedbacks. *J. of Hydrometeorol.*, 11, 1405- 1422. doi:10.1175/2010JHM1272.1.

Wang, K., Li, Z., and M., Cribb, 2006: Estimation of evaporative fraction from a combination of day and night land surface temperatures and NDVI: A new method to determine the Priestley–Taylor parameter. *Remote Sens. Environ*., 102, 293–305.

Wang, K. C., and R. E., Dickinson, 2012: A review of global terrestrial evapotranspiration: Observation, modeling, climatology, and climatic variability. *Rev. Geophys*., 50, RG2005.

Xia, Y., Mitchell, K., Ek, M., Sheffield, J., Cosgrove, B., Wood, E., et al., 2012: Continental-scale water and energy flux analysis and validation for the North American Land Data Assimilation System Project Phase 2 (NLDAS-2): 1. Intercomparison and application of model products. *J. Geophys. Res.*, 117, D03109.

Xia, Y., Mitchell, K., Ek, M., Cosgrove, B., Sheffield, J., Luo, L. F., et al., 2012: Continental-scale water and energy flux analysis and validation for North American Land Data Assimilation System Project Phase 2 (NLDAS-2): 2. Validation of model-simulated streamflow. *J. Geophys. Res.*, 117, D03110.

Xia, Y., Sheffield, J. S., Ek, M. B., Dong, J., Chaney, N., Wei, H., Meng, J., and E. F., Wood, 2014a: Evaluation of multi-model simulated soil moisture in NLDAS-2. *J. Hydrol.*, 512, 107–125.

Xia, Y., Ek, M., Mocko, D., Peters-Lidard, C., Sheffield, J., Dong, J., and E., Wood, 2014b: Uncertainties, correlations, and optimal blends of drought indices from the NLDAS multiple land surface model ensemble. *J. Hydrometeor*.

Xiao, Z. Q., Liang, S., Wang, J. D., Chen, P., Yin, X. J., Zhang, L. Q., and Song, J. L. (2014). Use of general regression neural networks for generating the GLASS leaf area index product from time-series MODIS surface reflectance. *IEEE Trans. Geosci. Remote Sens.,* 52(1), 209–223.

Xu, T. R., Liu, S. M., Liang, S., J., Qin, 2011a: Improving predictions of water and heat fluxes by assimilating MODIS land surface temperature products into common land model. *J. Hydrometeorol.*, 12, 227–244. 2011a.

Xu, T. R., Liang, S., S., Liu, 2011b: Estimating turbulent fluxes through assimilation of geostationary operational environmental satellites data using ensemble Kalman filter. *J. Geophys. Res.*, 116, D09109. 2011b.

Xu, Z., Liu, S., Li, X., Shi, S., Wang, J., Zhu, Z., Xu, T. R., Wang, W., and M., Ma, 2013: Intercomparison of surface energy flux measurement systems used during the HiWATER‐MUSOEXE. *J. Geophys. Res. Atmos*. 118 (23), 13140‐13157.

Xu, T., Bateni, S. M., Liang, S., Entekhabi, D., and K. Mao, 2014: Estimation of surface turbulent heat fluxes via variational assimilation of sequences of land surface temperatures from Geostationary Operational Environmental Satellites. *J. Geophys. Res. Atmos.*, 119(18), 10780-10798, doi:10.1002/.

Xu, T., Bateni, S. M., and S. Liang, 2015: Estimating turbulent heat fluxes with a weak-constraint data assimilation scheme: A case study (HiWATER-MUSOEXE). *IEEE Geosci. Remote Sens. Lett.*, 12(1), 68-72.

Xu, T., Bateni, S. M., Margulis, S. A., Song, L., and S., Lio, 2016: Partitioning evapotranspiration into soil evaporation and canopy transpiration via a two-source variational data assimilation system. *J. Hydrometeorol.*, 17(9), 2353-2370.

Xu, T., Bateni, S. M., Neale, C. M. U., Auligne, T., and S. Liang, 2018: Estimation of turbulent heat fluxes by assimilation of land surface temperature observations from GOES satellites into an ensemble Kalman smoother framework. *J. Geophys. Res. Atmos.*, 123(5), 2409-2423.

Xu, T., He, X., Bateni, S. M., Auligne, T., S. Liu, Xu, Z., Zhou, J., and Mao, K., 2019: Mapping regional turbulent heat fluxes via variational assimilation of land surface temperature data from polar orbiting satellites, *Remote Sens. Environ*., 221, 444-461.

Yao, Y., Liang, S., Cheng, J., Liu, S., Fisher, J., Zhang, X., et al. 2013: MODIS-driven estimation of terrestrial latent heat flux in China based on a modified Priestly-Taylor algorithm. *Agric. For. Meteorol.*, 171-172, 187–202.

Yao, Y., Liang, S., Li, X., Chen, J., Wang, K., Jia, K., et al. 2015: A satellite-based hybrid algorithm to determine the Priestley-Taylor parameter for global terrestrial latent heat flux estimation across multiple biomes. *Remote Sens. Environ.*, 165, 216–233.

Yilmaz, M. T., Anderson, M. C., Zaitchik, B., Hain, C. R., Crow, W. T., Ozdogan, M., Chun, J. A., and J., Evans, 2014: Comparison of prognostic and diagnostic surface flux modeling approaches over the Nile River basin. *Water Resour. Res.*, 50, 386–408, doi:10.1002/2013WR014194.

Zaitchik, B. F., Santanello, J. A., and S. V., Kumar, 2013: Representation of soil moisture feedbacks during drought in NASA unified WRF(NU-WRF), *J. Hydrometeorol.*, 14, 360–367.

Zhu, W., Jia, S., and A., Lv, 2017: A universal Ts-VI triangle method for the continuous retrieval of evaporative fraction from MODIS products. *J. Geophys. Res. Atmos*. 122, 10206‑10227. https://doi.org/10.1002/2017JD026964.

Zhuang, Q., and B. Wu, 2015: Estimating evapotranspiration from an improved tow-source energy balance model using ASTER satellite imagery. Water, 7(12), 6673-6688.